Rare-earth transition-metal intermetallics:

Structure-bonding-property relationships

by

Mi-Kyung Han

A dissertation submitted to the graduate faculty

in partial fulfillment of the requirements for the degree of

DOCTOR OF PHILOSOPHY

Major: Inorganic Chemistry

Program of Study Committee:
Gordon J. Miller, Major Professor
John D. Corbett
Vitalij Pecharsky
Patricia A. Thiel
L. Keith Woo

Iowa State University

Ames, Iowa

2006

Graduate College
Iowa State University

This is to certify that the doctoral dissertation of

Mi-Kyung Han

has met the dissertation requirements of Iowa State University

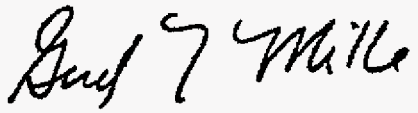

Major Professor

For the Major Program

Philippians 1: 6

Being confident of this, that he who began a good work

in you will carry it on to completion until the day of Christ Jesus.

~ to my precious children and lovely husband ~

TABLE OF CONTENTS

CHAPTER 1

General Introduction and Research Motivation

Introduction

1) Intermetallics

Rationalizing the structural properties and chemical bonding of materials has been a major objective of solid state chemistry. In particular, the structures and properties associated with rare-earth transition-metal intermetallics have generated interest within the solid state community because they exhibit various structure types and special electronic, magnetic, superconducting, and optical properties.[1-4] For example, $Nd_2Fe_{14}B$ is widely investigated for studying magnetic phase transitions and their permanent magnetic properties[5-7], and $RETM_2B_2C$ (RE = rare-earth or Sc, Y, La; TM = transition metal) have attracted much attention because of superconducting transition temperatures as high as T_C = 23 K and the coexistence of superconductivity and magnetic ordering phenomena[8-9].

In general, intermetallic compounds consist of two or more metallic or metalloid elements and show crystal structures different from the constituents. Substantial or complete disorder of the atoms among the crystallographic sites in an intermetallic structure generates numerous structural and stoichiometric flexibilities. Despite the large amount of intermetallic crystallographic data that have been accumulated, there is no general and consistent explanation for the structure-bonding-property relationships in terms of current electronic theory. Such fundamental algorithms, e.g., the octet rule, Wade's rules, and the 18-electron

Table 1. Summary of structure types of Hume-Rothery phases.[10]

Phase Type	Structure	*vec* range
α	f.c.c.	1.0 - 1.42
β	b.c.c.	1.36 - 1.59
μ	cubic	1.40 - 1.54
γ	b.c.c.	1.54 - 1.70
δ	cubic	1.55 – 2.00
ξ	h.c.p.	1.32 - 1.83
ε	h.c.p.	1.65 - 1.89
η	h.c.p.	1.93 – 2.0

rule, or other empirical models like Pauling's rules and bond-valence ideas of Brown are not completely effective for intermetallic phases.

Three major factors are commonly considered in connection with the stability of alloy phases: *valence electron concentration (vec), atomic size and chemical affinity.* The *valence electron concentration* can influence the formation of certain intermetallics, e.g. the Hume-Rothery phases. The structural trends of Hume-Rothery phases are rather well understood by their average valence electron concentration (*vec*) per atom. (Note: the *vec* can be counted in two ways; (1) the number of valence electrons per 'all' atoms, which is applied in the Hume-Rothery phases, and (2) the number of valence electrons per post-transition (or anionic) atoms). Table 1 summarizes the electronic phases of Hume-Rothery phases between 1.0 and 2.0 e^-/atom. *Atomic size* affects the packing efficiencies of intermetallic phases. The size of the minority components can influence the choice of $NaZn_{13}$- or $ThMn_{12}$- structure type for

various rare-earth iron silicides. Finally, *electronegativity* (A measure of their ability to accept electrons obtained by averaging ionization potential and *electron affinity* values for elements) plays an important role in the formation and observed structures of a special class of intermetallic phases, called Zintl phases. These compounds contain two kinds of metals: one is an electropositive metal (group 1 or 2 elements) and the other is a main group element from groups 13-16. The electropositive metals donate their valence electrons to the more electronegative main group elements, and the main group elements form an anionic network to achieve a closed shell electronic configuration. Therefore, the octet rule rationalizes the structure of nearly all "Zintl" compounds, which are usually insulating or semiconducting for stoichiometric compositions, and metallic for nonstoichiometric compositions.[11] Nevertheless, exploring the connection between structure and properties may achieve a fundamental understanding of intermetallic phase stability and properties so as to lead to the development of new functional materials for applications, such as permanent magnets or thermoelectric materials.

2) Iron-rich rare-earth intermetallics

Fe-rich, rare-earth intermetallics (RE–Fe) are a challenging group of compounds to study fundamental issues, because they exhibit excellent intrinsic magnetic properties as well as structural complexities, such as partial or mixed site occupancies, site preferences, and structural phase transitions. In RE–Fe compounds, the interplay between strongly correlated, localized RE 4*f* electrons and itinerant Fe 3*d* electrons gives rise to well known outstanding magnetic properties.[12] These magnetic properties also show dependence on composition and crystal structure of these materials.

The majority of compounds with a large coordination number at the rare-earth element crystallize in $NaZn_{13}$- (cubic), $ThMn_{12}$- (tetragonal), Th_2Ni_{17}- (hexagonal), Th_2Zn_{17}- (rhombohedral), or $RE_3(Fe,Ti)_{29}$-(monoclinic) structure types. The structures can be described by a complex packing pattern of different polyhedra. The coordinations of the rare-earth atom are schematically described in Figure 1.

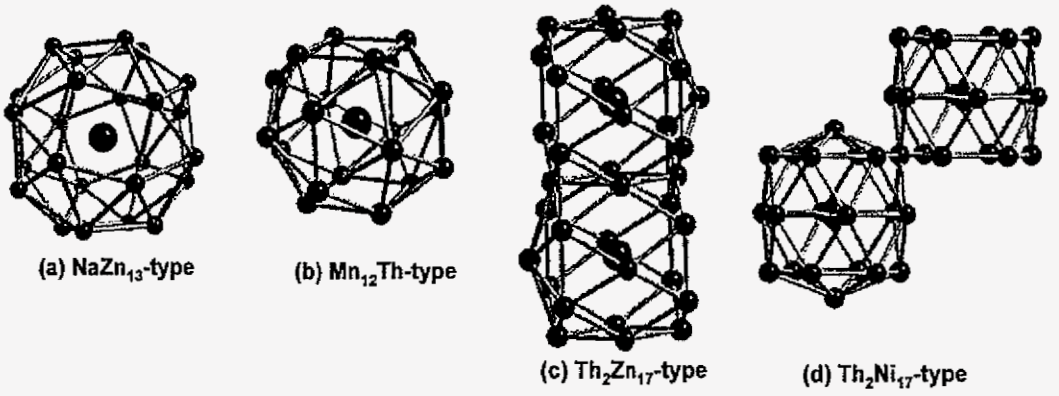

Figure 1. Coordination of RE atom by TM atoms in the following types of structures: (a) $NaZn_{13}$- , (b) $ThMn_{12}$- , (c) Th_2Zn_{17}- , and (d) Th_2Ni_{17}- type. Black and blue circle represent for RE atom and TM, respectively.

Both iron-rich $NaZn_{13}$- and $ThMn_{12}$-type structure exist, respectively, in the pseudo-binary $REFe_{13-x}T_x$ (T = Al, Si)[13-14] and $REFe_{12-x}T_x$ (T = Al, Si, Ga, Ti, V, Cr, Mn, Mo, W)[15]. RE_2Fe_{17}-type structures can be obtained in pseudobinary $RE_2Fe_{17-x}T_x$ (T = Al, Si, Ti, V, Cr, Mn, Co, Ga, Nb, Mo, W).[16-17]

The atomic radius of the rare-earth elements is an important factor to determine the crystal structure of iron-rich compounds. A large rare-earth atom prefers the $NaZn_{13}$-type phase, which has more coordinated iron around each RE than in the $ThMn_{12}$-phase.[18-19]

RE_2Fe_{17} compounds crystallize with two possible structures: Th_2Ni_{17}- and Th_2Zn_{17}-type.[20] In the case of heavier rare-earth metals the Th_2Ni_{17}-type structure often appears rather than the Th_2Zn_{17}-type structure, but the energy difference between these structures seems to be small since many RE_2Fe_{17} adopt both of structures, depending on the temperature. Th_2Zn_{17}-type structure is a high temperature phase or unstable phase. Fe-rich intermetallic compounds also crystallize in a monoclinic $RE_3(Fe,Ti)_{29}$-type structure,[21] which can be described as an alternated stacking of tetragonal $RE(Fe,Ti)_{12}$ and rhombohedral $RE_2(Fe,Ti)_{17}$ blocks.[22-23] Table 2 summarizes the existence of different structure types in Fe-rich rare-earth intermetallics.

Table 2. Existence of different structure types in Fe-rich rare-earth intermetallics.

	La	Ce	Pr	Nd	Sm	Eu	Gd	Tb	Dy	Ho	Y	Er	Tm	Yb	Lu
Ionic Radius:(+3e)	101.6	103.4	101.3	99.5	99.5	95	93.8	92.3	90.8	89.4	89.3	88.1	87	85.8	85
$NaZn_{13}$-	√	√	√	√											
$ThMn_{12}$-					√		√					√			
Th_2Ni_{17}-		√					√*			√	√	√	√	√	√
Th_2Zn_{17}-		√*	√	√	√						√*				
$RE_3(FeTi)_{29}$-				√	√		√				√				

* High temperature phase or unstable phase. Some RE-Fe compounds exist as ternary form with main group elements.

Dissertation Organization

The purpose of this thesis is to explore novel rare-earth, transition metal compounds and to investigate their structure and bonding and how these influence their properties. We have focused on the synthesis, characterization and electronic structure investigations, as well as physical properties of ternary rare-earth Fe-rich intermetallics, e.g., $LaFe_{13-x}Si_x$, and $Gd_{2-x}Fe_4Si_{14-y}$, etc. The main investigatory techniques used in this thesis are powder and single crystal X-ray diffractions, magnetic properties measurements, and electronic structure calculations. X-ray diffraction is a powerful technique which can provide information about atomic ordering and bonding within the structure. In addition to careful crystallography, electronic structure calculations are an essential tool for understanding the relationship between structure and chemical bonding in these compounds. Useful theoretical tools are the energy density of states (DOS), crystal orbital Hamilton population (COHP) and the electronic band structure. Manipulations of the density of states allow classification of bonding types and assignment of electron density to various atoms in a material. The projects described in the following pages will blend experiment and theory with the goal to achieve a better understanding of intermetallic phase stability and properties.

Chapter 1 gives a general introduction to this thesis.

Chapter 2 covers the general experimental techniques used in this thesis. It gives information about the equipments used, along with an overview of the analysis procedures used for characterizing the structures and properties.

Chapter 3 is the first chapter of experimental results. The crystal structures and phase analyses of the $LaFe_{13-x}Si_x$ system is discussed with respect to Si concentration.

The origin of the large entropy change of this system will be addressed from a structural perspective.

Chapter 4 presents results of electronic structure calculations on $LaFe_{13-x}Si_x$ systems. The magnetic properties, such as local magnetic moments and Curie temperature, are discussed with respect to Si concentration.

Chapter 5 is an investigation of rare-earth/iron/silicon systems, which show an interesting intergrowth feature and a complex superstructure. A series of polycrystalline rare-earth iron intermetallic compounds $RE_{2-x}Fe_4Si_{14-y}$ (R= Y, Gd, Tb, Dy, Ho, Er, Tm, Yb and Lu) was prepared by arc melting. Their structural characteristics and magnetic properties will be discussed. Result from transition electron microscopy (with professor Matthew Kramer *et al.*, Department of Materials Science and Engineering; Iowa State University) and Mössbauer spectroscopy (with professor Gary John Long, Department of Chemistry, University of Missouri-Rolla) also be presented as an attempts to characterize and understand the superstructure.

Chapter 6 is a theoretical investigation of $FeSi_2$ which shows the metal-semiconductor phase transition depending on the structure. We report our results for the total energy, the electronic density of states (DOS), and the band-gap diagram for actual and hypothetical structures of α-, β- and γ-phases. Band structure calculations shows the gap opening in β-$FeSi_2$ comes from the covalent mixing between the Fe 3*d* states and adjacent Fe atoms.

Chapter 7 reports the new compound $Tb_3Zn_{3.6(1)}Al_{7.4(1)}$ obtained from Al and Zn-rich ternary solutions. Structural characteristics and magnetic properties have been

investigated. The distribution of Zn and Al atoms are explained by TB-LMTO-ASA electronic structure calculations, which indicate that this new intermetallic phase can be classified among the so-called "polar intermetallics."

Chapter 8 presents a new structure type for Cr/Zn/Al compounds. Here, our interest lies mainly in the structural chemistry of such compounds.

Finally, **Chapter 9** is the conclusions produced from these studies and suggestions for future work on the samples studied.

References

1. Eisenmann, B.; Cordier, G. *In Chemistry, Structure and Bonding of Zintl Phases and Ions*; Kauzlarich, S. M., Ed.; VCH Publishers: New York, **1996**, p 61.

2. Corbett, J. D. *In Chemistry, Structure and Bonding of Zintl Phases and Ions*; Kauzlarich, S. M., Ed.,VCH Publishers: New York, **1996**, p 139.

3. Corbett, J. D. *Angew. Chem., Int. Ed.* **2000**, *39*, 670.

4. Miller, G. J.; Lee, C. -S.; Choe, W. in *Inorganic Chemistry Highlights* (Eds.: Meyer,G.; Naumann, D.; Wesemann, L.),Wiley-VCH, Weinheim, Germany, **2002**, p. 21.

5. Coelho, A. A.; Mohan, Ch. V.; Gama, S.; Kronmüller, H. *J. Magn. Magn. Mater.* **1996**, 163, 365.

6. Wang, H.; Zhao, F.; Chen, N.; Liu, G. *J. Magn. Magn. Mater.* **2005**, 295(3), 219.

7. Stankiewicz, J.; Bartolome, J.; Hirosawa, S. *Phys. Rev. B: Condens. Matte.* **2001**, 64(9), 094428.

8. Takagi, H.; Nohara, M.; Cava, R. J. *Physica B: Condens. Matter* (Amsterdam) **1997**, 292, 237.

9. Xu, M.; Canfield, P. C.; Ostenson, J.E.; Finnemore, D. K.; Cho, B. K.; Wang, Z. R.; Johnston, D. C. *Physica* **1994**, *C* 227, 321.

10. Barrett, C.; Massalski, T .B.; *Structure of Metals*, Pergamon Press, 3rd ed. **1980**, 248.

11. Corbett, J. D. *in Chemistry, Structure and Bonding of Zintl Phases and Ions;* Kauzlarich, S. M., Ed.; VCH publishers: New York, **1996**; Chapter 4.

12. Li, H. S.; Coey, J. M. D. *Handbook of Magnetic Materials* vol 6, ed Buschow, K. H. J. (Amsterdam: Elsevier) **1991**, p 1.

13. Palstra, T. T. M.; Mydosh, J. A.; Niewenhuys, G. J.; van der Kraan, A. M.; Buschow, K. H. J. *J. Magn. Magn. Mater.* **1983**, 36, 290.

14. Palstra, T. T. M.; Niewenhuys, G. J.; Mydosh, J. A.; Buschow, K. H. J. *Phys. Rev.* **1985**, B13, 4622.

15. Buschow, K. H. J. *J. Appl. Phys.* **1988**, 63, 3130.

16. Girt, Er.; Altounian, Z. *Phys. Rev.* **1998**, B57, 5711.

17. Girt, Er.; Altounian, Z. *J. Appl. Phys.* **2000**, 87, 4747.

18. Chang, H.; Chen, N.; Liang, J.; Rao, G. *J. Phys.; Condens. Matter.* **2003**, 15, 109.

19. Sakurada, S.; Tsutai, A.; Sahashi, M. *J. Alloys. Compds.* **1992**, 187, 67.

20. Han, X.; Jin, H.; Zhao, T. S.; Sun, C. C. *J. Phys.; Condens. Matter.* **1993**, 5, 8603.

21. Kalogirous, O.; Psycharis, V.; Saettas, L.; Niarchos, D. *J. Magn. Magn. Mater.* **1995**, 146, 335.

22. Li, H. S.; Cadogan, J. M.; Davis, R. L.; Margarian, A.; Dunlop, J. B. *Solid State Commun.* **1994**, 90, 487.

23. Shcherbakova, Ye. V.; Ivanova, G. V.; Yermolenko, A. S.; Belozerov, Ye. V.; Gaviko, V. S. *J. Alloys. compods.* **1992**, 182, 0199.

CHAPTER 2

Synthesis and Characterization

"The successful synthesis of single-phase, homogeneous (solid-state) products is often very much at the mercy of intrinsically slow, highly variable processes associated with mass transfer/diffusion rates within and between solid particles."[1]

Synthesis

The possibility to design inorganic materials with desired properties is a significant scientific challenge because, in preparative solid-state chemistry, it is difficult to predict either the existence of a hypothetical compound or the structures. Such design will depend on development of improved methods of synthesis, as well as information on structure and dynamics at an atomic level, which are obtained by a variety of experimental techniques and computational methods.

Materials

All starting elements were obtained from commercial sources and listed their sources and forms in Table 1. Most of them were used as received. Whenever appropriate, the various solid reactants were scraped to obtain a cleaner surface or pre-arc melted to eliminate the possible presence of the oxide surface before use.

Table 1. Starting materials used in the syntheses.

Element	Form	Purity[%]	Source	m.p.[K]	b.p.[K]
RE	shot	99.99~	Materials Preparation Center, Ames Lab	1071-1936	1469-3785
Fe	chips	99.98	Aldrich	1808	3023
Si	pieces	99.999	Aldrich	1683	2630
Cr	chips	99.995	Aldrich	2130	2945
Zn	granular	99.99	Fisher Scientific	692.73	1180
Al	foil	99.99	Aldrich	933.5	2740

Reaction Containers

The high-temperature preparation of samples may involve the unwanted reaction of the starting materials with the containers. The container should be inert during the reactions. Hence, tantalum tubes were chosen as inert reaction containers in this work because none of the rare-earth or transition metals used is known to form binary compounds with tantalum.[2] However, tantalum forms a variety of binary alloys with groups 13 and 14 elements.

The cleanness of the container is an important requirement. Therefore, the tantalum tubes were cleaned with an acid mixture containing of 55% concentrated H_2SO_4, 25% concentrated HNO_3 and 20% concentrated HF, by volume. The tubes were then rinsed with distilled water, dried in an oven, and crimped on one end. The tubes were sealed by arc welding in an argon atmosphere.[3] The reactants were then loaded into the prepared Ta containers. The open end of the tube was crimped shut, and then the sample tubes were sealed by arc welding as previously described. In order to protect the sealed tubes from oxidation at the high reaction temperatures, the sample tubes were placed in sealed evacuated

silica jackets. The silica jacket was heated with a natural gas/oxygen fueled torch to remove moisture from the silica and then to seal it.

Arc melting

Some of the intermetallic compounds investigated in this thesis were prepared by arc melting the stoichiometric quantities of the high purity elements on a water-cooled copper hearth using a tungsten electrode under a high-purity argon atmosphere. During the arc-melting procedure, a titanium or zirconium pellet was heated prior to melting the reactant mixture to further purify the argon atmosphere. The samples were remelted several times in order to ensure sample homogeneity.

Furnaces

Most of the high temperature reactions were performed using regular high-temperature resistance furnaces, which were controlled by a programmable temperature controller. The reaction time and temperature varied depending on demands for different reactions. Whenever possible, existing phase diagrams were used as a guide in determining reaction conditions. In most cases, the synthesis was performed according to the temperature profile in Figure 1. The first temperature, T_1, was set at a value allowing reactants to melt and to react with other elements. This ensured that the low melting reactants would not react with the container at high temperature. The second temperature, T_2, was used in attempts to grow single crystals. The typical heating rate r_1 was 10°C/min and cooling rates r_2 and r_3 were 0.1°C/min for the growth of single crystals.

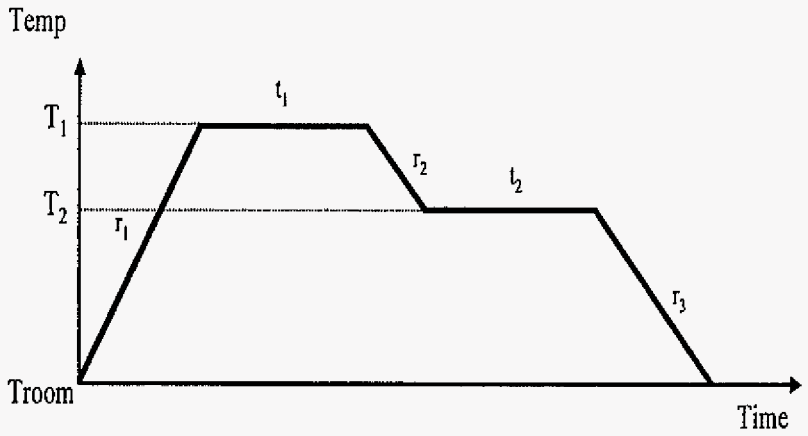

Figure 1. Typical temperature program for the synthesis.

Characterization Techniques

X-ray diffraction is the primary method for determining the phase and the crystalline structure.

Powder X-ray Diffraction

Powder X-ray diffraction patterns of the samples were obtained with a Huber image plate camera and monochromatic Cu $K\alpha_1$ radiation (λ = 1.540598 Å) at ambient temperature (ca. 295 ± 2K). Powdered samples were homogeneously dispersed on a Mylar film with the aid of a little petroleum jelly. The step size was set at 0.005° and the exposure time was 1 hr. Data acquisition was controlled via the *in-situ* program. By comparing line positions and intensities of the sample powder pattern with the calculated ones for a known structure type, the products were indexed and phases identified. The program *PowderCell* calculated

theoretical powder patterns. Lattice parameters were obtained from least squares refinement with the aid of a *Rietveld* refinement program[4].

Single Crystal X-ray Diffraction

Room-Temperature Single Crystal X-ray Diffraction Studies. Single crystals suitable for structure determination were selected from products (overall crystal dimensions : $0.1 \sim 0.2 \times 0.1 \sim 0.2 \times 0.1 \sim 0.3$ mm^3) and glued on glass fibers. Single-crystal data were collected on these crystals using a Bruker SMART APEX CCD diffractometer at room temperature using Mo $K\alpha_1$ radiation ($\lambda = 0.71073$ Å). Diffraction data were collected in a hemisphere or full-sphere of reciprocal space with 0.3° scans in ω for an exposure time of 10 sec per frame up to $2\theta = 56.55°$. Intensities were extracted and then corrected for Lorentz and polarization effects using the *SAINT* program.[5] The program *SADABS*[6] was used for empirical absorption correction. The structure refinements (full-matrix least-squares on F^2) were performed by using the *SHELXTL-PLUS* programs[7]. The refinement was based on F_0 using reflections with $I > 2\sigma(I)$. Program *XPREP*[8-9] was used to perform unit cell reduction and determination of possible space groups according to the systematic absences and the internal R-values of the data. Initial structural models were derived from direct methods calculations using *SHELXS* or from the positional parameters of an isostructural compound. Full matrix least squares refinements of the crystal structures were employed using program *SHELXL*.[10] Scale factors, positional, and isotropic thermal parameters were pursued until convergence was achieved at (shift/esd) < 0.02. Once isotropic refinements converged, the final anisotropic refinements were carried to convergence. Final refinements that included occupancy parameters were usually done to check the correctness of the model. Any

significant deviation from ideal occupancy meant that the intermetallic compound was non-stoichiometric or that the non-ideal site in the symmetric unit was occupied by different atoms. Final lattice parameters were obtained from careful indexing and comparisons of the experimental and calculated X-ray diffraction powder patterns. These parameters had smaller standard deviations and higher accuracy and were subsequently used for atomic distance and angle calculations using the program *DIAMOND.*[11]

Low-Temperature Single Crystal X-ray Diffraction Studies. The low- temperature data were obtained using a Bruker SMART 1000 CCD diffractometer with Mo Kα radiation ($\lambda = 0.71073$ Å). During these experiments, the temperature was stable within ± 1°C with respect to the value set for an experiment. Data collections and their refinements followed the same procedures as those of room-temperature.

Microprobe Analysis

Qualitative analysis was a routine test on interesting samples obtained from our synthetic work. The chemical compositions were analyzed by Energy dispersive spectroscopy (EDS) quantitative analysis using a JEOL 8400A scanning electron microscope, equipped with an IXRF Systems Iridium X-ray analyzer, and these compositions complemented the results from single crystal X-ray analysis. Samples for accurate quantitative analysis required a flat, microscopically smooth surface to maintain the validity of the path length calculation and to assure that the surface to be analyzed was homogeneous. The sample surface was polished by sandpaper and fine leather. Samples were inspected by back scattering and topological modes to determine the sites for elemental analysis. Whenever possible, the bulk compositions were used as standards to reduce any matrix

effects in the analysis. Otherwise, well-defined stoichiometric binary compounds and the pure elements were used as standards. Typical data collections utilized a beam of the 20 kV accelerating voltage and 30 nA beam current. This work was done by Dr. Alfred Kracher (Adjunct Assistant Professor; Department of Geological and Atmospheric Sciences; Iowa State University).

Microstructure characterization.

A Philips CM 30 transmission electron microscope (TEM) has been employed for TEM/high resolution TEM (HRTEM) investigations. TEM samples were prepared by using crash-flow method. This work was done by Dr. Yaqiao Wu (post-doc in professor Matthew Kramer's group; Department of Materials Science and Engineering; Iowa State University).

Property measurements

Magnetic susceptibility measurements were performed with a Quantum Design MPMS SQUID (QD MPMS) magnetometer. Measurements were usually made on pieces of polycrystalline material (5-150mg) in applied fields of 0.1~1 T, at temperatures from 1.85 - 300K. The magnetic susceptibility, χ, is fitted to a Curie-Weiss law which is given by

$$\chi = \frac{C}{(T - \Theta_w)}$$

where C is the Curie constant and Θ_w is the Curie-Weiss temperature. The Curie constant can be written in terms of the effective moment (μ_{eff}) as,

$$C = \frac{N\mu_{eff}^2}{3k_B}$$

here, N is the number of ions of magnetic elements, k_B is boltzman constant. μ_{eff} is the magnetic moment per formula unit.

The electrical resistance in zero field was measured with a Linear Research LR-700AC resistance bridge (f = 16 Hz, I = 1~3 mA) in the magnetic field - temperature environment of the same QD MPMS system, using a standard four - probe technique. The irregular shape of the polycrystalline sample was first polished to form a metal plate and then cut into a rectangular bar by using a wire saw. The dimensions of the sample was 1 × 1 × 3 mm^3. Electrical contact was made to the sample using Epo-tek H2OE silver epoxy, with typical contact resistances of 1-2 Ω. This work was done by Dr. Yuri Janssen (post-doc in professor Paul Canfield's group; Department of Physics and Astronomy; Iowa State University).

Electronic Structure Calculations

Tight-binding linear muffin-tin-orbital calculations. The electronic structures of many actual and hypothetical compounds were calculated self-consistently by using the tight-binding linear muffin-tin-orbital (TB-LMTO) method[12-15] within the atomic sphere approximation (ASA) using the LMTO Version 47 program. Exchange and correlation were treated in a local spin density approximation (LSDA).[16] All relativistic effects except spin-orbit coupling were taken into account using a scalar relativistic approximation.[17] Within ASA, space is filled with overlapping Wigner-Seitz (WS) atomic spheres. The radii of the WS spheres were obtained by requiring the overlapping potential to be the best possible approximation to the full potential according to an automatic procedure. The Löwdin

downfolding technique allows the derivation of few-orbital effective Hamiltonians by keeping only the relevant degrees of freedom and integrating out the irrelevant ones. The **k**-space integrations to determine the self-consistent charge density, densities of states (DOS) and crystal orbital Hamiltonian population (COHP)[18] were performed by the tetrahedron method[19]. The Fermi level was chosen as an internal reference level in all cases.

Extended Hückel tight binding calculations: The Extended Hückel method is an effective one-electron calculation of the orbital energies. These calculations provide information about the electronic structures of compounds such as the relative total energies, overlap populations, Mulliken population, as well as DOS and crystal orbital overlap population (COOP) curves. For a discussion of the Extended Hückel method and some examples of its applications, see references.[20-22]

References

1. Cheetham, A. K.; Day, P. *Solid State Chemistry*, Oxford University Press, Vol.1, "*Techniques*", **1987.**
2. Massalski, T. B. *Binary Alloy Phase Diagrams*; 2nd ed.; ASM international:**1992.**
3. Miller, A.E.; Dane, A. H.; Haberman, C. E.; Beaudry, B. J. *Rev. Sci. Inst.* **1963**, *34*, 644.
4. Hunter, B. A.; Howard, C. J. *Rietica*; Australian Nuclear Science and Technology Organization : Menai, Australia **2000.**
5. SMART; Bruker AXS, Inc.; Madison, WI, **1996.**
6. Blessing, R. H.: An empirical correction for absorption anisotropy. *Acta. Cryst.* **1995**, A 51, 33.
7. SHELXTL; Bruker ASX, Inc.: Madison, WI, **2000.**
8. Siemens Analytical X-Ray Systems Inc., Madison, USA.

9. Siemens Analytical X-Ray Instruments Inc.; SHELXTL PLUS, Release 5.0; Madison, USA, **1995**.

10. Sheldrick, G. M.; SHELXL-96. *Program for the Refinement of Crystal Structures*; University of Göttingen; Germany, **1996**.

11. Penningtona, W. T. *J. Appl. Cryst.* **1999**, 32, 1028.

12. Andersen, O. K. *Phys. Rev.* **1975**, B12, 3060.

13. Andersen, O. K.; Jepsen, O. *Phys. Rev. Lett.*, **1984**, 53, 2571.

14. Andersen, O. K.; Jepsen, O.; Glötzel, D. In *Highlights of Condensed-Matter Theory*; Bassani, F.; Fumi, F.; Tosi, M. P.; Lambrecht, W. R. L.; Eds.; North-Holland: New York, **1985**.

15. Andersen, O. K. *Phys. Rev. B*, **1986**, 34, 2439.

16. Von Barth, U.; Hedin, L. *J. Phys. C* **1972**, 5, 1629.

17. Koelling, D. D.; Harmon, B. N. *J. Phys. C* **1977**, 10, 3107.

18. Dronskowski, R.; Blöchl, P.: Crystal orbital Hamilton populations (COHP): energy-resolved visualization of chemical bonding in solids based on density-functional calculations. *J. Phys. Chem.* **1993**, 97, 8617.

19. Blöchl, P. E.; Jepsen, O.; Andersen, O. K. *Phys. Rev.* **1994**, B49, 16223.

20. Hoffmann, R. *Solids and Surfaces: A chemist's View of Bonding in Extended Structures*, VCH, 3, **1988**.

21. Hoffmann, R. *J. Chem. Phys.* **1963**, 39, 1397.

22. Burdett, J. K. *Chemical Bonding in Solids*, Oxford University Press, New York, **1995**.

CHAPTER 3

Structure and Bonding in $LaFe_{13-x}Si_x$: a MCE Material I. Structure

A paper to be submitted to *Inorg. Chem.*

Mi-Kyung Han, and Gordon J. Miller

Abstract

$LaFe_{13-x}Si_x$ ($1.0 \leq x \leq 5.0$) are an important series of compounds to study for possible efficient magnetic refrigeration. A systematic structural study of the compositional variation in $LaFe_{13-x}Si_x$ exhibits a structural transformation from the cubic $NaZn_{13}$-structure type to a tetragonal derivative due to preferential ordering of Fe and Si atoms. We observe that $LaFe_{13-x}Si_x$ crystallizes in the cubic structure for the range $1 \leq x \leq 2.6$, and tetragonal for $3.2 \leq x \leq 5$. Between $2.6 \leq x \leq 3.2$, it shows a two-phase mixture.

Temperature-dependent *single* crystal X-ray diffraction at various temperatures was performed on the cubic phases to examine the origin of the large magnetic entropy change. A thorough statistical and structural analysis of the data indicates that the noncentrosymmetric $F\bar{4}3c$ space group provides a more adequate atomic arrangement than the centrosymmetric $Fm\bar{3}c$ space group. This change in space group leads to divergence in specific sets of Fe-Fe distance below the Curie temperature. From electronic structure calculations (both Extended

Hückel and TB-LMTO) for the models, the $F\bar{4}3c$ model is more energetically favorable than the $Fm\bar{3}c$ model. Therefore, the giant magnetocaloric effect of cubic $LaFe_{13-x}Si_x$ alloys results from coupling between magnetic ordering and structural transformation, which is also shown in other magnetocaloric effect materials, such as $Gd_5Ge_{4-x}Si_x$.

Extended Hückel calculations on models of various icosahedral $Fe_{12-n}Si_n$ ($n = 1 \sim 5$) clusters and tight-binding LMTO calculations have been performed to study the effects of a main group element (Si) on stabilizing the cubic $NaZn_{13}$-type structure and influencing the transformation between cubic and tetragonal symmetry, as well as to study relationships among their chemical bonding, structure, and properties.

Introduction

Environmentally friendly, alternative refrigeration technologies have been the subject of intensive investigation to replace conventional ozone-depleting, energy-consuming refrigeration technology. Magnetic refrigeration offers the most energy efficient and ecologically clean cooling techniques over a wide range of temperatures up to room temperature and above,[1-3] and has been a focus of research over the past decade. Magnetic refrigeration is based on the magnetocaloric effect (MCE), which is an intrinsic property of any magnetic material and is characterized by a temperature change when a magnetic material is subjected to an adiabatic change of an external magnetic field.

This cooling effect is a consequence of the coupling of the magnetic sublattice of a material with an applied magnetic field, which results in a change in magnetic entropy of the

system. MCE is measured by that so-called adiabatic temperature change (ΔT_{ad}) or by the corresponding isothermal magnetic entropy change (ΔS_M).

It is well known that the total entropy S of a magnetic solid is the sum of the electronic, lattice and magnetic entropies (S_E, S_L and S_M, respectively). When a magnetic field is applied isothermally, the total entropy decreases due to the decrease in the magnetic contribution, and therefore the entropy change of a magnetic solid is given by

$$\Delta S_M(T,H) = S_M(T,H) - S_M(T,0) = \int_0^H \left(\frac{\partial S}{\partial H}\right)_T dH .$$

The magnetic entropy change is related to the change of the bulk magnetization as a function of magnetic field and the temperature through Maxwell's equation,

$$\left(\frac{\partial M}{\partial T}\right)_H = \left(\frac{\partial S}{\partial H}\right)_T ,$$

from which, we obtain the following expression:

$$\Delta S_M(T,H) = \int_0^H \left(\frac{\partial M}{\partial T}\right)_H dH .$$

The adiabatic temperature change is the corresponding temperature difference.

$$\Delta T_{ad}(S,H) = T(S,H) - T(S,0) = -\int_0^H \frac{T}{C_{H,P}}\left(\frac{\partial M}{\partial T}\right)_{H,P} dH$$

where $C_{H,P}$ is the heat capacity.

To search for applicable materials for magnetic refrigeration, it is necessary to identify materials with large $|\Delta S_M(T,H)|$. Moreover, because the $(\partial M/\partial T)_H$ value will be largest close to the Curie temperature, T_c, for a ferromagnetic material, a maximum $|\Delta S_M(T,H)|$ value can also be expected at T_c. Generally, due to their high magnetic

moments, rare-earth elements and their compounds are considered as the best candidate materials for finding a large MCE.

The MCE was first discovered in iron by Warburg in 1881[4]. In 1933, Giauque and MacDougall[5] first showed the practical use of the MCE to achieve temperatures below 1K by adiabatic demagnetization of paramagnetic $Gd_2(SO_4)_3 \cdot 8H_2O$. Zimm *et al.*[6] have demonstrated that Gd can be used to achieve cooling about 2 K/T at room temperature using a proof-of-principle magnetic refrigerator ($|\Delta S_M|$ = ~9.8 J/kg·K = 1.54 J/kg·K = 81.4 mJ/cm^3·K under 5 T field at Tc = 293 K). In 1997, Pecharsky and Gschneidner discovered a giant MCE in $Gd_5(Si_xGe_{1-x})_4$[7]. Subsequently, many other materials have been studied with respect to their magnetocaloric properties.

Recently, Hu *et al.*[8-16] suggested that $LaFe_{11.4}Si_{1.6}$ with the $NaZn_{13}$-structure type would be an appropriate material for efficient magnetic refrigeration, due to its first-order ferromagnetic transition and large magnetization at the Curie temperature of ~208 K. It shows a volume change, $|\Delta V/V|$, of ~1.05 % from ~11.48 Å to ~11.52 Å at T_c and that leads to a large magnetic entropy change ($|\Delta S_M|$ = 19.4 J/kg·K = 15.9 J/mol·K = 140 mJ/cm^3·K, at 208 K) which is comparable with that of other magnetic refrigerants, such as so-called the "giant magnetocaloric effect" materials ($Gd_5Ge_2Si_2$, $|\Delta S_M|$ = 18.5 J/kg·K = 18.27 J/mol·K = 140 mJ/cm^3·K under 5T at 276 K)[17] and $MnFeP_{1-x}As_x$ ($|\Delta S_M|$ = 18 J/kg·K = 2.98 J/mol·K = 132 mJ/cm^3· K, at 300 K)[18].

The pure binary RET_{13} (RE = rare earth, T = Fe, Co, Ni) compounds with the cubic $NaZn_{13}$-type structure do not exist for any of the transition elements except $LaCo_{13}$[19-20]; neither "$LaFe_{13}$" nor "$LaNi_{13}$" exists, which has been explained for two different reasons: (1)

$\Delta H_f^0(LaFe_{13})$ is predicted to positive[21]; and (2) "$LaNi_{13}$" is unstable with respect to $LaNi_5$ and unreacted Ni. However, the $NaZn_{13}$-type structure for RE-T system can be stabilized in pseudobinary $RET_{13-x}M_x$ (T = Fe, Co, Ni) systems by substituting small amounts of nonmagnetic, main group elements (M) such as Si or Al for some of the 3*d* metals.[22-23] It has been established that the third element plays an important role in the formation of other Fe-rich rare-earth intermetallic compounds, such as $RE(Fe, M)_{12}$[24-27] (M = Ti, V, Cr, or Mo) with the $ThMn_{12}$ type (1:12) structure, or $RE_2Fe_{17-x}M_x$ (M = Si, Ga, or Al) with the Th_2Zn_{17} type (2:17) structure.[28-29]

Depending on the fraction of the nonmagnetic element (M), the $RET_{13-x}M_x$ system (RE = rare-earth, T = Fe, Co, Ni, M = Si, Al) exhibits a structural transformation from cubic to a tetragonal derivative of the $NaZn_{13}$-structure type. For example, under our experimental conditions, the $LaFe_{13-x}Si_x$ system crystallizes in the cubic structure at room temperature for the range $1 \leq x \leq 2.6$, and shows the tetragonal structure within the range $3.2 \leq x \leq 5$, which is consistent with previous work[30]. Moreover, $LaFe_{13-x}Si_x$ shows a two-phase mixture within the range $2.6 < x < 3.2$. Also, in other $RET_{13-x}M_x$ systems, lower symmetry than cubic, such as tetragonal or orthorhombic, has been realized by decreasing the annealing temperature and increasing the annealing periods. Weihua *et al.*[31] have reported the structural transition from cubic to a body-centered orthorhombic structure in $LaFe_7Al_6$ by decreasing the annealing temperature from 1173 to 773 K and increasing the annealing period from 2 weeks to 2 months. ($LaFe_7Al_6$, a = 11.866 Å, V = 1670.76 Å^3 before annealing; then a = 8.561 Å, b = 8.206 Å, c = 11.812 Å, V = 829.81 Å^3 after annealing)

Their properties can also be tuned by adjusting the T/M ratio. For example, in

$LaFe_{13-x}Si_x$ compounds the Curie temperatures increase with increasing Si concentration, whereas the saturation magnetic moment decreases with increase of the concentration of the third element.[23, 32] Also, the magnetic transition changes gradually from first-order to second-order with increasing Si concentration.[33-34] All of these features imply a strong correlation among the electronic structure, properties, and the structural stability of $RET_{13-x}M_x$ systems.

Atomic radii of rare-earth elements and interatomic potentials have been used to predict the phase formation of $RET_{13-x}M_x$ structures.[33-34] However, the effect of rare-earth elements on the structural transformation might be smaller because of its rattling inside the cage of transition metals and third elements which surround the rare-earth elements. Also, it is difficult to obtain interatomic potentials of rare-earth containing compounds, because interatomic potentials are obtained based on theoretical cohesive energy curves. Such cohesive energy curves for rare-earth containing compounds are not specified in detail.

Up to now, all of the experimental data reported for $LaFe_{13-x}Si_x$ are based on polycrystalline samples containing various impurities.[10, 35-37] To our knowledge, however, a systematic through examination of these compounds, including their compositions, phase widths, atomic distributions, and electronic structures has not been reported so far. In order to better understand these features, it is particularly important to know the location of the substitutional atoms within the structure as the composition changes. To clarify these problems, in this work we have closely investigated three fundamental aspects of the $LaFe_{13-x}Si_x$ system by analyzing *single crystals*. These are (1) a detailed structural and theoretical study of the effects of a third element on stabilizing the structure and controlling the transformation of cubic $NaZn_{13}$-type structures to the tetragonal derivative, and (2) the relationship among structures, properties and bonding by analyzing the electronic structure of

$LaFe_{13-x}Si_x$ systems. Both of these aspects are believed to be essential for understanding how the minority components enhance the structural stability and influence the physical behavior of these magnetocaloric materials.

Experimental

Synthesis. The $LaFe_{13-x}Si_x$ ($1 \leq x \leq 6$) samples, each with a total mass of ~ 0.5g, were prepared by arc melting the stoichiometric quantities of the high purity elements on a water-cooled copper hearth using a tungsten electrode under a high-purity argon atmosphere. The starting materials (La rod, Ames Lab Rare-Earth Metals Preparation Center, 99.0 %; Fe chips (Aldrich, 99.98 %); Si pieces, Aldrich, 99.5 %) were pre-arc melted to remove impurities such as oxygen on the surface of the elements. During the arc-melting procedure, a titanium or zirconium pellet was heated prior to melting the reactant mixture to further purify the argon atmosphere. The samples were remelted several times in order to ensure sample homogeneity, and weight losses during the arc melting process were found to be less than 1-2 wt.%. The samples obtained were then wrapped in Ta foil (0.025 mm, Aesar, 99.8 %), sealed in evacuated fused silica capsules, and annealed at 1000 °C for 30 days and subsequently slowly cooled (about 80 °C/hr) to room temperature.

Chemical Analysis. Qualitative analysis was a routine test on interesting samples obtained from our synthetic work. The chemical compositions were analyzed by Energy dispersive spectroscopy (EDS) quantitative analysis of $LaFe_{13-x}Si_x$ ($1 \leq x \leq 6$) samples using JEOL 8400A scanning electron microscope, equipped with an IXRF Systems Iridium X-ray

analyzer, and these compositions complemented the results from single crystal X-ray analysis. Samples for accurate quantitative analysis required a flat, microscopically smooth surface to maintain the validity of the path length calculation and to assure that the surface to be analyzed was homogeneous. The sample surface was polished by sandpaper and fine leather. Samples were inspected by back scattering and topological modes to determine the sites for elemental analysis. Whenever possible, the bulk compositions were used as standards to reduce 36 any matrix effects in the analysis. Otherwise, well-defined stoichiometric binaries and the pure elements were used as standards.

Structure Determination. *Powder X-ray Diffraction Studies.* The phase analysis was performed by X-ray powder diffraction at room temperature and the crystal structure was confirmed by single-crystal X-ray diffraction. X-ray powder diffraction patterns of the samples were obtained with a Huber image plate camera and monochromatic Cu $K\alpha_1$ radiation (λ = 1.540598 Å) at ambient temperature (ca. 295 ± 2K). Powdered samples were homogeneously dispersed on a Mylar film with the aid of a little petroleum jelly. The step size was set at 0.005° and the exposure time was 1 hr. Data acquisition was controlled via the *in-situ* program. Lattice parameters were obtained from least squares refinement with the aid of a *Rietveld* refinement program.[38]

Room-Temperature Single Crystal X-ray Diffraction Studies. Suitable single crystals for structure determinations were selected from the sample (overall crystal dimensions: 0.1 ~ 0.2 × 0.1 ~ 0.2 × 0.1 ~ 0.3 mm^3) and glued on a glass fiber. Single-crystal data were collected on these crystals using a Bruker APEX CCD diffractometer at room temperature using Mo $K\alpha_1$ radiation (λ= 0.71073 Å). Diffraction data were collected in a hemisphere or full sphere

of reciprocal space with 0.3° scans in ω for an exposure time of 10 sec per frame up to 2θ = 56.55°. Intensities were extracted and then corrected for Lorentz and polarization effects using the SAINT program.[39] The program *SADABS*[42] was used for empirical absorption correction. The structure refinements (full-matrix least-squares on F^2) were performed by using the *SHELXTL-PLUS* programs.[40]

Low-Temperature Single Crystal X-ray Diffraction Studies. The low temperature data were obtained using a Bruker SMART 1000 CCD diffractometer with Mo Kα radiation. During the low-temperature experiments the temperature was stable within ± 1°C with respect to the value set for an experiment. Data collections and their refinements followed the same procedures as the room-temperature ones.

Electronic Structure Calculations. The electronic structures of many actual and hypothetical compounds were calculated self-consistently by using the tight-binding linear muffin-tin-orbital (TB-LMTO) method[41-44] within the atomic sphere approximation (ASA) using the LMTO Version 47 program. Exchange and correlation were treated in a local spin density approximation (LSDA).[45] All relativistic effects except spin-orbit coupling were taken into account using a scalar relativistic approximation.[46]

Within the atomic sphere approximation (ASA), space is filled with overlapping Wigner-Seitz (WS) atomic spheres. The radii of the WS spheres were obtained by requiring the overlapping potential to be the best possible approximation to the full potential according to an automatic procedure. The WS radii determined by this procedure are 4.41 ~ 4.50 Å for La, 2.51 ~ 2.60 Å for Fe and 2.51 ~ 2.54 Å for Si. The basis set included La 6*s*, 6*p*, 5*d* orbitals, Si 3*s*, 3*p* orbitals and Fe 4*s*, 4*p* and 3*d* orbitals. The Löwdin downfolding technique

allows the derivation of few-orbital effective Hamiltonians by keeping only the relevant degrees of freedom and integrating out the irrelevant ones. The **k**-space integrations to determine the self-consistent charge density, densities of states (DOS) and crystal orbital Hamilton populations (COHP)[47] were performed by the tetrahedron method[48]. The Fermi level was chosen as an internal reference level in all cases.

Extended Hückel tight binding calculations : To study the site preference of Si among 12 icosahedral sites in $LaFe_{13-x}Si_x$ compounds, semi-empirical, Extended Hückel calculations were performed on models of molecular icosahedra in which Si atoms occupy different atomic sites. The Extended Hückel method is an effective one-electron calculation of the orbital energies. These calculations provide information about the electronic structures of compounds such as the relative total energies, overlap populations, Mulliken population, as well as densities of states (DOS) and crystal orbital overlap population (COOP) curves. For a discussion of the Extended Hückel method and some examples of its application, see references.[49-52] By comparing total energies of each model, we can simply address the preference of Si atoms in a icosahedron. The parameters of the atomic orbitals used in the calculations are listed in Table 1.

------ Table 1 ------

Result and Discussion

Phase behavior in $LaFe_{13-x}Si_x$.

We studied the substitution effect of Si on the structures of $LaFe(Fe_{12-x}Si_x)$. Figure 1 shows two typical XRD patterns of $LaFe_{11.4}Si_{1.6}$ (a) and $LaFe_9Si_4$ (b) annealed at 1000°C. Comparison of Figures 1 (a) and (b) shows that with increasing Si content, x, the diffraction peaks of the cubic $NaZn_{13}$ phase split into separate peaks, further confirms the transformation from the cubic $NaZn_{13}$-type structure to the tetragonal derivative structure.

------ Figure 1 ------

Phase analysis of $LaFe_{13-x}Si_x$ was performed by X-ray powder diffraction (XRD) measurements at room temperature. Figure 2 (a) shows the XRD patterns of the series ($1 \leq x \leq 5$) studied here. According to experimental results, $LaFe_{13-x}Si_x$ compounds show single-phase cubic $NaZn_{13}$-type structure in the concentration range $1 \leq x \leq 2.6$, and the refined results obtained from least squares refinement with the aid of a *Rietveld* refinement program suggest that the Si atoms strongly prefer the crystallographic 96*i* position. For $LaFe_{10}Si_3$, X-ray diffraction showed that the cubic $NaZn_{13}$ phase still exists. However, many diffraction peaks show sign of splitting, indicating deviation from cubic symmetry. The composition around $2.6 < x < 3.2$ represents a transition range from cubic to the tetragonal structure. Whereas, for higher concentrations in Si ($3.2 \leq x \leq 5$), a reduction of symmetry was observed into the body-centered tetragonal cell (space group *I4/mcm*). The diffraction peaks were indexed accordingly. Then when the Si content x is increased to 6 ($x \geq \sim 6$), only trace amounts of tetragonal $NaZn_{13}$-type structure is observed in the product along with a major amounts of $LaFe_2Si_2$ and FeSi phase.

------ Table 1 and Figure 2 ------

Table 2 summarizes the lattice parameters of $LaFe_{13-x}Si_x$ obtained from the experiments. The lattice parameters were found to decrease with Si concentration. This behavior is expected from the difference between the metallic radii of Fe (1.25 Å) and Si (1.18 Å).[53] In Figure 2 (b), we also show the concentration dependence of the lattice parameter *a* on the Si content *x* in the $LaFe_{13-x}Si_x$ compounds. In Figure 2 (b), the circular dots represent the lattice parameters obtained from X-ray powder diffraction data and the triangles represent the lattice parameters from X-ray single crystal diffraction data. Those two different sets of lattice parameters match together well. So, in this paper, we will use single crystal lattice parameters for comparing bond distances at each composition and making models for electronic structure calculations.

Crystal Structure of $LaFe_{13-x}Si_x$.

$LaFe_{13-x}Si_x$ ($1 < x < 6$) adopts the $NaZn_{13}$-type and related structures. Depending on the Si concentration, it crystallizes in the cubic structure (space group $Fm\bar{3}c$, No. 226) and a tetragonal structure (space group *I4/mcm*, No. 140) at room temperature. The tetragonal structure is derived from the cubic $NaZn_{13}$-type structure by an atomic ordering of Fe and Si. The unit cell vectors of the two structures are related as follows:

$$a_{tet} = a_{cub}/\sqrt{2}, \quad b_{tet} = b_{cub}/\sqrt{2}, \text{ and } c_{tet} = c_{cub}.$$

Figure 3 shows the transformation of the unit cell projected along the *c* axis from the cubic $NaZn_{13}$-type to its tetragonal derivative structure.

------ Figure 3 ------

1) $LaFe_{13-x}Si_x$ ($1 \leq x \leq 2.6$): Cubic phases.

Figure 4 shows a slice of the structure of cubic $NaZn_{13}$-type $LaFe_{13-x}Si_x$ on the *ab* plane and the CsCl-type packing of La atoms with Fe-centered icosahedra.

------ Figure 4 ------

Each unit cell in the cubic structure contains eight formula units; the asymmetric unit contains three crystallographically inequivalent sites: 8*a*, 8*b*, and 96*i*. The La atoms occupy the 8*a* (¼, ¼, ¼) position; Fe_I atoms exclusively occupy the 8*b* (0, 0, 0) sites and Fe_{II}/Si are in 96*i* (0, *y*, *z*) position, so that we can formulate these compounds as $La[Fe(Fe_{12-x}Si_x)]$. The structure can be described as a CsCl-type packing of La and Fe_I-centered icosahedra, see Figure 4 (b). The La atoms are surrounded by 24 Fe_{II}/Si atoms in a "snub cube" arrangement with all equal La-Fe_{II}/Si distances as shown in Figure 5 (a). The snub cubes are nearly spherical polyhedra with site symmetry of O(432). The Fe_I atoms are located at the center of an icosahedron of 12 Fe_{II}/Si atoms with site symmetry of $T_h(m\bar{3})$. The two Fe_I-centered icosahedra are interconnected by stella quadrangulae such that they are arranged in an alternate pattern with adjacent icosahedra rotated 90° with respect to each other. Each Fe_{II}/Si site is surrounded by nine nearest Fe_{II}/Si atoms, one Fe_I atom and two La atoms.

We reexamined the room temperature lattice constants and the atomic coordinates of each site for several different compositions. In comparing our measured lattice constants with the literature values, the differences are rather small, whereas our values obtained from single-crystal X-ray refinements can give precise values for atomic positions. Details of the single crystal data collection parameters and crystallographic refinement results for cubic $LaFe_{13-x}Si_x$ are listed in Table 3. Atomic positions, site occupancy factors, and isotropic

displacement parameters for refined single crystal cubic $LaFe_{13-x}Si_x$ compounds are presented in Tables 4 and 5.

------ Table 3 ~ 5 ------

Neutron powder diffraction results[36] indicate that Si atoms substitute for Fe atoms randomly on the two different Fe sites, 8*b* and 96*i*. (Note: nuclear scattering lengths for each element is $b_{La} = 0.827 \times 10^{-12}$cm, $b_{Fe} = 0.954 \times 10^{-12}$cm, and $b_{Si} = 0.415 \times 10^{-12}$cm) However, based on the single crystal refinement, only the icosahedra-forming position, 96*i*, is distributed randomly by the Fe and Si atoms, but the centering position, 8*b*, is fully occupied by Fe atoms. Since the X-ray scattering factors of Fe and Si are quite different due to the wide separation in atomic numbers between the two elements, single-crystal X-ray diffraction is an effective method for the determination of the relative content of each element in a given crystal. The selected bond distances in the structure obtained by single crystal refinement are tabulated in Table 6. The atom labeling scheme used in the tables is explained in Figure 5, which also serves to illustrate the three building blocks from which the entire structure can be described: the snub cube, the centered icosahedron, and the stella quadrangula.

------ Figure 5 and Table 6 ------

The lattice parameter decreases from 11.488(1) Å to 11.405(1) Å with increasing silicon concentration (from x = 1.3 to x = 3.2). The distances from the central La atom to each of 24 atoms of the snub cube range from 3.3542(5) -3.3238(12). With increasing Si content, the La–Fe_{II}/Si distance decreases. The distances from the central Fe_I atoms to each of the 12 atoms of the icosahedron range from 2.4570(6) to 2.446(2). With increasing Si content, the Fe_I–Fe_{II}/Si distance decreases. There are two different distances within a single icosahedron,

6 longer distances (1) and 24 shorter distances (2). The stella quadrangula also contain two different distances, 4 longer distances (3) and 4 shorter distances (4). As shown in Table 5, interestingly, the inter-icosahedron bond lengths are significantly smaller than the intra-icosahedron ones. The longer inter-icosahedron distance (3) is hardly changed while the shortest Fe_{II}–Fe_{II} distances (4) decrease with increasing Si content. We will discuss the structural stability and magnetic properties upon Si concentration by analyzing the interaction of each building block later in this article.

2) $LaFe_{13-x}Si_x$ ($4 \leq x \leq 5$) : Tetragonal phases.

------ Figure 6 ------

Figure 6 shows a projection of the structure of tetragonal $LaFe_{13-x}Si_x$ on the *ab* plane and the CsCl-type packing of La atoms with Fe-centered icosahedra.

An ordered distribution of Fe_{II} and Si atoms on the 96*i* position of the cubic $NaZn_{13}$-type reduces the symmetry to the tetragonal space group, *I4/mcm*. Each unit cell in the tetragonal structure contains four formula units. The asymmetric unit contains five positions: 4*a*, 16*l*(1), 16*k*, 16*l*(2) and 4*d*. The La atoms occupy the 4*a* (0, 0, ¼) position; Fe_I atoms occupy the 4*d* (½, 0, ½) sites. When atomic ordering occurs, the 96*i* positions from the cubic $Fm\bar{3}c$ structure separate into three inequivalent positions, i.e. 16*k*, 16*l*(1), and 16*l*(2). The 16*k* (*x*, *y*, ½) sites and 16*l*(1) (*x*, *y*, *z*) sites are fully occupied by Fe_{II} atoms, while the 16*l*(2) (x, y, z) sites show mixed occupancy by Fe_{II} and Si atoms. The structure can be described as a CsCl-type packing of La and Fe_I-centered icosahedra, see Figure 6 (b).

------ Table 7 ~ 9 ------

Details of the single crystal data collection parameters and crystallographic refinement results for partially disordered tetragonal $LaFe_{13-x}Si_x$ are listed in Table 7. Atomic positions, site occupancy factors, and isotropic displacement parameters for refined single crystal data are presented in Tables 8 and 9. The Si atoms are found to share the only 16*l*(2) position with Fe_{II} atoms.

The near neighbor environments of the Fe/Si and La atoms in the tetragonal structure are very similar to that found for analogous atoms in the cubic $NaZn_{13}$-type structure. However, their bond lengths are slightly different, and their polyhedra are slightly distorted, see Figure 7.

------ Figure 7, Table 10 ------

The La atoms are surrounded by 24 Fe_{II}/Si atoms in a snub cube arrangement with three different La-Fe_{II}/Si distances from the central atom. The snub cube has site symmetry of D4. There are three different interactions between the central Fe_I atom and each of the 12 atoms of the icosahedron at distances of 2.424(2) Å, 2.440(1) Å and 2.478(1) Å. Therefore, the icosahedra centered by Fe_I atoms have site symmetry of $D2_h$. The stella quadrangulae also contain interactions at three distinct distances, 2.391(2) Å, 2.415 (2) Å, and 2.505(2) Å. Selected bond lengths for tetragonal $LaFe_{13-x}Si_x$ are tabulated in Table 10.

Distance Analysis of the Structural transformation.

When atomic ordering occurs, the cubic phase transforms into the tetragonal one. In order to explain the relation between cubic and tetragonal structures, we analyzed bond distances between atoms within the $La[Fe(Fe_{12-x}Si_x)]$.

------ Figure 8 ------

We can classify the Fe_{II}-Fe_{II} bond lengths into two types: the intracluster (**1**, and **2**), 6 longer distances **1** (red in Figure 8) and 24 shorter distances **2** (black in Figure 8) within a single icosahedron; and the intercluster (**3** and **4**), 4 longer distances **3** (blue in Figure 8) and 4 shorter distance **4** (cyan in Figure 8) between the icosahedron. The shortest Fe-Fe distance **4** in the system is the distance between the icosahedra (cyan color in Figure 8).

According to single crystal experimental results, most distances decrease as the Si concentration increases. The shortest distance **4** in the structure exhibits the most pronounced reduction (~1.39 %). The Fe_{II}-Fe_{II} nearest-neighbor interatomic distances between the neighboring icosahedra, **3** in Figure 8, remain nearly constant, being about 2.50(1) Å. The longer Fe_{II}-Fe_{II} distance within the icosahedron, **2** in Figure 8, increases slightly by 0.33 % from 2.685(1) to 2.694(1) Å. Whereas, the shorter Fe_{II}-Fe_{II} distance within the icosahedron, **1** in Figure 8, decreases by 0.63%, i.e. 2.559(1) to 2.543(1) Å.

The Fe_I-Fe_{II} distance, i. e., the radius of the icosahedron, decreases slightly by 0.45% with Si concentration, **5** in Figure 8. The La-Fe_{II} bond distance (**6**) shows 0.89% contraction from 3.354(1) to 3.324(1) Å. Further increase in Si concentration ($x \geq \sim 3.2$) leads to shorter contact between La and Fe_{II}, which is opposed due to a presumed repulsive La-Fe interatomic interaction potential (which leads to positive ΔH_f^0 for "$LaFe_{13}$"), thus cubic structure becomes unfavorable.

The distortion to the tetragonal structure appears as a contraction in the *ab*-plane which causes the distances between atoms in the icosahedra shorter in the *ab*-plane but longer along the *c*-axis. Based on our single crystal refinement and powder diffraction study for tetragonal $NaZn_{13}$-type structures, there are two kinds of interactions between the icosahedra in the structure, as shown in Figure 9. Fe_{II}-Fe_{II} interactions are the dominant linkage on the *ab*

plane, whereas on the *ac* plane Fe_{II}-Si interactions are dominant. As we mentioned before that the Fe_{II}-Fe_{II} bonds between icosahedra show largest contraction upon increasing the Si concentration. We will discuss the electronic structure corresponding to each plane later in this paper.

------ Figure 9 ------

Temperature dependence of structure.

Single crystal X-ray diffraction data were collected at various temperatures and were refined to obtain accurate lattice constants and atomic positions in order to examine the origin of the large magnetic entropy change, and we performed careful analysis of the structure on altering the magnetic state from paramagnetic to ferromagnetic with temperature. The lattice parameters as a function of temperature are shown in Figure 10.

Anomalies of the lattice parameters near T_C are observed. A similar feature was reported for other rare-earth–transition metal compounds.[54-56] Figure 10 shows that the lattice parameter for $LaFe_{11.7(1)}Si_{1.3(1)}$ increases from 11.4544(13) to 11.5116(13) Å across the magnetic phase transition, resulting in a volume expansion, $|\Delta V/V|$, of 1.51 %. The change of lattice parameter of $LaFe_{11.7(1)}Si_{1.3(1)}$ is sharp, implying a possible first order transition between the low temperature ferromagnetic phase and the high temperature paramagnetic phase. In contrast, $LaFe_{10.6(1)}Si_{2.4(1)}$ shows a small and broad change of lattice parameter. The lattice parameter for $LaFe_{10.6(1)}Si_{2.4(1)}$ increases from 11.4479(13) to 11.4731(13) Å, resulting in a volume expansion, $|\Delta V/V|$, of just 0.66 %.

------ Figure 10 ------

We do notice an unusual lattice parameter change near the Curie temperature, shown in Figure 10. This result may be associated with the metamagnetic phase transition above the Curie temperature which was reported by Fujita, et al.[13-14,57] A metamagnetic phase transition is related to electronic structure, such as spin fluctuations or to an exchange interaction of magnetovolume effects at finite temperature.[58-61] These results are explained in terms of the double minimum structure in the free energy as a function of magnetic moment (M) and volume (V), that is, these phase transitions are caused by the difference in the energy gain against temperature.

This volume change near the Curie temperature can be explained by magnetovolume effect. Above the Curie temperature in the paramagnetic state, there are randomly oriented magnetic dipoles. With decreasing temperature, the compound seems to display a normal thermal contraction. However, below the Curie temperature, all magnetic dipoles in the material tend to align themselves into the ferromagnetic state and make the volume expansion. Generally, two different kinds of interactions are reported for Fe-rich intermetallics depending on the distance of nearest-neighbor Fe atoms: When the distance between nearest neighbor Fe atoms are larger than the critical value of about 2.45Å, the magnetic alignment between nearest neighbor Fe atoms are ferromagnetic. The alignment is antiferromagnetic for smaller distances.[56] In this experiment, we can notice that, with increasing Si concentration, the change of lattice parameter and Fe-Fe bond lengths before and after transition gradually decreases, thus the effect of them on the magnetic alignment gradually changes from ferromagnetic to antiferromagnetic. $LaFe_{11.7(1)}Si_{1.3(1)}$ shows larger volume expansion than $LaFe_{10.6\,(1)}Si_{2.4(1)}$, thus it has more ferromagnetic ordering to induce larger magnetization change near its Curie temperature. Therefore, on the basis of Maxwell

relation between magnetization and the entropy changes, larger magnetization change in $LaFe_{11.7(1)}Si_{1.3(1)}$ induces larger entropy changes. To understand the mechanism for such a large entropy change at the Curie temperature, detailed theoretical and experimental work has been carried out to investigate the coupling between magnetism and lattice in $LaFe_{13-x}Si_x$ system.

On the space groups of room- and low-temperature modifications of $LaFe_{13-x}Si_x$.

Cubic, Fe-rich $LaFe_{13-x}Si_x$ phases have been arranged the $Fm\bar{3}c$ space group both at room and low temperatures.[30] Since a giant magnetocaloric effect results from coupling between magnetic ordering and structural transformation[62-63], it was assumed that the cubic $LaFe_{13-x}Si_x$ alloys undergo some kind of structural perturbation while preserving the $Fm\bar{3}c$ space group. Up to now, all of the structural information was based on powder x-ray diffraction data, since X-ray-quality single crystals could not be obtained; detailed structural evaluation driven by temperature around T_c is not yet well understood.

Based on powder diffraction experiments, the higher symmetry $Fm\bar{3}c$ group was chosen as the right one, and the room- and low-temperature structures were refined based on this space group. Indeed, the $Fm\bar{3}c$ group yields good structural results even for single crystal data at room and low temperatures (see R values in Tables 11).

------ Table 11 ------

However, the possibility of the non-centrosymmetric $F\bar{4}3c$ group could not excluded, and we decided to refine the structures in this space group and compare results with those for

$Fm\bar{3}c$. According to the Hamilton test[64], the $F\bar{4}3c$ space group can always be accepted with higher that 99% probability below the transition temperature, while at higher temperatures the probability level is lower. In all tests, the $Fm\bar{3}c$ space group was never a statistically preferred choice. The conclusions reached on the space group from the Hamilton test must be also structurally represented in terms of atomic arrangements, before they can be accepted as valid.

Diffraction extinction conditions for the Bragg reflections indicate two possible space groups: non-centrosymmetric $F\bar{4}3c$ and centrosymmetric $Fm\bar{3}c$. For details about these groups see, for instance, the International Tables for Crystallography.[65] The main geometrical effect of symmetry reduction $Fm\bar{3}c \rightarrow F\bar{4}3c$ is to remove the mirror plane in the icosahedral clusters but to cause hardly any changes between the clusters, illustrated in Figure 11.

------ Figure 11 ------

We performed detailed analysis of the interatomic distances for the two space groups. The majority of the distances matched each other within one standard deviation despite the difference in the atomic coordinates of the Fe_{II}/Si site between the two space groups (e.g. Fe_I-Fe_{II}/Si, Fe_{II}/Si - Fe_{II}/Si bonds in Figure 12).

------ Figure 12 ------

However, during the symmetry reduction $Fm\bar{3}c \rightarrow F\bar{4}3c$, bonds involving Fe_{II} sites are split into two groups, there is a large change in distances between the two space groups (Figure 12). This divergence is larger than three standard deviations, and it becomes even more pronounced around the ordering/transition temperature. This bond analysis clearly indicates that the $F\bar{4}3c$ space group provides a more adequate atomic arrangement than the

$Fm\bar{3}c$ space group, and thus, should be accepted as a true space group for the cubic, Fe-rich La(Fe, Si)$_{13}$ phases. From electronic structure calculation (Hückel and LMTO47) for the two space groups, $F\bar{4}3c$ is more energetically favorable than $Fm\bar{3}c$. We will discuss this later in the electronic structure calculation section.

The simultaneous change in the volume, V, of the system and coupling between magnetic ordering and structural perturbation should be the crucial reason for the great magnetic entropy change in the $LaFe_{13-x}Si_x$ system. The decrease in magnetocaloric effect with Si concentration might be due to the reduction in the volume change near T_c with Si concentration, because large volume expansion leads to a large increase in the magnetic moment, thus the entropy change also increases. Similar discontinuity of the lattice parameter is also observed for the intermetallic FeRh compound at the phase transition temperature, which also shows a giant MCE. However, this compound has the irreversible volume change, $|\Delta V/V| = \sim 0.9\ \%$.[66]

Ordering of Atoms on the Icosahedral Network.

According to known experiments, ternary main group elements randomly occupy the 96*i* sites in the cubic structures of $LaFe_{13-x}Si_x$, and prefer to occupy the 16*i*(2) sites in the tetragonal structure.

Because an icosahedron serves as the basic building block of the $LaFe_{13-x}Si_x$ structure, the site preference of the stabilizing atoms can be explored by carrying out the relative stabilities of the stereoisomers (or *polytypes* in mathematical terminology)[67] for various arrangements of Fe and Si atoms among the vertices of the icosahedron based on the analysis

of the total electronic energy. The model for random occupation of atoms in each icosahedron was built by considering several structures with different atomic arrangements of Fe and Si atoms. Distribution of different atoms over two or more independent sites in a structure is known as a coloring problem.[68]

Figure 13 shows all possible stereoisomers of $A_{13-n}B_n$ (n = 0, 1, 2, 3) centered-icosahedra upon replacing several different number of A atoms by B atoms. The enumeration of all possible stereoisomers for centered or noncentered icosahedra are well discussed by B. K. Teo[69-72] and by K. J. Nordell[73] using Polya's theorem.

------ Figure 13 ------

As an example, an A-centered icosahedron A_9B_4, for the composition $LaFe[Fe_8Si_4]$, has ten distinct ways of arranging the eight A and four B atoms among the vertices of the icosahedron. The relative energies of the ten possible arrangements are numbered from lowest (1) to highest (**10**) energy configurations in Figure 14 (a): Fe atoms are blue and Si atoms are green. A graphical representation of the relative total energies of icosahedron upon the number of homoatomic contact is shown in Figure 14 (b).

------ Figure 14 ------

In order to examine the variation in total energy of each atomic arrangement, we treated La atoms as classical cations, donating three electrons to the metallic framework. Therefore, it is more accurate to describe $LaFe_9Si_4$ as $^{3}_{\infty}[Fe(Fe_8Si_4)]^{3-}$ with 91 valence electrons. ($LaFe_9Si_4 = 91e^-$, Fe:8, Si:4, La:3).

According to molecular orbital calculations of total energies, we can formulated two site preference rules: (1) the most stable structures are those with the fewest number of homoatomic Si-Si contacts, shown in Figure 14 (a); and (2) the energies increase linearly

with the number of homoatomic contacts, shown in Figure 14(b). These rules are extremely helpful in the assignment of the third element among icosahedral sites in the $La(Fe_{13-x}Si_x)$ system and understanding the relative stabilities of the system upon Si concentration. A similar plot for $\{Cu(Cu_4Al_8)\}^{2-}$ in Figure 14 (b) gives rise to the same conclusion.[80]

The calculated total energies for various atomic arrangements for three different compositions, i.e., $LaFe_{11}Si_2$, $LaFe_{10}Si_3$, and $LaFe_9Si_4$, are shown in Figure 15. Because the relative orders of the calculated total energies are meaningful, the absolute energies are scaled by subtracting the total energies for one stereoisomer from the most stable structure at each composition. Each line in Figure 15 represents a different atomic configuration. For example, $LaFe_{11}Si_2$ has three different electronic arrangements because it has three different lines in the column including the baseline as zero. Similarly, $LaFe_{10}Si_3$ has five different arrangements.

In general, the lower total energies should be thermodynamically more stable. In Figure 15, the energy differences between the lowest atomic configuration and next lowest one for the compositions $LaFe_{10}Si_3$, $LaFe_{11}Si_2$, and $LaFe_9Si_4$ are 0.35eV, 0.61eV, and 0.8eV, respectively. The shaded red box in Figure 15 indicates the region that we can reach experimentally by arc melting, about ~ 0.4 eV (corresponding to ca. 4750K). Within this temperature region, the $LaFe_9Si_4$ has one or two electronic arrangements that can contribute to create an ordered structure. However, $LaFe_{10}Si_3$ and $LaFe_{11}Si_2$ have more than three possible arrangements, so that the entropic effects of a mixture or all of these arrangements certainly favor the disordered arrangement of atoms in these two systems at elevated temperatures. This prediction accounts well for the previous results of *cubic* $BaCu_5Al_8$[80]

which has smaller energy difference between each energy configuration, and of the structural transformation of $LaFe_7Al_6$[31] by annealing at low temperature for prolonged times.

------ Figure 15 ------

We have also performed various calculations on full three-dimensional (3-D) structures of tetragonal $LaFe_9Si_4$ using several different arrangements of these clusters. The total energies clearly show that even though **1** in Figure 16 has the lowest energy configuration for a molecular icosahedron, arrangement **5** in Figure 16 shows the lowest energy after building the 3-D structure. This result is consistent with the site preference rule driven from the molecular icosahedron calculation that the network wants to minimize the number of homoatomic contacts. Results from the theoretical calculations are graphically summarized in Figure16.

------ Figure 16 ------

In tetragonal $LaFe_9Si_4$ with space group *I*4/*mcm*, the energy of Model **3** is the lowest because it creates the smallest number of homoatomic contacts within the 3-D structure. Si entering into the 16*l*(2) site of the tetragonal structure, Model 3, has a lower energy than Model 2 which has Si entering 16*l*(1) sites, and than model 4 whose Si enters 16*k* site. Therefore, Si atoms will preferentially occupy 16*l*(2) sites in the tetragonal $LaFe_9Si_4$. The next preferred sites are 16*l*(1), for $x \geq 4$. The 16*k* site is completely avoided. This theoretical calculated site preference of Si atom is consistent with the experimental result obtained by the x-ray diffraction refinement. According to the information obtained from these molecular icosahedron and 3-D structure calculations, it is clearly more energetically favorable for the Si atoms to be well separated from each other.

Conclusion

The X-ray powder and single crystal diffraction was performed on $LaFe_{13-x}Si_x$ intermetallics to investigate their structure-bonding-property relationships. The main results of present work are summarized as follows.

1. $LaFe_{13-x}Si_x$ crystallizes in the cubic structure for the range $1 \leq x \leq 2.6$, and tetragonal for $3.2 \leq x \leq 5$. Between $2.6 \leq x \leq 3.2$, it shows a two-phase mixture.
2. Temperature-dependent *single* crystal X-ray diffraction at various temperatures was performed on the cubic phases in order to examine the origin of the large magnetic entropy change. The bond analyses at various temperatures clearly indicate that the $F\bar{4}3c$ space group provides a more adequate atomic arrangement than the $Fm\bar{3}c$ space group. Therefore, the giant magnetocaloric effect of cubic $LaFe_{13-x}Si_x$ alloys results from coupling between magnetic ordering and structural transformation
3. Based on Fe-Fe interatomic distance analyses, the bonding character within *ac* plane induces the shorter *c*-axis than $\sqrt{2}\,a$, while further drives the structural transformation.
4. With increasing Si concentration, the change of lattice parameter and Fe-Fe bond lengths before and after transition gradually decreases, thus the effect of them on the magnetic alignment gradually changes from ferromagnetic to antiferromagnetic.

References

1. Brown, G. V. *J. Appl. Phys.* **1976**, 47, 3673.

2. Gschneidner, K. A. Jr.; Pecharsky, V. K.; Tsokol, A. O. *Rep. Prog. Phys.* **2005**, 68, 1479.

3. Brück, E. *J. Phys. D: Appl. Phys.* **2005**, 38, R381.

4. Warburg, E. *Ann. Phys.* **1881**, 13, 141.

5. Giauque, W. F.; MacDougall, D. P. *Phys. Rev.* **1933**, 43, 768.

6. Zimm, C.; Sternberg, A.; Pecharsky, V.; Gschneidner, K. A. Jr.; Osborne, M.; Anderson, I. *Adv. Cryog. Eng.* **1998**, 43, 1759.

7. Pecharsky, V. K.; Gshneidner, K. A. Jr. *J. Magn. Magn. Mater.* **1999**, 200, 44.

8. Hu, F. X.; Shen, B. G.; Sun, J. R.; Cheng, Z. H.; Rao, G. H.; Zhang, X. X. *Appl. Phys. Lett.* **2001**, 78, 3675.

9. Hu, F. X.; Shen, B. G.; Sun, J. R.; Cheng, Z. H.; Zhang, X. X. *J. Phys.;Condens. Matter.* **2000**, 12, L691.

10. Zhang, X. X.; Wen, G. H.; Wang, F. W.; Wang, W. H.; Yu, C.H; Wu, G. H. *Appl. Phys. Lett.* **2000**, **77**, 3072.

11. Hu, F. X.; Shen, B. G.; Sun, J. R.; Cheng, Z. H. *Phys. Rev.* **2001**, B64, 012409.

12. Fujieda, S.; Fujita, A.; Fukamichi, K.; Yamazaki, Y.; Lijima, Y. *Appl. Phys. Lett.* **2001**, 79, 653.

13. Fujita, A.; Fukamichi, K. *IEEE Trans. Magn.* **1999**, 35, 3796.

14. Fujita, A.; Akamatsu, Y.; Fukamichi, K. *J. Appl. Phys.* **1999**, 85, 4756.

15. Hu, F.; Shen, B.; Sun, J.; Cheng, Z.; Rao, G.; Zhang, X. *Appl. Phys. Lett.* **2004**, 78, 3675.

16. Fujita, A.; Fujieda, S.; Hasegawa, Y.; Fukamichi, K. *Phys. Rev.* **2003**, B67, 104416.

17. Pecharsky, V. K.; Gschneidner, K. A. Jr. *Appl. Phys. Lett.* **1997**, 70, 3299.

18. Tegus, O.; Brück, E.; Buschow, K. H. J.; de Boer, F. R. *Nature* (London) **2002**, 415, 150.

19. Buschow, K. H. J. *Rep. Progr. Phys.* **1977**, 40, 1197.

20. Palstra, T. T. M.; Nieuwenjuys, G. J.; Mydosh, J. A.; Buschow, K. H. J. *J. Appl. Phys.* **1984**, 55, 2367.

21. Rao, G. H.; Wu, S.; Yan, X. H.; Zhang, Y. L.; Tang, W. H.; Liang, J. K. *J. Alloys. compds.* **1993**, 202, 101.

22. Palstra, T. T. M.; Nieuwenhuys, G. J.; Maudosh, J. A.; Buschow, K. H. J. *Phys. Rev.* **1985**, B31, 4622.

23. Palstra, T. T. M.; Mydosh, J. A.; Nieuwenhuys, G. J., Van Der Kraan, A. M.; Buschow, K. H. J. *J. Magn. Magn. Mater.* **1983**, 36, 290.

24. Sun, H.; Akayama, M.; Tatami, K.; Fujii, H. *Physica* B **1993**, 183, 33.

25. Kuz'min, M. D. *J. Appl. Phys.* **2000**, 88, 7217.

26. Buschow, K. H. J. *J. Appl. Phys.* **1988**, 63, 3130.

27. del Moral, A.; Algarabel, P. A.; Marquina, C.; de la Fuente, C.; Ibarra, M. R. *J. Magn. Magn. Mater.* **1994**, 131, 247.

28. Huang, M.; Ching, W. Y.; Zong, Q. G. *J. Appl. Phys.* **1997**, 81, 5112.

29. Long, G. J.; Marasinghe, G. K.; Mishra, S.; Pringle, O. A.; Hu, Z.; Yelon, W. B.; Middleton, D. P.; Buschow, K. H. J. Grandjean, F. *J Appl. Phys.* **1994**, 76, 5383.

30. Tang, W. H.; Liang, J. K.; Rao, G. H.; Yan, X. H. *Phys. Status Solidi* **1994**, 141, 217.

31. Weihua, T.; Jingkui, L. *Phys. Rev.* **1994**, B49, 49.

32. Wen, G. H.; Zheng, R. K.; Zhang, X. X.; Wang, W. H.; Chen, J. L.; Wu, G. H. *J. Appl. Phys.* **2002**, 91, 8537.

33. Chang, H.; Chen, N.; Liang, J.; Rao, G. *J. Phys.;Condens. Matter* **2003**, 15, 109.

34. Sakurada, S.; Tsutai, A.; Sahashi, M. *J. Alloys. Compds.* **1992**, 187, 67.

35. Tang, W.; Liang, J.; Chen, X.; Rao, G. *J. Appl. Phys.* **1994**, 76, 4095.

36. Wang, F.; Wang, G.; Hu, F.; Kurbakov, A.; Shen, B.; Cheng, Z. *J. Phys: condens. Matter*, **2003**, 15, 5269.

37. Liu, X.; Altounian, Z.; Ryan, D. H. *J. Phys.; Condens. Matter,* **2003**, 15, 7385.

38. Hunter, B. A.; Howard, C. J. *Rietica*; Australian Nuclear Science and Technology Organization : Menai, Australia, **2000**.

39. SMART; Bruker AXS, Inc.; Madison, WI, **1996.**

40. Blessing, R. H.: An empirical correction for absorption anisotropy. *Acta. Cryst.*. **1995**, A 51, 33.

41. Andersen, O. K. *Phys. Rev.* **1975**, B12, 3060.

42. Andersen, O. K.; Jepsen, O. *Phys. Rev. Lett.* **1984**, 53, 2571.

43. Andersen, O. K.; Jepsen, O.; Glötzel, D. In *Highlights of Condensed-Matter Theory*; Bassani, F.; Fumi, F.; Tosi, M. P.; Lambrecht, W. R. L.; Eds.; North-Holland: New York, **1985**.

44. Andersen, O. K. *Phys. Rev.* **1986**, B34, 2439.

45. Von Barth, U.; Hedin, L. *J. Phys. C* **1972**, 5, 1629.

46. Koelling, D. D.; Harmon, B.N. *J. Phys. C* **1977**, 10, 3107.

47. Dronskowski, R.; Blöchl, P. *J. Phys. Chem.* **1993**, 97, 8617.

48. Blöchl, P. E.; Jepsen, O.; Andersen, O.K. *Phys Rev.* **1994**, B49, 16223.

49. Hoffmann R. *Solids and Surfaces: A chemist's View of Bonding in Extended Structures*, VCH, 3 **1988**.

50. Hoffmann, R. *J. Chem. Phys*. **1963**, 39, 1397.

51. Burdett, J. K. Chemical Bonding in Solids, Oxford University Press, New York, **1995**.

52. Ammeter, J. H.; Bürgi, H. -B; Thibeault, J. C.; Hoffmann, R. *J. Am. Chem. Soc.* **1978**, 100, 3686.

53. Huheey, J. E.; Keiter, E. A.; Keither, R. L. *Inorganic Chemistry: Principles of Structure and Reactivity*, 4th Ed., Harper Collins College Publishers, **1993**, pp. 292.

54. Kamar´ad, J.; Arnold, Z.; Morellon, L.; Algarabel, P. A.; Ibarra, M. R.; Fuerst, C. D. *J. Appl. Phys.* **1996**, 79, 4656.

55. Gratz, E. *et al. J. Phys.: Condens. Matter.* **1995**, 7, 597.

56. Givord, D.; Lemaire, R. *IEEE Trans. Magn.* **1974**, 10, 109.

57. Fujita, A.; Fujieda, S.; Fukamichi, K. *Phys. Rev.* **2001**, 65, 014410.

58. Saito, H.; Yokoyama, T. ; Terada, Y. ; Fukamichi, K.; Mitamura, H. ; Goto, T. *Solid State Commun.* **2000**, 113, 447.

59. Goto, T.; Shindo, Y.; Ogawa, S.; Harada, T.; *Physca* B **1997**, 237, 482.

60. Yamada, H. *Phys. Rev.* **1993**, B47, 11211.

61. Yamada, H.; Terao, K. *J. Phys. : Condens. Matter* **1994**, 6, 10805.

62. Choe, W.; Pecharsky, V. K.; Pecharsky, A. O.; Gschneidner, K. A. Jr. ; Young, V. G. Jr.; Miller, G. J. *Phys. Rev. Lett.* **2000**, 84, 4617.

63. Pecharsky, V. K.; Gschneidner, K. A. Jr. *Adv Mater* **2001**, 3, 683.

64. Hamilton, W. C. *Acta Cryst.* **1965**, 18, 502.

65. Hahn, T. editor, *International Tables for Crystallography*, vol. A, fifth edition, Kluwer Academic Publishers, **2002**.

66. Annaorazov, M. P.; Nikitin, S. A.; Tyurin, A. L.; Asatryan, K. A.; Dovletov, A. K. *J. Appl. Phys.* **1996**, 79, 1689.

67. McLarnan, T. J.; Moore, P. B. In *Structure and Bonding in Crystals*, Vol. II; O'Keeffe, M., Navrotsky, A., Eds.; Academic Press: New York, **1981**; p 133.

68. Miller, G. J. *Eur. J. Inorg. Chem.* **1998**, 5, 523.

69. Teo, B. K.; Zhang, H.; Kean, Y.; Dang, H.; Shi, X. *J. Chem. Phys.* **1993**, 9 (4), 2929.

70. Teo, B. K.; S, A.; Elber, R.; Zhang, H. *Inorg. Chem.* **1998**, 37, 2482.

71. McLarnan, T. *J. Solid State Chem.* **1978**, 26, 235.

72. Burdett, J. K. *Inorg. Chem.* **1975**, 14, 375.

73. Nordell, K. J.; Miller, G. J., *Inorg. Chem.* **1999**, 38, 579.

Table 1. Atomic parameters for Extended Hückel Calculations.

	Orbital	H_{ii}(eV)	ζ_1	C_1	ζ_2	C_2
Fe	4 *s*	-9.22	1.9			
	4 *p*	-5.37	1.9			
	3 *d*	-12.28	5.55	0.5411	1.8	0.6734
Si	3 *s*	-17.3	1.63			
	3 *p*	-9.2	1.43			

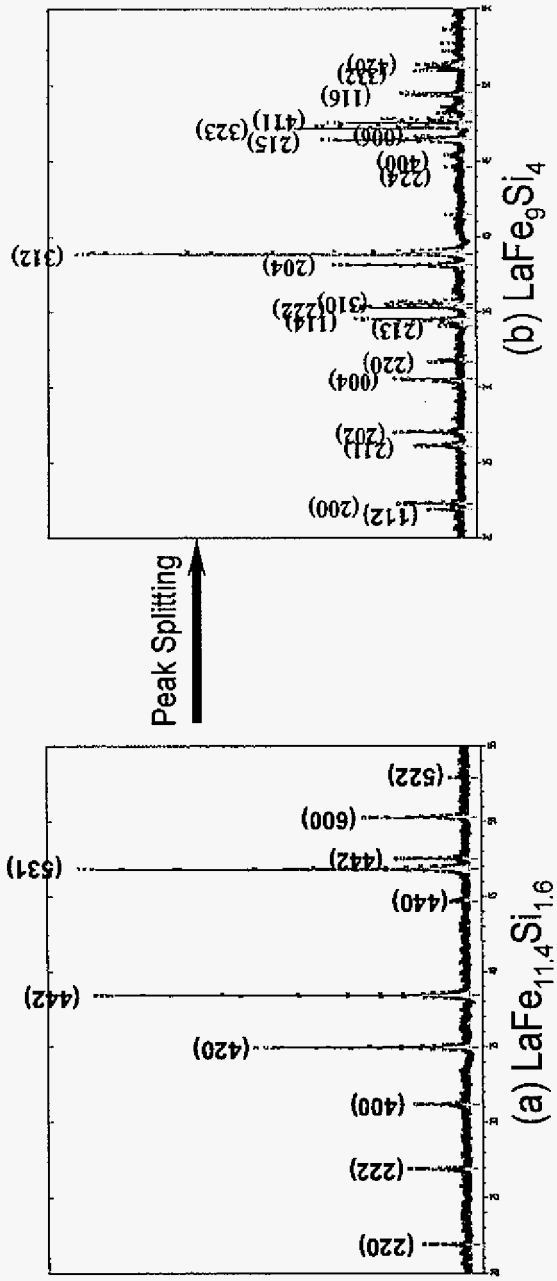

Figure 1. Typical XRD powder patterns of (a) $LaFe_{11.4}Si_{1.6}$ and (b) $LaFe_9Si_4$ annealed at 1000°C

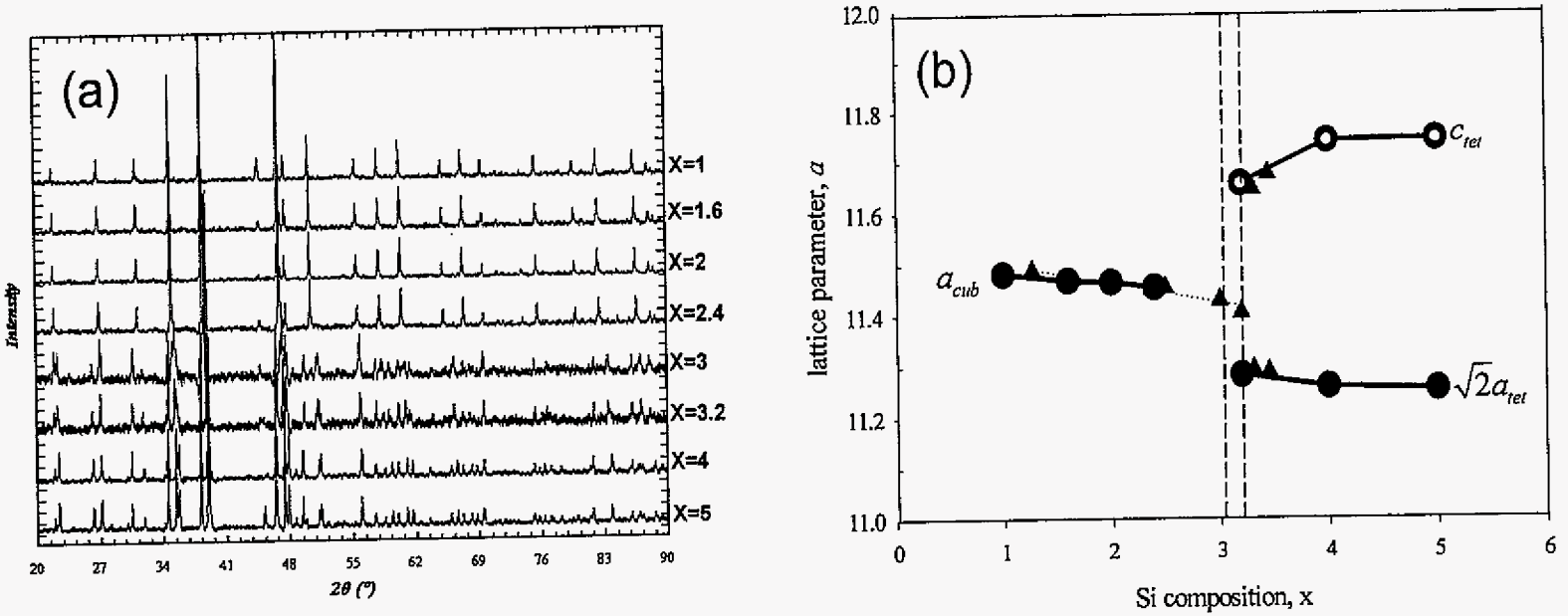

Figure 2. (a) The XRD patterns of $LaFe_{13-x}Si_x$ at room temperature. (Cu K_α radiation). (b)The concentration dependence of the lattice parameter a (or $\sqrt{2}a_{tet}$ and c for tetragonal) of the $NaZn_{13}$-type structure in the $LaFe_{13-x}Si_x$ compounds at room temperature. ▲ represent for the single crystal lattice parameter.

Table 2. Crystallographic data of $LaFe_{13-x}Si_x$ at room temperature.

Loaded composition,x	Structure type	Space group	Unit cell dimensions, Å		
			a	*a*	*c/a*
1.0	$NaZn_{13}$	$Fm\bar{3}c$	11.4811(2)	.....	.....
1.6	$NaZn_{13}$	$Fm\bar{3}c$	11.4685(3)	.....	.....
2.0	$NaZn_{13}$	$Fm\bar{3}c$	11.4651(2)	.....	.....
2.4	$NaZn_{13}$	$Fm\bar{3}c$	11.4564(3)	.....	.....
3.2	$Ce_2Ni_{17}Si_9$*	$I4/mcm$	7.9795(2)	11.6580(3)	0.68
4.0	$Ce_2Ni_{17}Si_9$	$I4/mcm$	7.9628(2)	11.7421(3)	0.68
5.0	$Ce_2Ni_{17}Si_9$	$I4/mcm$	7.9588(3)	11.7454(5)	0.68

* $Ce_2Ni_{17}Si_9$ -type structure is a fully ordered tetragonal variant of the cubic $NaZn_{13}$-type.

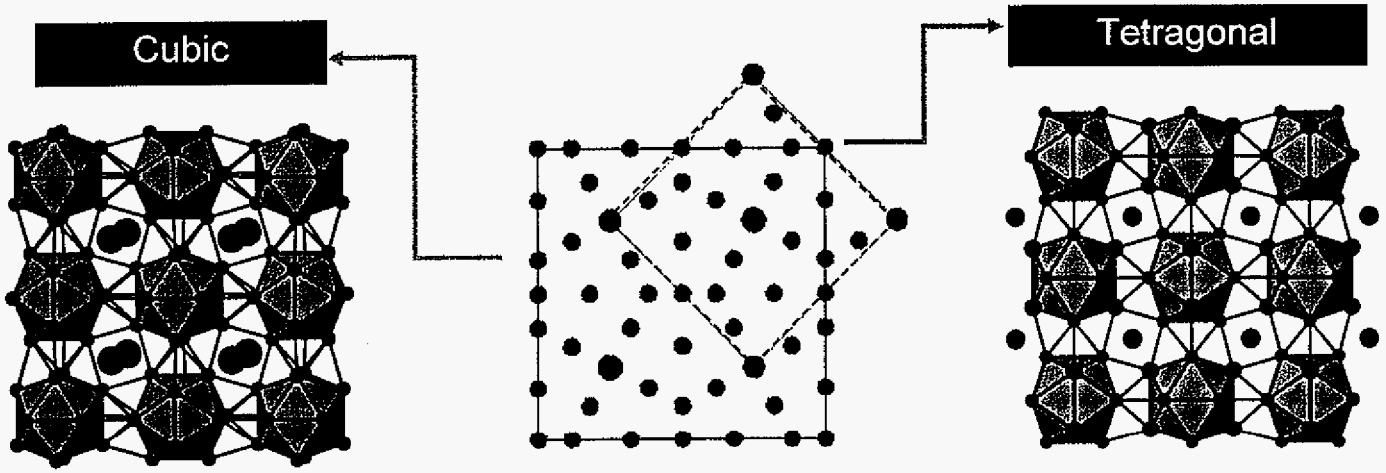

Figure 3. The transformation of unit cell projection along the *c*-axis from cubic $NaZn_{13}$-type to its tetragonal derivative. The solid line indicates the cubic unit cell, and the dash line indicates the tetragonal one.

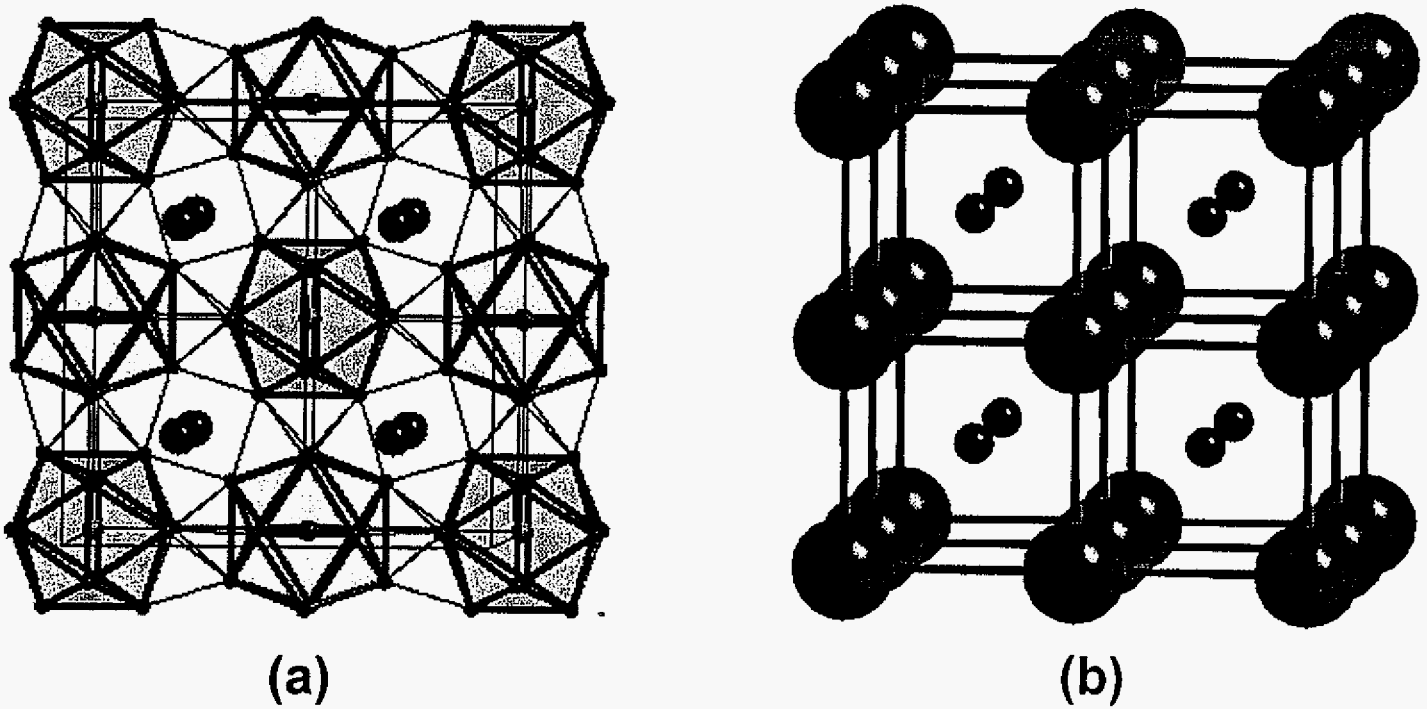

Figure 4. (a) A slice of cubic $LaFe_{13-x}Si_x$ structure. The large red circles are La atoms in 8*a*, the smaller green circles are the Fe_I atoms in 8*b*, and the small blue circles are the Fe_{II}/Si atoms in 96*i*. (b) The CsCl-type packing of La atoms (small circles) and Fe_I-centered icosahedra (large circles).

Table 3. Crystallographic Data from Single-Crystal X-ray Diffraction Measurements for $LaFe_{11.73(5)}Si_{1.27(7)}$ **(1)**, $LaFe_{11.36(5)}Si_{1.64(7)}$ **(2)**, $LaFe_{11.01(11)}Si_{1.99(20)}$ **(3)**, $LaFe_{10.64(8)}Si_{2.36(11)}$ **(4)**, $LaFe_{10.47(10)}Si_{2.53(14)}$ **(5)**, $LaFe_{10.17(15)}Si_{2.83(18)}$ **(6)**, and $LaFe_{9.76(43)}Si_{3.24(36)}$ **(7)** at 300K.

Identification code	1	2	3	4	5	6	7
Crystal system	cubic	cubic	cubic	cubic	cubic	cubic	cubic
Space group	*F m -3 c*	*F m -3 c*	*F m -3 c*	*F m -3 c*	*F m -3 c*	*F m -3 c*	*F m -3 c*
a (Å)	11.4881(13)	11.4706(13)	11.4631(13)	11.4531(13)	11.4463(13)	11.4288(13)	11.4051(13)
Formula weight	6630.4384	6548.2688	6470.5408	6388.3712	6350.6176	6283.9936	6192.9408
Volume, Å^3	1516.16(30)	1509.2(3)	1506.28(30)	1502.34(30)	1499.67(30)	1492.80(29)	1483.53(29)
Z	8	8	8	8	8	8	8
dcal(g/cm^3)	4.373	4.339	4.296	4.252	4.235	4.210	4.174
Abs. coeff., mm^{-1}	13.875	13.432	27.082	25.634	12.755	13.58	12.465
F(000)	1532	1503	3118	2930	1460	1503	1436
Crystal size, mm^3	0.19×0.15×0.26	0.16×0.18×0.25	0.20×0.12×0.21	0.16×0.12×0.27	0.18×0.25×0.28	0.2×0.24×0.32	0.21×0.21×0.36
$2\theta_{max}$, °	56.22	56.22	56.22	56.22	56.22	56.22	56.22
Reflections collected	1882	1860	1496	1872	1887	1764	1504
Indep. reflections	95	95	95	95	96	94	92
R(int)	0.029	0.0251	0.0416	0.0633	0.0556	0.0336	0.0329
Data / parameters	95 / 10	95 / 11	95 / 11	95 / 11	96 / 10	94 / 11	92/ 11
Goodness-of-fit on F^2	1.283	1.121	1.291	1.184	1.334	1.410	1.535
R1, [I>2s(I)]	0.0106	0.0099	0.028	0.0151	0.0221	0.0218	0.0343
wR2[I>2s(I)]	0.0237	0.0245	0.0611	0.034	0.057	0.0507	0.0885
R1, (all data)	0.0111	0.0099	0.0283	0.0151	0.0221	0.0218	0.0343
wR2(all data)	0.024	0.0245	0.0612	0.034	0.057	0.0507	0.0885
(Δr)max, min (e/Å3)	0.65/-0.52	0.32/-0.33	1.31/-0.99	0.53/-0.40	0.93/-1.40	0.67/-0.99	1.19/-1.74

[a] $R1 = \sum \| |F_o| - |F_c| \| / \sum |F_o|$; $R_w = \left[\sum w(|F_o| - |F_c|)^2 \right] / \sum w(F_o)^2]^{1/2}$; $w = 1 / \sigma^2(F_o)$

Table 4. Atomic coordinates and the fractional coordinates of the 96*i* sites

	Wyck.	x	y	z
La	8*a*	¼	¼	¼
Fe_I	8*b*	0	0	0
Fe_{II}/Si	96*i*	0	y	z

Identification code	96*i*	x	y	z	Occ. (Fe_{II} / Si)
1		0	0.1791(1)	0.1169(1)	0.89(1) / 0.11(1)
2		0	0.1792(1)	0.1170(1)	0.86(1) / 0.14(1)
3		0	0.1791(1)	0.1172(1)	0.83(2) / 0.17(2)
4		0	0.1791(1)	0.1175(1)	0.80 (1) / 0.20(1)
5		0	0.1792(1)	0.1174(1)	0.79(1) / 0.21(1)
6		0	0.1791(1)	0.1177(1)	0.76(2) / 0.24(2)
7		0	0.1790(2)	0.1181(2)	0.73(2) / 0.27(3)

Table 5. Anisotropic displacement parameters ($Å^2 \times 10^3$) for cubic $LaFe_{13-x}Si_x$ structure.

Identification code		Wyck.	U11	U22	U33	U23	U13	U12
1	La	8*a*	7(1)	7(1)	7(1)	0	0	0
	Fe_I	8*b*	8(1)	8(1)	8(1)	0	0	0
	Fe_{II}/Si	96*i*	8(1)	7(1)	9(1)	1(1)	0	0
2	La	8*a*	8(1)	8(1)	8(1)	0	0	0
	Fe_I	8*b*	8(1)	8(1)	8(1)	0	0	0
	Fe_{II}/Si	96*i*	7(1)	9(1)	8(1)	0	0	1(1)
3	La	8*a*	4(1)	4(1)	4(1)	0	0	0
	Fe_I	8*b*	6(1)	6(1)	6(1)	0	0	0
	Fe_{II}/Si	96*i*	5(1)	5(1)	7(1)	1(1)	0	0
4	La	8*a*	7(1)	7(1)	7(1)	0	0	0
	Fe_I	8*b*	8(1)	8(1)	8(1)	0	0	0
	Fe_{II}/Si	96*i*	9(1)	10(1)	8(1)	-1(1)	0	0
5	La	8*a*	6(1)	6(1)	6(1)	0	0	0
	Fe_I	8*b*	8(1)	8(1)	8(1)	0	0	0
	Fe_{II}/Si	96*i*	7(1)	8(1)	6(1)	1(1)	0	0
6	La	8*a*	10(1)	10(1)	10(1)	0	0	0
	Fe_I	8*b*	12(1)	12(1)	12(1)	0	0	0
	Fe_{II}/Si	96*i*	11(1)	11(1)	11(1)	-1(1)	0	0
7	La	8*a*	9(1)	9(1)	9(1)	0	0	0
	Fe_I	8*b*	11(2)	11(2)	11(2)	0	0	0
	Fe_{II}/Si	96*i*	11(1)	10(1)	10(1)	0(1)	0	0

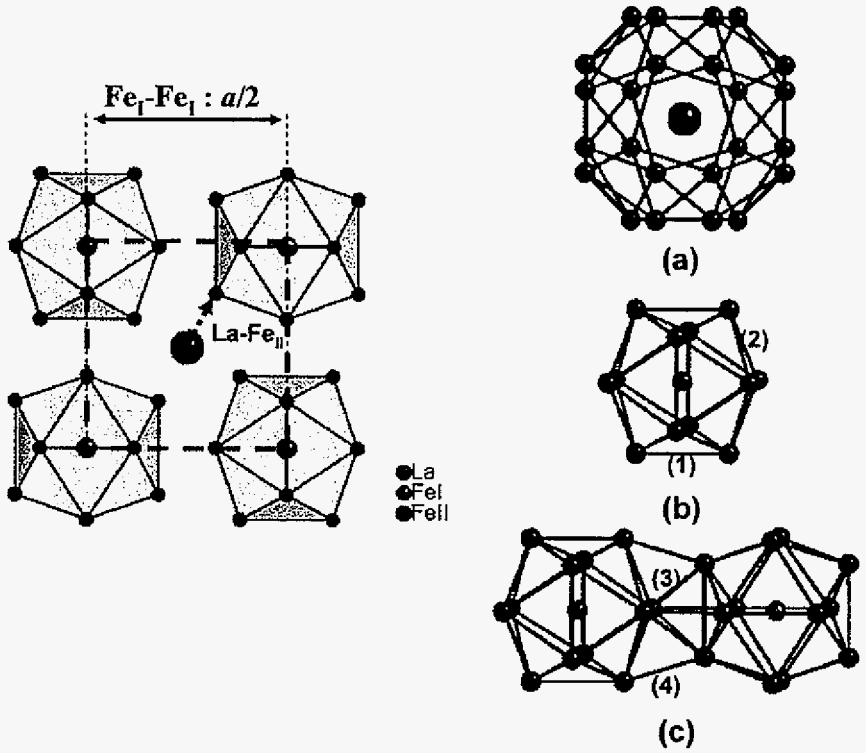

Figure 5. (a) The snub cube around each La atom (red) and twenty-four vertexes-polyhedron. (b) Fe_I-centered icosahedron. (c) Two icosahedra are connected by a stella quadrangula with two distances of (**3**) and (**4**).

Table 6. Interatomic distances for cubic-$LaFe_{13-x}Si_x$

Identification code	1	2	3	4	5	6	7
La-Fe_{II} (8*a*-96*i*, 24×)	3.3542(5)	3.3483(4)	3.3453(8)	3.3409(5)	3.3390(6)	3.3325(7)	3.3238(12)
Fe_I-Fe_I (Å)[a] (8*b*-8*b*, 54×)	5.744(1)	5.737(1)	5.732(1)	5.727(1)	5.723(1)	5.714(1)	5.703(1)
Fe_I-Fe_{II} (Å) (8*b*-96*i*, 12×)	2.4570(6)	2.4545(5)	2.4533(13)	2.4533(8)	2.4519(9)	2.4495(12)	2.446(2)
Fe_{II}-Fe_{II} (Å)							
Intra icosahedron (96*i*-96*i*, 6×) (1)	2.685(1)	2.684(1)	2.687(1)	2.690(1)	2.688(1)	2.691(1)	2.694(1)
(96*i*-96*i*, 24×) (2)	2.5590(6)	2.5560(6)	2.5539(15)	2.5530(9)	2.5518(10)	2.5480(14)	2.543(3)
Inter icosahedron (96*i*-96*i*, 4×) (3)	2.5016(9)	2.4987(8)	2.501(2)	2.5008(13)	2.4983(16)	2.499(2)	2.500(4)
(96*i*-96*i*, 4×) (4)	2.4503(8)	2.4444(7)	2.4408(19)	2.4345(11)	2.4333(13)	2.4257(17)	2.416(3)

[a] Each Fe-Fe distance is calculated from the lattice parameter and the fractional coordinates.

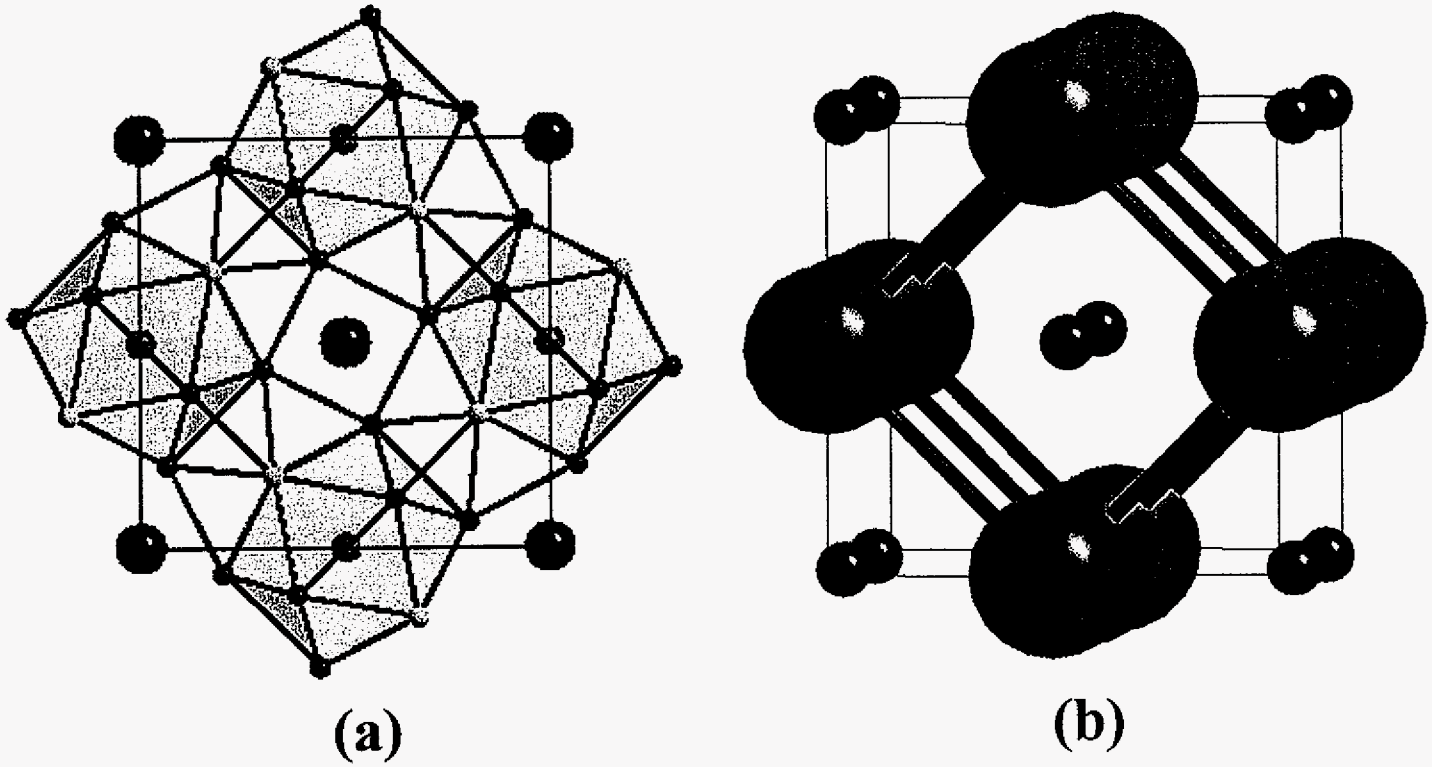

Figure 6. (a) A slice of tetragonal $LaFe_{13-x}Si_x$ structure on the *ab* plane. Red circles are La atoms, blue and yellow represent for Fe and Si, respectively. (b) The CsCl-type packing of La atoms (small circles) and Fe_I-centered icosahedra (large circles)

Table 7. Crystallographic Data from Single-Crystal X-ray Diffraction Measurements for $LaFe_{9.71(3)}Si_{3.29(6)}$ **(8)**, $LaFe_{9.55(3)}Si_{3.45(7)}$ **(9)** at 300K.

Identification code	**8**	**9**
Crystal system	tetragonal	tetragonal
Space group	*I 4/m c m*	*I 4/m c m*
a (Å)	7.9876(11)	7.9834(11)
c(Å)	11.646(2)	11.676(2)
Formula weight	3090.9184	3073.152
Volume, $Å^3$	743.02(21)	744.17(21)
Z	4	4
dcal(g/cm^3)	4.160	4.130
Abs. coeff., mm^{-1}	23.176	23.14
F(000)	1388	1388
Crystal size, mm^3	0.21 × 0.26 × 0.25	0.20 × 0.26 × 0.25
$2\theta_{max}$, °	56.22	56.22
Reflections collected	2947	1833
Indep. reflections	267	266
R(int)	0.1581	0.5656
Data / parameters	267 / 26	266 / 26
Goodness-of-fit on F^2	1.160	0.621
R1, wR2[I>2s(I)]	0.0359, 0.0801	0.0343, 0.069
R1, wR2(all data)	0.0395, 0.0814	0.0755, 0.0773
(Δr)max, min (e/Å3)	2.31/-1.62	1.47/-1.57

Table 8. Atomic coordinates and equivalent isotropic displacement parameters. U(eq) is defined as one third of the trace of the orthogonalized U_{ij} tensor.

		Wyck.	Occ.	x	y	z	U(eq)
$LaFe_{9.71(3)}Si_{3.29(6)}$ **(8)**	La	4*a*		0	0	¼	8(1)
	Fe	4*b*		½	0	½	9(1)
	Fe	16*k*		0.2015(2)	0.0647(2)	½	9(1)
	Fe	16*l*(1)		0.3807(1)	0.1193(1)	0.3214(1)	9(1)
	Fe	16*l*(2)	0.178(14)	0.3243(2)	0.1757(2)	0.1194(2)	10(1)
	Si	16*l*(2)	0.822(14)	0.3243(2)	0.1757(2)	0.1194(2)	10(1)
$LaFe_{9.55(3)}Si_{3.45(7)}$ **(9)**	La	4*a*		0	0	¼	7(1)
	Fe	4*b*		½	0	0	7(1)
	Fe	16*k*		0.2013(2)	0.648(2)	0	8(1)
	Fe	16*l*(1)		0.3808(1)	0.1192(1)	0.1785(2)	8(1)
	Fe	16*l*(2)	0.137(17)	0.3240(2)	0.1760(2)	0.3799(3)	8(1)
	Si	16*l*(2)	0.863(17)	0.3240(2)	0.1760(2)	0.3799(3)	8(1)

Table 9. Anisotropic displacement parameters ($Å^2 \times 10^3$) for tetragonal $LaFe_{13-x}Si_x$ structure.

		Wyck.	U11	U22	U33	U23	U13	U12
$LaFe_{9.71(3)}Si_{3.29(6)}$ **(8)**	La	4*a*	7(1)	7(1)	10(1)	0	0	0
	Fe	4*b*	7(1)	7(1)	11(1)	0	0	-1(1)
	Fe	16*k*	8(1)	9(1)	11(1)	0	0	1(1)
	Fe	16*l*(1)	9(1)	9(1)	10(1)	-1(1)	1(1)	-1(1)
	Fe	16*l*(2)	8(1)	8(1)	13(1)	0(1)	0(1)	2(1)
	Si	16*l*(2)	8(1)	8(1)	13(1)	0(1)	0(1)	2(1)
$LaFe_{9.55(3)}Si_{3.45(7)}$ **(9)**	La	4*a*	7(1)	7(1)	8(1)	0	0	0
	Fe	4*b*	9(1)	9(1)	5(2)	0	0	-4(1)
	Fe	16*k*	8(1)	8(1)	7(1)	0	0	0(1)
	Fe	16*l*(1)	8(1)	8(1)	9(1)	1(1)	-1(1)	1(1)
	Fe	16*l*(2)	8(1)	8(1)	9(2)	0(1)	0(1)	0(1)
	Si	16*l*(2)	8(1)	8(1)	9(2)	0(1)	0(1)	0(1)

* The anisotropic displacement factor exponent takes the form: $-2\pi^2[h^2a^2U_{11} + ... + 2\,h\,k\,a\,b\,U_{12}]$

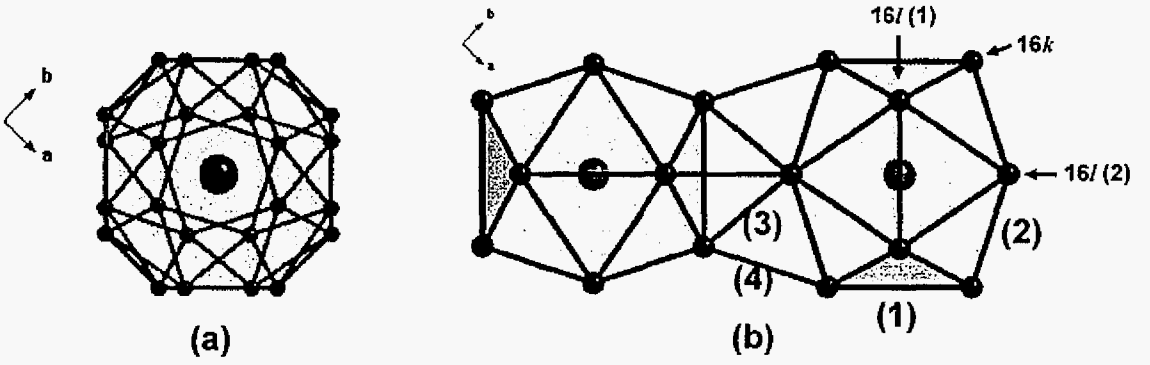

Figure 7. (a) Snub cube containing La (center) atom. (b) Two adjacent icosahedra unit linked by stella quadrangula

Table 10. Interatomic distances in tetragonal $LaFe_{13-x}Si_x$

Identification code		8	9
La-Fe_{II}	(4*a*-16*k*, 8×)	3.367(1)	3.372
	(4*a*-16*l*(1), 8×)	3.293(1)	3.293(1)
	(4*a*-16*l*(2), 8×)	3.316(1)	3.312(2)
Fe_I-Fe_I (Å)[a]	(4*d*-4*d*, 12×)	5.648(1)	5.645
	(4*d*-4*d*, 8×)	5.823(1)	5.838
Fe_I-Fe_{II} (Å)	(4*d*-16*k*, 4×)	2.440(1)	2.441(1)
	(4*d*-16*l*(1), 4×)	2.478(2)	2.480
	(4*d*-16*l*(2), 4×)	2.424(2)	2.431(3)
Fe_{II}-Fe_{II} (Å)			
Intra icosahedron	(16*l*(1)-16*l*(2), 8×)	2.497(2)	2.494(2)
	(16*k*-16*l*(1), 8×)	2.562(1)	2.566
	(16*k*-16*l*(2), 8×)	2.566(2)	2.573
	(16*k*-16*k*, 2×)	2.641(2)	2.641
	(16*l*(1)-16*l*(1), 2×)	2.696(2)	2.691
	(16*l*(2)-16*l*(2), 2×)	2.781(5)	2.804
Inter icosahedron	(16*k*-16*k*, 2×)	2.391(2)	2.387
	(16*l*(1)-16*l*(2), 2×)	2.415(2)	2.411
	(16*k*-16*l*(2), 4×)	2.505(2)	2.508

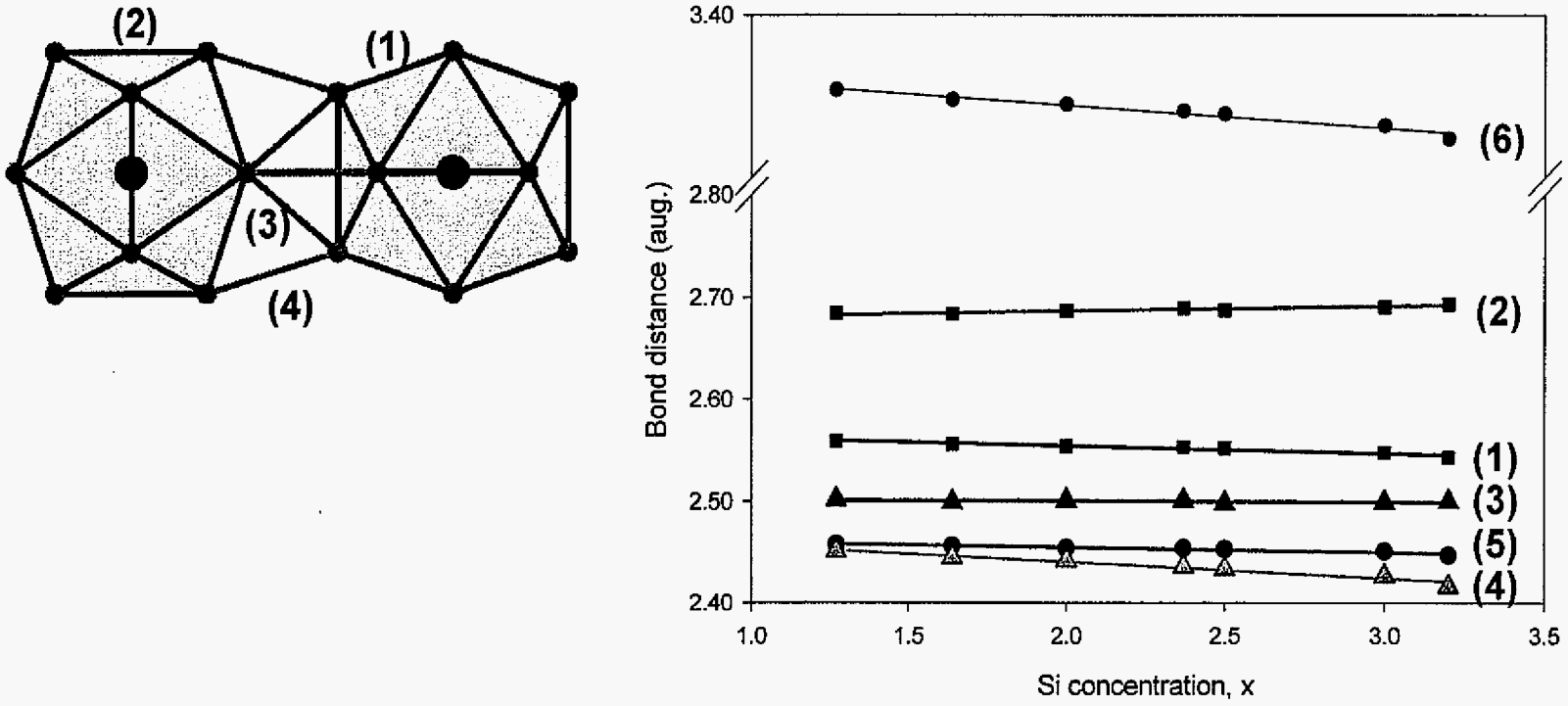

Figure 8. Schematic view of interatomic Fe-Fe distances: each color represents different distance. **1** and **2** are intra icosahedron (■) Fe_{II}-Fe_{II} distances, **3** and **4** for inter icosahedron (▲), **5** is for the Fe_I-Fe_{II} distance (●), and **6** is for the La-Fe_{II} distance (♦).

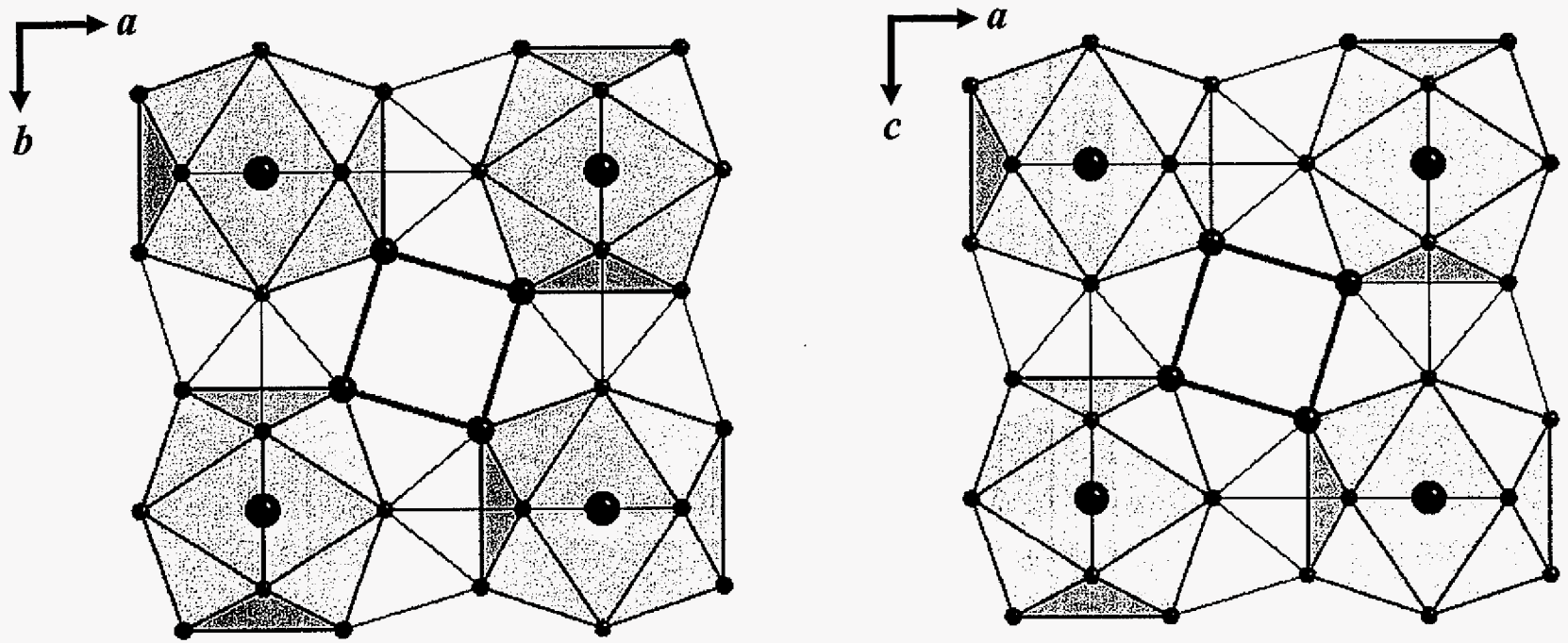

Figure 9. Two different kinds of interaction between icosahedra in the tetragonal $LaFe_9Si_4$ structure.

(a) A projection of the structure of cubic $LaFe_{13-x}Si_x$ on the *ab*-plane (b) on the *ac*-plane

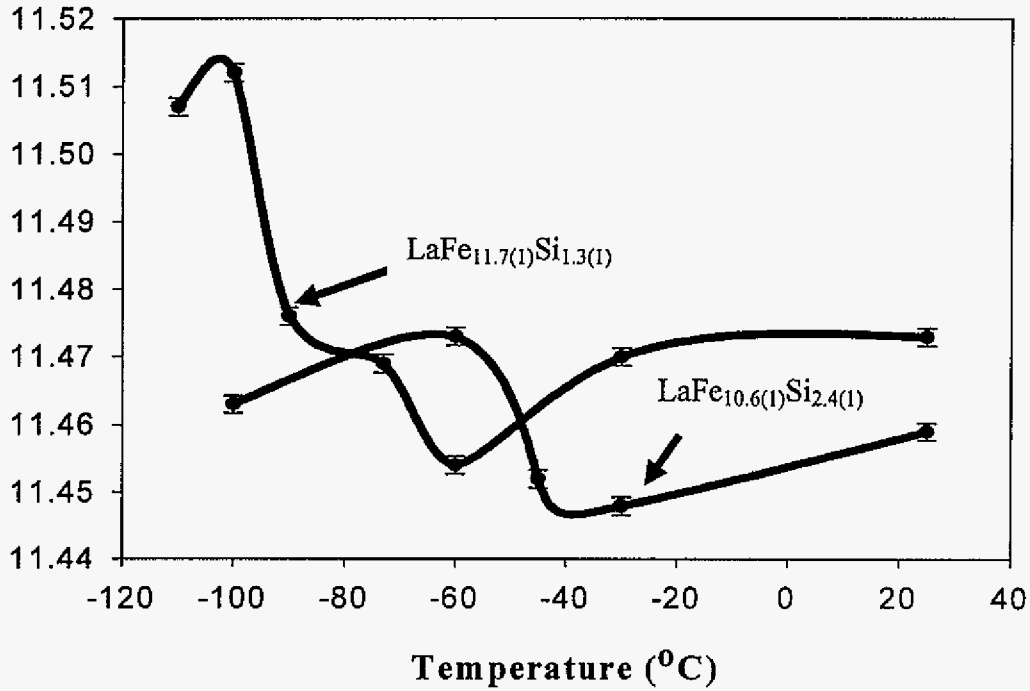

Figure 10. Temperature dependence of the lattice parameter for $LaFe_{11.7(1)}Si_{1.3(1)}$ and $LaFe_{10.6(1)}Si_{2.4(1)}$ obtained from the single crystal diffraction.

Table 11. (a) X-ray single crystal data and structure refinements for $LaFe_{10.6(1)}Si_{2.4(1)}$ at various temperature.

I. Data Collections.					
Temperature, K	**293**	**243**	**228**	**213**	**173**
Crystal system	cubic	cubic	cubic	cubic	cubic
a ,Å	11.4624(13)	11.4479(13)	11.4524(13)	11.4711(13)	11.4605(13)
Abs.coeff., mm^{-1}	25.571	25.669	25.638	25.513	25.584
$2\theta_{max}$, °	56.36	56.44	56.42	56.32	56.36
Index ranges, *h*	-13, 14	-13, 13	-13, 13	-15, 14	-14, 15
k	-10, 14	-15, 8	-5, 14	-15, 12	-15, 12
l	-14, 14	-5, 14	-15, 8	-12, 14	-14, 12
Reflections collected	1850	1117	1104	1884	1915

II. Solution and Refinement.

Space group	**Fm3bc**	**F4b3c**	**Fm3bc**	**F4b3c**	**Fm3bc**	**F4b3c**	**Fm3bc**	**F4b3c**	**Fm3bc**	**F4b3c**
Independent reflections	95	159	94	158	94	158	95	161	95	161
R(int)	0.0309	0.0305	0.0436	0.0426	0.0379	0.0358	0.0375	0.0371	0.0377	0.0373
Data / parameters	95 / 11	159/ 14	94 / 11	158 / 14	94 /11	158 / 14	95 / 11	161/ 14	95 / 11	161/ 14
Goodness-of-fit on F^2	1.265	1.261	1.550	1.369	1.547	1.375	1.307	1.305	1.347	1.271
R1 [I>2σ(I)]	**0.0109**	**0.0102**	**0.0183**	**0.0172**	**0.0198**	**0.0205**	**0.0136**	**0.0129**	**0.0107**	**0.0101**
wR2	**0.0243**	**0.0243**	**0.0469**	**0.0423**	**0.0456**	**0.0439**	**0.0314**	**0.0293**	**0.0259**	**0.0256**
Extinction coeff. ($\times 10^{-4}$)	3.8(5)	3.5(4)	4.2(9)	3.2(6)	3.6(9)	2.8(6)	4.0(7)	3.4(5)	3.3(5)	3.1(4)
$\Delta(\rho)_{max}$($e.Å^{-3}$)	0.48	0.52	0.65	0.60	0.67	0.75	0.53	0.43	0.30	0.38
$\Delta(\rho)_{min}$ ($e.Å^{-3}$)	-0.34	-0.34	-0.58	-0.58	-0.65	-0.55	-0.43	-0.49	-0.45	-0.39

Table 11. (continued) (b) X-ray single crystal data and structure refinements for $LaFe_{11.1(1)}Si_{1.9(1)}$ at various temperature.

I. Data Collections.					
Temperature, K	**293**	**228**	**195**	**183**	**173**
Crystal system	cubic	cubic	cubic	cubic	cubic
a ,Å	11.4635(13)	11.4588(13)	11.4838(13)	11.4916(13)	11.4904(13)
Abs.coeff., mm^{-1}	26.256	26.289	26.117	26.064	26.072
$2\theta_{max}$, °	56.36	56.38	56.24	56.20	56.2
Index ranges, *h*	-14, 12	-10, 15	-14, 12	-14, 12	-12, 14
k	-14, 9	-9, 14	-14, 9	-14, 9	-15, 10
l	-15, 10	-11, 14	-15, 10	-15, 10	-14, 9
Reflections collected	1481	1387	1482	1507	1474

II. Solution and Refinement.										
Space group	**Fm3bc**	**F4b3c**	**Fm3bc**	**F4b3c**	**Fm3bc**	**F4b3c**	**Fm3bc**	**F4b3c**	**Fm3bc**	**F4b3c**
Independent reflections	95	160	95	160	95	160	95	161	95	161
R(int)	0.0488	0.0480	0.0507	0.0504	0.0464	0.0455	0.0462	0.0455	0.0446	0.0436
Data / parameters	95 / 11	160/ 14	95 / 11	160 / 14	95 /11	160/ 14	95 / 11	161/ 14	95 / 11	161/ 14
Goodness-of-fit on F^2	1.282	1.284	1.244	1.241	1.286	1.247	1.285	1.222	1.300	1.271
R1 [I>2σ(I)]	**0.0324**	**0.0311**	**0.0340**	**0.0339**	**0.0351**	**0.0324**	**0.0300**	**0.0286**	**0.0314**	**0.0296**
wR2	**0.0650**	**0.0634**	**0.0785**	**0.0771**	**0.0709**	**0.0662**	**0.0634**	**0.0573**	**0.0679**	**0.0674**
Extinction coeff. ($\times 10^{-4}$)	4.0(13)	3.3(9)	6.0(19)	5.2(7)	4.6(15)	3.8(10)	4.1(13)	3.0(8)	3.7(14)	3.2(10)
$\Delta(\rho)_{max}$(e.Å^{-3})	1.66	1.28	2.29	1.85	1.78	1.47	1.52	1.29	1.73	1.57
$\Delta(\rho)_{min}$ (e.Å^{-3})	-1.33	-0.87	-1.39	-0.96	-1.13	-1.07	-1.37	-1.17	-1.14	1.02

Table 11. (continued) (c) X-ray single crystal data and structure refinements for $LaFe_{11.7(1)}Si_{1.3(1)}$ at various temperature.

I. Data Collections.					
Temperature, K	**293**	**243**	**213**	**200**	**173**
Crystal system	cubic	cubic	cubic	cubic	cubic
a ,Å	11.4635(13)	11.4626(13)	11.4626(13)	11.4740(13)	11.4919(13)
Abs.coeff., mm^{-1}	26.256	13.714	26.117	27.294	27.722
$2\theta_{max}$, °	56.36	56.36	56.24	56.30	56.6
Index ranges, *h*	-14, 12	-15, 15	-15, 15	-14, 15	-15, 14
k	-14, 9	-15, 11	-15, 11	-14, 14	-15, 14
l	-15, 10	-15, 15	-15, 15	-15, 13	-15, 13
Reflections collected	1481	2262	2273	1878	1925

II. Solution and Refinement.										
Space group	**Fm3bc**	**F4b3c**	**Fm3bc**	**F4b3c**	**Fm3bc**	**F4b3c**	**Fm3bc**	**F4b3c**	**Fm3bc**	**F4b3c**
Independent reflections	95	160	96	163	96	163	96	163	97	164
R(int)	0.0488	0.0480	0.0440	0.0432	0.0452	0.0455	0.0399	0.0392	0.0460	0.0452
Data / parameters	95 / 11	160/ 14	96/ 11	163 / 14	96 /11	160/ 14	96 / 11	163/ 14	97 / 11	164/ 14
Goodness-of-fit on F^2	1.282	1.284	1.290	1.257	1.314	1.277	1.412	1.269	1.347	1.323
R1 [I>2σ(I)]	**0.0324**	**0.0311**	**0.0162**	**0.0160**	**0.0178**	**0.0175**	**0.0216**	**0.0195**	**0.0233**	**0.0214**
wR2	**0.0650**	**0.0634**	**0.0408**	**0.0379**	**0.0423**	**0.0412**	**0.0453**	**0.0404**	**0.0501**	**0.0467**
Extinction coeff. ($\times 10^{-4}$)	4.0(13)	3.3(9)	1.4(7)	o.7(5)	1.7(7)	1.0(5)	1.9(7)	1.2(5)	2.1(8)	1.7(6)
$\Delta(\rho)_{max}$($e.Å^{-3}$)	1.66	1.28	1.14	0.79	1.48	1.14	1.29	0.80	1.09	0.93
$\Delta(\rho)_{min}$ ($e.Å^{-3}$)	-1.33	-0.87	-0.58	-0.51	-0.61	-0.52	-0.97	-0.76	-0.99	-0.72

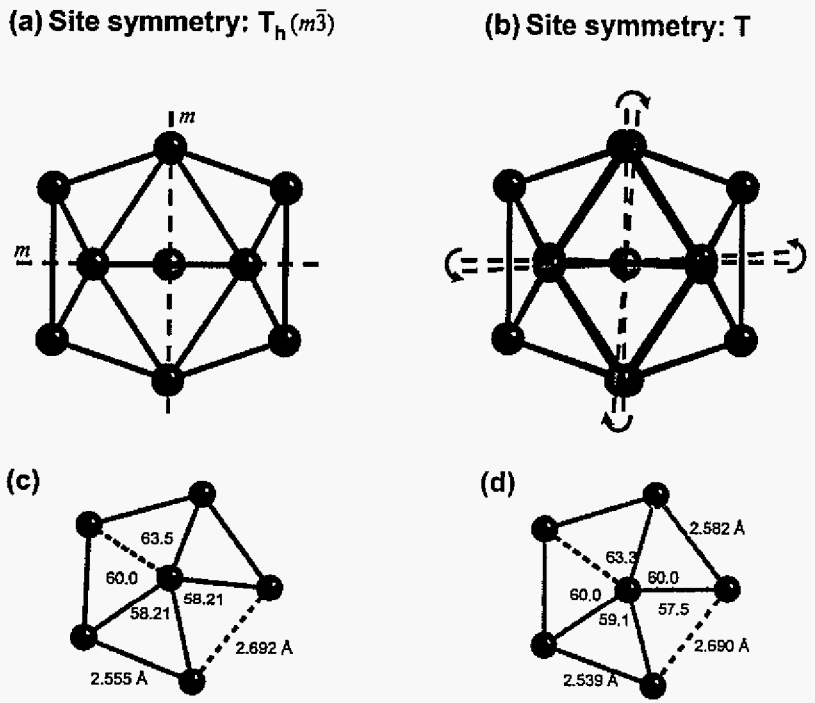

Figure 11. The main geometrical effect of symmetry reduction $Fm\bar{3}c \rightarrow F\bar{4}3c$, (a) icosahedron in $Fm\bar{3}c$ space group with mirror plane m (dashed red lines); (b) icosahedron in $F\bar{4}3c$ space group with displaced atomic arrangement; (c) and (d) Fe_{II}-Fe_{II} interaction in icosahedron.

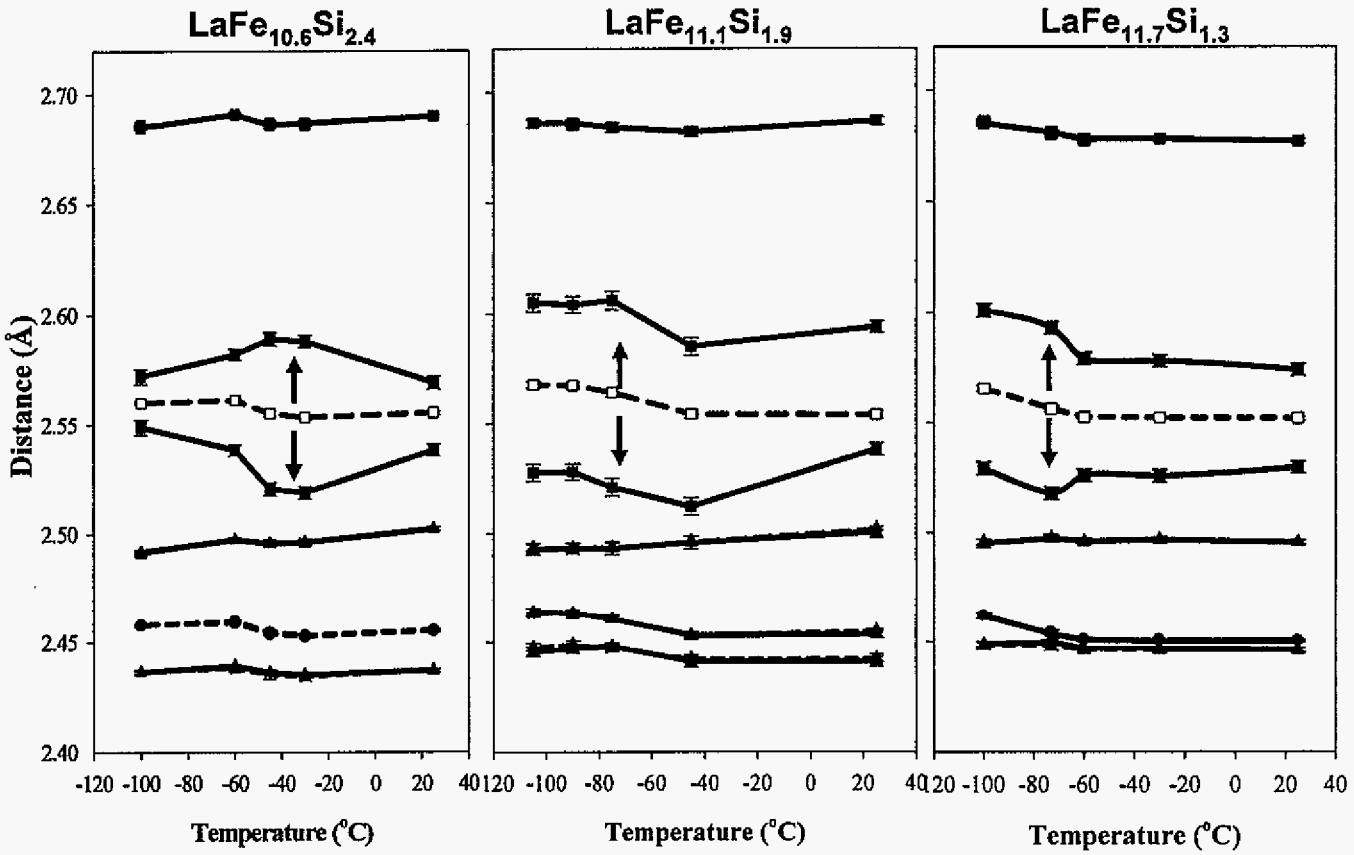

Figure 12. Comparison of bond distances between Fe_{II}-Fe_{II} bond of two different space group. Dashed lines are the distances in the $Fm\bar{3}c$, and solid lines for in the $F\bar{4}3c$. Red arrows indicate the largest distance deviation between two space groups.

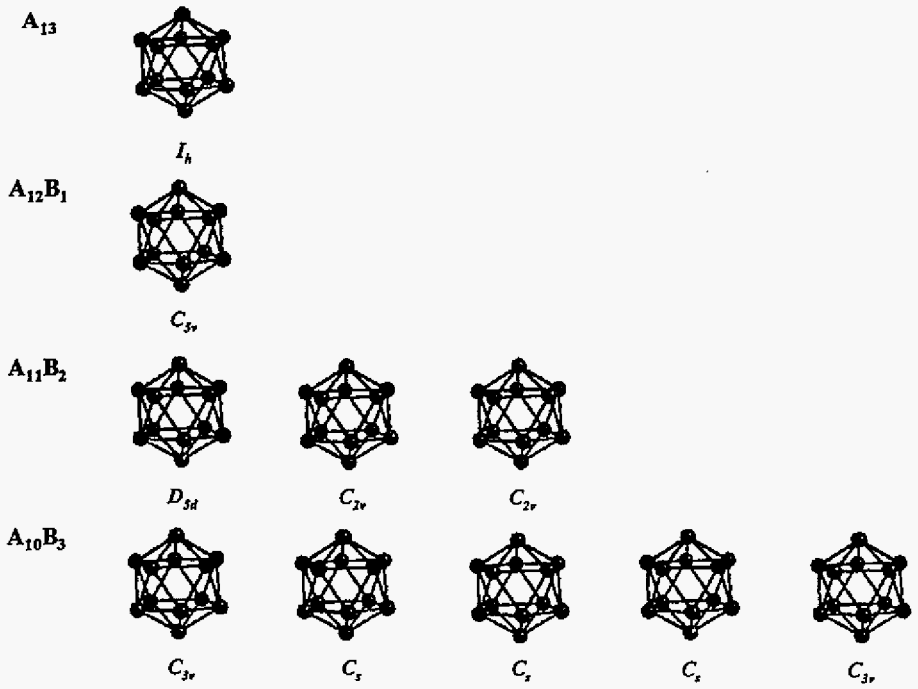

Figure 13. All possible stereoisomers and point group symmetries of $A_{13-n}B_n$ (n = 1, 2, 3) centered icosahedra. (Centered atoms are not shown in the figure)

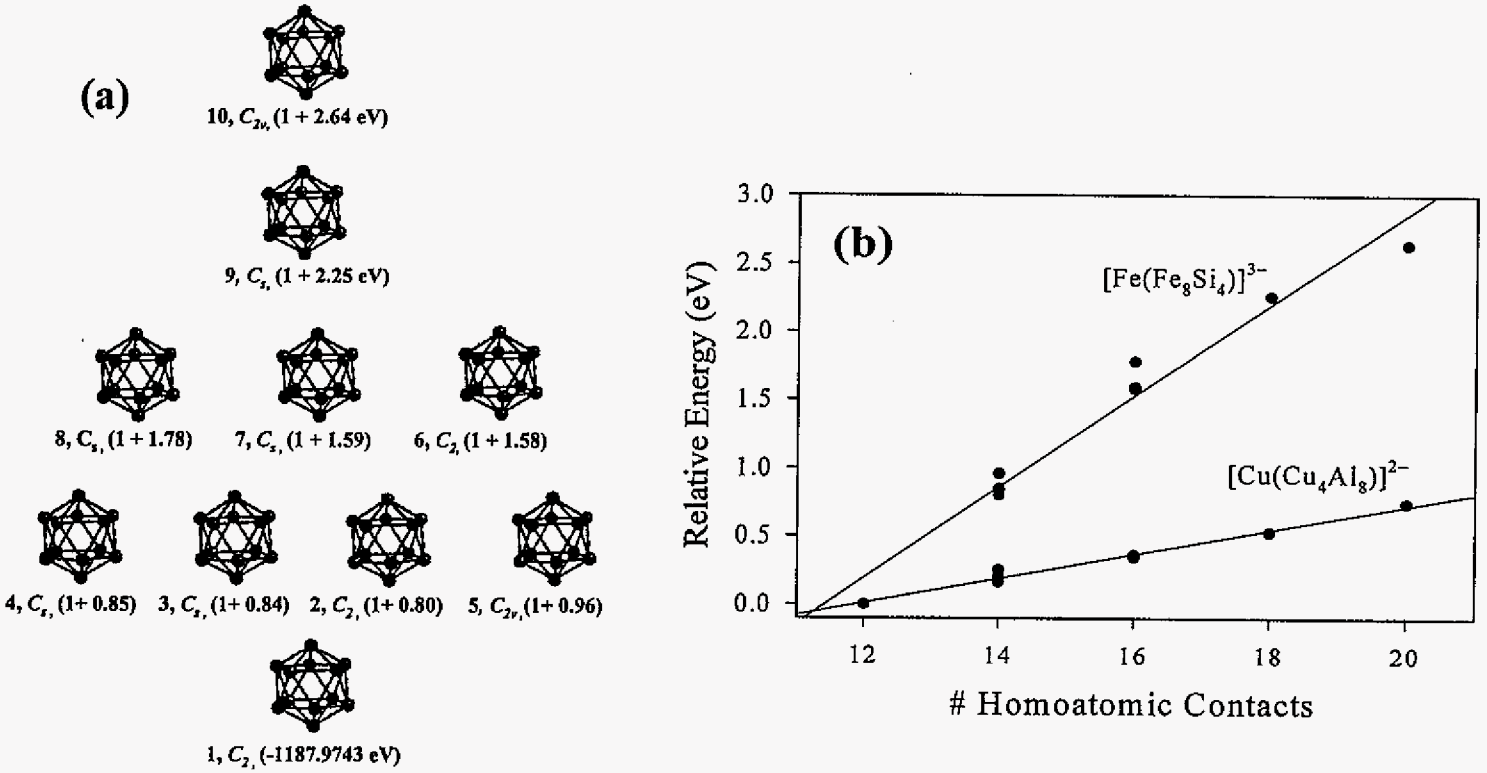

Figure 14. (a) All possible stereoisomers of $LaFe_9Si_4$ with relative energy and point group symmetry. The Fe and Si atoms are represented by blue and green circles, respectively. (b) A graphical representation of the relative total energies of icosahedron upon the number of homoatomic contact.

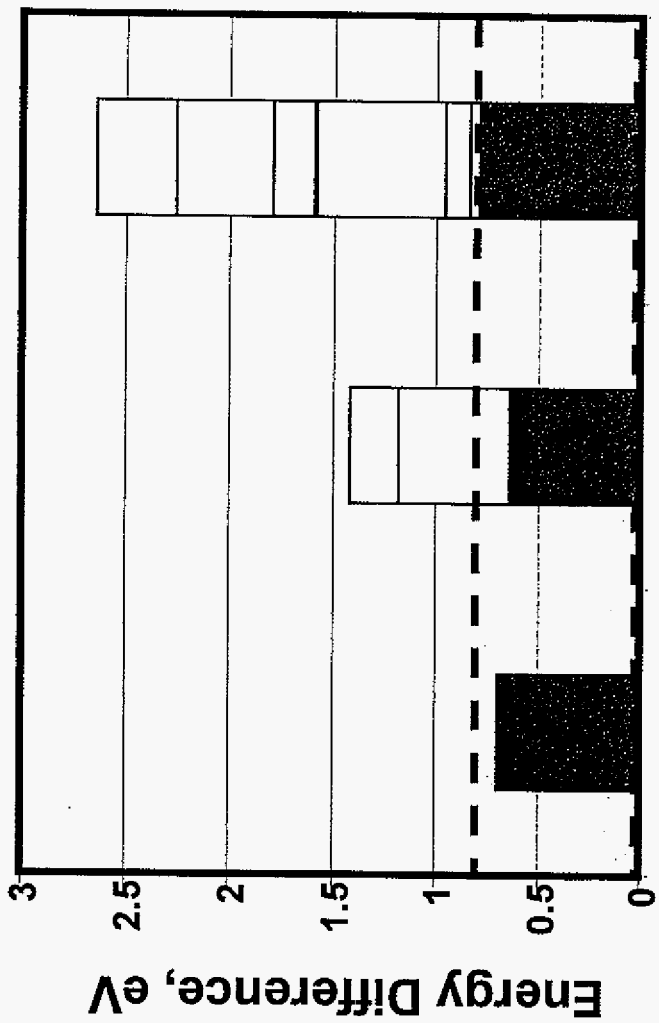

Figure 15. The energy difference between nearest configurations: The zero energy difference is the lowest electronic configuration among possible electronic configuration.

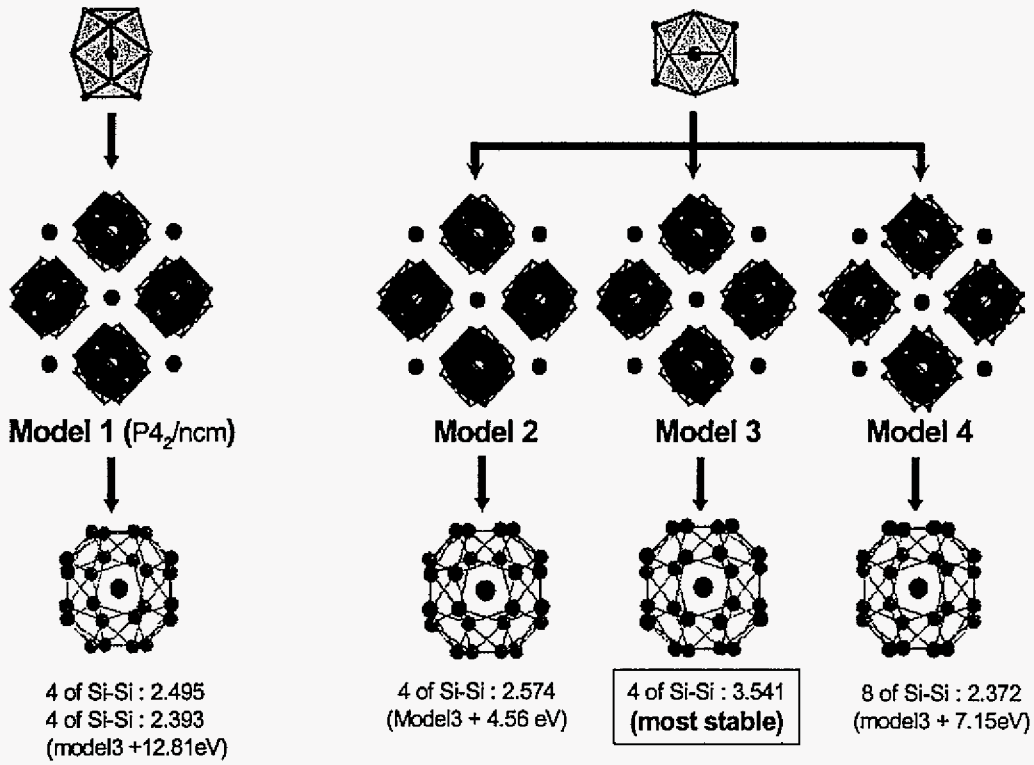

Figure 16. Schematical view of models for $LaFe_9Si_4$ structure using different starting molecular icosahedron.

CHAPTER 4

Structure and Bonding in $LaFe_{13-x}Si_x$: a MCE Material II. Electronic Structure and Property Relationships.

*Mi-Kyung Han,[a] and Gordon J. Miller[a]**

[a]Department of Chemistry, Iowa State University, Ames, Iowa 50011

Abstract

Electronic structure calculations have been performed on $LaFe_{13-x}Si_x$ systems using tight-binding linear muffin-tin-orbital (TB-LMTO) method. The effects of a third element on stabilizing the structure and controlling the transformation of cubic $NaZn_{13}$-type structures to the tetragonal derivative have been investigated. The magnetic properties, such as local magnetic moments and Curie temperature of $LaFe_{13-x}Si_x$ compounds are discussed with respect to Si concentration.

Introduction

$NaZn_{13}$-type $LaFe_{13-x}Si_x$ compounds have been considered as potential materials for efficient magnetic refrigeration, due to its large magnetic entropy change at the Curie temperature. The Si atoms in $LaFe_{13-x}Si_x$ compounds play an important role in stabilizing the structure and phase formation, as well as influence the physical properties. Systematic calculations of the electronic structure in the $LaFe_{13-x}Si_x$ are of fundamental importance to

understand the electronic and magnetic properties of these compounds. Present studies have two aims, namely, that of (a) investigating the influence of main group elements, such as Si, on structural stability and phase formation, and that of (b) achieving an understanding of the relationship between their bonding and magnetic properties.

Calculation Methods

The electronic structures of many actual and hypothetical compounds were calculated self-consistently by using the tight-binding linear muffin-tin-orbital (TB-LMTO) method[1-4] within the atomic sphere approximation (ASA) using the LMTO Version 47 program. Exchange and correlation were treated in a local spin density approximation (LSDA).[5] All relativistic effects except spin-orbit coupling were taken into account using a scalar relativistic approximation.[6] Within the atomic sphere approximation (ASA), space is filled with overlapping Wigner-Seitz (WS) atomic spheres to best mimic the full potential. The radii of the WS spheres were obtained by requiring the overlapping potential to be the best possible approximation to the full potential according to an automatic procedure. The WS radii determined by this procedure are 4.41 ~ 4.50 Å for La, 2.51 ~ 2.60 Å for Fe and 2.51 ~ 2.54 Å for Si. The basis set included La 6*s*, 6*p*, 5*d* orbitals, Si 3*s*, 3*p* orbitals and Fe 4*s*, 4*p* and 3*d* orbitals. No empty sphere is needed. The Löwdin downfolding technique allows the derivation of few-orbital effective Hamiltonians by keeping only the relevant degrees of freedom and integrating out the irrelevant ones. The **k**-space integrations to determine the self-consistent charge density, densities of states (DOS) and crystal orbital Hamilton populations (COHP)[7] were performed by the tetrahedron method[8]. The Fermi level was chosen as an internal reference level in all cases.

Model Structures

The calculations were done on the artificially designed model structures of $LaFe_{13-x}Si_x$ compounds, focusing on "$LaFe_{13}$", $LaFe_{11}Si_2$, tetragonal-$LaFe_9Si_4$, and "cubic"-$LaFe_9Si_4$. Although, these calculations did not include the cases for x = 1 and 3, still we can investigate the composition dependence on the electronic and magnetic properties of the $LaFe_{13-x}Si_x$ system. "$LaFe_{13}$" is a hypothetical compound, so the lattice parameter is extrapolated from the trend in lattice parameter *vs.* Si composition. For $LaFe_{11}Si_2$ and tetragonal-$LaFe_9Si_4$, experimentally known lattice parameters and total volumes are used. Based on single crystal X-ray diffraction refinements and results from extended Hückel calculations for the "coloring"of the $[Fe_{12-x}Si_x]$ icosahedron, a model for $LaFe_{11}Si_2$ was created with an orthorhombic unit cell (space group of *Cmca* (No. 64)) of ordered atoms (179 atoms/unit cell) in the structure. 52 *k*-points in the irreducible wedge of the first Brillouin zone were used for calculating average quantities. During the iteration procedure the total energy converged to within 10^{-5} Ryd. Table 1 summarizes the atomic parameters for model structures.

------ Table 1 ------

Result and Discussion

Non Spin-polarized calculation. Figure 1 shows the total densities of states (DOS) and different partial densities of states for non-spin-polarized calculations on the $LaFe_{13-x}Si_x$ structure.

------ Figure 1 ------

In Figure 1, the partial densities of states of the Fe_{II}-3*d* orbitals are shaded in gray, whereas the Fe_I-3*d* orbitals are represented by a thick line. The overall shapes of all DOS curves are very similar: The most pronounced feature is two broad peaks near the Fermi level. The structure below ~ - 9 eV is due to mainly Fe *s* and *p* states. Between ~ -8.5 eV and E_F the DOS is mainly due to the 3*d* bands of Fe atoms. The profile of the total DOS is close to the partial DOS of the Fe_{II}-3*d* functions, which suggests that the icosahedra dominate the electronic properties. The structure at ~ 3 eV above E_F corresponds to La 4*f* states. As the Si concentration increases, peaks around - 10 to - 14 eV occur from the Si *s* and *p* electrons. The primary distinctive features along $LaFe_{13-x}Si_x$ are broadening of the bandwidth and lowering the value of density of states at the Fermi level, $N(E_F)$ as x increases. Table 2 summarizes the value of DOS at the Fermi level. These calculations without spin polarization show high DOS at the Fermi level. Consequently, according to the Stoner criteria[9], such a high density of states at the Fermi level in the paramagnetic phase indicates the possibility of ferromagnetic behavior, and spin-polarized calculations should be performed to understand their electronic structures.

Spin-polarized calculation. Different initial magnetic models, shown in Table 3, were attempted, but only two models (Model I and Model IV) converged for "$LaFe_{13}$" (denoted **MOD (1)**), both of which retain a ferromagnetic ordering between Fe_I and Fe_{II}. For $LaFe_{11}Si_2$ (denoted **MOD (3)**) case, all different initial magnetic models give converged with ferromagnetic ordering between Fe_I and Fe_{II}. For $LaFe_9Si_4$ (denoted **MOD (5)**) also prefer to have ferromagnetic ordering between Fe_I and Fe_{II}, which has lower total energy than antiferromagnetic ordering by 0.04 eV/f.u.. These calculations confirm that the interatomic distance play an important role in ordering of Fe atoms. We will discuss this aspect later on this paper.

------ Table 3 ------

In the ferromagnetic phases the total DOS at E_F is reduced compared to the DOS at E_F in the paramagnetic state, which is caused by a band splitting due to exchange correlation effects. The total electronic energy showed all magnetic models to be stable than the nonmagnetic ones for each compound and the total energy difference decreased with increasing x. The final results for the spin-polarized calculations are listed in Table 4.

------ Table 4, Figure 2 ------

Since the quantitative result of TB-LMTO-ASA calculations are sensitive to the number of **k** points sampled, atomic sphere radii, and unit cell volume, we have kept these parameters constant for a given composition to discuss the effect of Si on magnetic properties. Therefore, later on this paper, we will only discuss about the electronic structures of **MOD (2)**, **MOD (3)**, and **MOD (4)**.

From our computational results, the substitution by Si in $LaFe_{13-x}Si_x$ compounds leads to considerable changes in the DOS: (1) There is a monotonic reduction in the DOS at the

Fermi level E_F with increasing x; (2) E_F shows continuous increase upon increasing Si concentration; (3) As shown in Figure 1, the lower part of the DOS drops by nearly 4 eV as valence *s*, *p* orbitals on Si overlaps with mainly 4*s*, 4*p* and 3*d* bands of Fe. In particular, the Fe 3*d* - Si 3*p* overlap leads to a broadening of the Fe_I and Fe_{II} 3d bands and causes a decrease in the values of both the majority- and minority-spin DOS values at the Fermi level (bandwith is inversely proportional to band height); (4) The splitting between the spin up and spin down DOS curves decrease. In Figure 2, the DOS for $LaFe_{13}$ shows an almost filled majority-spin band and half-filled minority-spin band. However, as Si is introduced, the splitting between spin up/spin down decrease, thus it causes decreases in magnetic moments.

------ Table 5 ------

Table 5 (a) summarizes the integrated DOS for majority-spin and minority-spin states of the $LaFe_{13-x}Si_x$ compounds. Relative differences in the DOS produce a net moment given by

$$m = \sum_E (N(E)\uparrow - N(E)\downarrow) \qquad (1)$$

where $N(E)\uparrow$ and $N(E)\downarrow$ are the integrated density of states of the majority-spin and minority-spin electrons respectively.[10] Chemical substitution for Fe by Si causes to decrease in Fe-Fe exchange splitting, which contributes to the decrease in magnetization upon increasing Si concentration. Table 5 (b) shows the average moments at each atom for the $LaFe_{13-x}Si_x$ series. As we can see, the total magnetic moments per formula unit decrease as x increases. The La and Si atoms have small moments that are oppositely oriented to the Fe moments. The moments for the Fe_I sites decrease most rapidly upon Si concentration, since

the different Fe moments and their x dependences can be attributed to (1) different local bonding environments of individual atoms, and (2) charge densities of Fe atoms. Also, Table 5 (c) reveals a charge transfer from Fe_I to Si atoms. Table 6 summarizes the nearest-neighbor Fe-Fe number in $LaFe_{13-x}Si_x$. In "$LaFe_{13}$", the Fe-Fe coordination number for Fe_I sites is 12, and 10 for Fe_{II} sites. These coordination numbers of each site decrease statistically upon increasing Si in the system. So, this dilution of the Fe atoms can be another reason for the decrease in magnetization upon increasing Si concentration. Therefore, the low magnetization is caused by the transfer of Fe_I-conduction electrons to the Si band as well as the rapid reduction of near-neighbor distances and number of near-neighbor Fe atoms.

------ Table 6 ------

Figure 3 shows the partial DOS of Fe_I (Fe atom at the center of icosahedron) and Fe_{II} atoms, focusing on the 3*d*-orbital contribution. As mentioned before, the main effect of Si is to expand the Fe 3*d* bandwidth. Moreover, the 3*d* band of Fe_I shows more significant broadening by Si introduction than the 3*d* band of Fe_{II}. These differences arise because near-neighbor distances for Fe_I are shorter than those for Fe_{II} atoms, and so the 3*d* electrons of Fe_I atoms are more delocalized than those of Fe_{II} atoms. The Fe_I minority spin 3*d* states are perturbed to slightly lower energy.

------ Figure 3 ------

Relationship between Curie temperature and Si concentration.

The magnetic behavior of $LaFe_{13-x}Si_x$ is complex. The Curie temperatures (T_c) of $LaFe_{13-x}Si_x$ compounds increase with x, although the lattice contracts.[11-12] Furthermore, the saturation magnetization decreases with increasing Si content. It is well known that in rare-earth-iron intermetallic compounds, the Curie temperature is strongly affected by the strength of the exchange coupling of Fe-Fe moments which sensitively depends on the Fe-Fe interatomic distance.[13] As Givord *et al.* have shown the threshold of switch Fe-Fe exchange interaction between ferromagnetic and antiferromagnetic is 2.45 Å. Fe moments with short bonds ($\leq$ 2.45 Å) are antiferromagnetically coupled while those with long bonds ($\geq$ 2.45 Å) are ferromagnetically coupled.[14] Either an increase in Fe-Fe interatomic distances or a decrease in the fraction of short Fe-Fe bonds are expected to enhance the overall Fe-Fe exchange coupling interaction, and consequently the Curie temperature.

Previous investigations have tried to explain the change in Curie temperature for $NaZn_{13}$-type intermetallic compounds by analyzing the Fe-Fe interactions, which is sensitive to the Fe-Fe distance and the number of nearest neighbors,[15-21] but the underlying physical mechanism is not well understood up to date.

Based on our own investigation of Fe-Fe bond distances using single crystal refinement of several $LaFe_{13-x}Si_x$ compounds, there are two kinds of bond length variations: (1) inter-icosahedral contacts shorter than 2.45 Å shorten with Si content, and (2) intra- and inter-icosahedral contacts exceeding 2.45 Å show little change with Si content (some even expand). Similar Fe-Fe bond distances were also found in several ferromagnetic and antiferromagnetic materials, listed in Table 7. Although the shortest Fe-Fe distances are close among several different materials, we see a range of magnetic interactions. Therefore,

relatively short Fe-Fe distances do not necessarily imply antiferromagnetic ordering between nearest Fe-Fe interactions. Extensive investigations of volume effects in several interstitial[22] and substitutional modifications[23] of R_2Fe_{17} and $RFe_{12-x}M_x$ compounds have also shown that antiferromagnetic interactions are not simply related to short interatomic Fe-Fe distances.

------ Table 7 ------

However, analysis of interatomic distances shows that the fraction of contacts shorter than 2.45 Å decreases upon increasing Si content, see Figure 4, which reduce the effect of antiferromagnetic Fe-Fe exchange interactions and leads to an increase in the Curie temperature.

------ Figure 4 ------

There are more appropriate theories, such as the spin fluctuation theory of Mohn and Wohlfarth, to describe the Curie temperature enhancement in terms of changes in the electronic structure. Mohn and Wohlfarth explained the large increases of Curie temperature for substitutional modifications of Re_2Fe_{17} by a decrease in spin fluctuations, which is caused by lowering the density of states at the Fermi level upon substitution.[25] In order to explain qualitatively the increase of T_c in $LaFe_{13-x}Si_x$, we can also use the following relation obtained for iron-rich alloys in the spin-fluctuation theory of Mohn and Wohlfarth,

$$T_c \sim \frac{M_0^2}{10\mu_B^2 \cdot \chi_0} \qquad (2)$$

where M_0 is the magnetic moment at 0 K and χ_0 is the exchange-enhanced susceptibility, given by[26]

$$\frac{1}{\chi_0} = \frac{1}{4\mu_B^2}\left(\frac{1}{N_\uparrow(E_F)} + \frac{1}{N_\downarrow(E_F)} - 2I\right) \qquad (3)$$

where $N_\uparrow(E_F)$ and $N_\downarrow(E_F)$ are the majority- and minority-spin density of states at the Fermi energy. I is a measure of the strength of the exchange interaction in the metal and μ_B is the Bohr magneton. For $LaFe_{13-x}Si_x$, the value of M_0 are close to each other (± ~2 μ_B deviation for experimentally measured magnetic moments[12]), therefore χ_0 is the determining factor for the Curie temperature variation in Eq. (2). Since the parameter I is known to be rather constant regardless of the local environment of Fe in the alloys,[28] the quantitative behavior of χ_0 in Eq. (3) is determined mainly by the quantities $N_\uparrow(E_F)$ and $N_\downarrow(E_F)$. According to the results of spin-polarized calculation, shown in Table 3 for the substitutional alloys $LaFe_{13-x}Si_x$, the total DOS at the Fermi level decrease upon Si concentration. Therefore, this leads to an increase of T_c.

Structural transformation from cubic to tetragonal.

When atomic ordering occurs, the cubic phase transforms into the tetragonal one. Based on our bond distance analysis, we found that there are two kinds of interaction between the icosahedra in the structure, as shown in Figure 5. The dominant distinguishable interactions on the *ab* plane are Fe_{II} -Fe_{II} interactions, whereas on the *ac* plane Fe_{II}-Si interactions are dominant. As we mentioned before that the Fe_{II}/Si-Fe_{II}/Si bonds between icosahedra show largest contraction upon increasing the Si concentration. This directional interaction can be explained by a COHP analysis. As shown from the COHP curves in Figure 5, the Fe-Si bond is nearly optimized with no Fe-Si antibonding states occupied, whereas the

Fe-Fe contact has some antibonding character at the Fermi level. This bonding character within *ac* plane induces the shorter *c*-axis than $\sqrt{2}\,a$, while further drives the structural transformation.

------ Figure 5 ------

On the space groups of room- and low-temperature modifications of $LaFe_{13-x}Si_x$.

Bond distance analyses of single crystal diffraction studies of $LaFe_{13-x}Si_x$ alloys show some kind of structural perturbation while preserving the $Fm\bar{3}c$ space group near the Curie temperature. Statistical analysis of diffraction data cannot rule out a non-centrosymmetric $F\bar{4}3c$space group for these cubic phases. In this space group, each icosahedron loses its inversion center. Taking into consideration these results we deemed it valuable to analyze the electronic structure of $LaFe_{13-x}Si_x$ in order to correlate it with the large magnetic entropy change at the Curie temperature. Table 8 lists the crystal parameters used in this calculation. The radius of each atom is obtained by requiring that the overlapping potential be the best possible approximation to the full potential, and is determined by an automatic procedure.[27] The Wigner-Seitz radii of each atom are nearly equal for two different space groups. The total energies of two possible space group of $LaFe_{13-x}Si_x$ using two different parameters (parameters at room temperature and low temperature) were calculated and the results are summarized in Table 9. At room temperature, the $F\bar{4}3c$ is slightly more stable than $Fm\bar{3}c$, but the energy difference is less than 1K/formula unit, which implies there is no energetically gaining energy by lowering symmetry. However, near the Curie temperature, it shows still

the $F\bar{4}3c$ is more stable than $Fm\bar{3}c$ but the energy difference is more than 0.08 eV (~ 950 K), which means that we cannot neglect the space group of $F\bar{4}3c$ at lower temperatures.

------ Table 8, Table 9 ------

Conclusion

Electronic structures of many actual and hypothetical compounds of $LaFe_{13-x}Si_x$ were calculated using tight-binding linear muffin-tin-orbital (TB-LMTO) method. The main results of present work are summarized as follows.

1. The main group elements, Si atoms, stabilize the structure by contributing their 3*p* orbitals to hybridize with Fe-3*d* orbitals, thus cause decrease in the DOS at the Fermi level E_F.
2. Calculated magnetic moments decrease with Si concentration, because of the rapid reduction of near-neighbor distances and number of near-neighbor Fe atoms, as well as the charge transfer of Fe_I-conduction electrons to the Si band.
3. Using the spin-fluctuation theory of Mohn and Wohlfarth, the increases in Curie temperature of these compounds can be understood.
4. By comparing relative total energies of two possible space groups in cubic $LaFe_{13-x}Si_x$ system, the $F\bar{4}3c$ is more stable than $Fm\bar{3}c$ near Curie temperature. Therefore, the giant magnetocaloric effect of cubic $LaFe_{13-x}Si_x$ alloys results from coupling between magnetic ordering and structural transformation

References

1. Andersen, O. K. *Phys. Rev.***1975**, B12, 3060.

2. Andersen, O. K.; Jepsen, O. *Phys. Rev. Lett.* **1984**, 53, 2571.

3. Andersen, O. K.; Jepsen, O.; Glötzel, D. In *Highlights of Condensed-Matter Theory*; Bassani, F.; Fumi, F.; Tosi, M. P.; Lambrecht, W. R. L.; Eds.; North-Holland: New York, **1985**.

4. Andersen, O. K. *Phys. Rev. B*, **1986**, 34, 2439.

5. Von Barth, U.; Hedin, L. *J. Phys. C* **1972**, 5, 1629.

6. Koelling, D. D.; Harmon, B. N. *J. Phys. C* **1977**, 10, 3107.

7. Dronskowski, R.; Blöchl, P. *J. Phys. Chem.* **1993**, 97, 8617.

8. Blöchl, P. E.; Jepsen, O.; Andersen, O. K. *Phys. Rev.* **1994**, B49, 16223.

9. Stoner, E. C. *Proc. R. Soc. London* **1938**, 165, 372.

10. Buschow, K. H. J *Rep. Prog. Phys.* **1977**, 40, 1179.

11. Palstra, T. T .M.; Nieuwenhuys, G. J.; Mydosh, J. A.; Buschow, K. H. J. *Phys. Rev.* **1985**, B31, 462.

12. Palstra, T. T. M; Mydosh, J. A.; Nieuwenhuys, G. J.; van der Kran, A. M.; Buschow, K. H. J. *J. Magn. Magn. Mater.* **1983**, 36, 290.

13. Marasinghe, G. K.; Exekwenna, C.; James, W. J.; Hu , Z.; Yelon, W. B. *J Appl. Phys.* **1997**, 81(8), 5103.

14. Givord, D.; Lemaire, R. *IEEE Trans. Magn.* **1974**, 10, 109.

15. Hu, F. X.; Shen, B. G.; Sun, J. R.; Cheng, Z. H.; Rao, G. H.; Zhang, X. X. *Appl. Phys. Lett.* **2001**, 78, 3675.

16. Hu, F. X.; Shen, B. G.; Sun, J. R.; Cheng, Z. H.; Zhang, X. X. *J. Phys.;Condens. Matter*, **2000**, 12, L691.

17. Zhang, X. X.; Wen, G. H.; Wang, F.W. *Appl. Phys. Lett.* **2000**, 77, 3072.

18. Hu, F. X.; Shen, B. G.; Sun, J. R.; Cheng, Z. H. *Phys. Rev.* **2001**, B64, 012409.

19. Fujieda, S.; Fujita, A.; Fukamichi, K.; Yamazaki, Y.; Lijima, Y.; *Appl. Phys. Lett.* **2001**, 79, 653.

20. Fujita, A.; Fukamichi, K. *IEEE Trans. Magn.* **1999**, 35, 3796.

21. Fujita, A.; Akamatsu, Y.; Fukamichi, K. *J Appl. Phys.* **1999**, 85, 4756.

22. Jaswal, S. S.; Grandjean, F.; Long, G. J.; Buschow, K. H. J. (Eds.), Proc. NATO_ASI, Series E281, *Interstitial Intermetallic Alloys*, Kluwer Academic publishers, Dordrecht, **1995**, p.411.

23. Woods, J. P.; Patterson, B. M.; Fernando, A. S.; Jaswal, S. S.; Welipitya, D; Sellmyer, D, J. *Phys. Rev.* **1995**, *B* 51, 1064.

24. Yamamoto, H.; Matsuura, Y.; Fujimura, S.; Sagawa, M. *Appl. Phys. Lett.* **1984**, 45, 1141.

25. Mohn, P.; Wohlfarth, E. P. *J. Phys. F: Metal Phys.* **1987**, 17, 2421.

26. Wohlfarth, E. P. *Phys Lett.* **1962**, 3, 17.

27. Jepsen, O.; Andersen, O. K. Z. *Phys. B* **1995**, 97, 35.

28. Janak, J. F. *Phys. Rev.* **1977**, B16 (1), 255.

Table 1. Structural parameters for electronic structure of different models

Identification code	**MOD (1)[a]**	**MOD (2)[c]**	**MOD (3)[c]**	**MOD (4)[c]**	**MOD (5)[b]**
Formula	$LaFe_{13}$	$LaFe_{13}$	$LaFe_{11}Si_2$	$LaFe_9Si_4$	$LaFe_9Si_4$
Crystal system	Cubic	orthorhombic	orthorhombic	orthorhombic	Tetragonal
Space group	F*m3c*	*C* m c a	*C* m c a	*C* m c a	*I* 4/m c m
Lattice parameters	$a = 11.5047$ Å	$a = 11.4631$ Å $a = b = c$	$a = 11.4631$ Å $a = b = c$	$a = 11.4631$ Å $a = b = c$	$a = 7.9634$ Å $c = 11.6896$ Å
Silicon sites	None	None	Fe1, Fe5	Fe1, Fe2 Fe5, Fe6	Si
Atomic coordinates	**Atom x y z** La ¼ ¼ ¼ Fe 0 0 0 Fe1 0 0.18 0.12	**Atom x y z** La 1/4 3/4 1/4 Fe 0 0 0 Fe 1/2 0 0 Fe1 0 0.88280 0.32090 Fe2 0 0.11720 0.32090 Fe3 0.17910 0.00000 0.61720 Fe4 0.61720 0.17910 0.00000 Fe5 0 0.67910 0.38280 Fe6 0 0.32090 0.38280 Fe7 0.11720 0.00000 0.82090 Fe8 0.82090 0.11720 0.00000			**Atom x y z** La 0 0 ¼ Fe 0 ½ 0 Fe1 0.621 0.121 0.677 Fe2 0.439 0.298 0 Si 0.824 0.324 0.616

[a] The atomic parameters were obtained from the extrapolation from the trend in lattice parameter *vs*. Si composition

[b] The atomic parameters were obtained from powder X-ray diffraction refinement.

[c] The atomic parameters for orthorhombic models (**MOD (2), MOD (3),**and **MOD (4)** were obtained by lowering the symmetry of experimental values of cubic $LaFe_{11}Si_2$ structure.

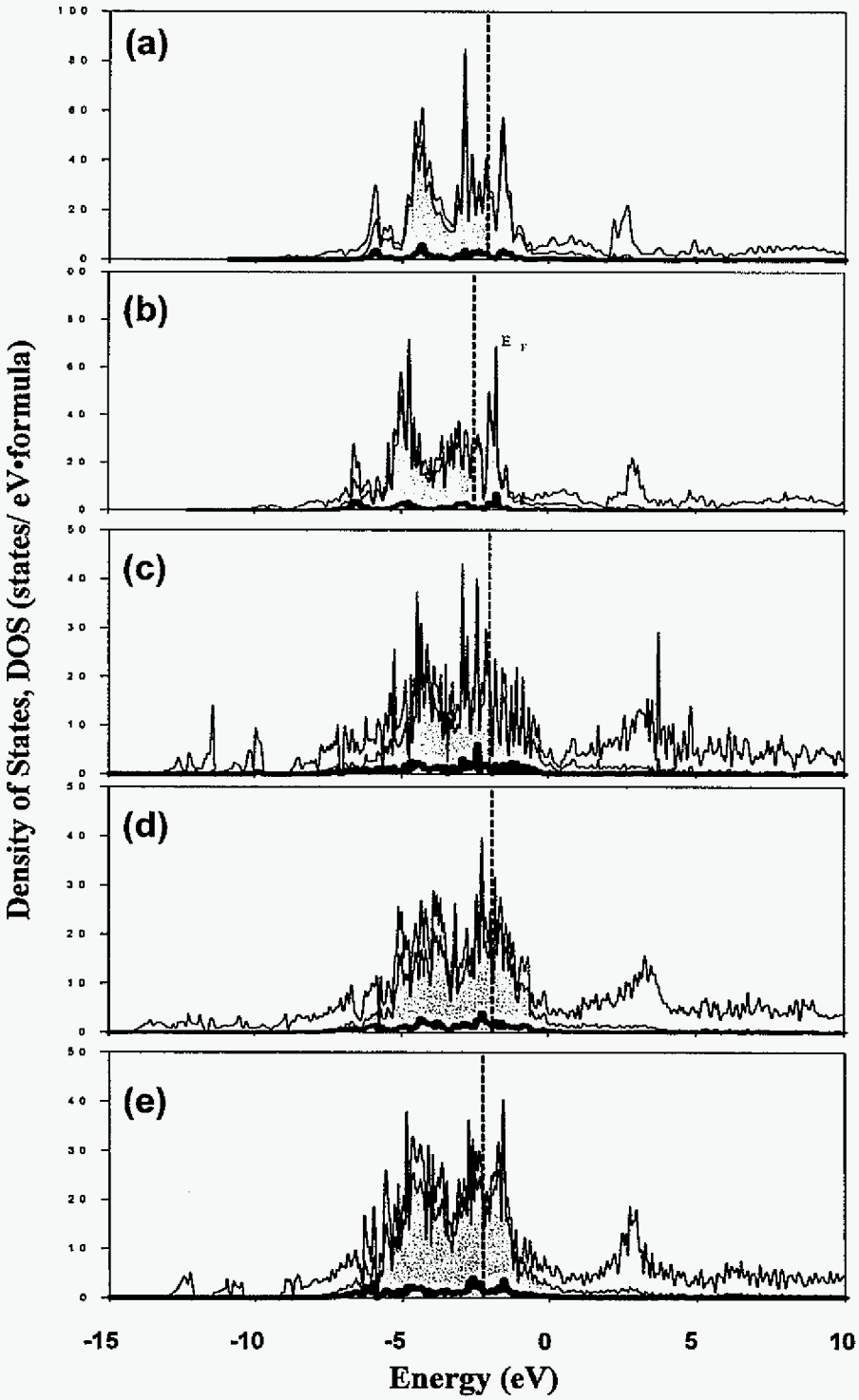

Figure 1. Total density of state (DOS) for non spin polarized $LaFe_{13-x}Si_x$.(a) **MOD (1)**, (b) **MOD(2)**, (c) **MOD(3)**, (d) **MOD(4)**, and (e) **MOD(5)**. Dashed lines represent for Fermi level (E_F).

Table 2. The value of $N(E_F)$ of non spin-polarized calculation for $LaFe_{13-x}Si_x$

	MOD (1)	MOD (2)	MOD (3)	MOD (4)	MOD(5)
N(EF), states/eV•f.u.	40.9467	28.6078	22.2728	15.1787	22.4209
Fermi level, eV	-2.1427	-2.5619	-2.2924	-1.9409	-2.0408

Table 3. Four models of magnetic ordering. Two different arrows represent opposite magnetic moments.

	La	Fe_I	Fe_{II}
Model I	↑	↑	↑
Model II	↑	↑	↓
Model III	↑	↓	↑
Model IV	↑	↓	↓

Table 4. The value of $N(E_F)$ of spin polarized calculation and relative total energy.

	MOD (1)	MOD (2)	MOD (3)	MOD (4)	MOD(5)
$N_\downarrow(EF)$,states/eV•f.u.	4.65	7.85	8.40	7.00	9.51
$N_\uparrow(EF)$,states/eV•f.u.	7.00	8.60	7.45	7.65	6.01
N(EF),states/eV•f.u.	11.65	16.45	15.85	14.65	15.51
$\Delta E_{\text{nonspin-spin}}$, eV/f.u.	0.0826	0.0552	0.0479	0.0336	0.0247
Fermi level, eV	-1.9802	-2.3843	-2.1718	-1.8322	-2.0127

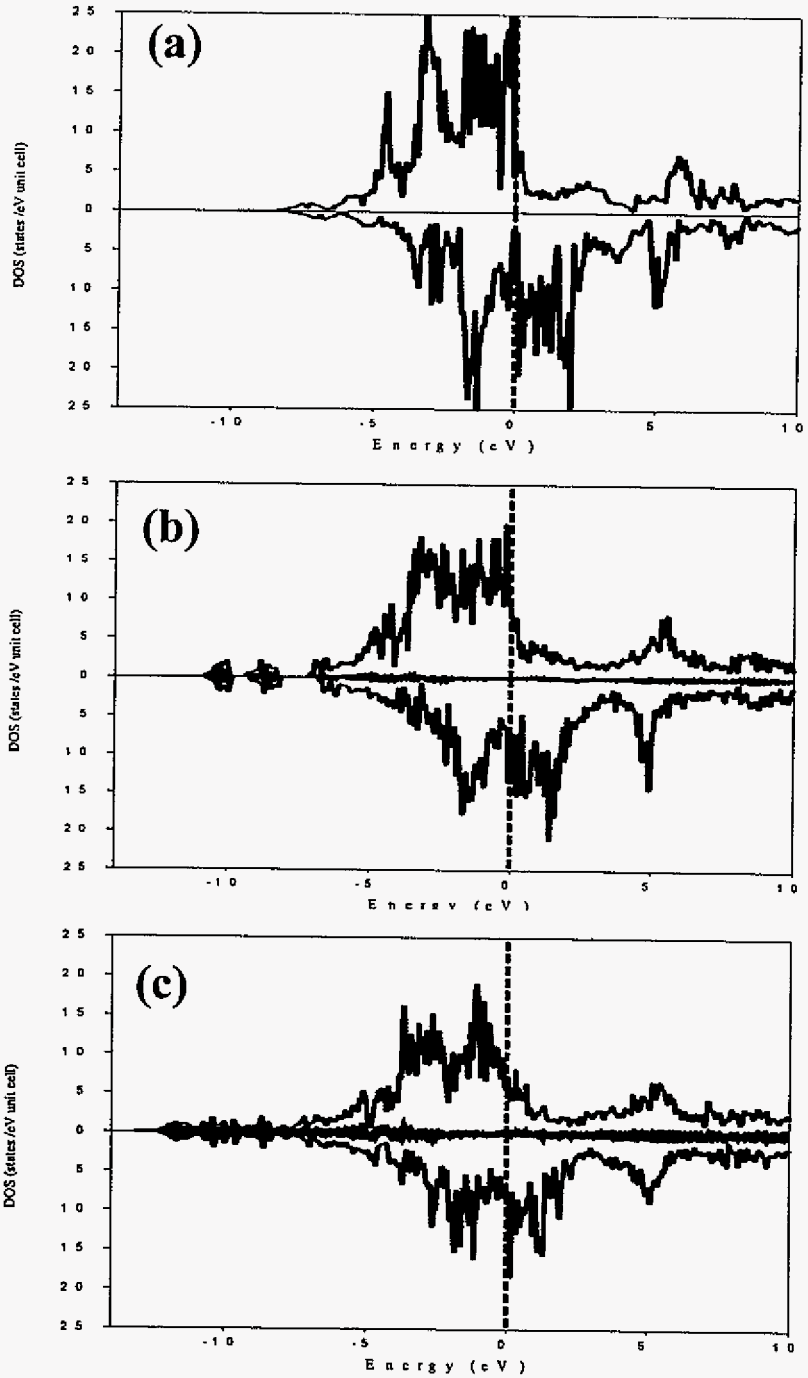

Figure 2. Total density of state (DOS) of spin polarized $LaFe_{13-x}Si_x$. (a) **MOD(2)**, (b) **MOD(3)**, and (c) **MOD(4)**, Dashed lines represent for Fermi level (E_F), set to zero. Positive values correspond to the majority spin band negative values to the minority spin band. The shaded areas are the partial DOS contributions from Si atoms.

Table 5. (a) Integrated density of states (IDOS), (b) Calculated magnetic moments (μ_B), and (c) Charge occupancies of $LaFe_{13-x}Si_x$.

	MOD (2)	**MOD (3)**	**MOD (4)**
Composition	**$LaFe_{13}$**	**$LaFe_{11}Si_2$**	**$LaFe_9Si_4$**
(a) Integrated density of states (IDOS)			
IDOS, spin up	67.75	59.70	53.12
IDOS, spin down	39.25	39.30	37.87
Δ (spin up - spin down)	**28.50**	**20.40**	**15.25**
(b) Calculated magnetic moments (μ_B)			
La	-0.4869	-0.3944	-0.2667
Fe_I	1.7785	1.4239	0.9728
Fe_{II}	2.2695	1.9601	1.8557
Si	-	-0.1228	-0.0790
Total Mag.Mom.μ_B/formula	28.18	20.45	15.24
Average Fe Ms (μ_B)	2.2317	1.9113	1.7575
(c) Charge Occupancies of each atoms			
La	2.8113	2.9732	3.1233
Fe_I	0.3158	0.3704	0.4521
Fe_{II}	-0.2606	-0.226	-0.2034
Si	0	-0.5251	-0.4872

Table 6. The nearest-neighbor Fe-Fe number in $LaFe_{13-x}Si_x$

	Fe_I	Fe_{II}
MOD (2)	12	10
MOD (3)	10	8 or 9
MOD (4)	8	7

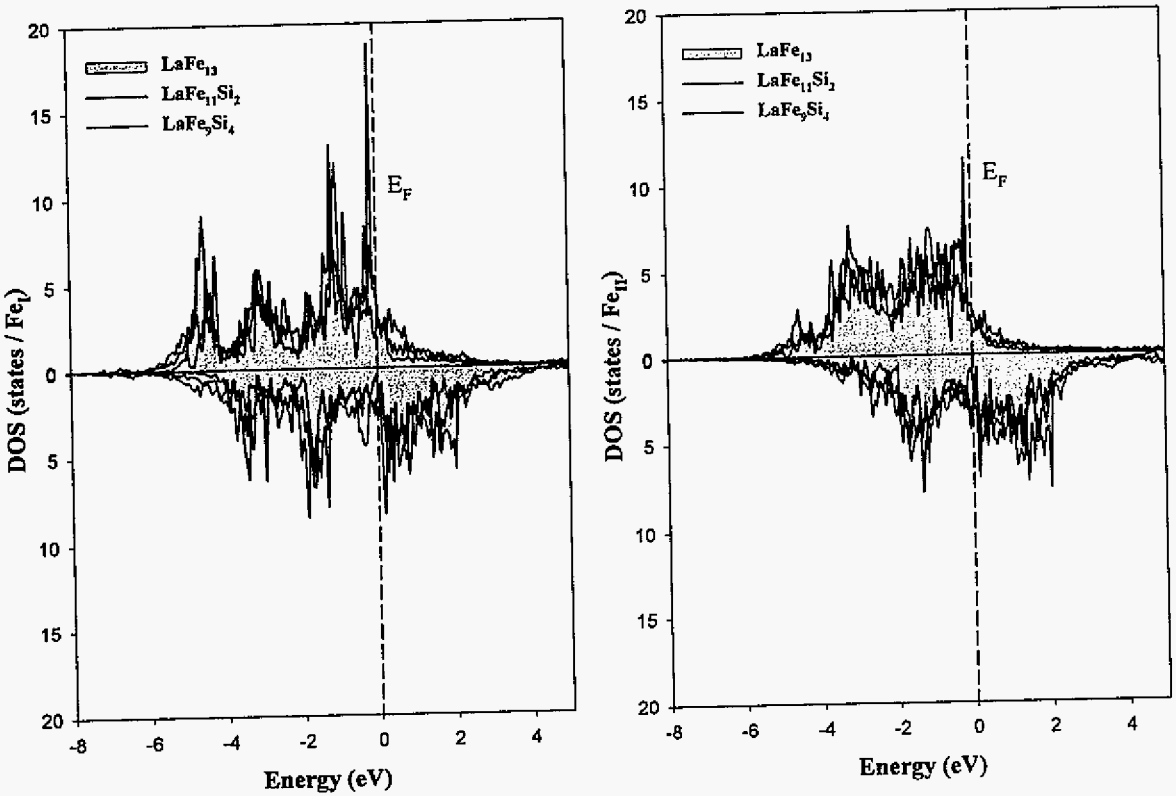

Figure 3. Partial density of state (DOS) of the Fe 3*d* states: (a) Fe_I and (b) Fe_{II}. The shaded areas are the partial DOS of Fe 3*d* in $LaFe_{13}$, the blue line and red line correspond to the 3*d* Fe band for $LaFe_{11}Si_2$, and $LaFe_9Si_4$, respectively.

Table 7. Comparison of shortest Fe-Fe distance in several ferromagnetic and antiferromagnetic materials.

Compounds	Structure	Fe-Fe distance (Å)	Ordering Temperature (°C)	Reference
α-Fe	W	2.48	$T_c = 771$	28
$LaFe_{10.9}Al_{2.1}$	$NaZn_{13}$	2.47	$T_c = -73$	29
$LaFe_{11.4}Al_{1.6}$	$NaZn_{13}$	2.46	$T_N = -69$	30
Lu_2Fe_{17}	Th_2Ni_{17}	2.39	$T_c = 498$	31
Ce_2Fe_{17}	Ce_2Fe_{17}	2.38	$T_N = -48$	32
$Nd_2Fe_{14}B$	$Nd_2Fe_{14}B$	2.40	$T_N = 312$	24

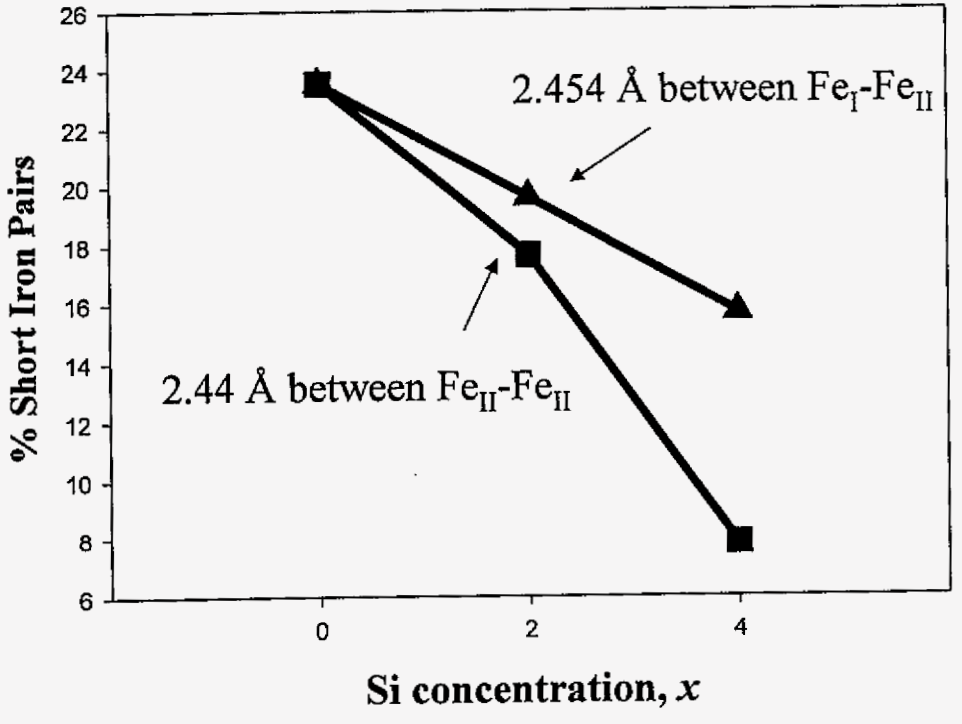

Figure 4. Fraction of shortest interatomic distance in $LaFe_{13-x}Si_x$ structure.

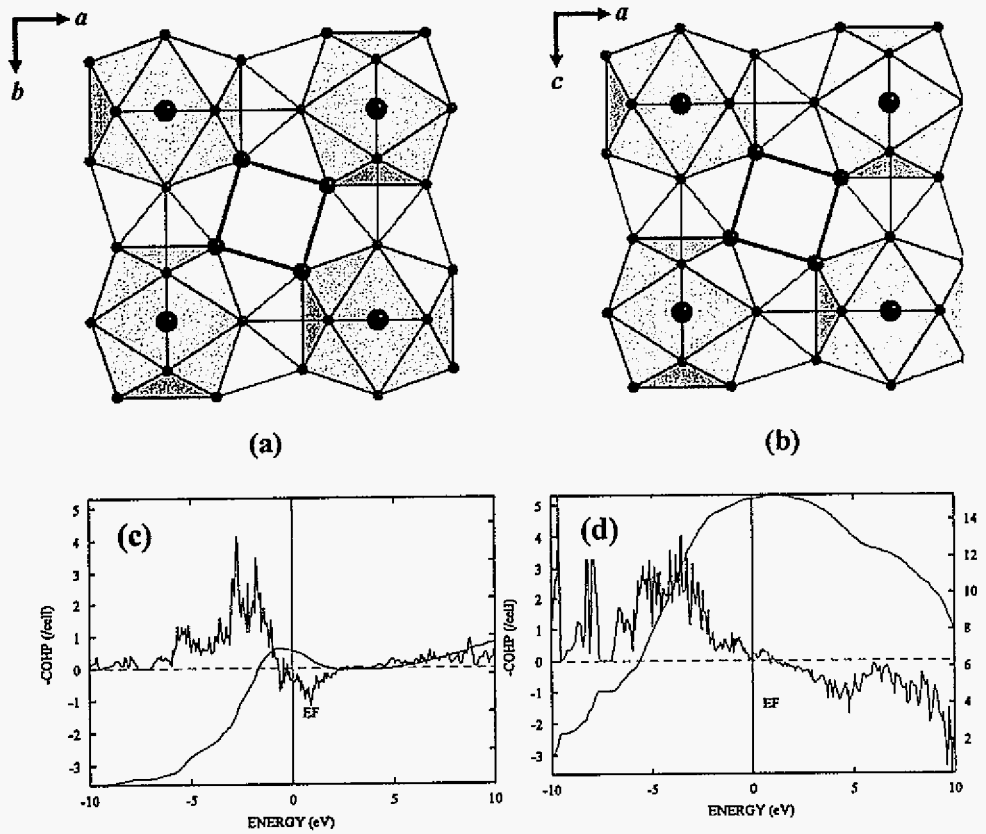

Figure 5. Two different kinds of interactions between icosahedra in the tetragonal $LaFe_9Si_4$ structure.

Projection of the structure of cubic $LaFe_{13-x}Si_x$ on the *ab* plane (b) on *ac* plan (c) COHP curve for Fe-Fe bond, and (d) COHP curve for Fe-Si bond in $LaFe_9Si_4$.

Table 9. Crystal parameters used in the calculation. Lattice constants are taken from actual experiment.

Temperature, °C	25		- 90	
Lattice parameter, a (Å)	11.4881		11.4680	
Wigner-Seitz sphere radii, (Å)				
La	2.234		2.230	
Fe_I	1.386		1.384	
Fe_{II}	1.379		1.376	
Space group				
x, y and z parameters	$x = 0.0$	$x = 0.4986$	$x = 0.0$	$x = 0.4967$
	$y = 0.1169$	$y = 0.1169$	$y = 0.1169$	$y = 0.1168$
	$z = 0.1791$	$z = 0.1791$	$z = 0.1793$	$z = 0.1792$

Table 10. The calculated total energies for two different space group at two different temperatures.

	Room Temperature	*Low Temperature*
	$\Delta E_{(F\bar{4}3c-Fm\bar{3}c)}$	$\Delta E_{(F\bar{4}3c-Fm\bar{3}c)}$
Lattice parameter (a)	11.4881	11.4680
Total $E_{Non\text{-}mag.}$, eV	-0.0005	-0.087
Total $E_{mag.}$, eV	-0.0030	-0.0143

CHAPTER 5

$RE_{2-x}Fe_4Si_{14-y}$ (RE = Y, Gd-Lu) Intergrowth Structures: Superstructures, Properties and Electronic Structure

*Mi-Kyung Han,[a] Yaqiao Wu[b], Gary John Long[c], Matthew Kramer[b], and Gordon J. Miller[a]**

[a] Department of Chemistry, Iowa State University
[b] Department of Materials Science and Engineering, Iowa State University
[c] Department of Chemistry, University of Missouri-Rolla

Abstract

New ternary rare-earth iron silicides $RE_{2-x}Fe_4Si_{14-y}$ (RE = Y, Gd-Lu) were synthesized by arc-melting the elemental components. These compounds crystallize in the hexagonal system with $a \approx 3.9$ Å, $c \approx 15.3$ Å. The structures are built up of rare-earth silicide planes with approximate compositions "$RE_{1.2}Si_{1.9}$" alternating with β-$FeSi_2$-derived (*hkl*)-type slabs. The rare-earth silicide sheets show intrinsic disorder of RE and Si atoms due to interatomic distance constraints. Investigation by transition electron microscopy (TEM) reveals a superstructure in the crystallographic *ab*-plane. Fe Mössbauer studies to understand the iron environments in superstructure are currently in progress. Magnetic susceptibility suggests no magnetic coupling between rare-earth elements, and resistivity measurements indicate poor metallic behavior with a large residual resistivity at low temperatures (consistent with disorder). TB-LMTO-ASA electronic structure calculations show the Fermi level falls at a pseudogap in the densities of states.

Introduction

In recent years numerous ternary rare-earth iron silicides have been synthesized, and many of them exhibit interesting properties[1-2], such as superconductivity[3], heavy-fermion behavior[4-5], Kondo effect[6], or valence fluctuations[7-8]. Therefore, these compounds provide the opportunity for better understanding of the many interesting physical properties that arise from the variation of the interplay between the *f*-electrons of the rare-earth element and the conduction electrons, as well as the contribution of 3*d*-band electrons to itinerant magnetism. Another interesting category of silicides is semiconducting silicides in particular those with a direct gap and a bandgap energy smaller than that of silicon because of their potential applications in the electronics and energy-conversion fields. The direct gap silicides that has attracted most attention so far is iron disilicide due to the availability of the components iron and silicon and the low-toxicity of the compound, as well as its fairly good lattice match to silicon.[9-10] Much effort has been made to modify optical or transport properties of these materials as well as develop new alternative materials. Here, intermetallic compounds with high contents of silicon offer an interesting alternative. Especially, if homogeneous ternary silicides phases can be formed from these semiconducting materials and isomorphous metallic silicides, it should be extend the possibility of tuning the properties of these materials.

For the time being, more than 100 rare-earth iron silicides are known, and they crystallize in more than 20 different crystal structures.[11] However, most of the known ternary rare-earth iron silicides have lower silicon contents, e.g., $REFe_2Si_2$ with the $BaAl_4$- type structure, and $RE_2Fe_3Si_5$ with the $Sc_2Fe_3Si_5$ - type structure. The $RE_{2-x}Fe_4Si_{14-y}$ compounds reported here have higher silicon content.

In the course of our investigations of ternary rare-earth transition-metal intermetallics, we prepared the series $RE_{2-x}Fe_4Si_{14-y}$. These compounds were initially prepared as part of a project to explore rare-earth transition-metal silicides with interesting magnetocaloric properties. $Y_2Fe_4Si_9$[12] is very similar to the structure reported here, however the atomic position of one site is different from that found in this structure. The structure of these ternary compounds may be viewed as consisting of atomic layers of two kinds stacked along the *c*-axis. One kind, designated RE-M layers, contains all of the rare-earth (RE) and some main group elements (M); the other layer, designated T-M layers, contain all of the transition metal atoms (T) and the remaining main group elements. In searching the literature, similar atomic layered topologies have been found in several series of ternary intermetallics of the rare-earths (RE) and transition metals (T) with triels (group 13: Al, Ga). Various aspects of these structures have been briefly reviewed by W. Jeitschko.[12-15] In Table 1, we give a summary of crystal structures that have a similar layered topology. Almost all of these structures were refined in a hexagonal space group.

------ Table 1 ------

This structure is isotypic with those of the $Sc_{1.2}Fe_4Si_{9.9}$[16]except slight difference in the occupancies of the partially occupied sites. Furthermore, no observation was made for the superstructure in $Sc_{1.2}Fe_4Si_{9.9}$ compound. We report herein ternary rare-earth compounds with high silicon contents, and show that they exhibit interesting superstructure behavior. In addition to the planar rare-earth silicide net, these compounds contain (*hkl*)-type slabs based upon β-$FeSi_2$. The addition of Si-based ternaries to this class of intergrowth intermetallics compounds is important because β-$FeSi_2$ has potential applications in solar cells and optoelectronic devices due to its semiconducting properties with a direct gap of about 0.79

eV. Therefore, tuning this band gap by varying the RE element in the structure may be possible. We also report on our results of electronic structure calculations. Subsequently, we focused our efforts on understanding their electrical and magnetic properties, and their structural characteristics, such as what "drives" the particular superstructure? Clearly, a better understanding of the properties of these materials requires a better understanding of the structure and the nature of the possible disorder.

Experimental

Synthesis. New ternary rare-earth iron silicides $RE_{2-x}Fe_4Si_{14-y}$ (RE = Y, Gd, Tb, Dy, Ho, Er, Tm, Yb, and Lu) were synthesized by arc-melting the stoichiometric quantities of elements on a water-cooled copper hearth using a tungsten electrode in an atmosphere of ultrapure argon gas. The starting materials (rare-earth elements, (Ames Lab Rare-Earth Metals Preparation Center, 99.99 ~ 99.9999 %); Fe chips (Aldrich, 99.98 %); Si pieces (Aldrich, 99.5 %)) were pre-arc melted to remove impurities such as oxygen on the surfaces of the elements. During the arc-melting procedure, a titanium or zirconium pellet was heated prior to melting the reactant mixture to further purify the argon atmosphere. The samples were remelted several times in order to promote homogeneity, and weight losses during the arc melting process were found to be less than 1-2 wt.%. All of these ternary silicides are stable in air for long periods (more than 2 years) and show silvery metallic luster.

Chemical Analysis. Qualitative analysis was a routine test on interesting samples obtained from our synthetic work. The chemical compositions were analyzed by Energy Dispersive Spectroscopy (EDS) quantitative analysis using a JEOL 8400A scanning electron microscope, equipped with an IXRF Systems Iridium X-ray analyzer, and these compositions complemented the results from single crystal X-ray analysis. Samples for accurate quantitative analysis required a flat, microscopically smooth surface to maintain the validity of the path length calculation and to assure that the surface to be analyzed was homogeneous. The sample surface was polished by sandpaper and fine leather. Samples were inspected by back scattering and topological modes to determine the sites for elemental analysis. Whenever possible, the bulk compositions were used as standards to reduce any matrix effects in the analysis. Otherwise, well-defined stoichiometric binary component and the pure elements were used as standards. Table 2 summarizes the standards that used in this analysis.

------ Table 2 ------

Microstructure characterization. A Philips CM 30 transmission electron microscope (TEM) has been employed for TEM/high resolution TEM (HRTEM) investigations. TEM samples were prepared by using crash-flow method.[16]

Structure Determination. The samples were characterized by single crystal and powder X-ray diffraction (XRD) techniques at ambient temperature. The powders of all samples are dark gray. The powder diffraction patterns of the samples were obtained with a Huber image plate camera equipped with monochromatic Cu $K\alpha_1$ radiation ($\lambda = 1.540598$ Å). Powdered samples were homogeneously dispersed on a Mylar film with the aid of a little petroleum

jelly. The step size was set at 0.005° and the exposure time was 1 hr. Data acquisition was controlled via the *in-situ* program. The lattice parameters of $RE_{2-x}Fe_4Si_{14-y}$ (RE = Y, Gd - Lu) were obtained from least squares refinement with the aid of a Rietveld refinement program[17] and summarized in the Table 3. A block-like single crystals (overall crystal dimension: 0.1 ~ 0.2 × 0.1 ~ 0.2 × 0.1 ~ 0.3 mm^3) were selected from the product and was mounted on glass fibers. These diffraction experiments utilized a Brucker APEX CCD-diffractometer equipped with monochromated Mo Kα radiation (λ = 0.71073 Å), and diffraction data were collected at room temperature over a hemisphere or full sphere of reciprocal space with 0.3° scans in ω and with an exposure time of 10 sec per frame up to 2θ = 56.55°. Intensities were extracted and then corrected for Lorentz and polarization effects using the *SAINT* program.[18] The program *SADABS*[19] was used for empirical absorption correction. Structure refinements (full-matrix least-squares on F^2) were performed using the *SHELXTL-PLUS* programs.[20]

Electronic Structure Calculations. The electronic structures of hypothetical compounds were calculated self-consistently by using the tight-binding linear muffin-tin-orbital (TB-LMTO) method[21-24] within the atomic sphere approximation (ASA) using the LMTO Version 47 program. Exchange and correlation were treated in a local spin density approximation (LSDA).[25] All relativistic effects except spin-orbit coupling were taken into account using a scalar relativistic approximation.[26]

Within the atomic sphere approximation (ASA), space is filled with overlapping Wigner-Seitz (WS) atomic spheres. The radii of the WS spheres were obtained by requiring the overlapping potential to be the best possible approximation to the full potential according to an automatic procedure. The WS radii determined by this procedure are 4.41 ~ 4.50 Å for

rare-earth elements, 2.51 ~ 2.60 Å for Fe and 2.51 ~ 2.54 Å for Si. The basis set included 6*s*, 6*p*, 5*d* orbitals for the rare-earth element, 3*s*, 3*p* orbitals for Si and 4*s*, 4*p* and 3*d* orbitals for Fe. The Löwdin downfolding technique allows the derivation of few-orbital effective Hamiltonians by keeping only the relevant degrees of freedom and integrating out the irrelevant ones. The **k**-space integrations to determine the self-consistent charge density, densities of states (DOS) and crystal orbital Hamilton populations (COHP)[27] were performed by the tetrahedron method[28]. The Fermi level was chosen as an internal reference level in all cases.

Physical Properties Measurements

Magnetic Measurement. DC magnetization data were collected using a Quantum Design MPMS (QD-MPMS) superconducting quantum interference device (SQUID) magnetometer with a 7 T superconducting magnet. Measurements were made usually on pieces of polycrystalline material (5-150 mg) in applied fields of 0.1~1 T, at temperatures from 1.85 – 300 K.

Resistivity Measurement. The electrical resistance in zero field was measured with a Linear Research LR-700AC resistance bridge (f = 16 Hz, I = 1~3 mA) in the magnetic field-temperature environment of the same QD MPMS system, using a standard four-probe technique.

Result and Discussion

A series of polycrystalline rare-earth iron intermetallic compounds $RE_{2-x}Fe_4Si_{14-y}$ (RE = Y, Gd - Lu) has been prepared by arc melting. X-ray diffraction only showed reflections due to the $Sc_{1.2}Fe_4Si_{9.9}$-structure for Gd, Tb, Dy, Ho, Er, Tm, Lu, and Y, but the ytterbium compound contains iron disilicide as secondary phases. The lattice parameters obtained from these data are listed in Table 3.

------ Table 3 and Figure 1 ------

The plot of the cell volumes, shown in Figure 1, reflects the well-known lanthanide contraction and does not show any significant discontinuities. We have found this structure type only for the heavier lanthanides, while the lighter lanthanides adopt different structures such as $NaZn_{13}$, and $ThMn_{12}$. This might be explained by a size argument since the early lanthanide atoms are considerably larger than the late ones. Frequently, the structures of the compounds involving the early and the late lanthanides differ due to different coordination numbers (CN) of these atoms. For example, the rare-earth atom has CN 24 in the $NaZn_{13}$-type structure, while in $RE_{2-x}Fe_4Si_{14-y}$, the rare-earth atomic positions have six irons and 11 silicon neighbors yielding CN 17. Therefore, the light rare-earth elements prefer to have large CN, whereas the heavy rare-earth elements adopt this structure with smaller CN. (Note: There are several different factors controlling the formation of $NaZn_{13}$-type structure and discussed in previous chapter 3)

Structure description

Ternary rare-earth iron silicides $RE_{2-x}Fe_4Si_{14-y}$ (RE = Y, Gd, Tb, Dy, Ho, Er, Tm, Yb and Lu) crystallize in the hexagonal space group *P6₃/mmc* (No. 194) at ambient temperature.

Among the five crystallographic sites identified in the structure, only three of which 4*f* (1/3, 2/3, *z*), 4*f* (1/3, 2/3, *z*), and 4*e* (0, 0, *z*) sites are fully occupied by Fe and Si(1) and Si(2) atoms, respectively; The other two sites 2*d* (2/3, 1/3, ¼) and 6*h* (*x*, *y*, ¼) are assigned to RE and Si(3), respectively.

------ Figure 2 ------

Figure 2 shows a representation of the crystal structure of $RE_{2-x}Fe_4Si_{14-y}$ perpendicular to the *b* axis, and emphasizes each atomic layer. The crystal structures of these ternary compounds consist of two alternating building blocks along the *c*-axis: (1) intrinsically disordered rare-earth silicide planes; and (2) ordered β-$FeSi_2$-derived slabs. However, the chemical bonding within and between the layers in the structure is of similar strength, based on interatomic distances.

β-$FeSi_2$-derived slabs

Figure 3 shows the $FeSi_2$ structural motif found in this series of compounds and compares it to that of β-$FeSi_2$. Semiconductor β-$FeSi_2$ crystallizes in the orthorhombic structure with the space group *Cmca* and the unit cell parameters $a = 9.863$, $b = 7.791$ and $c = 7.833$ Å. In Figure 3c shows the Fe arrangement in (001) planes of $RE_{2-x}Fe_4Si_{14-y}$ to be regular, which differs from the (111) projection of Fe planes in β-$FeSi_2$ due to Fe-Fe bonds. $FeSi_2$ slabs in both structures are constructed by placing Fe atoms in one-half of the interstices of a cubic array of Si atoms. Iron atoms in this layer has highly distorted cubic environment and these distorted cubic share their edges, shown in Figure 3c. The Fe-Si interatomic distances found in this structure range between 2.3 and 2.6 Å, which well match to those of β-$FeSi_2$. In β-$FeSi_2$, for example, Fe and Si atoms are separated by 2.3~2.4 Å. In

addition, the sum of the covalent radii of Si (1.17 Å) and Fe (1.24 Å) gives an expected interatomic distance of 2.41 Å, which is close to our experimental Fe-Si distances.

------ Figure 3 ------

Disordered RE/Si planes

The RE atoms at the 2*d* (2/3, 1/3, ¼) sites and silicon atoms at the 6*h* (*x*, *y*, ¼) sites form a disordered atomic plane with a triangular pattern, shown in Figure 4. The disorder occurs because simultaneous occupation of every Gd site and every Si(3) site would create physically unacceptable Gd-Si(3) distances, 1.355 Å, as well as Si(3)-Si(3) distance within a triangle of 1.604Å. As a result, the occupancies of the RE and Si(3) atoms refer lower than the full amount allowed by that specific crystallographic position to partial occupancies of ~ 60 % for the RE site and ~ 31 % for the Si(3) site. Therefore, these rare-earth silicide planes have approximate compositions of "$RE_{1.2}Si_{1.9}$". Similar types of disorder among RE and main group (M) atoms in RE/M planes were observed in several different systems, such as RE/Pt/Ga[29], RE/Ni/Ga/Ge[30], RE/Co/Ga[31], RE/Os/Al[32], and RE/Ru/Ga[33].

------ Figure 4 ------

Details of the single crystal data collection parameters and crystallographic refinement results for $RE_{2-x}Fe_4Si_{14-y}$ (RE = Y, Gd-Lu) are listed in the Table 4. The resulting occupancies and atomic parameters are listed in the Table 5. The refined chemical formula is in good agreement with the composition obtained by the elemental analysis.

------ Table 4 and Table 5 ------

Superstructure

The intrinsic disordering of the RE and Si(3) sites suggests that the unit cell found might be a subcell of the true cell and that a superstructure with ordered RE and Si(3) sites may exist. The numerous attempts to fit larger cells were made, e.g. Kwei, *et al.*[34] suggested a supercell with tripled in *a* and *b* relative to the observed unit cell of $Ce_2Pt_6Gd_{15}$, and Kanatzidis, M., *et al.*[35] and Jeitschko, W., *et al.*[36] independently reported an atomic ordered superstructure with a $\sqrt{3}$ larger *a* axis in $Y_{0.67}Ni_2Ga_{5-x}Ge_x$ and $RE_2Pt_6Al_{15}$ compounds, respectively.

The TEM picture and STOE image plate picture of $RE_{2-x}Fe_4Si_{14-y}$ (RE = Gd and Y) are indicative of regular arrangement of RE and Si atoms, and provide useful information in understanding the crystal structure of these compounds. Typical HRTEM image for $Gd_{1.2}Fe_4Si_{9.9}$ and $Y_{1.2}Fe_4Si_{9.9}$ are shown in Figure 5b, and 5e, respectively. The HRTEM results of $Gd_{1.2}Fe_4Si_{9.9}$ along $[11\bar{2}0]$ (Figure 5c) and the corresponding selected area electron diffraction pattern (SAEDP) shown in Figure 5b indicate a *d*-spacing between (0002) planes of about 7.67 Å, which is one-half of the crystallographic *c*-axis. This result is consistent with two disordered Gd/Si(3) layers in a unit cell. A 2H layered structure is identified based on the indexed SAEDP. The HRTEM image obtained along [0001] (Figure 5c and 5e) and the corresponding indexed SAEDP, shown in Figure 5d and 5f, reveal strong hexagonal subcell reflections with rather weak superstructure reflections from $4a \times 4b$ supercell in the crystallographic *ab* plane. Apparently, four-fold hexagonal axis has not been observed for the other nearly isotypic compounds.

TEM characterizations on samples of Dy/Fe/Si, Ho/Fe/Si, Tb/Fe/Si, Yb/Fe/Si, Y/Fe/Si, Lu/Fe/Si, Er/Fe/Si, and Tm/Fe/Si also indicate that all these samples have 2H

layered structure along [1 1 $\bar{2}$ 0] orientation, as same as that of Gd/Fe/Si compound, as whown in Figure 6a - 6h, respectively.

------ Figure 5 and Figure 6 ------

Figure 7 shows STOE images of $Gd_{1.2}Fe_4Si_{9.9}$ along [100] and [010]. Weak streaks are observed along the c^*-axis of the reciprocal unit cell, thus indicating of irregular nonperiodic stacking of Gd/Si(3) planes along the hexagonal axis. However, the [100] and [010] picture further confirm the existence of a supercell structure. Therefore, we conclude from these results that the Re/Si(3) planes have a $4a \times 4b$ superstructure within the *ab*-plane, but that this shows stacking disorder along the *c*-axis.

------ Figure 7 ------

An ordered model of "$RE_{1.2}Si_{1.9}$" plane

Because of the diffuse character of X-ray diffraction intensity along the c* axis, it was not possible to refine a superstructure model. Thus, we can only postulate a possible superstructure model. The ordered model structure is shown in the right-hand part of Figure 8. This model required a lowering of the crystal symmetry from $P6_3/mmc$ (no. 194) to $P6_3/m$ (no. 176). In each $4a \times 4b$ supercell plane, this model involved removing 7 Gd atoms and 33 Si(3) atoms from $[GdSi_3]_{16}$, which resulted in a hexagonal superstructure with a cell content of $Gd_{1.25}Fe_4Si_{9.875}$, and is very close to the observed composition $Gd_{1.20(1)}Fe_4Si_{9.88(4)}$ obtained from the structure refinement and EDS. The superstructure have an ordered arrangement with regular interatomic distances, i.e. 2.861Å for Gd-Si(3) and 2.346 Å for Si(3)-Si(3). This Gd-Si(3) plane contains Si-Si dimers and a trimer in a regular pattern. Since these layers are

7.67Å apart, these layers are randomly positioned relative to the remainder of the structure between the Gd-Si(3) layers. Therefore, this shows ordered two-dimensional structure with disordered along the *c*-axis.

------ Figure 8 ------

The corresponding supercell structure belongs to the space group $P6_3/m$ (no. 176) with lattice parameter of $a' = 15.8064$ Å and $c' = c$. From a simulated precession pattern using the ATOMS Version 5.0.7 program, we can see that this superstructure model gives a similar diffraction pattern as shown in SAEDP picture, see Figure 9. Middle figure at Figure 9 emphasize the similarity between them. It has a hexagon at the center with six triangles in it. However, it shows small variation of intensities of peak because the intensity can be varied by ordering of the atoms.

------ Figure 9 ------

The RE atoms are coordinated to 6 iron atoms and 11 silicon atoms and occupy the center of the trigonal prism of Si atoms with all faces capped with Si(3) and a trigonal prism by 6 Fe atoms, shown in Figure 10. The Gd-Si bond distances are 2.860, 2.913 and 3.139 Å and Gd-Fe distance is 3.163Å. There are two kinds of coordination around the Fe atoms, shown Figure 11. One Fe atom is eight-coordinate, the other is seven coordinate, and these cubic shares their edges. To investigate different Fe environment in the structure, iron Mössbauer spectroscopy is currently in progress.

------ Figure 10 and Figure 11 ------

Electronic Structure and Bonding Relationships

To understand the possible chemical bonding features influencing the stability of

$RE_{2-x}Fe_4Si_{14-y}$ system, TB-LMTO-ASA electronic structure calculations were performed on "YFe_4Si_{10}" as the representative composition due to avoids the contribution of 4*f* orbitals of rare-earth elements, and on β-$FeSi_2$ as a comparison. YFe_4Si_{10} has monoclinic $P2_1$ space group and ordered Y and Si plane. β-$FeSi_2$ is well known as a semiconductor with the band gap of 0.79 eV. Interestingly, TB-LMTO-ASA electronic structure calculations for "YFe_4Si_{10}" show the Fermi level falls near a pseudogap in the DOS curve. Considering the similarity of overall shape of DOS curve to that of β-$FeSi_2$, it may show similar properties. Indeed physical measurement shows it as a poor metal. In addition, the effects of substitution of other lanthanide elements on the electronic structures and their properties are currently in progress.

------ Figure 12 ------

Physical Properties Measurements

------ Figure 13 ------

Figure 13 shows the temperature dependence of the magnetic susceptibility and its inverse for a polycrystalline sample of $Gd_{1.2}Fe_4Si_{9.8}$ measured between 1.85 K and 300 K. From these data there is no clear indication of magnetic order down to 1.85 K. A least-squares fit of the Curie-Weiss law yields an effective magnetic moment $\mu_{eff} = \sim 8.1/\mu_B$/f.u., which is slightly higher than the theoretical value for isolated Gd atoms ($7.94/\mu_B$). This suggests that there is little contribution from Fe atoms to the magnetic moment in the compound, and no magnetic coupling between rare-earth elements down to < 2 K. It follows the Curie-Weiss law down to 50 K with a Weiss temperature of −12 K. The effective

magnetic moments for each RE ion in $RE_{2-x}Fe_4Si_{14-y}$ as extracted from fits to $\chi(T)$ are listed in Table 6 and compared to the corresponding free ion values.

------ Table 6 ------

No magnetic ordering for each rare-earth samples are observed to the lowest temperatures measured, shown in Figure 14. Reciprocal susceptibilities of each rare-earth sample are plotted as a function of temperature in Figure 15. All samples show similar $1/\chi$ *vs.* temperature plots.

------ Figure 14 and Figure 15 ------

Figure 16 shows the normalized resistivity for a polycrystalline sample of $Gd_{1.2}Fe_4Si_{9.8}$. Resistivity measurements indicate poor metallic behavior with a large residual resistivity at low temperatures which is attributed to the disordered structure. This result is consistent with the results from electronic calculations.

------ Figure 16 ------

Conclusion

We synthesized new ternary rare-earth iron silicides $RE_{2-x}Fe_4Si_{14-y}$ (RE = Y, Gd-Lu) by arc-melting the elemental components. The structures are built up of disordered rare-earth silicide planes with approximate compositions "$RE_{1.2}Si_{1.9}$" alternating with β-$FeSi_2$-derived (*hkl*)-type slabs. On the basis of the transition electron microscopy, an ordered arrangement of these planes with a supercell of $4a \times 4a$ was proposed. Fe Mössbauer studies to understand the iron environments in the superstructure are currently in progress. Magnetic susceptibility suggests no magnetic coupling between rare-earth elements. Electrical conductivity

measurement indicates poor metallic behavior of these compounds, which is in good agreement with the theoretical ones calculated for ordered superstructure model using TB-LMTO-ASA electronic structure calculations.

References

1. P. Rogl in Handbook of *Physics and Chemistry of Rare Earths*, edited by Gschneidner, K. A. Jr.; Eyring, L. (Elsevier Science Publishers, North-Holland, Amsterdam, **1984**), Vol. 7, pp. 1–264.

2. Leciejewicz, J.; Szytula, A. in *Handbook of Physics and Chemistry of Rare Earths*, edited by Gschneidner, K. A. Jr.; Eyring, L. (Elsevier Science Publishers, Amsterdam, **1989**), Vol. 12, p. 133.

3. Cashion, J. D.; Shenoy, G. K.; Niarchos, D.; Viccaro, P. J.; Aldred, A.T.; Falco, Charles M. *J. Appl. Phys.* **1981**, 52, 2180.

4. Li, H. S.; Coey, J. M. D. *Handbook of Magnetic Materials* **1991** vol 6, ed Buschow, K. H. J. (Amsterdam: Elsevier) pp. 1.

5. Franse, J. J. M.; Radwanski, R. J. *Handbook of Magnetic Materials* **1993** vol 7 ed Buschow, K. H. J. (Amsterdam: Elsevier) p. 307.

6. Singh, Y.; Ramakrishnan, S.; Hossain, Z.; Geibel, C.; *Phys. Rev. B: Condens. Matt. Matt. Phys.* **2002**, 66(1), 014415.

7. Noguchi, S.; Okuda, K.; Abliz, M.; Goto, K.; Kindo, K.; Haga, Y.; Yamamoto, E.; Onuki, Y. *Physica B*, **1998**, 246-247, 456.

8. Gordon, R. A.; Warren, C. J.; Alexander, M. G.; Disalvo, F. J.; Pöttgen, R. *J. Alloys. Comp.* **1997**, 248, 27.

9. Bost, M. C.; Mahan, J. E. *J. Appl. Phys.* **1985**, 58, 2696.

10. Bost, M. C.; Mahan, J. E. *J. Appl. Phys.* **1988**, 64, 2034.

11. Villars, P.; Calvert, L. D. *Pearson's Handbook of Crystallographic Data for Intermetallic Phases,* ASM International Materials Park, OH, Desk ed., **1997**.

12. Galadyshevskij, E. I.; Bodak, O. I.; Jarovets, V .I.; Gorelenko, Ju. K.; Skolzdra, R. V. *Ukr. Fiz.Zh.* **1978**, 23, 77.

13. Niermann, J.; Jeischko, W. *Z. Anorg. Allg. Chem.* **2002**, 628, 2549.

14. Schlüter, M.; Jeitschko, W. *J. Solid State Chem.* **2003**, 172, 27.

15. Niermann, J.; Jeitschko, W. *Inorg. Chem.* **2004**, 43, 3264.

16. Williams, B. D.; Carter, B. *Transmission Electron Spectroscopy*, Plenum press, NY, London, **1996**.

17. Hunter, B. A.; Howard, C. J. *Rietica*; Australian Nuclear Science and Technology Organization: Menai, Australia, **2000**.

18. SMART; Bruker AXS, Inc.; Madison, WI, **1996**.

19. Blessing, R. H. *Acta. Cryst.* **1995,** A 51, 33.

20. SHELXTL; Bruker ASX, Inc.: Madison, WI, **2000**.

21. Andersen, O. K. *Phys. Rev.* **1975,** B12, 3060.

22. Andersen, O. K.; Jepsen, O. *Phys. Rev. Lett.* **1984**, 53, 2571.

23. Andersen, O. K.; Jepsen, O.; Glötzel, D. In *Highlights of Condensed-Matter Theory*; Bassani, F.; Fumi, F.; Tosi, M. P., Lambrecht, W. R. L., Eds.; North-Holland: New York, **1985**

24. Andersen, O. K. *Phys. Rev.* **1986,** B34, 2439.

25. Von Barth, U.; Hedin, L. *J. Phys. C* **1972**, 5, 1629.

26. Koelling, D. D.; Harmon, B. N. *J. Phys. C* **1977**, 10, 3107.

27. Dronskowski, R.; Blöchl, P. *J. Phys. Chem.* **1993**, 97, 8617.

28. Blöchl, P. E.; Jepsen, O.; Andersen, O.K. *Phys. Rev.* **1994**, B49, 16223.

29. Kwei, G. H.; Lawson, A. C.; Larson, A. C.; Morosin, B.; Larson, E.M.; Canfield, P.C. *Acta. Cryst.*. **1996**, B52, 580.

30. Zhuravleva, M. A.; Chen, X. Z.; Wang, X.; Schultz, A. J.; Ireland, J.; Kannewurf, C. K.; Kanatzidis, M. G. *Chem. Matt.* **2002**, 14(7), 3066.

31. Schluter, M.; Jeitschko, W. *Z. Anorg. Allg. Chem.* **2000**, 626(10), 2217.

32. Cordier, G.; Doersam, G.; Kniep, R. *J. Magne. Magne. Mat.* **1988**, 76-77 653.

33. Schluter, M.; Jeitschko, W. *J. Solid State Chem.* **2003**, 172(1), 27.

34. Kwei, G. H.; Lawson, A. C.; Larson, A. C.; Morosin, B.; Larson, E. M.; Canfield, P. C. *Acta. Cyrst.* **1996**, B52, 580.

35. Zhuravleva, M. A.; Chen, X. Z.; Wang, X.; Schultz, A. J.; Ireland, J.; Kannewurf, C.K .; Kanatzidis, M. G. *Chem. Mater.* **2002**, 14, 3066.

36. Niermann, J.; Jeitschko, W. *Z. Anorg. Allg. Chem.* **2004**, 630, 261.

Table 1. A summary of crystal structures with layered topology in of ternary intermetallics of the rare-earth (RE) and transition metals (T) with main group elements (M).

	RE - M layer	T - M layer	Space group	Occ.(%) RE	M
$Y_{0.6}Co_2Ga_{5.33}Ge_{0.67}$	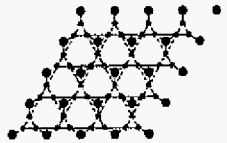		*P*-6*m*2 (187)	60	33
$Gd_{1.33}Pt_3Al_8$ $Gd_{1.33}Pt_3Al_{6.7}Si$	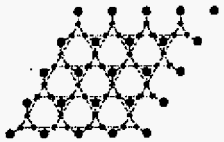		R-3*m* (166)	67 62	35 29
$Gd_{0.67}Pt_2Al_5$ $Gd_{0.67}Pt_2Al_4Si$ $Ce_{1.278}Pt_4Ga_{9.884}$ $Y_{1.357}Pt_4Al_{9.92}$ $Zr_{1.00}Pt_4Al_{10.22}$ $Y_{0.67}Ni_2Ga_{4.33}Ge_{0.67}$ $RE_{1.2}Fe_4Si_{9.9}$	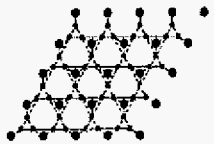		*P*6$_3$/*mmc* (194)	69 53 64 68 50 67 60	37 32 31 33 37 33 31
$Y_2Co_3Ga_9$	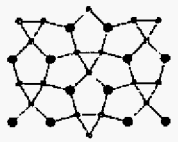		*Cmcm*	100	100
$Y_3Ru_{4.060}Al_{11.940}$ $Nd_3Os_{4.43}Al_{11.57}$ $Gd_3Os_{4.44}Al_{11.56}$			*P*6$_3$/*mmc* (194)	100	100

Table 2. Summary of standards used in chemical analysis.

Elements	Line	Analyzing crystal	Standard	Phases	Composition
Fe	Kα	LIF	Fe (metal)		
Si	Kα	TAP	Si, 100%		
<u>Rare-earths (alternatively)</u>					
Y	Lα	TAP	YMn_2	Single phase	$Y_{1.13}Fe_4Si_{10.05}$
Gd	Lα	LIF	$GdFe_2$	Single phase	$Gd_{1.13}Fe_4Si_{9.65}$
Tb	Lα	LIF	Tb_2Fe_{17}	Single phase	$Tb_{1.23}Fe_4Si_{10.07}$
Dy	Lα	LIF	$DyFe_2$	$FeSi_2$(P4/mmm), ~ 5%	$Dy_{1.12}Fe_4Si_{9.56}$
Ho	Lα	LIF	Ho_2Fe_{17}	Trace amount of impurity	$Ho_{1.27}Fe_4Si_{9.60}$
Er	Lα	LIF	Er_2Fe_{17}	Trace amount of impurity	$Er_{1.23}Fe_4Si_{9.94}$
Lu	Lα	LIF	Lu_2Fe_{17}	Single phase	$Lu_{1.26}Fe_4Si_{10.23}$

Table 3. Lattice constants of $RE_{2-x}Fe_4Si_{14-y}$ (RE = Y, Gd - Lu) obtained from X-ray powder diffraction.

Rare-earth	a (Å)	c (Å)	V (Å^3)
Y	3.9397(1)	15.3014(1)	205.681(2)
Gd	3.9557(1)	15.3194(3)	207.247(6)
Tb	3.9404(1)	15.3084(2)	205.847(4)
Dy	3.9370(1)	15.2913(2)	205.258(5)
Ho	3.9353(1)	15.2657(2)	204.754(5)
Er	3.9326(1)	15.2873(2)	204.734(5)
Tm	3.9280(1)	15.2483(4)	203.751(9)
Yb	3.9225(1)	15.2696(3)	203.459(7)
Lu	3.9298(1)	15.2833(1)	204.402(2)

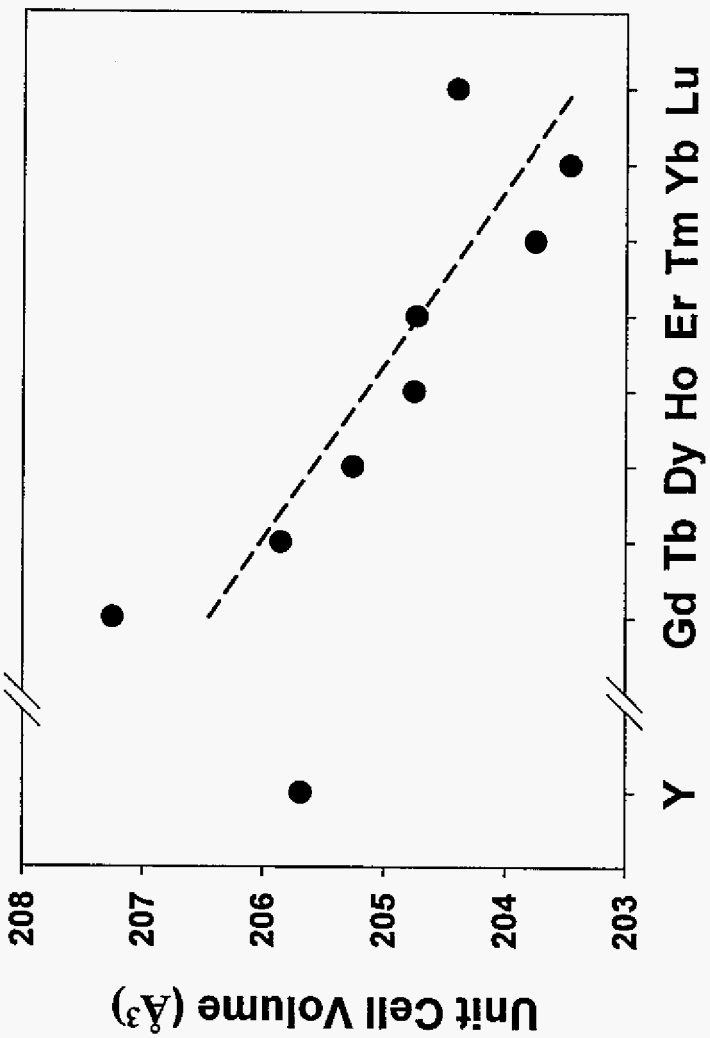

Figure 1. Cell volumes *vs.* radii of rare-erath elements in $RE_{2-x}Fe_4Si_{14-y}$ (RE = Y, Gd - Lu).

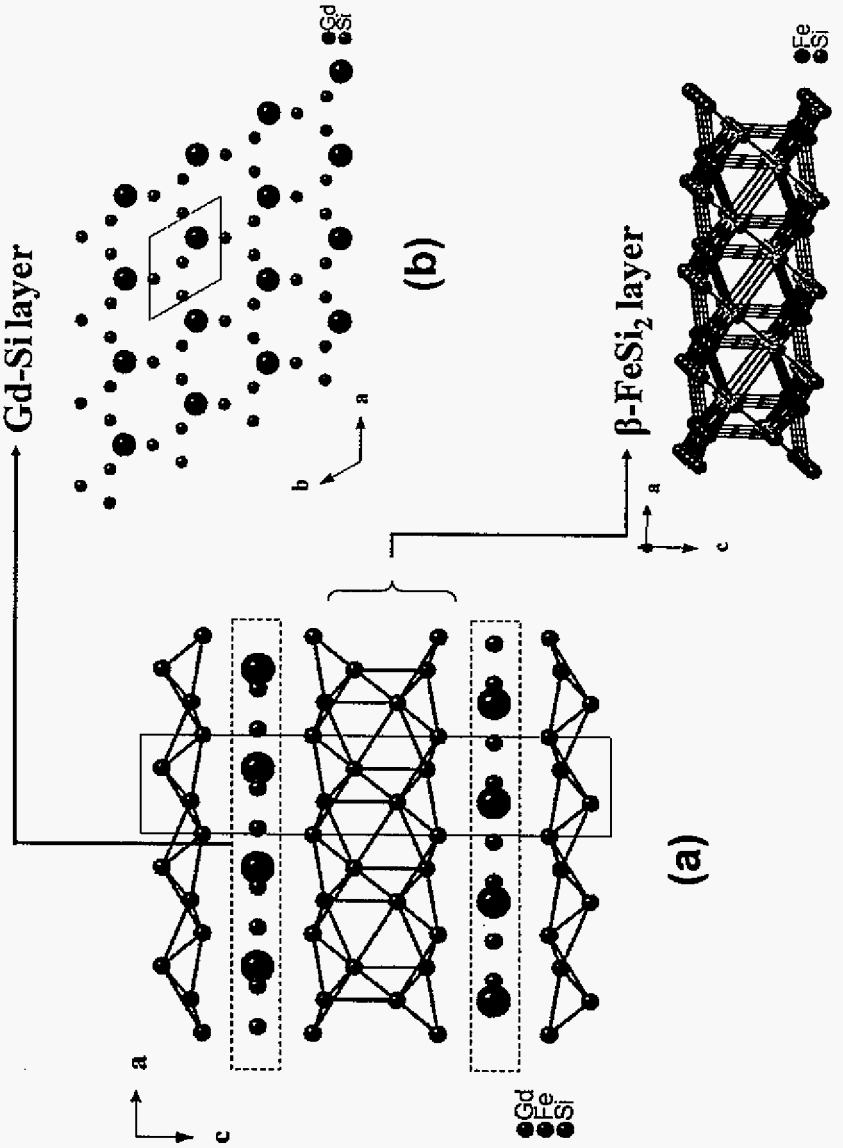

Figure 2. (a) Crystal structure of $RE_{2-x}Fe_4Si_{14-y}$ viewed perpendicular to the *b* axis.
(b) Gd-Si plane, viewed along the *c*-axis, (c) $FeSi_2$ layer.

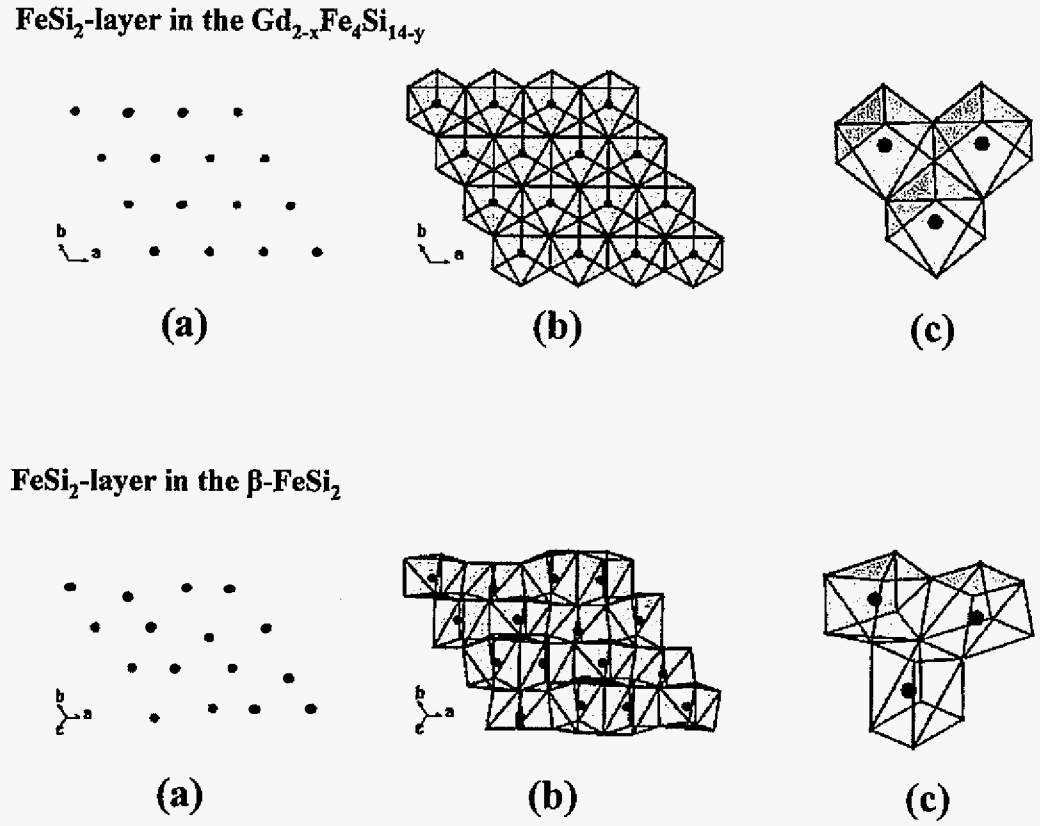

Figure 3. Comparison of Fe/Si layer with β-$FeSi_2$. (a) The "topology" of the Fe parts in two structures, (b) polyhedron of Fe atoms with nearest Si neighbors, and (c) edge shared octahedra.

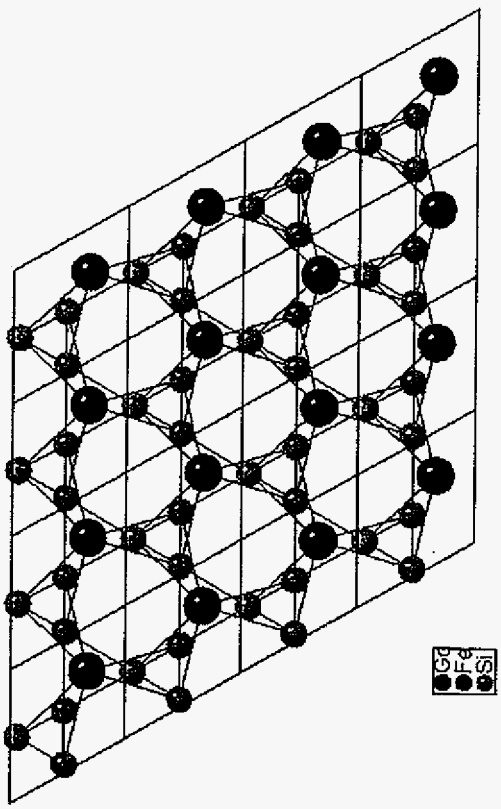

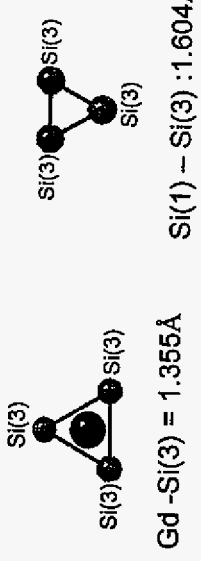

Figure 4. The RE-Si plane, viewed along the c-axis.

Table 4. Crystallographic Data from Single-Crystal X-ray Diffraction Measurements for $RE_{2-x}Fe_4Si_{14-y}$ (RE = Y, Gd, Er, Yb, Tm) at 300K

Identification code		Y	Gd	Tb	Dy	Ho	Er	Tm	Yb	Lu
Dimensions,	*a* Å	3.9351(6)	3.9516(6)	3.9353(6)	3.9313(6)	3.9451(6)	3.9296(6)	3.9206(6)	3.9493(6)	3.9161(6)
	c Å	15.285(3)	15.342(3)	15.311(3)	15.270(3)	15.330(3)	15.242(3)	15.233(3)	15.327(3)	15.223(3)
Volume,	Å^3	204.98(6)	207.47(6)	205.35(6)	204.38(6)	206.63(6)	203.83(6)	202.78(6)	207.03(6)	202.18(6)
Z		1	1	1	1	1	1	1	1	1
Absorption coeff., mm^{-1}		16.679	15.93	18.46	19.136	19.566	20.541	21.357	21.615	22.883
F(000)		289	294	321	322	323	324	325	327	326
2θ range up to (°)		55.96	55.7	46.34	46.4	55.8	56.06	46.52	55.74	56.26
Index ranges in *h, k, l*		±4, ±4, ±16	±5, ±4, ±20	±4, ±4, ±16	±4, ±4, ±16	±5, ±4, ±19	±5, ±4, ±19	±4, ±4, ±16	±5, ±4, ±19	±5, ±4, ±19
Reflections collected		1533	1118	1146	1131	1474	1553	1143	1557	1559
Independent reflections		128	128	82	82	126	126	82	127	127
R(int)		0.0301	0.0178	0.0328	0.0301	0.0415	0.0454	0.0284	0.0354	0.0312
Data / parameters		128 / 20	128 / 20	82 / 19	82 / 19	126 / 19	126 / 19	82 / 20	127 / 19	127 / 19
Goodness-of-fit on F^2		1.216	1.261	1.410	1.357	1.207	1.184	1.254	1.154	1.266
Final R indices [I>2σ(I)]		0.0204	0.0185	0.0186	0.0125	0.0170	0.0189	0.0190	0.0188	0.0186
wR2		0.0501	0.0431	0.0533	0.0352	0.0339	0.0491	0.0482	0.0483	0.0466
Extinction coefficient		0.023(4)	0.0111(19)	0.034(5)	0.014(2)	0.098(5)	0.014(3)	0.025(4)	0.021(3)	0.015(2)
residual peaks, e/Å^{-3}		2.6 /-0.6	1.9/ -0.5	0.6 / -0.5	1.0 / -0.5	1.5 / -0.5	1.6 / -1.4	1.1 / -0.6	2.7/ -0.8	1.6 / -0.6

$$^{a}R1 = \sum \left| |F_o| - |F_c| \right| / \sum |F_o|; \quad R_w = \left[\sum w(|F_o| - |F_c|)^2 \right] / \sum w(F_o)^2]^{1/2}; w = 1/\sigma^2(F_o)$$

Table 5. Atomic parameters of $RE_{2-x}Fe_4Si_{14-y}$ (RE = Y, Gd-Lu)

	Atom	Wyck	Occ.	x	y	z	U(eq)
$Y_{1.21(1)}Fe_4Si_{9.86(4)}$	Y	*2d*	0.606(5)	2/3	1/3	¼	7(1)
	Fe	*4f*		1/3	2/3	0.3925(1)	7(1)
	Si(1)	*4f*		2/3	1/3	0.4543(1)	7(1)
	Si(2)	*4e*		0	0	0.6326(1)	8(1)
	Si(3)	*6h*	0.310(6)	0.0647(14)	0.5324(7)	¼	14(1)
$Gd_{1.20(1)}Fe_4Si_{9.88(4)}$	Gd	*2d*	0.598(3)	2/3	1/3	¼	7(1)
	Fe	*4f*		1/3	2/3	0.3928(1)	7(1)
	Si(1)	*4f*		2/3	1/3	0.4546(1)	7(1)
	Si(2)	*4e*		0	0	0.6320(1)	9(1)
	Si(3)	*6h*	0.313(7)	0.0627(17)	0.5313(9)	¼	15(2)
$Tb_{1.19(1)}Fe_4Si_{9.91(5)}$	Tb	*2d*	0.596(4)	2/3	1/3	¼	4(1)
	Fe	*4f*		1/3	2/3	0.6073(1)	5(1)
	Si(1)	*4f*		2/3	1/3	0.5456(2)	6(1)
	Si(2)	*4e*		0	0	0.6325(2)	8(1)
	Si(3)	*6h*	0.318(8)	0.0720(20)	0.5358(11)	¼	18(2)
$Dy_{1.16(1)}Fe_4Si_{10.02(4)}$	Dy	*2d*	0.578(3)	2/3	1/3	¼	5(1)
	Fe	*4f*		1/3	2/3	0.6075(1)	6(1)
	Si(1)	*4f*		2/3	1/3	0.5457(2)	7(1)
	Si(2)	*4e*		0	0	0.6329(1)	8(1)
	Si(3)	*6h*	0.336(6)	0.0730(18)	0.5365(9)	¼	20(2)
$Ho_{1.20(1)}Fe_4Si_{9.84(4)}$	Ho	*2d*	0.602(3)	2/3	1/3	¼	6(1)
	Fe	*4f*		1/3	2/3	0.6077(1)	6(1)
	Si(1)	*4f*		2/3	1/3	0.5455(1)	6(1)
	Si(2)	*4e*		0	0	0.6332(1)	7(1)
	Si(3)	*6h*	0.307(7)	0.0667(16)	0.5334(8)	¼	14(2)
$Er_{1.06(1)}Fe_4Si_{9.90(4)}$	Er	*2d*	0.528(3)	2/3	1/3	¼	7(1)
	Fe	*4f*		1/3	2/3	0.6078(1)	6(1)
	Si(1)	*4f*		2/3	1/3	0.5456(1)	6(1)
	Si(2)	*4e*		10000	0	0.6331(1)	7(1)
	Si(3)	*6h*	0.316(7)	0.0684(16)	0.5342(8)	¼	14(2)
$Tm_{1.21(1)}Fe_4Si_{9.85(5)}$	Tm	*2d*	0.605(4)	2/3	1/3	¼	5(1)
	Fe	*4f*		1/3	2/3	0.3920(1)	5(1)
	Si(1)	*4f*		2/3	1/3	0.4547(2)	6(1)
	Si(2)	*4e*		0	0	0.6338(2)	7(1)
	Si(3)	*6h*	0.309(8)	0.0740(20)	0.5372(12)	¼	15(2)
$Yb_{1.07(1)}Fe_4Si_{9.91(4)}$	Yb	*2d*	0.535(3)	2/3	1/3	¼	7(1)
	Fe	*4f*		1/3	2/3	0.6072(1)	6(1)
	Si(1)	*4f*		2/3	1/3	0.5454(1)	7(1)
	Si(2)	*4e*		0	0	0.6319(1)	8(1)
	Si(3)	*6h*	0.319(7)	0.0618(16)	0.5309(8)	¼	16(2)
$Lu_{1.21(1)}Fe_4Si_{9.76(4)}$	Lu	*2d*	0.606(3)	2/3	1/3	¼	6(1)
	Fe	*4f*		2/3	1/3	0.6082(1)	5(1)
	Si(1)	*4f*		1/3	2/3	0.5456(1)	6(1)
	Si(2)	*4e*		0	0	0.6343(1)	7(1)
	Si(3)	*6h*	0.294(7)	0.0704(16)	0.4648(8)	¼	11(2)

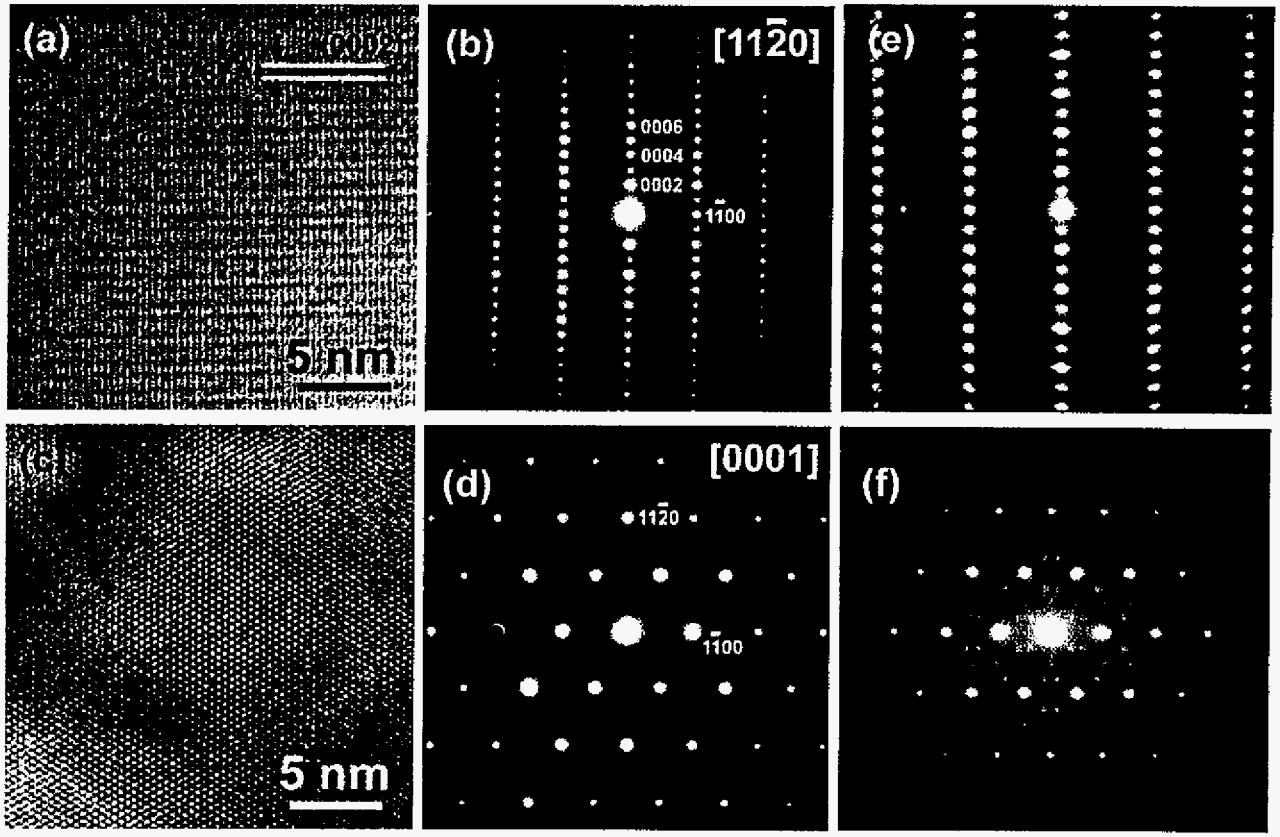

Figure 5. left : HRTEM images of $Gd_{1.2}Fe_4Si_{9.9}$ compound (a) along [11 $\bar{2}$ 0] orientation and (b) along [0001] orientation.

Middle : SAEDPs of $Gd_{1.2}Fe_4Si_{9.9}$ compound (c) along [11 $\bar{2}$ 0] orientation and (d) along [0001] orientation.

Right : SAEDPs of $Y_{1.2}Fe_4Si_{9.9}$ compound (e)along [11 $\bar{2}$ 0] orientation and (f) along [0001] orientation.

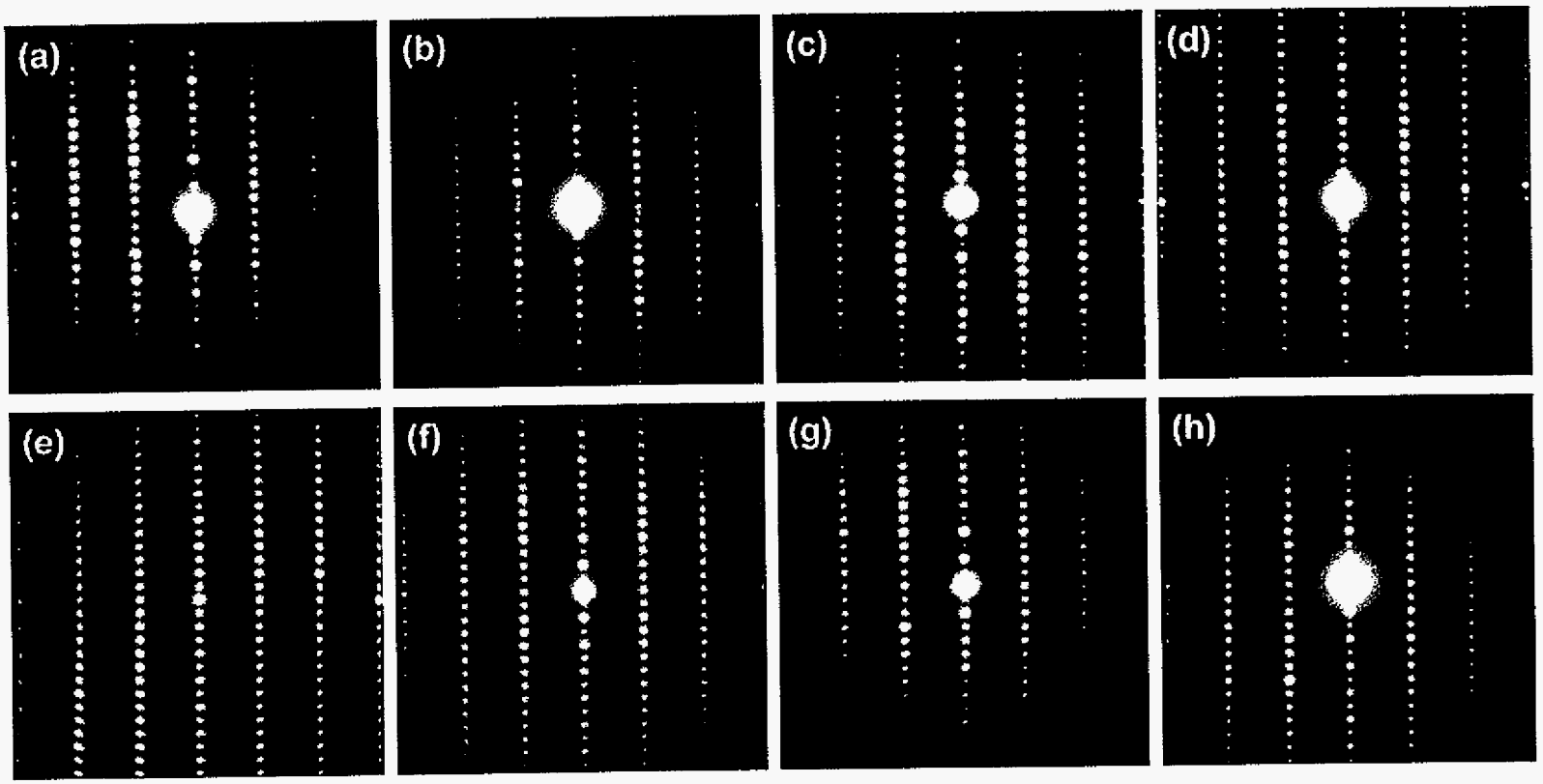

Figure 6. SAEDPs of Dy/Fe/Si (a), Ho/Fe/Si (b), Tb/Fe/Si (c), Yb/Fe/Si (d), Y/Fe/Si (e), Lu/Fe/Si (f), Er/Fe/Si (g) and Tm/Fe/Si (h), showing 2H layered structure along $[11\bar{2}0]$ orientation.

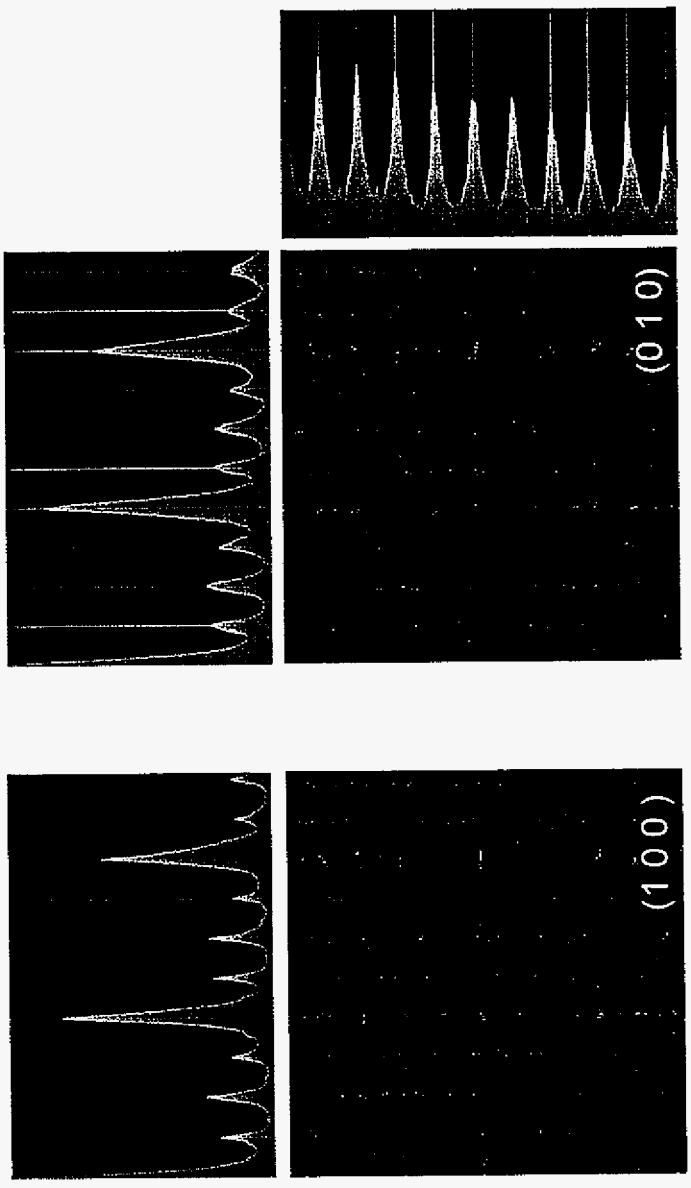

Figure 7. STOE image of $Gd_{1.20(1)}Fe_4Si_{9.88(4)}$.

$Gd_{1.20(1)}\ Fe_4\ Si_{9.88(4)}$	× 16 →	$Gd_{18}\ Fe_{64}\ Si_{158}$
$P\ 6_3/m\ m\ c$ (no. 194)	Space group	$P\ 6_3/m$ (no. 176)
a = 3.9516(6) Å	Unit cell dimensions	a = 15.8064 Å
c =15.3419(31) Å		c = 15.3421 Å
207.47(6) Å^3	Cell volume	3319.57 Å^3

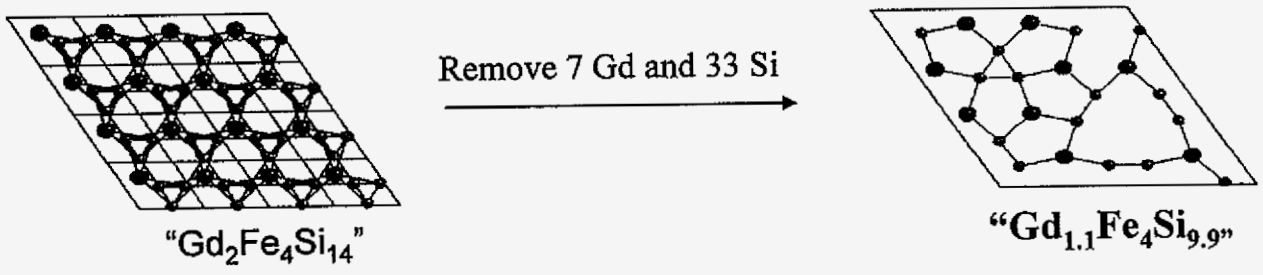

Figure 8. The RE/Si(3) plane, viewed along the *c*-axis (left); An ordered model (right).

Space group: $P6_3/m$ Direct cell: $a = 15.8064$, $c = 15.3421$, $\gamma = 120$
Lambda: 0.71070

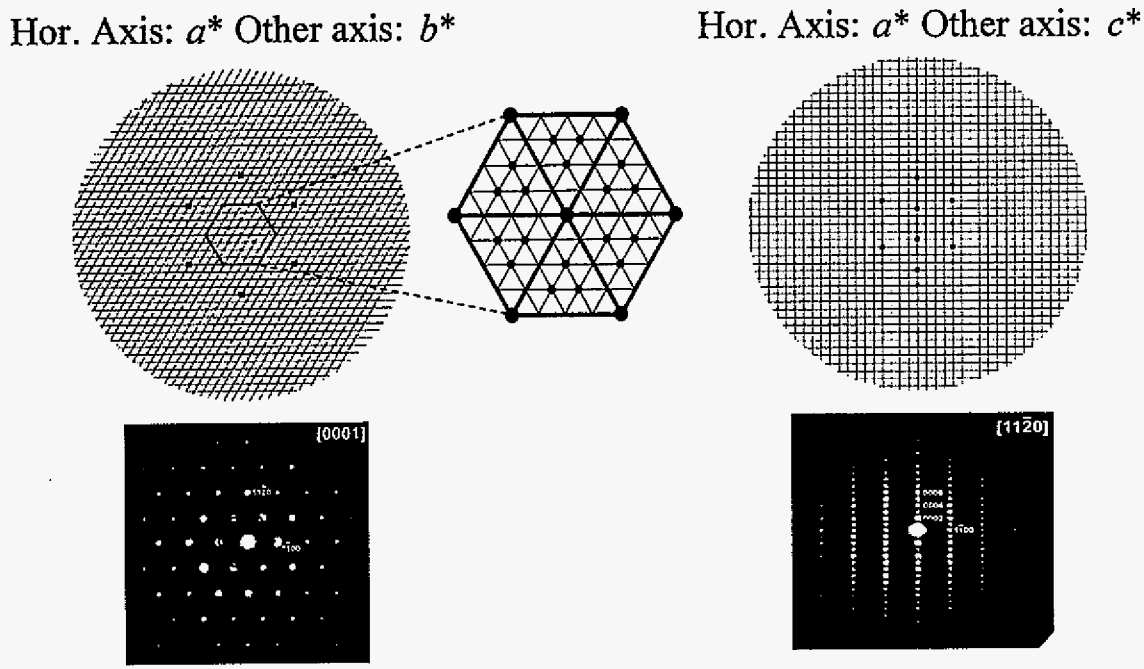

Figure 9. Precession pattern calculated using "ATOMS" program.

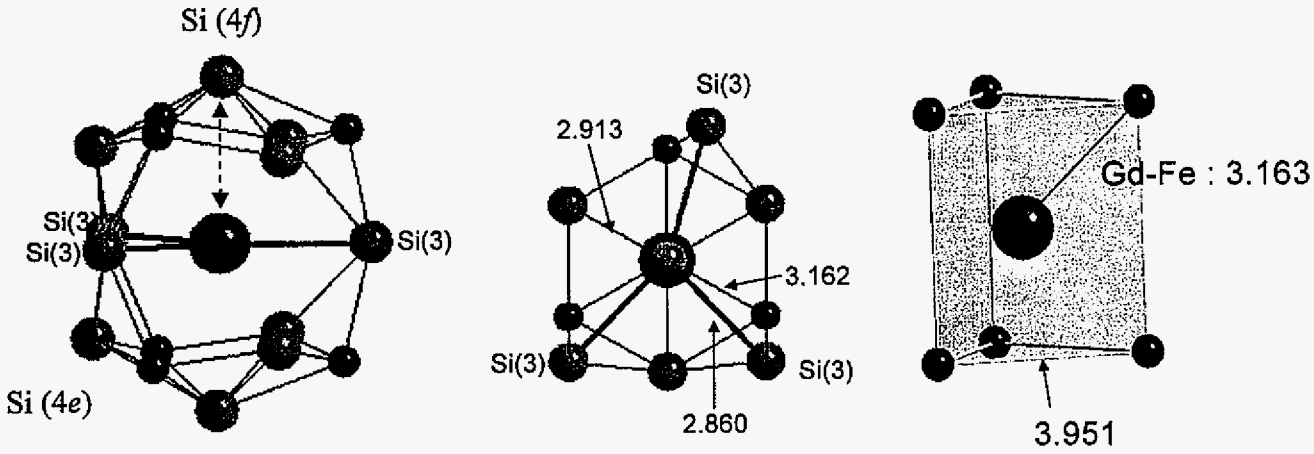

Figure 10. Local coordination of Gd in the superstructure of $Gd_{1.20(1)}Fe_4Si_{9.88(4)}$. The red circle represent for Gd atom and surround by 6 iron atoms (blue circle) and 11 silicon atoms (cyan circle). The distance between Gd and Si (4*f* site), indicated double headed arrow, is 3.139 Å.

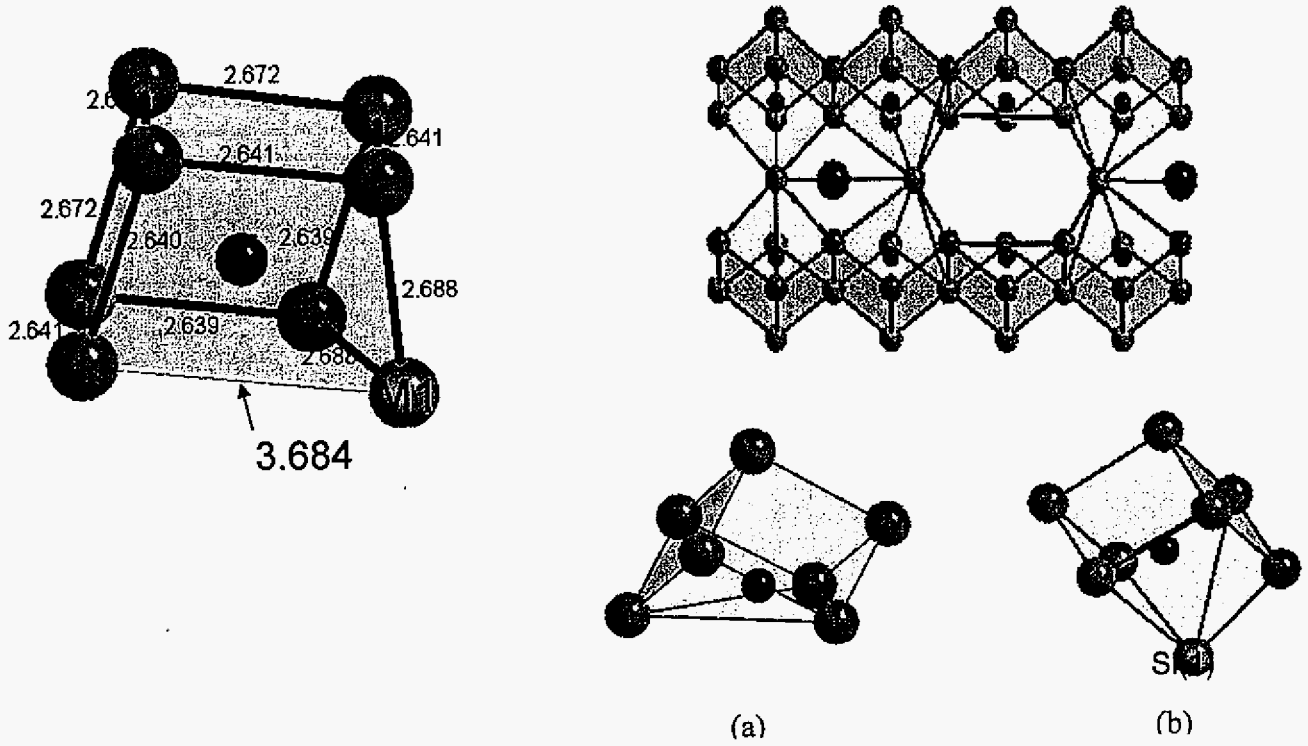

Figure 11. Coordination environments of Fe atoms in superstructure model. (a) Fe atoms coordinated 7 Si nearest neighbors, (b) Fe atoms coordinated 8 Si nearest neighbors. The ratio between these two Fe environments is 1:15.

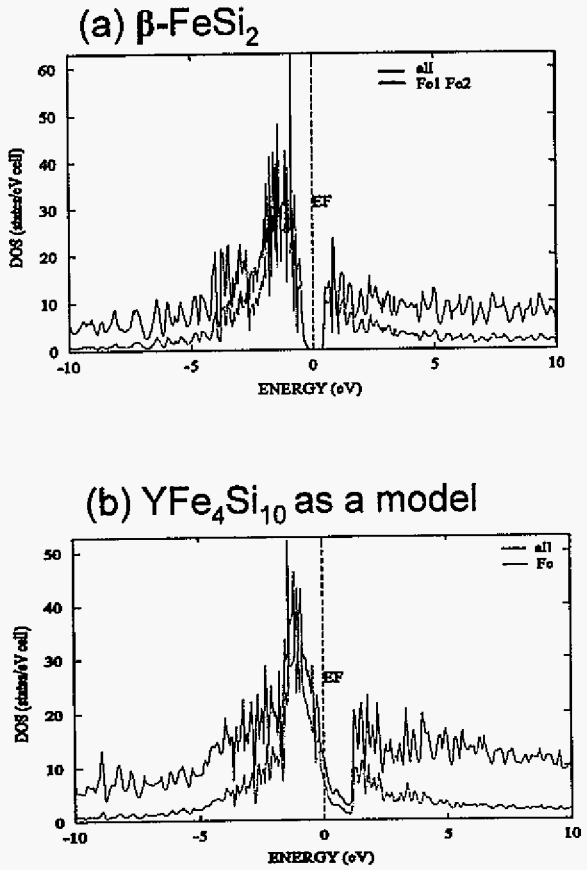

Figure 12. Density of states of (a) β-$FeSi_2$, and (b) model structure of YFe_4Si_{10}.

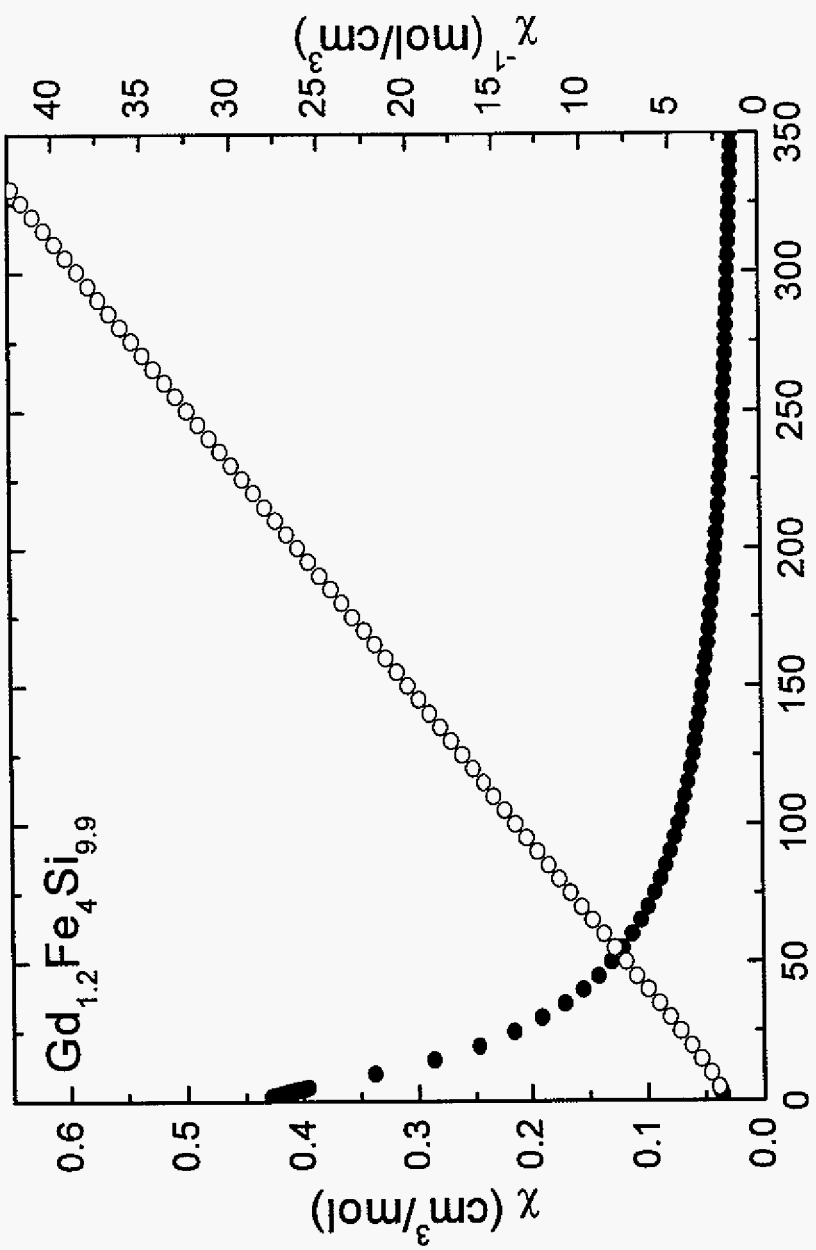

Figure 13. Temperature dependence of magnetic susceptibility and its inverse of the $Gd_{1.2}Fe_4Si_{9.8}$ polycrystalline sample.

Table 6. Magnetic properties of compounds $RE_{2-x}Fe_4Si_{14-y}$*

	Effective magnetic moment (μ_B/f.u)		Θ_w(K)
	μ_{free}	μ_{eff}	
Gd	7.94	8.1	-12
Tb	9.72	9.62	0.3
Dy	10.65	9.89	1.5
Ho	10.61	10.81	14.8
Er	9.58	9.34	4.2
Tm	7.57	8.06	0.1
Lu	-	0	-

* Effective moments, μ_{eff}, are obtained from fits according to the modified Curie-Weiss law, and compared to the corresponding free ion (RE^{3+}) moments, μ_{free}.

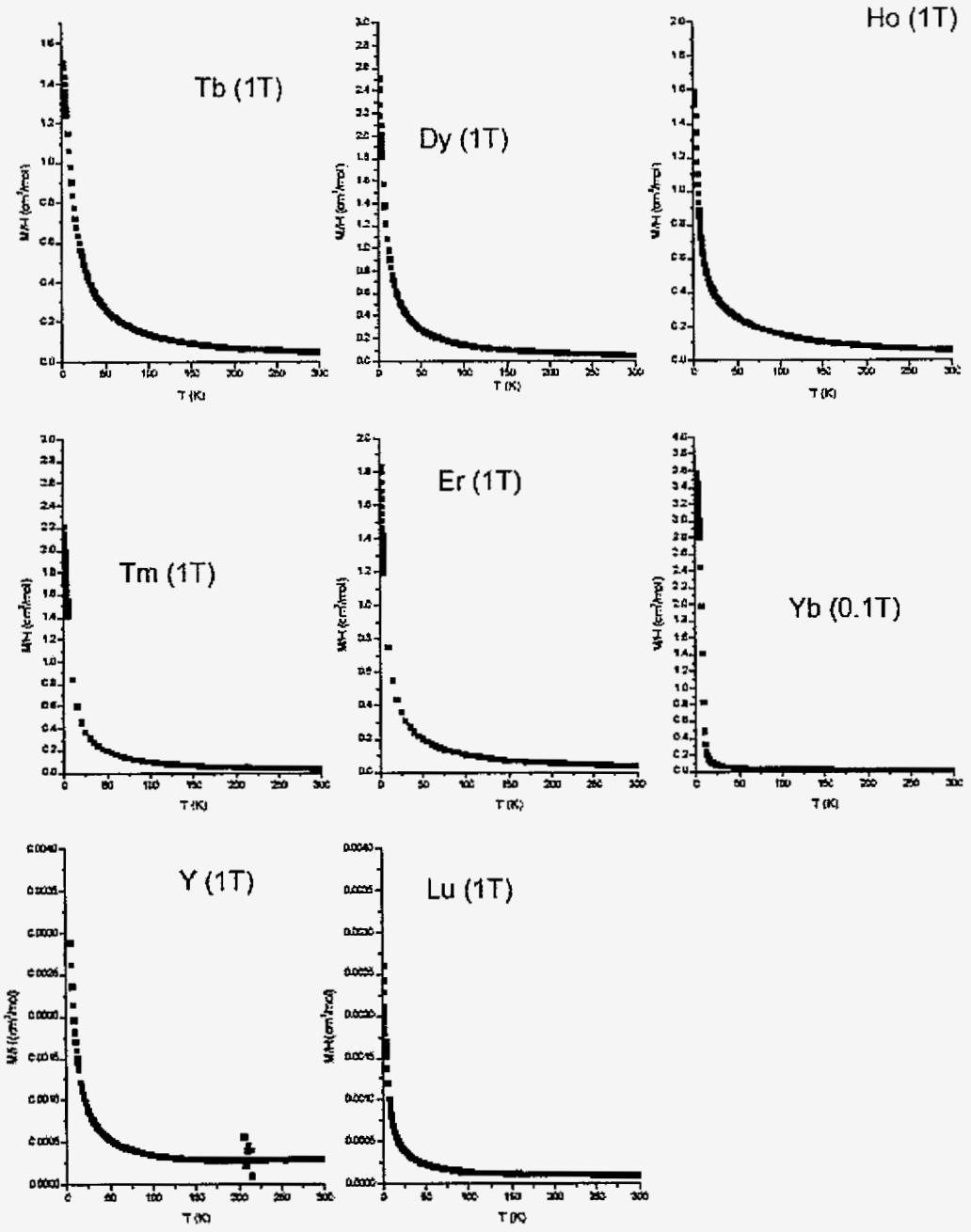

Figure 14. Temperature dependence of magnetic susceptibility of $RE_{2-x}Fe_4Si_{14-y}$.

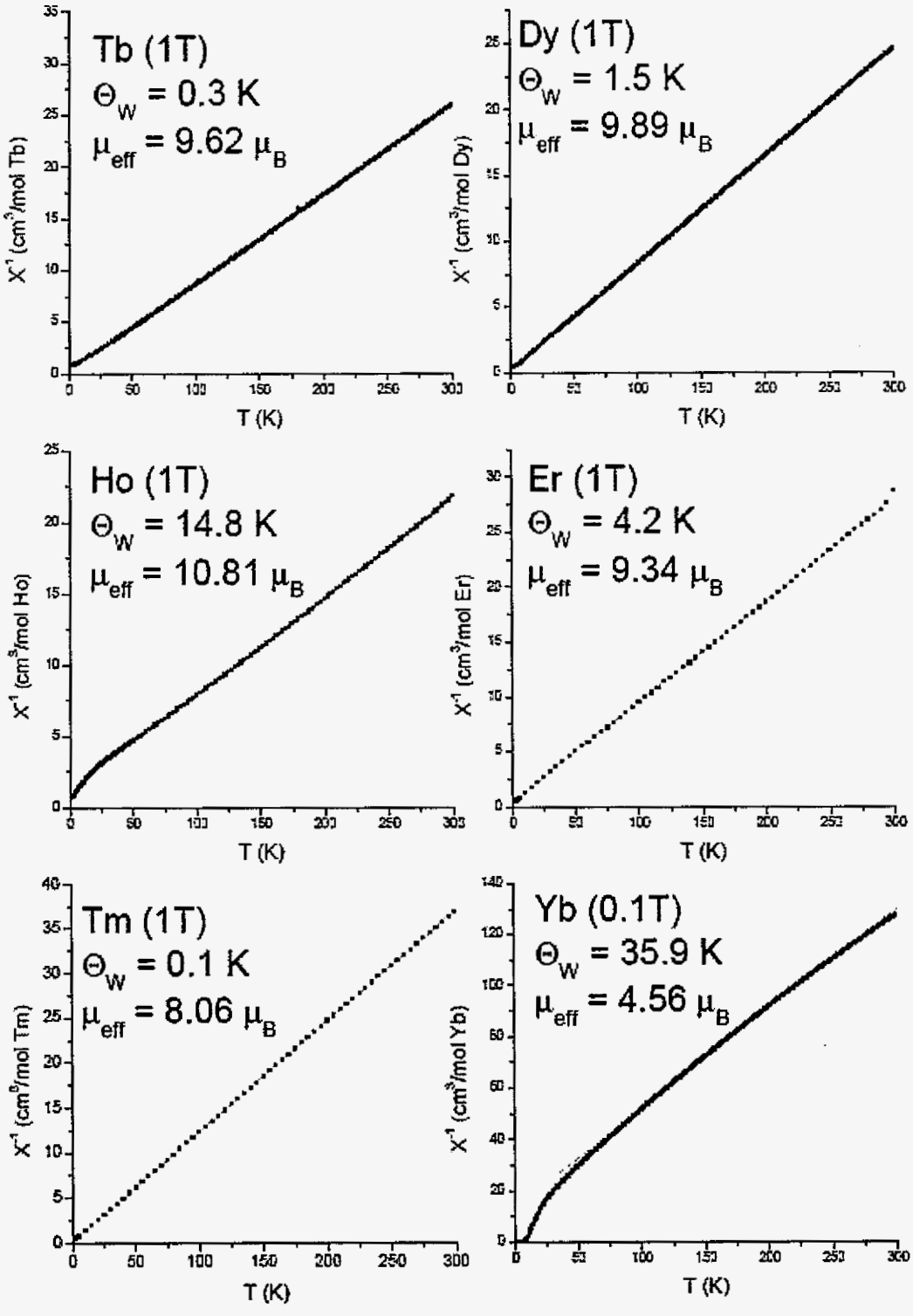

Figure 15. Temperature dependence of the reciprocal susceptibilities of each rare-earth samples. The magnetic field strengths are also indicated.

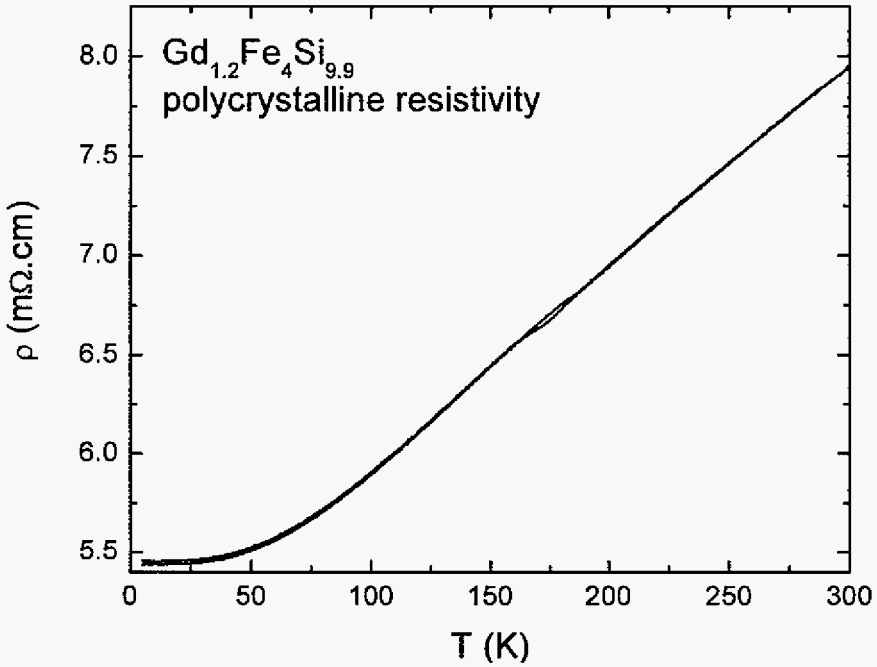

Figure 16. Temperature dependence of the normalized resistivity of the $Gd_{1.2}Fe_4Si_{9.8}$ polycrystalline sample

CHAPTER 6

Investigation of the Metal-Semiconductor Phase Transition in $FeSi_2$ by TB-LMTO-ASA Calculations

*Mi-Kyung Han,[a] Michael Purdham[b], and Gordon J. Miller[a]**

[a] Department of Chemistry, Iowa State University
[b] REU student in Computational Materials Chemistry funded by the National Science Foundation (NSF)

Abstract

The electronic structures of α-, β- and γ-phases of $FeSi_2$ were calculated self-consistently by using the tight-binding linear muffin-tin-orbital (TB-LMTO) method. The relative stability of these phases was discussed in terms of calculated total energies. The formation of the band gap in β-$FeSi_2$ has been described in terms of a shortening of the Fe-Fe interatomic distances and a deformation of the Si cages surrounding the Fe atoms by analyzing of the band-gap diagram for a progressive distortion of the γ-phase structure into the β-structure.

Introduction

Transition metal disilicides, in particular those with a direct gap and a bandgap energy smaller than that of silicon, has attracted particular attention because of their potential applications in Si-based device technology. Several of them have been identified as semiconductors, e.g. $TiSi_2$, $CrSi_2$, $MnSi_{1.73}$, β-$FeSi_2$, $OsSi_2$, and $LaSi_2$.[1] The direct gap silicide

that has attracted most attention so far is iron disilicide due to the availability of the components iron and silicon and the low-toxicity of the compound, as well as its fairly good lattice match to silicon.[2-3] Among various phases of iron silicides, Fe_3Si, FeSi, α-$FeSi_2$, and β-$FeSi_2$, β-$FeSi_2$ has attracted particular attention due to its semiconducting properties with a direct band gap of about 0.79 eV.[4-5]

Depending on growth conditions, iron disilicide exhibits several phases, some of which are stable in the bulk (α- and β-phases), while some other (γ-phase) exists only as thin films.[6] γ-$FeSi_2$ crystallizes in the CaF_2 structure type (space group $Fm\bar{3}m$, unit cell parameter, a = 5.37 Å)[7], i.e., in a face-centered-cubic lattice with Fe at the origin, 4*a* (0, 0, 0), and Si atoms at positions, 8*c* (¼, ¼, ¼). In this structure, each Si atom is tetrahedrally coordinated by four Fe atoms, and each Fe atom has eight Si nearest-neighbors in a cube. The low temperature phase, β-$FeSi_2$, is a semiconductor. It crystallizes in an orthorhombic structure with the space group *Cmca* and the unit cell parameters $a = 9.863$, $b = 7.791$ and $c = 7.833$ Å. This unit cell contains sixteen formula units. The asymmetric unit contains four crystallographically inequivalent sites: two Fe sites (8*d*, 8*f*) and two Si sites (16*g*(1), 16*g*(2)). The structure of β-$FeSi_2$ can be described as a distorted fluorite structure. Onda et al. reported an irreversible phase transition from the γ-phase to the β-phase induced by thermal annealing.[8] The high-temperature phase, α-$FeSi_2$, is a metal with a tetragonal lattice (space group *P4/mmm*, the unit cell parameters $a = 2.6840$, and $c = 5.1280$ Å)[9]. This structure is characterized by Fe-based, planar square nets with Si atoms forming adjacent pairs. Thus, $FeSi_2$ exhibits a semiconductor-metal, and structural transition when temperature is increased to 937°C. The three different structure types of $FeSi_2$ are listed in Table 1.

------ Table 1 ------

The presence of α- and β- phases with a metallic to semiconductor transition makes $FeSi_2$ an interesting system to explore how the electronic structure may influence the observed transition. The electronic structure of $FeSi_2$ has been calculated by several groups[10-13]. The formation of the band gap in β-$FeSi_2$ has been described in terms of a Jahn-Teller distortion by Christensen.[14] He suggested that the deformations of the cubic cages of silicon atoms around the iron sites in the γ-phase lead to changes in the coordination thus dive the cubic γ- structure into the β-form. However, the modifications on the electronic properties caused by structural transformation have not been clearly understood yet. Therefore, this paper presents the results of a theoretical investigation into the electronic structures of iron disilicides, especially focusing on the structural transformation and the driving force of the band gap opening.

In previous chapter, we showed $RE_{2-x}Fe_4Si_{14-y}$ compounds, which consist of β-$FeSi_2$ as a building block, have a pseudogap in electronic structure. Therefore, to derive a guiding principle to understand the nature of properties of $RE_{2-x}Fe_4Si_{14-y}$ compounds, it is necessary to investigate band structures of $FeSi_2$ in detail.

Computational Details

The electronic structures of many actual and hypothetical compounds were calculated self-consistently by using the tight-binding linear muffin-tin-orbital (TB-LMTO) method[15-18] within the atomic sphere approximation (ASA) using the LMTO Version 47 program. Exchange and correlation were treated in a local spin density approximation (LSDA).[19] All relativistic effects except spin-orbit coupling were taken into account using a scalar relativistic approximation.[20] Within ASA, space is filled with overlapping Wigner-Seitz (WS)

atomic spheres. The radii of the WS spheres were obtained by requiring the overlapping potential to be the best possible approximation to the full potential according to an automatic procedure. The WS radii determined by this procedure are 2.42 Å for Fe, 2.48 Å for Si. The basis set included Si 3*s*, 3*p* orbitals and Fe 4*s*, 4*p* and 3*d* orbitals. To optimize the calculations, empty spheres have been introduced (WS radii = 2.16 ~ 2.45). The Löwdin downfolding technique allows the derivation of few-orbital effective Hamiltonians by keeping only the relevant degrees of freedom and integrating out the irrelevant ones. The **k**-space integrations to determine the self-consistent charge density, densities of states (DOS) and crystal orbital Hamilton population (COHP)[21] were performed by the tetrahedron method[22]. The Fermi level was chosen as an internal reference level in all cases. We want to point out that the calculated energy depends on the ratio of the atomic sphere radii between Fe and Si. Figure 1 shows the energy dependence of ratio of WS radii used. When the Fe and Si ratio is 1.04, it gives the lowest total energy. This shows that these methods are not reliable for quantities of energy gap. Therefore we will not discuss the size of gap opening.

Model Structures

The lattice parameters for actual compounds were taken from experiment,[23-24] and are given in Table I. The model structures were initially taken as the orthorhombic unit cell, where *a* is two times the fcc edge (5.37 Å) and *b*, *c* are the diagonals of the fcc square faces. Therefore, the vectors $(a - b)/2$, $(a + b)/2$, and $a/2$ in β-$FeSi_2$ correspond to the basic vectors *a* of the cubic γ -$FeSi_2$ ($a = 5.37$ Å). The axial transformation between the two structures can be presented in matrix form:

$$\begin{pmatrix} x \\ y \\ z \end{pmatrix}_{\beta-FeSi_2} = \begin{pmatrix} 1 & -1 & 0 \\ 1 & 1 & 0 \\ 0 & 0 & 2 \end{pmatrix} \begin{pmatrix} x \\ y \\ z \end{pmatrix}_{\gamma-FeSi_2}$$

And then, it transforms into the observed orthorhombic cell by decreasing *a* and increasing *b* and *c* very close to the experimental values ($a = 9.86$, $b = 7.79$, and $c = 7.83$ Å).

To investigate the driving mechanism for the energy gap opening we made a series of models by progressive shifting of the Fe sites, so that first-neighbor Fe-Fe pairs become closer during the transformation from γ- to β-$FeSi_2$. Thus, the orbital overlaps between them increase. However, the tetrahedral coordination of Fe atoms around Si atoms remains, except for a slight change in the bond lengths, which is summarized in Table 2. The projection of the model structures is illustrated in Figure 2.

------ Figure 2 and Table 2 ------

Results and Discussion

The electronic structure of $FeSi_2$ has been calculated before by several groups.[10-13] Here, we repeat for complete understanding the electronic structures in detail. Our calculation results are in good agreement with other earlier calculations.

We report our results for the total energy, the electronic density of states (DOS), and the band-gap diagram for actual and hypothetical structures of α-, β- and γ-phases. The differences between the nonmagnetic and ferromagnetic total energies for each phase are small ($< 10^{-5}$eV), while the magnetic moment has almost zero value. Later, we will only discuss the electronic structure of the nonmagnetic cases. From the total energy calculations

for α-, β- and γ-phases at experimental lattice constants, we found that β-$FeSi_2$ has the lowest energy compared to other two, α- and γ-phases, i.e. E_{tot}(α-$FeSi_2$) – E_{tot}(β-$FeSi_2$) = 0.53 eV/f.u. and E_{tot}(γ-$FeSi_2$) – E_{tot}(β-$FeSi_2$) = 0.61 eV/f.u.

Density of States (DOS)

Figure 3 shows the total densities of states (DOS) and different partial densities of states for non-spin-polarized calculations on α-, β- and γ- $FeSi_2$.

------ Figure 3 ------

In Figure 3, the partial densities of states of the Si - 3*p* orbitals are shaded in gray, whereas the Fe - 3*d* orbitals are represented by a thick red line. The overall shapes of all DOS curves are very similar: The Si 3*s* band is located between –14 and –8 eV relative to the Fermi energy E_F. From about –8 eV up to the Fermi level (E_F) the Si 3*p* states overlap with the Fe 3*d* states. The structure above E_F corresponds to the remaining Fe 3*d* states. The major differences in DOS among the three phases are as follows: (1) In γ- $FeSi_2$, the Fermi level is located in a very sharp and strong peak of Fe states mixed with Si 3*p* states, indicating that the γ- $FeSi_2$ structure is electronically unstable. Usually, a structure with high density of state at the Fermi level can lower its energy by undergoing a spin polarization or structural distortion. For γ-$FeSi_2$, spin polarization does not indicate any lowering of the total energy because the difference between the nonmagnetic and ferromagnetic total energies is small ($\Delta E = 1.2104\times10^{-5}$ eV), a structural distortion of γ- $FeSi_2$ phase is expected. (2) The Fermi level of α-$FeSi_2$ is located in a pronounced minimum, which reduces the band structure energy and explains its relative stability with respect to the unstable γ- $FeSi_2$ structure. The

very sharp peaks near the Fermi level in the DOS correspond to d_{z^2}-like level (3) β- $FeSi_2$ is a semiconductor with E_F right at the gap of DOS.

The progressive change in position of E_F indicates a possible relationship for α-$FeSi_2$ with the low-temperature β- phase through a structural transformation with γ- $FeSi_2$ as an intermediate phase.

Band structure

------ Figure 4 ------

In γ- $FeSi_2$, the eight Si atoms align on the corners of a cube surrounding a Fe atom located at the center create the point group O_h at the Fe site so the *d* orbitals will be split into two degenerate sets, t_{2g} (d_{xy}, d_{xz}, d_{yz}) and e_g (d_{z^2}, $d_{x^2-y^2}$). In Figure 4(a), we can see this splitting at the Γ position.

The band structure of α-$FeSi_2$, in Figure 4 (b), shows a Jahn-Teller- like distortion. The doubly degenerate e_g level is split into two levels, an upper $d_{x^2-y^2}$ and a lower d_{z^2} and the triply degenerate t_{2g} level is split into two different levels, an upper d_{xy} and a doubly degenerate d_{xz} and d_{yz}. The energy level schemes for the γ- and α-phases are illustrated in Figure 5.

------ Figure 5 ------

Therefore, band structure calculations show that a Jahn-Teller- like distortion drives unstable γ-$FeSi_2$ phase into energetically stable α-$FeSi_2$ phase. Therefore, the Si environment changes from tetragonal to square planar.

In the band structure of β-$FeSi_2$, a complicated valence-conduction energy-band structure evolves. The valence band edge at Γ has mainly Fe $3d_{yz}$ character with a small

admixture of Si $3p_y$ character and thus, pointing in the Fe-Fe direction to make Fe-Fe interaction, while the bottom of conduction band is formed exclusively by the Fe t_{2g} states.

Origin of band gap opening

We report our results of the total energy, the electronic density of states (DOS), and the band-gap diagram for a progressive distortion of the γ- structure into the β-phase.

------ Figure 6 ------

The Fe-Fe distance in γ-$FeSi_2$ is large (~ 3.797 Å) enough to minimize the overlap between Fe $3d$ wavefunctions on different Fe atoms. The band of γ-$FeSi_2$ is mainly showing the mixing of Fe $3d$ and Si $3p$ orbitals. Figure 6 shows that the band-gap opening is produced by the shortening of the Fe-Fe interatomic distance and the deformation of the Si cages surrounding the eight-fold coordinated Fe atoms. When the Fe-Fe interatomic distance is small enough (Fe-Fe distance in Model 4 = 2.965 Å) to make overlap between Fe $3d$ wavefunctions, there is a splitting of the $3d$ band. The total energies also decrease by shortening the Fe-Fe interatomic distance, shown in Figure 7.

------ Figure 7 ------

Therefore, the nature of the band gap is very structure sensitive and that a slight decrease in Fe-Fe interatomic distance induces a change in the nature of the gap.

The energy-band structures of model structures are shown in Figure 8. When compared to β-$FeSi_2$ (model 4) the band structure has most noticeably changed around the point Γ. From the band structure of model 1, we can see that the valence band edges with mainly Fe d_{yz} character mix with the bottom of conduction band, which are exclusively the Fe t_{2g} states. Band structure calculations for the models without short Fe-Fe interatomic

distance (< 3.0 Å) do not show an energy gap. These Fe $d - d$ orbital mixing are progressively decrease by making Fe-Fe interatomic distances. Thus, the gap opening is must significantly influenced by the inclusion of Fe-Fe orbital interactions, because the gap comes from the covalent mixing between the Fe 3*d* states and adjacent Fe atoms.

Even though the Fe-Fe distances are longer than those of γ-$FeSi_2$ (Fe-Fe distance = ~ 4.0 Å) in $RE_{2-x}Fe_4Si_{14-y}$ compounds, these compounds show pseudogap in their electronic structure calculation. Therefore we expect more complicate involvement of rare-earth element in the properties. We need more through investigation to understand the nature of gap opening in $RE_{2-x}Fe_4Si_{14-y}$ compounds.

Conclusion

The electronic structures of α-, β- and γ-phases iron disilicides were calculated self-consistently by using the tight-binding linear muffin-tin-orbital (TB-LMTO) method. The main results of present work are summarized as follows:

1. The relative stability of these phase was discussed in terms of calculated total energies: β-$FeSi_2$ has the lowest energy compared to other two, α- and γ-phases, i.e. $E_{tot}(\alpha\text{-}FeSi_2) - E_{tot}(\beta\text{-}FeSi_2) = 0.53$ eV/f.u. and $E_{tot}(\gamma\text{-}FeSi_2) - E_{tot}(\beta\text{-}FeSi_2) = 0.61$ eV/f.u.
2. The analysis of the band-gap diagram for a progressive distortion of the γ-phase structure into the β-structure shows that the origin of the band gap opening in β-$FeSi_2$ is produced by the shortening of the Fe-Fe interatomic distances and the deformation of the Si cages surrounding the Fe atoms.

References

1. Maex, K.; Van Rossum, M. *Properties of Metal Silicides* **1995**; INSPEC, the Institution of Electrical Engineers, London, United Kingdom, No.14.

2. Bost, M. C.; Mahan, J. E. *J. Appl. Phys.* **1985**, 58, 2696.

3. Bost , M. C.; Mahan, J. E. *J. Appl. Phys.* **1988**, 64, 2034.

4. Yang, Z.; Homewood, K. P.; Finney, M. S.; Harry, M.; Reeson, K. J. *J. Appl. Phys.* **1995**, 78, 1958.

5. Katsumata, H. *J. Appl. Phys.* **1996**, 80, 5995.

6. *Binary Alloy Phase Diagrams*, edited by Massalski, T. B. (American Society for Metals Interantional, Materials Park, OH, **1986**), Vol. 2, p.1108.

7. Vazquez de Parga, A. L.; De La Figuera, J.; Ocal, C.; Miranda, R. *Europhys. Lett.* **1992**, 18, 595.

8. Onda, N.; Henz, J.; Müller, E.; Mäder, K.; Von Känel, H. *Appl. Surf. Sci.* **1992**, 56-58, 421.

9. Egert, B.; Panzner, G. *Phys. Rev.* **1984**, B29, 2091.

10. Eppenga, R. *J. Appl. Phys.* **1990**, 68, 3207.

11. Filonov, A. B.; Migas, D. B.; Shaposhnikov, V. L.; Dorozhkin, N. N.; Petrov, G. V.; Borisenko, V. E.; Henrion, W.; Lange, H. *J. Appl. Phys.* **1996**, 79, 7708.

12. Antonov, V. N.; Jepsen, O.; Henrion, W.; Rebien, M.; Stauß, P.; Lange, H. *Phys. Rev.* **1998**, B57, 8934.

13. Kulatov, E.; Nakayama, H.; Ohta, H. *J. Phys. Soc. Japan.* **2001**, 70, 2199.

14. Christensen, N. E. *Phys Rev.* **1990**, B 42, 7148.

15. Andersen, O. K. *Phys. Rev.***1975**, B12, 3060.

16. Andersen, O. K.; Jepsen, O. *Phys. Rev. Lett.* **1984**, 53, 2571.

17. Andersen, O. K.; Jepsen, O.; Glötzel, D. In *Highlights of Condensed-Matter Theory*; Bassani, F.; Fumi, F.; Tosi, M. P., Lambrecht, W. R. L., Eds.; North-Holland: New York, **1985**

18. Andersen, O. K. *Phys. Rev.* **1986**, B34, 2439.

19. Von Barth, U.; Hedin, L. *J. Phys. C* **1972**, 5, 1629.

20. Koelling, D. D.; Harmon, B. N. *J. Phys. C* **1977**, 10, 3107.

21. Dronskowski, R.; Blöchl, P. *J. Phys. Chem.* **1993**, 97, 8617.

22. Blöchl, P. E.; Jepsen, O.; Andersen, O.K. *Phys. Rev.* **1994**, B49, 16223.

23. Schellenberg, L.; Braun, H. F.; Muller, J. *J. Less-Common Met.* **1988**, 144, 341.

24. Villars, P.; Calvert, L. D. Pearson's Handbook of Crystallographic Data for Intermetallic Phases, ASM International Materials Park, OH, Desk ed., **1997**.

Table 1. Comparison of three different structure types for $FeSi_2$

	α-$FeSi_2$	γ-$FeSi_2$	β-$FeSi_2$
Space group	*P* 4/m m m (no. 123)	*F* m -3 m (no. 225)	*C* m c a (no. 64)
Lattice parameter	$a = 2.6840$ Å $c = 5.1280$ Å	$a = 5.3700$ Å	$a = 9.8630$ Å $b = 7.7910$ Å $c = 7.8330$ Å
	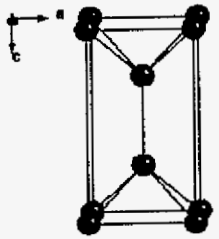	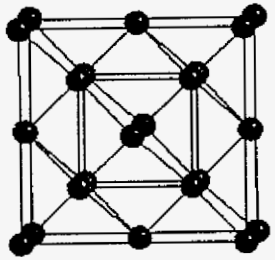	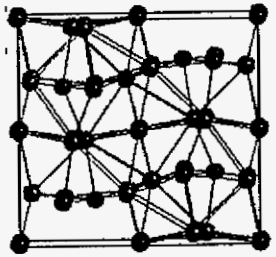
Atomic coordinates	**Atom x y z** Si ½ ½ 0.27 Fe 0 0 0	**Atom x y z** Si ¼ ¼ ¼ Fe 0 0 0	**Atom x y z** Fe1 0.21430 0 0 Fe2 ½ 0.30860 .18500 Si1 0.12900 0.27660 .05160 Si2 0.37270 0.04460 0.22560
Comments	This structure exists at temperatures above 937°C. Metallic	Unstable Hypothetical structure Metallic	This structure exists at temperatures below 937°C. Semiconductor

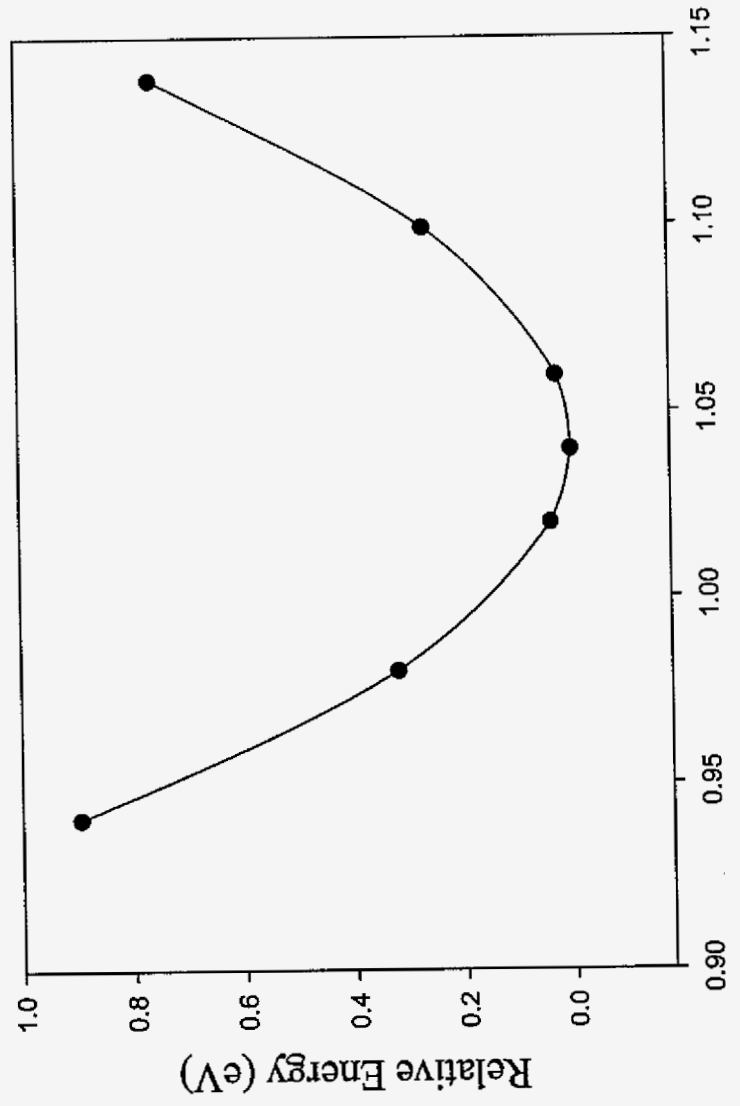

Figure 1. The calculated energy dependence on the ratio of the atomic sphere between Fe and Si.

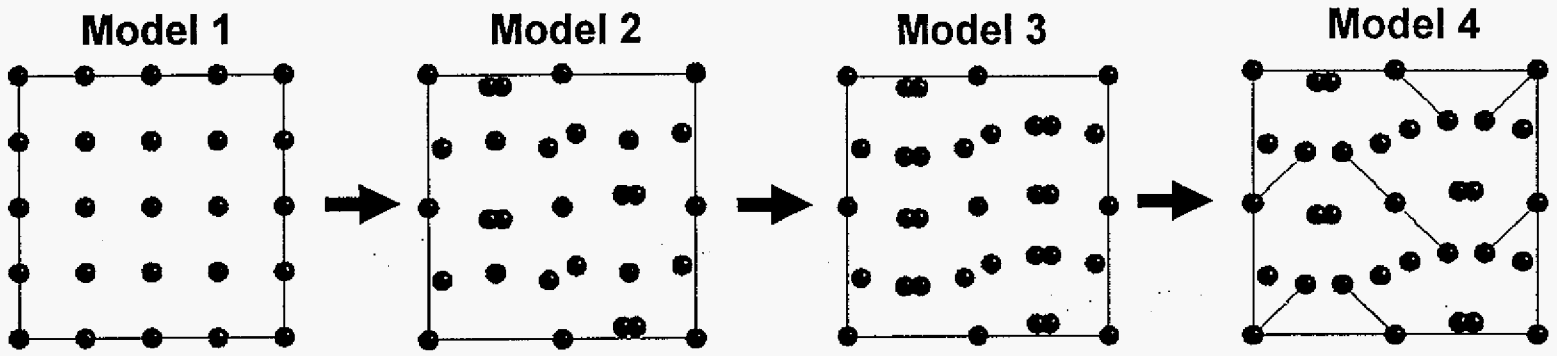

Figure 2. Projections of the model structures along the *a*-axis. Model 1, Model 4 represent for the structure of γ-$FeSi_2$ and β-$FeSi_2$, respectively.

Table 2. Average distance decrease amount for each model compared to Model 1.

	Model 2	Model 3	Model 4
Fe-Fe,%	7	15	22
Fe-Si, %	1	2	3
Si-Si, %	1	3	5

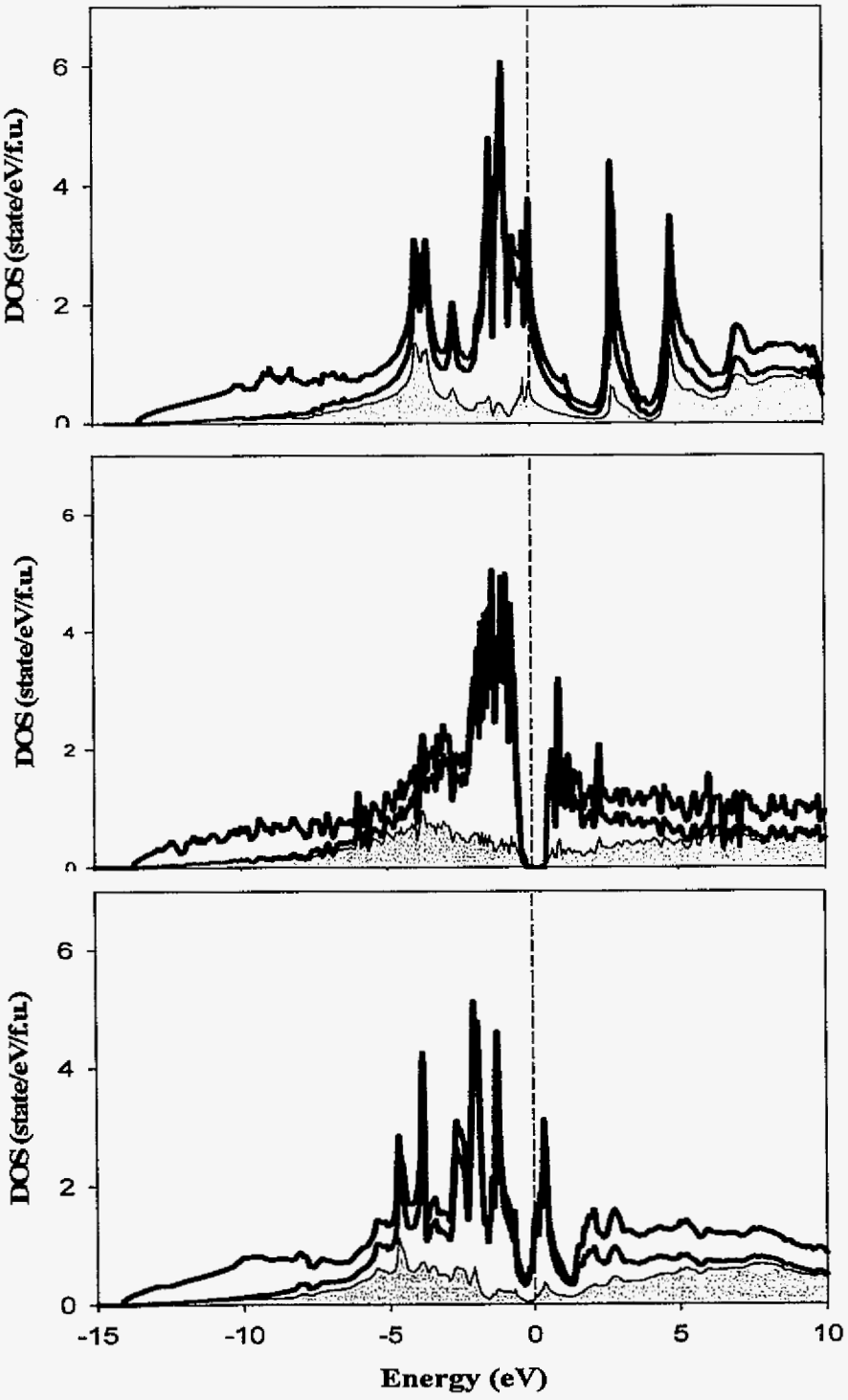

Figure 3. Density of states of $FeSi_2$. (a) γ- (b) β- and (c) α- phase. Black lines represent for total DOS. Red lines are partial DOS for Fe-3*d* and Si-3*p* orbitals. Shaded areas are partial DOS for Si-3*p* orbitals.

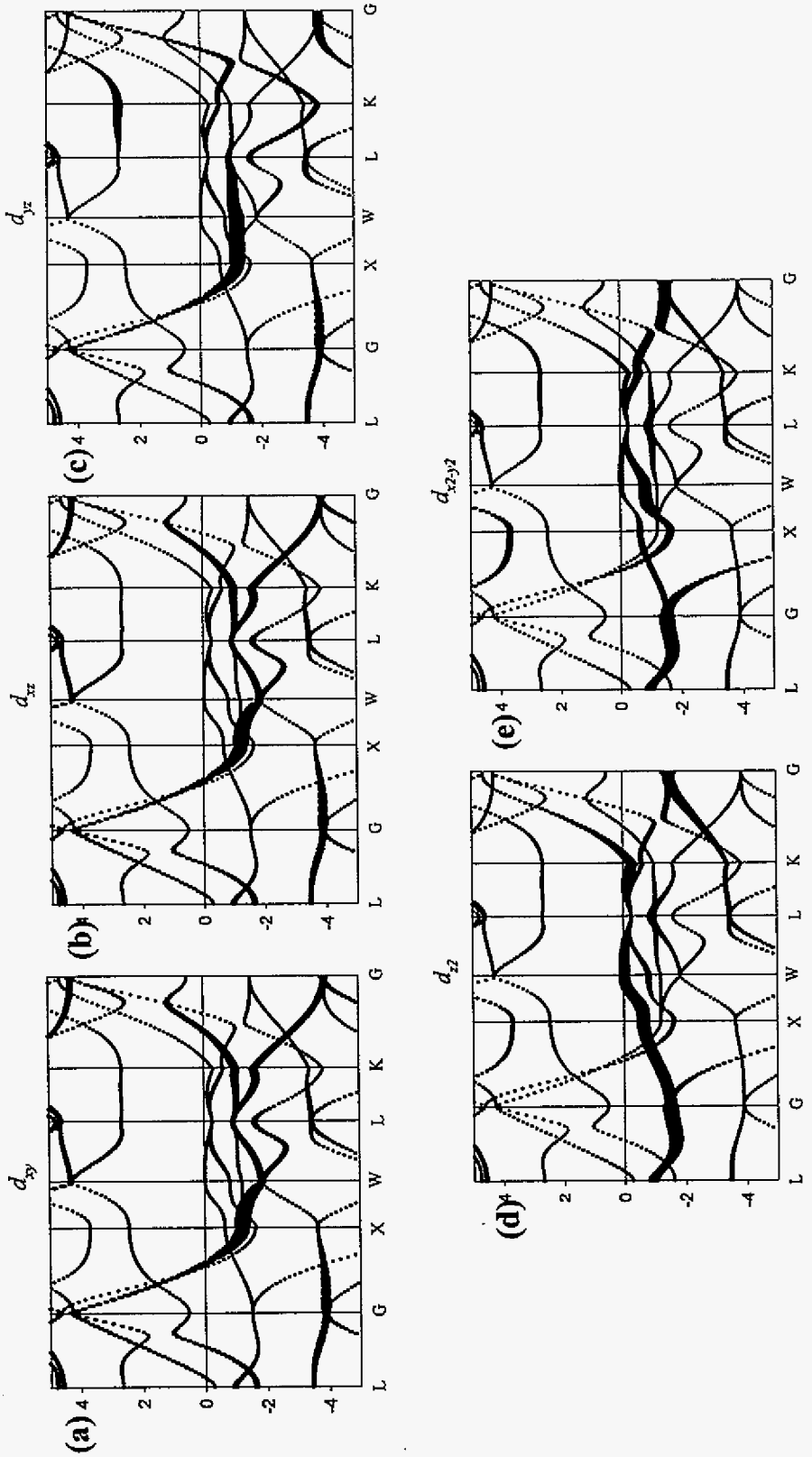

Figure 4. (a) Calculated energy bands of γ-$FeSi_2$, showing the (a) d_{xy}, (b) d_{yz}, (c) d_{xz}, (d) d_{z^2} and (e) $d_{x^2-y^2}$ on Fe site. The Fermi level is denoted by the horizontal line at zero energy.

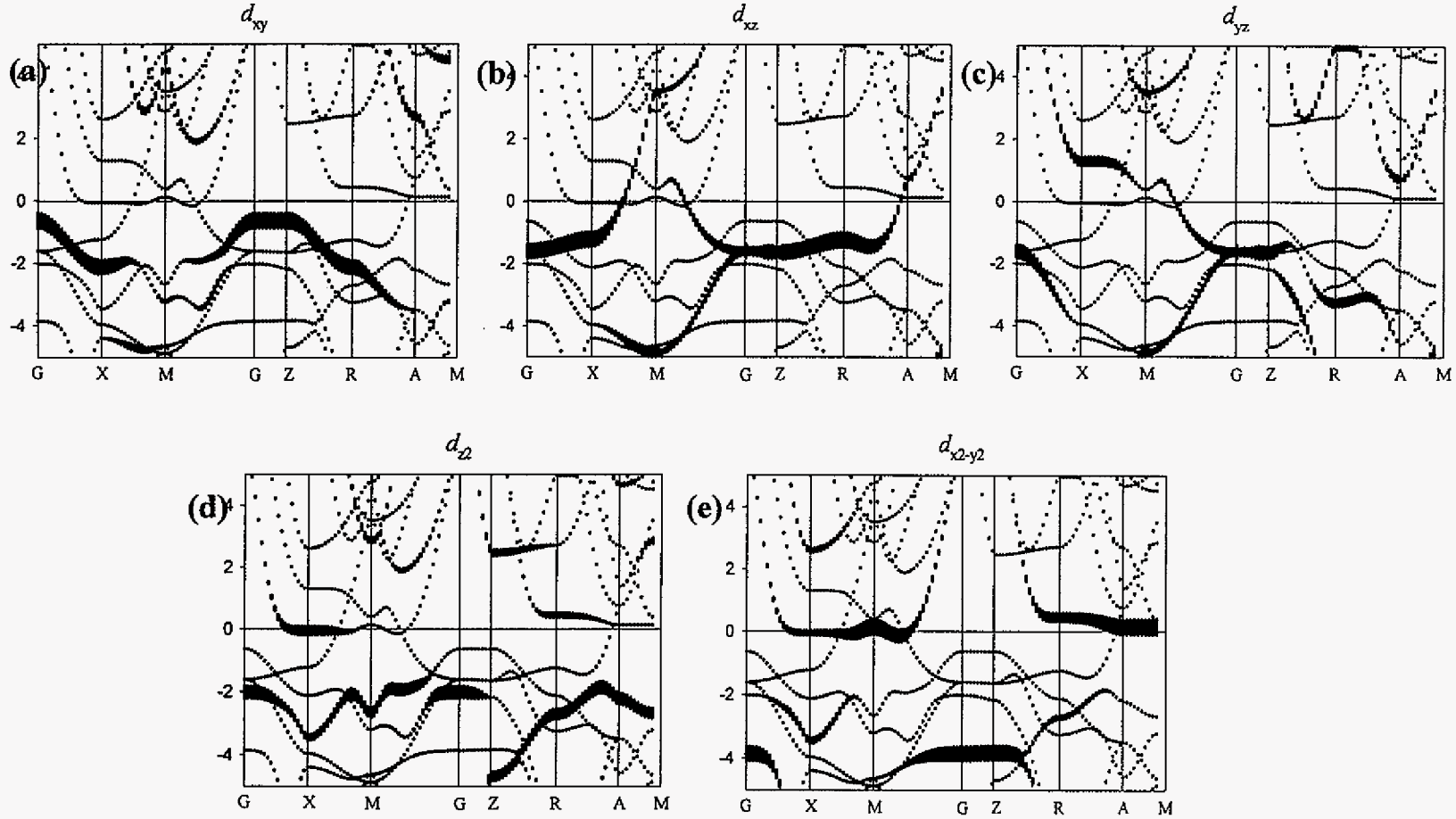

Figure 4. (b) Calculated energy bands of α-$FeSi_2$, showing the (a) d_{xy}, (b) d_{yz}, (c) d_{xz}, (d) d_{z^2} and (e) $d_{x^2-y^2}$ on Fe site. The Fermi level is denoted by the horizontal line at zero energy.

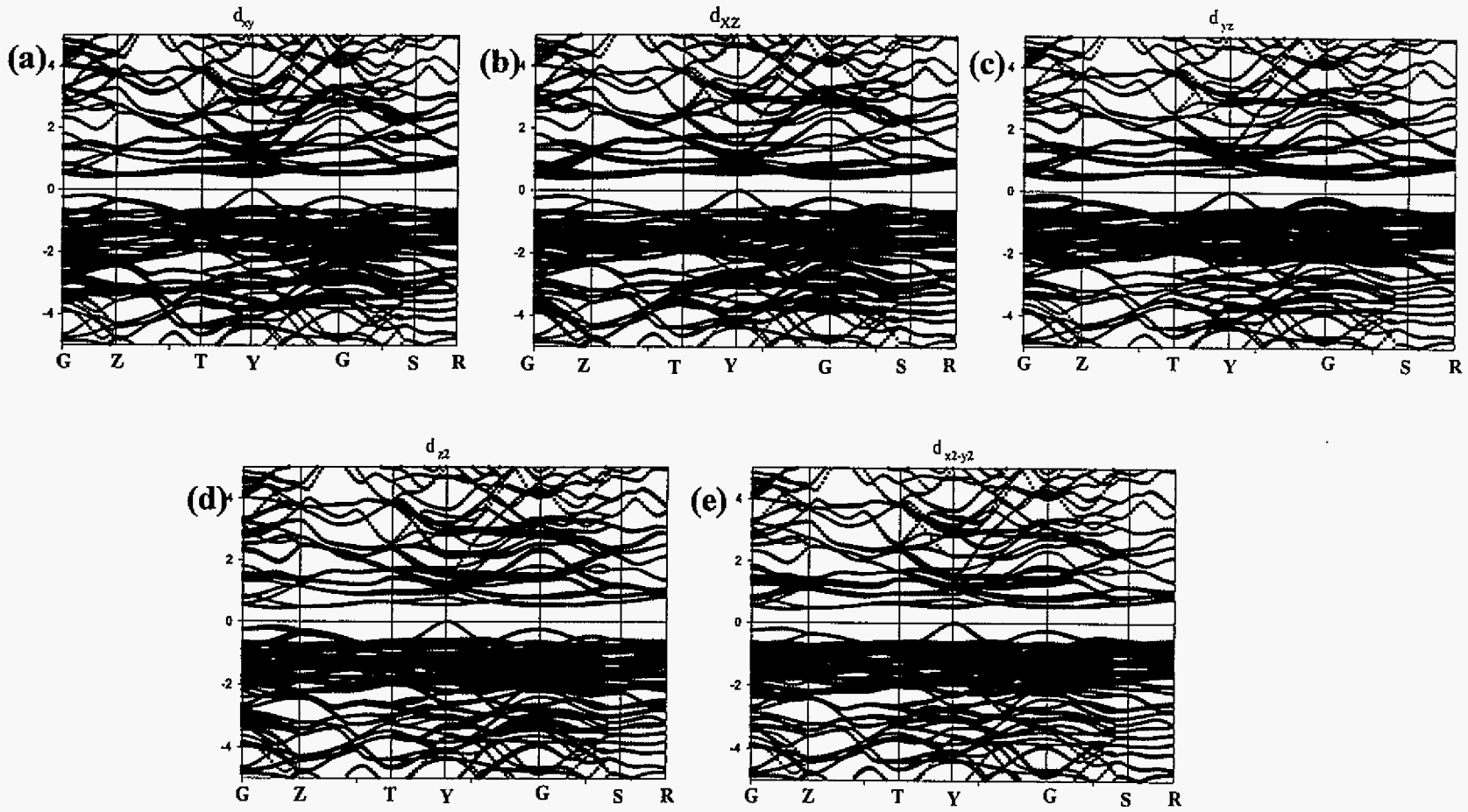

Figure 4. (c) Calculated energy bands of β-$FeSi_2$, showing the (a) d_{xy}, (b) d_{yz}, (c) d_{xz}, (d) d_{z^2} and (e) $d_{x^2-y^2}$ on Fe site. The Fermi level is denoted by the horizontal line at zero energy.

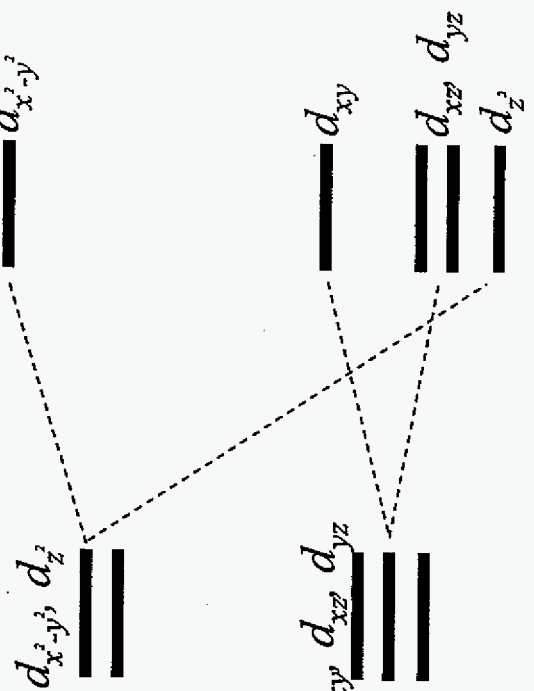

Figure 5. Energy level schemes for γ- (left) and α-phase (right).

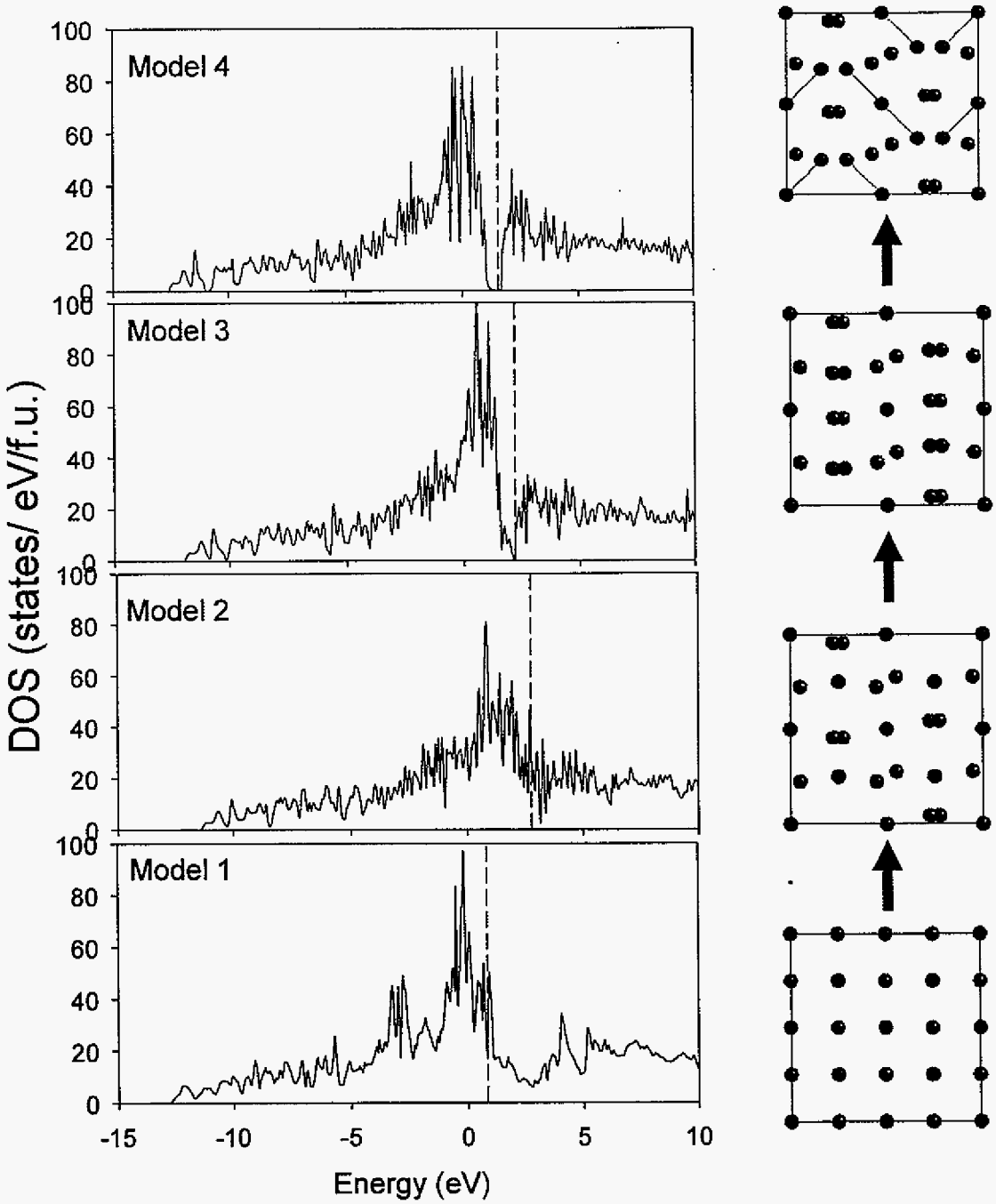

Figure 6. (a) Total density of states and (b) projections of model structure.

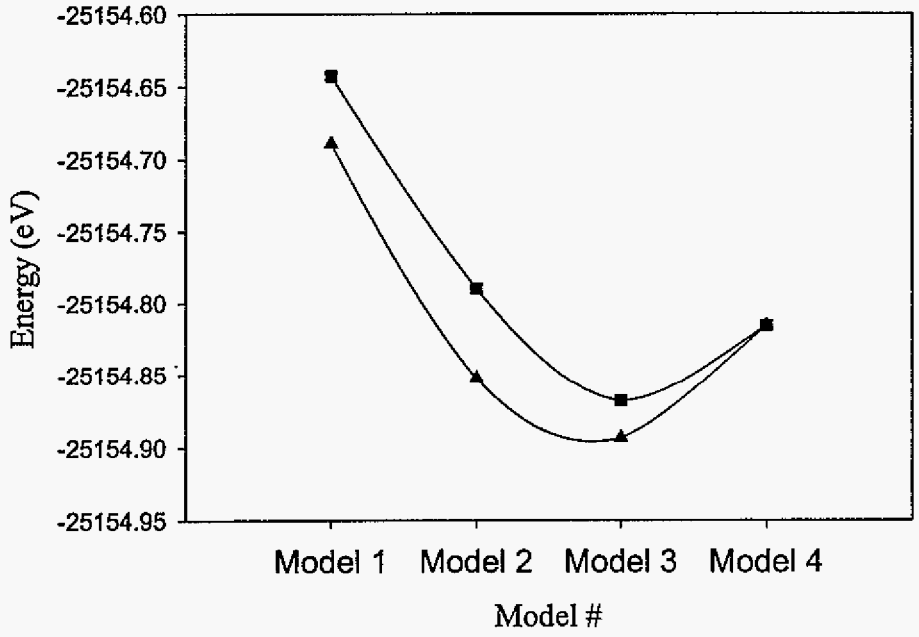

Figure 7. Total energies of calculated model structure. Square and triangle represent for non spin-polarized, and spin-polarized calculation results, respectively.

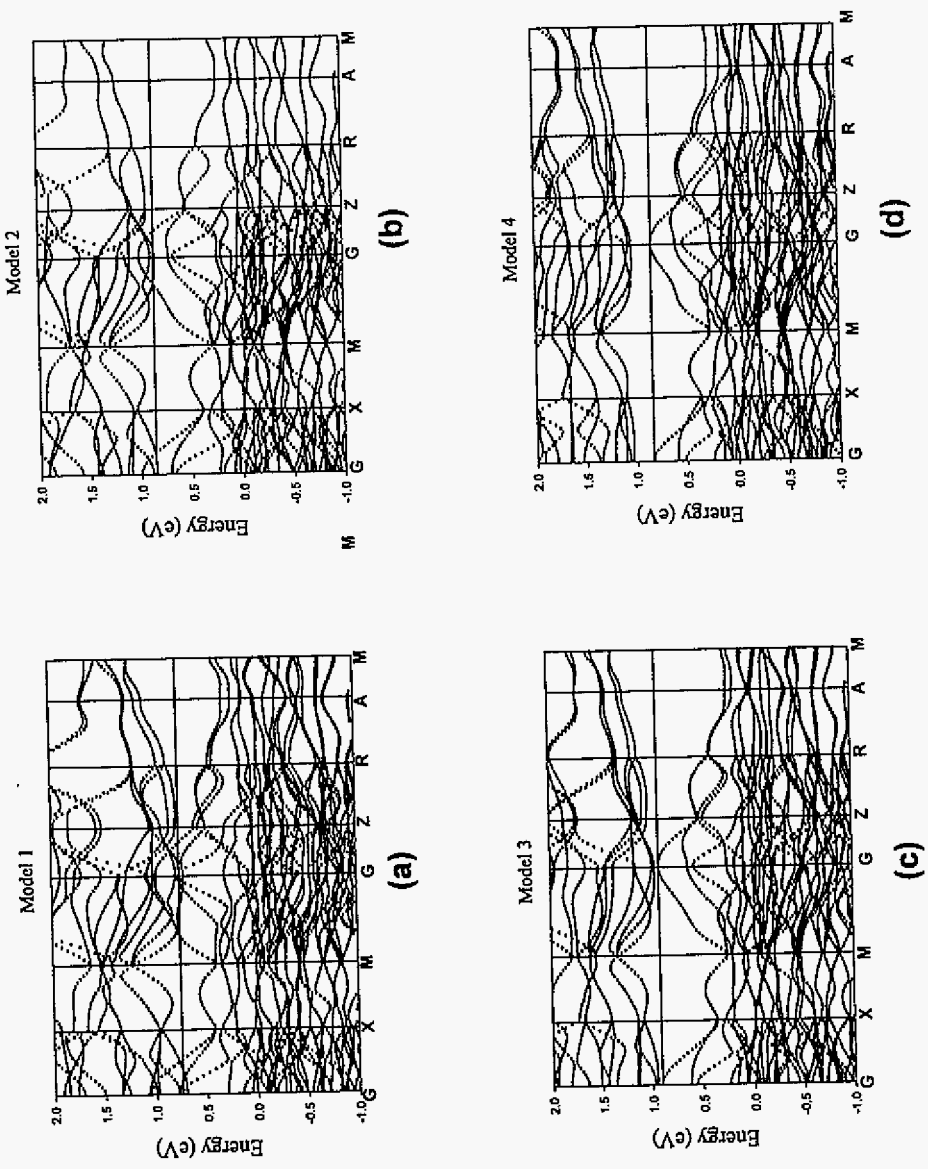

Figure 8. Energy band structures of models (a) Model 1, (b) Model 2, (c) Model 3, and (d) Model 4. The Fermi level is denoted by the horizontal line at zero energy.

CHAPTER 7

The Coloring Problem in Intermetallics: Bonding and Properties of $Tb_3Zn_{3.6}Al_{7.4}$ with the La_3Al_{11} Structure Type

*Mi-Kyung Han,[a] Emilia Morosan,[b] Paul C. Canfield,[b] and Gordon J. Miller[a]**

[a] Department of Chemistry, Iowa State University
[b] Department of Physics and Astronomy, Iowa State University

Reprinted by permission: *Z. Kristallogr.* **2005**, 220, 95-101.

Abstract

Single crystals of the new compound $Tb_3Zn_{3.6(1)}Al_{7.4(1)}$ were obtained from Al and Zn-rich ternary solutions. The title compound crystallizes in the orthorhombic La_3Al_{11} structure type (space group *Immm* (No. 71), $Z = 2$; $a = 4.2334(1)$ Å, $b = 9.9725(3)$ Å, $c = 12.4659(1)$ Å). The inverse susceptibility above ca. 50 K shows Curie-Weiss behavior, and a metamagnetic transition is apparent in the field-dependent magnetization around $H_c \approx 20$ kG. The resistivity increases linearly with temperature, indicating the metallic character of this material. TB-LMTO-ASA electronic structure calculations indicate that this new intermetallic phase has all bonding states optimized in the $[Zn_{4-x}Al_{7+x}]$ network, which classifies this compound among the so-called "polar intermetallics." The calculations also

provide a rationalization of the nonrandom ordering of Zn and Al atoms, which can be attributed to optimizing (Zn,Al)-(Zn,Al) orbital interactions.

Introduction

Polar intermetallics form a class of intermetallic compounds that are attracting increasing attention for studying chemical bonding between metals as well as for their potential physical properties.[1-4] There are at present no simple rules to identify such compounds in general, although the tendency is for an electropositive element, i.e., alkali, alkaline earth, or rare earth element, to combine with a molar excess of electronegative metals from among the late- and/or post-transition elements. Analysis of the theoretical electronic structure indicates that orbital interactions between the electronegative metals cross from bonding to antibonding at the Fermi level, which implies that metal-metal bonding within the electronegative framework is optimized.[1] The energy densities of states can show a pseudo-gap at the Fermi level, but this feature is not a prerequisite. If the minority electropositive component is among the rare earth elements, interesting physical properties are possible via the valence 4*f* orbitals, e.g., heavy fermion or magnetic ordering.[5]

Among polar intermetallic structures, the tetragonal $BaAl_4$ structure type (also known as the $ThCr_2Si_2$-type) is the most prolific[6] and is particularly suited for placing rare earth elements into single tetragonally symmetric environments for studying the consequences of uniaxial magnetic anisotropy. $BaAl_4$-type tetra-aluminides with rare earth elements are reported for La-Sm,[6] but these are characterized at elevated temperatures and are probably Al-deficient, i.e., $LnAl_{4-y}$, due to optimizing chemical bonding in the Al framework. At

lower temperatures, the vacancies order into the La_3Al_{11} structure type.[7] One means to stabilize the $BaAl_4$ structure type with rare earth elements, then, is to substitute metals that are poorer in valence electrons than Al, e.g., Au or Zn, and these do exist, e.g., $LnAu_xAl_{4-x}$ (Ln: La-Tb; $0.75 \leq x \leq 2.00$).[8, 9] As there are two distinct crystallographic sites for the electronegative metals in the $BaAl_4$ structure type, the distribution of two different elements introduces additional structural complexity, which is called the *coloring problem*.[10] Energetic factors controlling the site preferences for different elements in a structure can be separated into "site energies" and "bond energies." Moreover, exploration of this structure type reveals that it exists for 12-14 valence electrons assigned to the electronegative component.[2, 11, 12] With this flexibility in mind, we are studying rare-earth – zinc- aluminum phases, and in this report we report the synthesis, structure and properties of two new compounds in the Tb-Zn-Al system that form the La_3Al_{11} structure type.

Experimental

Synthesis. Single crystals of $Tb_3Zn_{4-x}Al_{7+x}$ ($x = 0.4$) were grown from high temperature ternary solutions, rich in Al and Zn.[13-15] These solutions were prepared from the pure elements, terbium (Materials Preparation Center, Ames Lab, 99.0%), aluminum ingots (Aesar 99.999%) and zinc ingots (Aesar 99.999%), in the molar ratio 10% Tb: 45% Zn: 45% Al. This (Al, Zn)-rich self-flux was chosen because it introduces no additional elements to the melt. The constituent elements were placed in an alumina crucible and sealed in a silica ampoule under a partial argon pressure. After initially heating the ampoule to above ca. 900°C, it was slowly cooled to 650°C. Subsequently, the excess solution was decanted, and

well-formed orthorhombic crystals were obtained. Their lengths were usually 2-5 mm, slightly more for a few larger crystals, whereas the cross-section varied from ~1×1 mm^2 (needle-like rods) to ~1×4 mm^2, resulting in a plate-like aspect for some crystals.

Structure Determination. The sample was characterized by single crystal and powder X-ray diffraction (XRD) techniques at ambient temperature. The powder diffraction pattern of the sample was obtained with a Huber image plate camera and monochromatic Cu $K\alpha_1$ radiation (λ = 1.540598 Å). Powdered samples were homogeneously dispersed on a Mylar film with the aid of a little petroleum jelly. The step size was set at 0.005° and the exposure time was 1 hr. Data acquisition was controlled via the in-situ program. In the X-ray powder pattern, only diffraction maxima expected for the corresponding $Tb_3Zn_{3.6(1)}Al_{7.4(1)}$ pattern were observed. The lattice parameters of a = 4.2334(1) Å, b = 9.9725(3) Å, c = 12.4659(1) Å were obtained from least squares refinement with the aid of a Rietveld refinement program.[16] A needle-like single crystal was selected from the product and was mounted on a Bruker APEX CCD-diffractometer equipped with monochromated Mo $K\alpha$ radiation (λ = 0.71073 Å), and diffraction data were collected at room temperature over a hemisphere of reciprocal space with 0.3° scans in ω and with an exposure time of 10 sec per frame up to 2θ = 56.55°. The SAINT program[17] was used for the data extraction and then corrected for Lorentz and polarization effects, and SADABS[18] was used for empirical absorption correction. Structure refinements (full-matrix least-squares on F^2) were performed using the SHELXTL package of crystallographic programs.[19] The crystallographic data are presented in Table 1; atomic coordinates and displacement parameters are listed in Table 2; selected interatomic distances are given in Table 3.

------ Tables 1-3 ------

Electronic Structure Calculations. Tight-binding, linear muffin-tin orbital (TB-LMTO) electronic structure calculations were carried out using the atomic sphere approximation (ASA) using the LMTO Version 47 program.[20-23] Exchange and correlation were treated in a local spin density approximation (LDA). All relativistic effects except spin-orbit coupling were taken into account using a scalar relativistic approximation.

Within the atomic sphere approximation (ASA), space is filled with small overlapping Wigner-Seitz (WS) atomic spheres. The radii of the WS spheres were obtained by requiring the overlapping potential to be the best possible approximation to the full potential according to an automatic procedure. No empty spheres were necessary in this system. The WS radii determined by this procedure are 3.774 Å for Tb, 2.712 Å for Zn and 2.940 Å for Al. The basis set included Tb 6*s*, 6*p*, 5*d* orbitals, Al 3*s*, 3*p*, and 3*d* orbitals and Zn 4*s*, 4*p* and 3*d* orbitals. The Tb 4*f* orbitals were treated as core functions occupied by eight electrons. The Löwdin downfolding technique allows the derivation of few-orbital effective Hamiltonians by keeping only the relevant degrees of freedom and integrating out the irrelevant ones. The **k**-space integrations to determine the self-consistent charge density, densities of states (DOS) and crystal Hamiltonian orbital populations (COHP)[24] were performed by the tetrahedron method. The Fermi level was chosen as an internal reference level in all cases.

Physical Properties. Magnetization measurements on a plate-like crystal of $Tb_3Zn_{3.6}Al_{7.4}$ were performed in a Quantum Design MPMS SQUID magnetometer (T = 1.8-350 K, H_{max} = 55 kG), with H = 1 kG. The electrical resistance in zero field was measured with a Linear Research LR-700 AC resistance bridge (f = 16 Hz, I = 1-3 mA) in the magnetic field–temperature environment of the same QD MPMS system, using a standard four-probe

technique. The heat capacity measurement was done in a Quantum Design PPMS system, using the relaxation technique and subtracting the sample holder and grease contribution, which were measured separately.

Result and Discussion

------ Figure 1 ------

Crystal Structure of $Tb_3Zn_{3.6}Al_{7.4}$. $Tb_3Zn_{3.6}Al_{7.4}$ is a new compound adopting the La_3Al_{11} structure type at ambient temperature.[7] Its orthorhombic crystal structure is illustrated in Figure 1 and emphasizes the coordination polyhedra surrounding the two distinct terbium atoms. Among the four crystallographic sites for the electronegative Zn and Al components (colored red or blue in Figure 1), only the 2*d* site is fully occupied by Al atoms. These Al atoms are surrounded by eight (Zn, Al) atoms in a elongated square prism as well as four Tb atoms in a distorted square – the entire environment is closely related to the Al surroundings in cubic rare-earth trialuminides ($LnAl_3$).[6] The other three sites (M1, M2 and M3) show mixed, yet nonrandom occupation by Zn and Al. Zn atoms strongly prefer the M1 (8*l*) sites (red spheres), which are coordinated by a pseudo-square pyramidal environment in the (Zn, Al) network. The axial direction shows a particularly short M1-M1 distance of 2.475(3) Å. Al atoms preferentially occupy the remaining two M2 and M3 sites. There are two types of polyhedra surrounding the terbium atoms (Figure 1), which are distinguished by shaded and nonshaded yellow spheres. The Tb1 atoms (shaded yellow spheres) are coordinated by 16 Zn/Al atoms in an environment that closely resembles that of the Ba atoms in the $BaAl_4$ structure type. The Tb2 sites are encapsulated by 14 Al/Zn atoms at distances less than 3.5 Å with the coordination polyhedra completed by two M1 atoms at a distance of ca. 3.76 Å.

Electronic Structure and Bonding Relationships. To understand the possible chemical bonding features influencing the stability of $Tb_3Zn_{3.6}Al_{7.4}$, TB-LMTO-ASA electronic structure calculations were performed on "$Tb_3Zn_4Al_7$" as the representative composition with the M1 site fully occupied by Zn atoms and the M2 and M3 sites fully occupied by Al atoms. The total DOS curve broken down into the different atomic contributions to the DOS as well as the COHP curve for all (Zn, Al)-(Zn, Al) contacts less than 3.00 Å in the $[Zn_4Al_7]$ network are shown in Figure 2. The Fermi level, indicated by the dashed line, falls in the region of nonzero but low DOS, which, according to the accompanying COHP curve, corresponds to the energy region where (Zn, Al)-(Zn, Al) bonding levels crossover to antibonding levels. Therefore, metal-metal bonding within the electronegative part of the structure of "$Tb_3Zn_4Al_7$," on average, is optimized. Hence, $Tb_3Zn_{3.6}Al_{7.4}$ behaves like other "polar intermetallic" compounds, and the observed composition is significantly influenced by orbital interactions in the $[Zn_4Al_7]$ network. In fact, similar COHP analyses of "$\square_3Zn_4Al_7$," "Tb_3Al_{11}" and "$\square_3Al_{11}$" ($\square$ means that the Tb site was treated as vacant, i.e., contributing no orbitals to the set of valence orbitals in the structure) all give optimum metal-metal bonding near 38 valence electrons per formula unit, which exactly corresponds to "$Tb_3Zn_4Al_7$." A similar outcome was deduced for ternary rare-earth gold aluminides, $Ln_3Au_2Al_9$.[25] COHP analyses of the specific orbital interactions in the $[Zn_4Al_7]$ network, shown in Figure 3, indicate that the M1-M1 (Zn-Zn) interaction is optimized and Al-Al antibonding states are already occupied, while heteronuclear Zn-Al bonding states are not yet filled. Within a rigid band model, a few additional valence electrons can be accommodated into the electronic states of "$Tb_3Zn_4Al_7$" to optimize the heteronuclear Zn-Al interactions by replacing some Zn atoms with Al atoms: "$Tb_3Zn_{4-x}Al_{7+x}$."

------ Figures 2 and 3; Table 4 ------

To understand the site preference of Zn and Al atoms throughout the structure of $Tb_3Zn_{3.6}Al_{7.4}$, several different models of "$Tb_3Zn_4Al_7$" were constructed and their total energies were evaluated. To conduct this comparison, the Wigner-Seitz radii for Tb, Zn and Al, respectively, were kept constant for the different models. Table 4 lists the different models by identifying the Wyckoff sites (M1, M2 and M3) occupied by the Zn and Al atoms. To include models that showed other distributions of Zn and Al atoms in the $[Zn_4Al_7]$ network, the space group had to be modified to *Pmmm* or *Imm2* (NOTE: our study here is not exhaustive, but representative). In total, six different models were studied, and according to the relative total energies, Zn prefers to occupy the M1 (8*l*) sites, which is confirmed by our diffraction experiments. Table 4 also lists the percentages of Zn-Zn, Zn-Al and Al-Al interactions per unit cell for the M1-M1 pairs as well as the other contacts in the complete structure. In particular, when the M1 sites give the fewest number of homoatomic Al-Al contacts, the lowest energy arrangement is obtained, and the total energies increase linearly with the number of homoatomic Al-Al contacts. The corresponding COHP curves for the M1-M1 interactions for the different pairs of elements, shown in Figure 4, indicate that Al-Al interactions have antibonding character, while Zn-Zn interactions have optimized bonding character at the calculated Fermi level. However, in "$Tb_3Zn_4Al_7$," the energy differences between the different structural models are small enough (i.e., 50-80 meV per formula unit) to assume that the influence of configurational entropy at elevated temperatures will favor a partially ordered arrangement of Zn and Al atoms, as is observed in the X-ray diffraction experiments. In the corresponding $Ln_3Au_2Al_9$, the "coloring problem" is dictated by eliminating Au-Au contacts, while the energies of the different configurations are

significantly separated from the low energy configuration that there is no mixed occupancy observed other than at the M1 site.[25]

------ Figures 4 and 5 ------

Physical Measurements. The temperature dependence of the inverse susceptibility (calculated as $1/\chi = H/M$) is shown in Figure 5, whereas the inset presents the low temperature region of the susceptibility for the applied field H = 1 kG. The inverse susceptibility above ca. 50 K is consistent with Curie-Weiss behavior of the magnetization. A linear fitting of the inverse susceptibility in the paramagnetic state gives a value of the effective moment μ_{eff} = 9.86 μ_B, which is close to the theoretical value for Tb^{3+} of 9.72 μ_B, and a value of θ_P, for this field orientation, of – 29.7 K. The slightly enhanced effective moment may be due to small weighing error, or a consequence of its estimate based on a measurement along just one crystallographic direction. Anisotropic measurements would allow for an estimate of the polycrystalline average susceptibility, which we expect to give a more accurate value of μ_{eff}.

A magnetization measurement as a function of field is shown in Figure 6 for the field directed along the long axis of the plate-like sample. One metamagnetic transition is apparent around $H_c \approx 20$ kG, leading to a magnetization of 7.1 μ_B at our maximum applied field of H = 55 kG, smaller then the saturated 9.0 μ_B calculated value. This is consistent with more metamagnetic transitions occurring above 55 kG, or with the Tb^{3+} magnetic moments being confined by the crystal electric field CEF to easy axes different from the main crystallographic directions. To verify the former hypothesis, measurements up to higher fields are required, whereas to address the latter assumption, at a minimum anisotropic magnetization measurements would be necessary.

------ Figures 6 and 7 ------

The low temperature susceptibility for H = 1 kG (shown as an inset in Figure 5) indicates antiferromagnetic ordering below the Néel temperature T_N = 22.6 K. This transition temperature, as well as a potential spin reorientation temperature can also be identified in the $d(\chi T)/dT$ (around 21.6 K and 18.6 K respectively) and $C_p(T)$ (at 22.5 K and 18.9 K, shown in Figure 7a and 7b). Based on all of the above measurements, we can summarize that the transition temperatures in $Tb_3Zn_{3.6}Al_{7.4}$ are $T_N = (22.05 \pm 0.45)$ K and $T_1 = (18.75 \pm 0.15)$ K.

------ Figure 8 ------

The resistivity increases linearly with temperature (Figure 8), indicating metallic character of this material. However, the large residual resistivity at T = 2 K (~26 μΩ·cm) leads to a reduced residual resistivity ratio (RRR) of ca. 1.95, which is consistent with mixed (non-integral) site occupancies in this compound.

Conclusion

We have reported on a new intermetallic compound $Tb_3Zn_{3.6}Al_{7.4}$ that adopts the La_3Al_{11} structure type. Crystals suitable for both structural and property measurements were grown from an equimolar Zn:Al flux. Single crystal diffraction indicated that the Zn and Al atoms are partially ordered in this structure. Electronic structure calculations attribute the observed composition to optimizing metal-metal bonding in the electronegative (Zn, Al) framework, while the specific ordering is strongly influenced by specific orbital interactions, i.e., the bond-energy terms in the total electronic energy. Magnetic, calorimetric and resistivity measurements on $Tb_3Zn_{3.6}Al_{7.4}$ indicate metallic character with

antiferromagnetically coupled Tb^{3+} sites, which show a metamagnetic transition in the field-dependent magnetization around $H_c \approx 20$ kG.

References

1. Miller, G. J.; Lee, C.-S.; Choe, W.: Structure and Bonding Around the Zintl Border. In: *Inorganic Chemistry Highlights* (Eds. Meyer, G.; Naumann, D.; Wesemann, L.), p. 21-53. Wiley-VCH **2002**.

2. Häussermann, U.; Amerioun, S.; Eriksson, L.; Lee, C. -S.; Miller, G. J. *J. Am. Chem. Soc.* **2002**, 124 4371.

3. Amerioun, S.; Häussermann, U. *Inorg. Chem.* **2003**, 42, 7782.

4. Lupu, C.; Downie, C.; Guloy, A.; Albright, T.; Mao, J. -G. *J. Am. Chem. Soc.* **2004**, 126, 4386.

5. Gout, D.; Benbow, E.; Gourdon, O.; Miller, G. J. *J. Solid State Chem. 2003*, 176, 538.

6. Villar, P.; Calvert, L. D.: *Pearson's Handbook of Crystallographic Data for Intermetallic Phases, 2nd Ed.* ASM International, Metals Park, OH, USA, **1991**.

7. Gomes de Mesquita, A. H.; Buschow, K. H. J. *Acta Cryst.* **1967**, 22, 497.

8. Hulliger, F. *J. Alloys Compds.* **1995**, 218, 255.

9. Hulliger, F.; Nissen, H. -U.; Wessicken, R. *J. Alloys Compds.* **1994**, 206, 263.

10. Miller, G. J. *Eur. J. Inorg. Chem.* **1998**, 523.

11. Zheng, C.; Hoffmann, R. *Z. Naturforsch.* **1986**, B41, 292.

12. Burdett, J. K.; Miller, G. J. *Chem. Mater.* **1990**, *2*, 12.

13. Fisk, Z.; Remeika, J. P.: in: K. A. Gschneidner, L. R. Eyring (Eds.), Handbook of Physics and Chemistry of Rare Earths, **12**, North-Holland, Amsterdam, (**1989**) 53.

14. Canfield, P. C.; Fisk, Z *Philos. Mag.* **1992**, B65, 1117.

15. Canfield, P. C.; Fisher, I. R. *J. Crystal Growth* **2001**, 225, 155.

16. Hunter, B. A.; Howard, C. J. *Rietica*; Australian Nuclear Science and Technology Organization : Menai, Australia (**2000**).

17. SMART; Bruker AXS, Inc.; Madison, WI (**1996**).

18. Blessing, R. H. *Acta. Cryst.* **1995**, A51, 33.

19. SHELXTL; Bruker ASX, Inc.: Madison, WI, (**2000**).

20. Tank, R. W.; Jepsen, O.; Burckhardt. A.; Andersen, O. K. *TB-LMTO-ASA Program*, Vers. 4.7; Max-Planck-Institut für Festkörperforschung: Stuttgart, Germany, (**1998**).

21. Skriver, H. L.: *The LMTO Method*; Springer-Verlag: Berlin, Germany, (**1984**).

22. Jepsen, O.; Sob, M.; Andersen, O. K.: *Linearized Band-Structure Methods in Electronic Band-Structure and its Applications*; Springer Lecture Note; Springer-Verlag: Berlin, Germany, (**1987**).

23. Andersen, O. K.; Jepsen, O. *Phys. Rev. Lett.* **1983**, 53, 2571.

24. Dronskowski, R.; Blöchl, P. *J. Phys. Chem.* **1993**, 97, 8617.

25. Nordell, K. J.; Miller, G. J.: *Angew. Chem. Int. Ed. Engl.* **1997**, 36, 2008.

Table 1. Crystallographic data for $Tb_3Zn_{3.6(1)}Al_{7.4(1)}$.

Composition	$Tb_3Zn_{3.6}Al_{7.4}$
Temperature	293(2) K
Crystal size	$0.15 \times 0.15 \times 0.20$ mm^3
Space group	*Immm* (No. 71)
Unit cell dimensions	$a = 4.2281(8)$ Å
	$b = 9.966(2)$ Å
	$c = 12.469(3)$ Å
Volume	525.38(18) Å^3
Z	2
Diffractometer	Bruker Apex
Wavelength	0.71073 Å (Mo Kα)
2θ range for data collection	2.62 to 56.55°.
Index ranges	$-5 \le h \le 5, -13 \le k \le 12, -16 \le l \le 12$
Reflections collected	1653
Independent reflections	389 [R(int) = 0.0838]
Completeness to $2\theta_{max}$	95.1 %
Data / parameters	389 / 31
Goodness-of-fit on F^2	1.206
R indices (all data)	R1[a] = 0.0280, wR2[b] = 0.0669
Extinction coefficient	0.0244(10)
Largest diff. peak and hole	1.758 and –2.333 e$^-$·Å^{-3}

[a] $R1 = \sum \| |F_o| - |F_c| \| / \sum |F_o|$; [b] $wR2 = \left[\sum w \left(|F_o|^2 - |F_c|^2 \right)^2 / \sum w |F_o|^4 \right]^{1/2}$;

$w = 1 / \left[\sigma^2 \left(F_o^2 \right) + (0.0244P)^2 + 1.4365P \right]$; $P = \left(F_o^2 + 2F_c^2 \right) / 3$

Table 2. Atomic coordinates, site occupation factors and isotropic temperature displacement parameters (in $Å^2$) for $Tb_3Zn_{3.6}Al_{7.4}$.

Atom	Site	*x*	*y*	*z*	Site Occ.		U_{iso} ($Å^2$)
Tb1	2*a*	0	0	0	1		0.007(1)
Tb2	4*i*	0	0	0.3146(1)	1		0.008(1)
M1	8*l*	0	0.3758(1)	0.3410(1)	0.73(1)	Zn	0.012(1)
					0.27	Al	
M2	4*h*	0	0.2104(3)	1/2	0.14(1)	Zn	0.011(1)
					0.86	Al	
M3	8*l*	1/2	0.2280(3)	0.3538(2)	0.09(1)	Zn	0.012(1)
					0.91	Al	
Al4	2*d*	1/2	0	1/2	1		0.011(1)

Table 3. Selected interatomic distances (Å) in $Tb_3Zn_{3.6(1)}Al_{7.4(1)}$ with frequency per formula unit indicated.

Atom-Atom	Distance (Å)	Atom-Atom	Distance (Å)
Tb1-M1	3.151(1) 8×	M1-M1	2.475(3) 2×
Tb1-M3	3.266(1) 4×	M1-M2	2.578(2) 4×
Tb1-M2	3.578(1) 4×	M1-M3	2.582(2) 8×
		M1-M3	2.640(2) 4×
Tb2-M2	3.121(2) 4×		
Tb2-M1	3.125(1) 8×	M2-M3	2.797(1) 8×
Tb2-Al4	3.132(1) 4×	M2-Al4	2.978(2) 4×
Tb2-M3	3.142(1) 8×		
Tb2-M3	3.429(1) 4×		
Tb2-M1	3.760(1) 4×	M3-Al4	2.913(3) 4×

Table 4. Zn and Al distributions at M1, M2 and M3 sites and bond types in the $[Zn_4Al_7]$ network for six model structures of $Tb_3Zn_4Al_7$. Al atoms exclusively occupy the Al4 site (see Table 2).

	Models					
Sites	**1** (*Immm*)	**2** (*Immm*)	**3** (*Pmmm*)	**4** (*Pmmm*)	**5** (*Pmmm*)	**6** (*Imm2*)
M1 (8)	Zn	Al	½ Zn ½ Al	Al	½ Zn ½ Al	½ Zn ½ Al
M2 (4)	Al	Al	Zn	Zn	Al	Al
M3 (8)	Al	Zn	Al	½ Zn ½ Al	½ Zn ½ Al	½ Zn ½ Al
(eV/formula)	0	0.08	0.05	0.09	0.07	0.09
Bonds	Percentage with distances less than 2.50 Å (M1-M1 contacts)					
Al-Al	0	100	50	100	50	0
Zn-Al	0	0	0	0	0	100
Zn-Zn	100	0	50	0	50	0
	Percentage with distances more than 2.50 Å					
Al-Al	50	25	31.3	25	25	31.3
Zn-Al	50	75	62.5	62.5	62.5	62.5
Zn-Zn	0	0	6.2	12.5	12.5	6.2

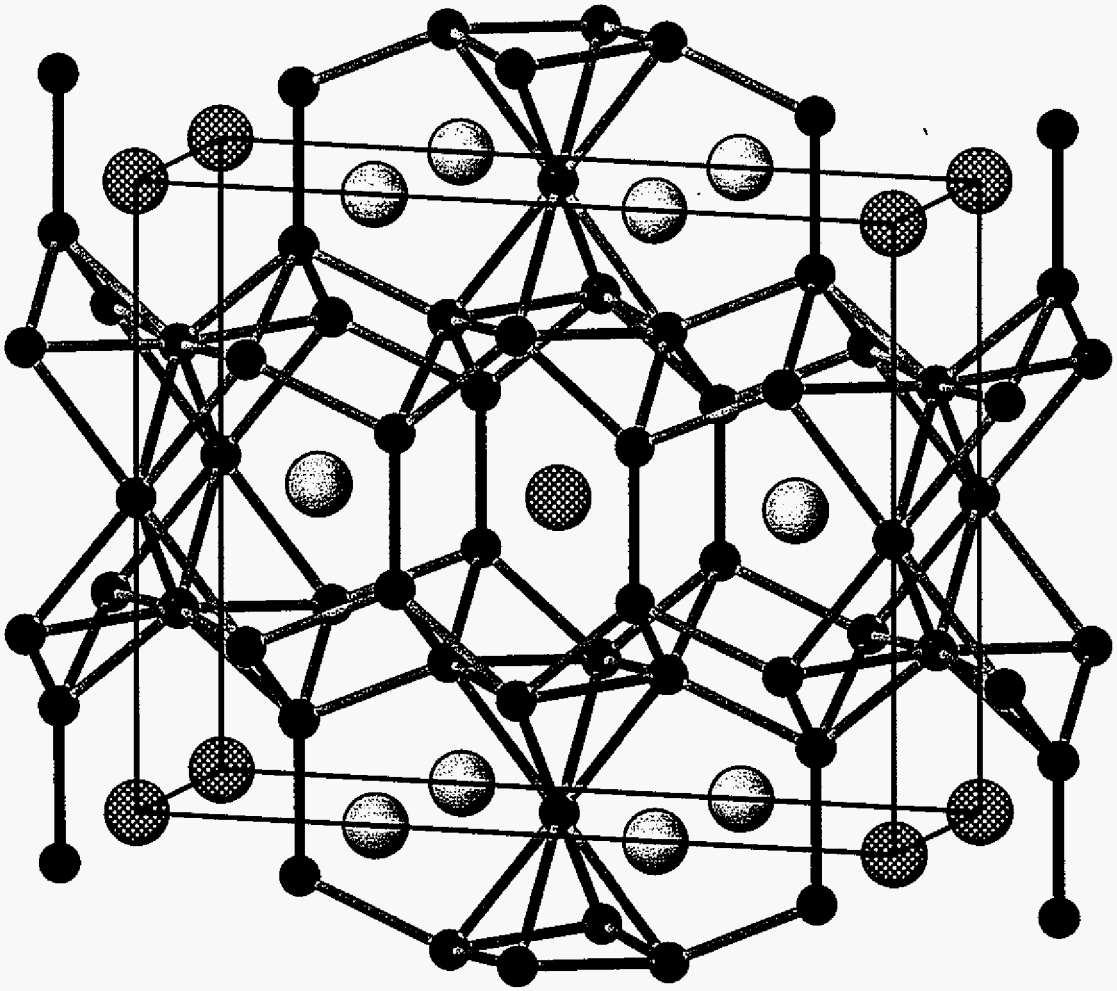

Figure 1. Clinographic projection of orthorhombic $Tb_3Zn_{3.6(1)}Al_{7.4(1)}$ along the [100] direction and emphasizing the polyhedral surroundings of the Tb sites. Tb1: shaded yellow; Tb2: yellow; M1: red; M2-M4: blue spheres. Interatomic distances less than 2.50 Å: black; distances between 2.50 and 3.00 Å: light blue.

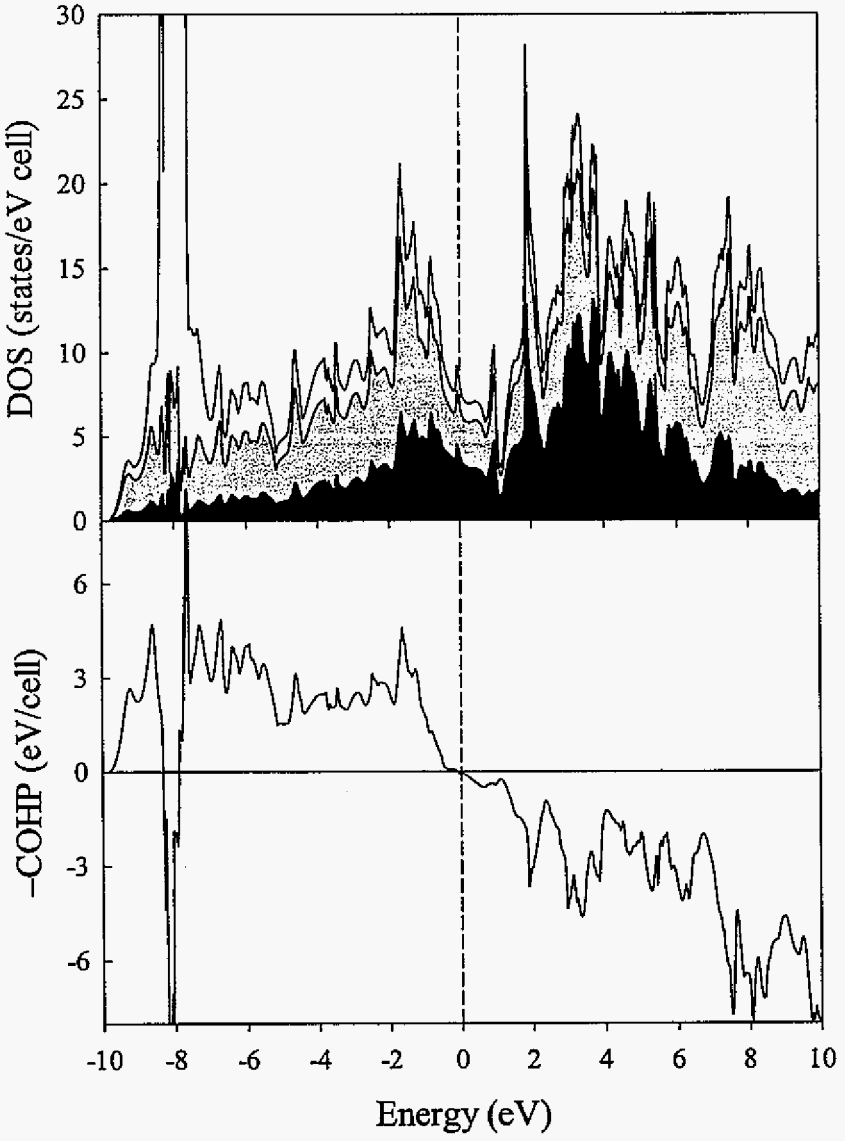

Figure 2. (Top) Total DOS curve for "$Tb_3Zn_4Al_7$" separated into atomic contributions. Black: Tb; Gray: Al; White: Zn. (Bottom) Total COHP curve for all (Zn,Al)-(Zn,Al) contacts less than 3.00 Å in the [Zn_4Al_7] network of "$Tb_3Zn_4Al_7$." The dashed line indicates the Fermi level.

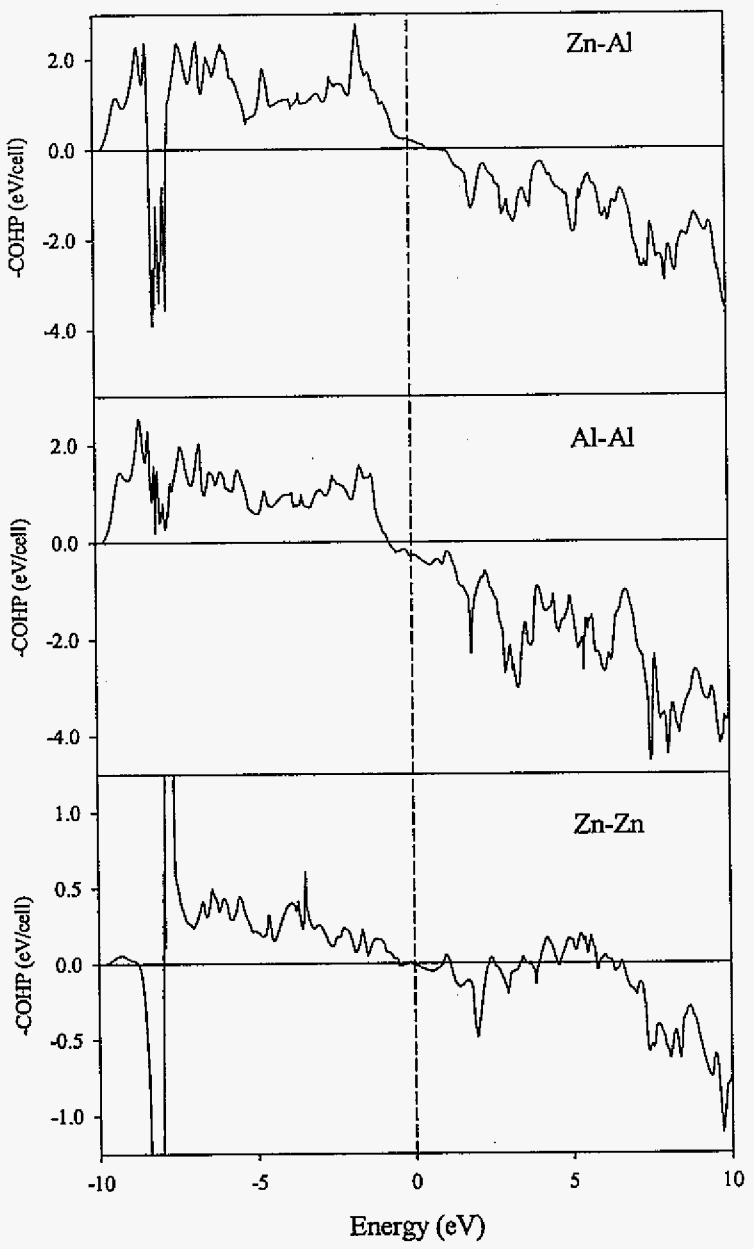

Figure 3. COHP curves for (top) Zn-Al, (middle) Al-Al, and (bottom) Zn-Zn interactions less than 3.00 Å in the $[Zn_4Al_7]$ network of "$Tb_3Zn_4Al_7$." The dashed line marks the Fermi level. (–COHP values > 0: bonding levels; –COHP values < 0: antibonding levels.)

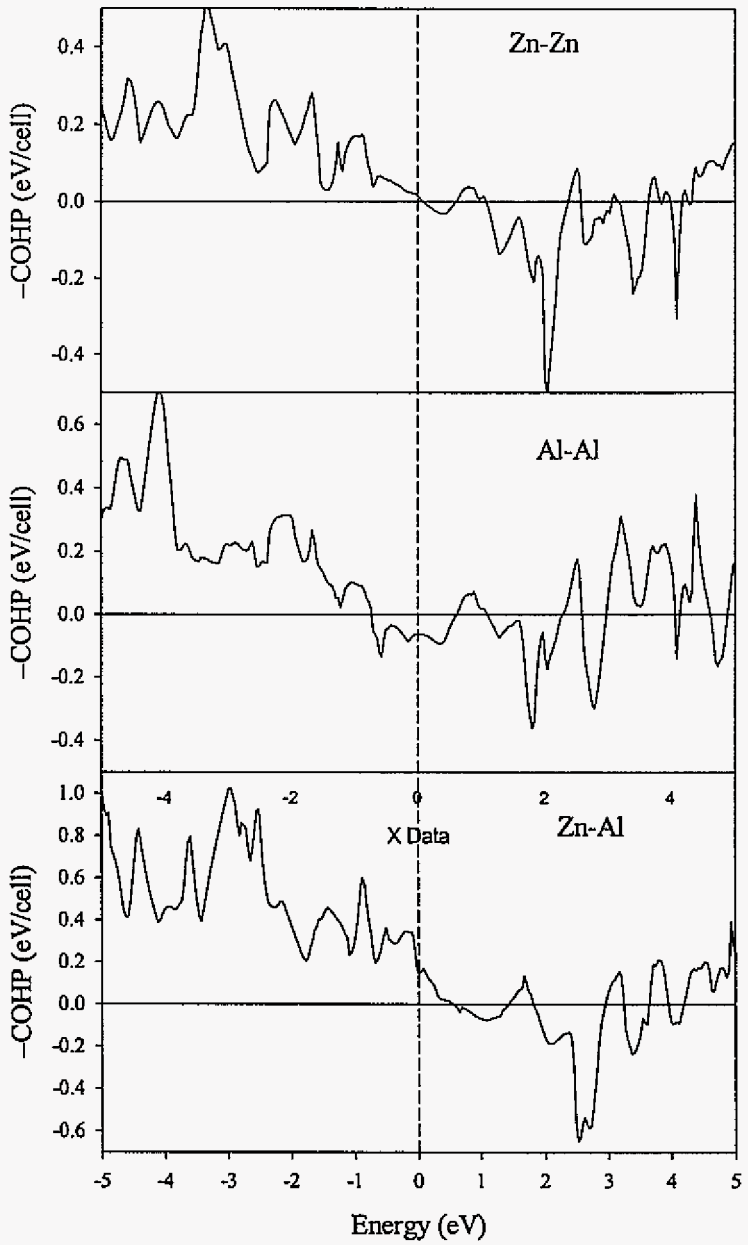

Figure 4. M1-M1 (d = 2.475 Å) COHP curves for (top) Zn-Zn, (middle) Al-Al, and (bottom) Zn-Al contacts in various models of "$Tb_3Zn_4Al_7$." The dashed line indicates the Fermi level. (–COHP values > 0: bonding levels; –COHP values < 0: antibonding levels.)

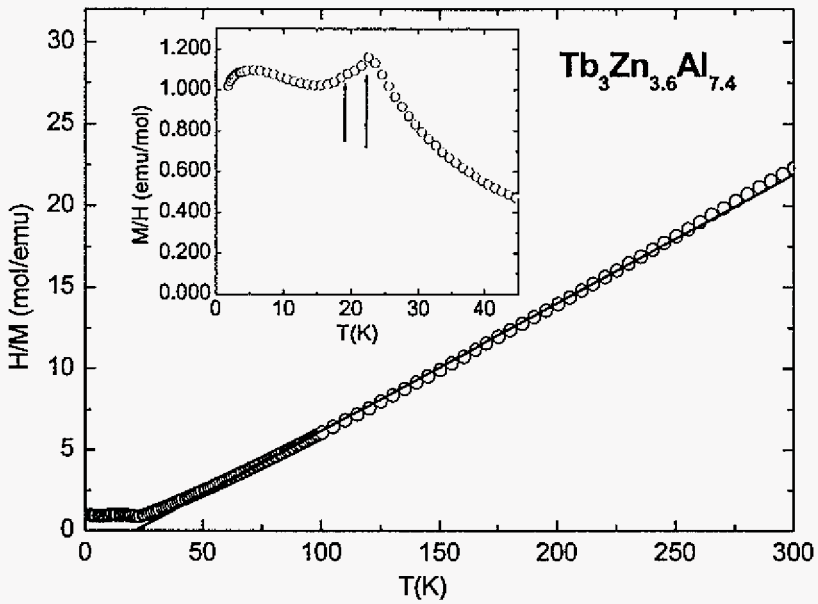

Figure 5. Inverse susceptibility (open circles) and the linear Curie-Weiss fit for high temperatures (solid line); inset: low-temperature susceptibility with the arrows indicating the transition temperatures.

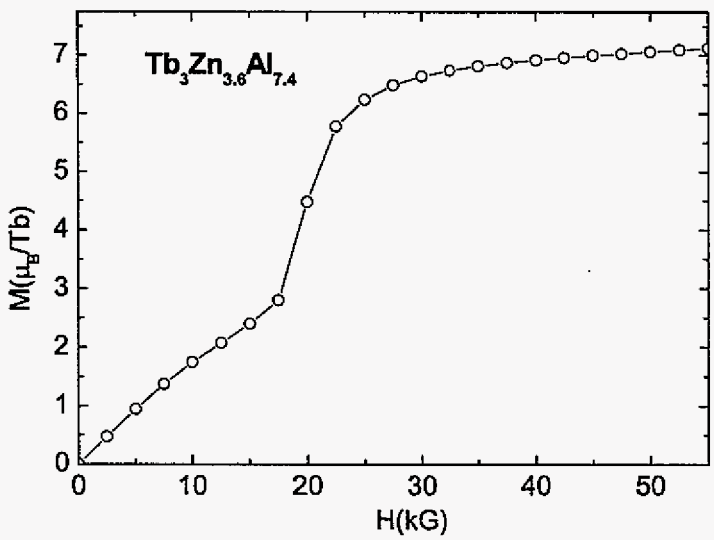

Figure 6. Field dependent magnetization for $T = 2$ K and H up to 55 kG.

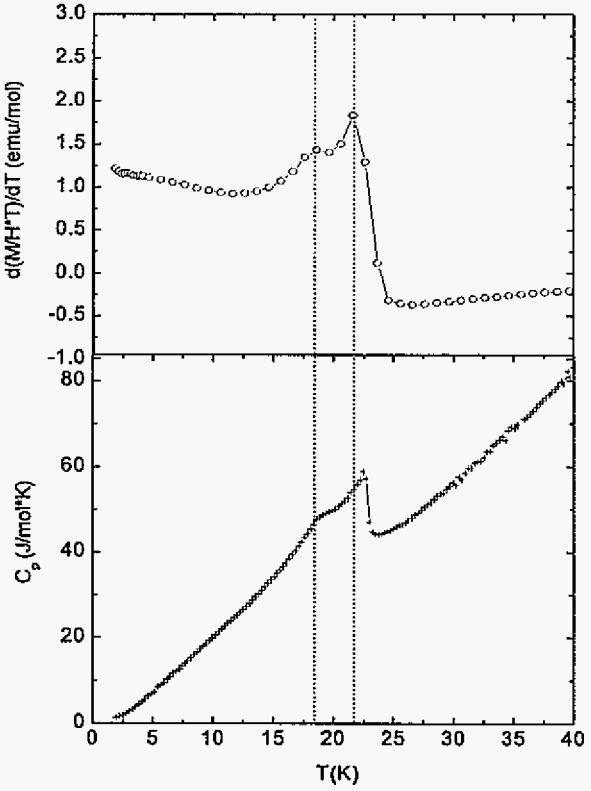

Figure 7. Low-temperature (top) $d(\chi T)/dT$ and (bottom) heat capacity $C_p(T)$. The dotted lines mark the peak positions as determined from the top curve.

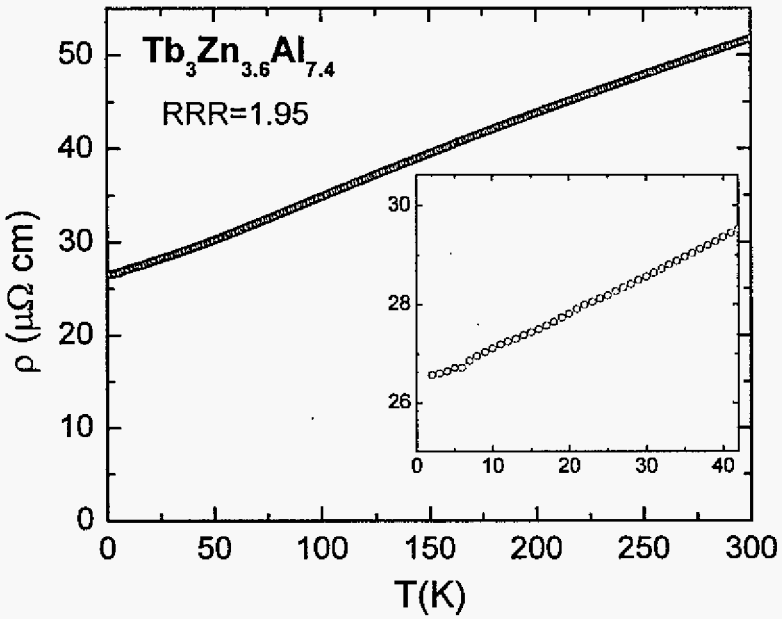

Figure 8. Zero-field resistivity data (inset: enlarged low-temperature part).

CHAPTER 8

$Zn_{39}(Cr_xAl_{1-x})_{81}$: A New Intergrowth Structure Involving Icosahedra

Mi-Kyung Han and Gordon J. Miller

Abstract

The crystal structure of $Zn_{39}(Cr_xAl_{1-x})_{81}$ has been determined by X-ray single crystal diffraction. The crystal structure belongs to the trigonal space group $R\bar{3}m$ with lattice parameters $a = 7.59(2)$, and $c = 36.9(1)$ Å. It has a layered structure of similar to icosahedral Mn-Al quasicrystalline compounds.

Introduction

In the course of a systematic search for novel compounds in the Cr-Zn-Al system, a hitherto unknown structure of $Zn_{39}(Cr_xAl_{1-x})_{81}$ has been observed. The preliminary result for the ternary Cr/Zn/Al system will be discussed in this chapter. Up to date, only one ternary Cr/Zn/Al compound has been reported without specific crystallographic data. (Al_3Cr_8Zn with $MoSi_2$-type structure; space group = *I*4/*mmm*, and unit cell parameter is $a = 2.99$, and $c = 8.60$Å).[1] To the best of our knowledge, this new ternary compound adopts a new structure type.

Experimental

Synthesis. Initial, the procedures involved reaction compositions of $Al_{(1.2\sim1.4)}Cr_{(0.3\sim0.4)}Zn$ to explore new ternary aluminum compounds. Most of the products contained an intense peak with small impurity peaks in the X-ray powder diffraction patterns. X-ray single crystal refinements were done for several crystals and subsequently reloaded these stoichiometric ratios based on the single crystal refinements. Stoichiometric amounts of starting materials with $Al_{(1.20\sim1.34)}Cr_{(0.87\sim0.75)}Zn$ composition were loaded into Ta tubes under an inert Ar atmosphere (total mass of ~0.5g). The Ta crucibles were placed into fused silica tubes, sealed under vacuum (~1×10^{-4} Torr) and subjected to the following treatment: they were heated to 700°C at the rate 135°/hr, kept at 700°C for 7 days to melt the reactants, cooled to 450°C in 5hr, and kept isothermally at 450°C for 7 days and then slowly cooled to room temperature at the rate 53 °/hr. Several different sets of experiment with different annealing profiles were done. The reaction container (Ta tube) reacted with starting materials at over the reaction temperatures exceeding 800°C. The reactant compositions and the products identified by X-ray powder diffraction are listed in Table 1. In many of the products, multiple phases were observed in the powder patterns, in which cases the major phases are underlined. We have not, or yet, achieved optimized conditions; we need further experiments to make a single phase. However, among the samples, the reaction composition of (3) $Al_{1.25}Cr_{0.82}Zn$ shows almost single phase product (more than 90% based on the intensity of highest peak comparison). This composition agrees with compositions for obtained from both EDX analysis and single crystal refinements. According to our powder pattern analysis, shown in Figure 1, we see a strong dependence on starting composition, because even slight changes in the composition show drastic changes in the final products. Figure 2 shows that the measured

powder pattern of sample (3), $Al_{1.25}Cr_{0.82}Zn$, is well matched with the calculated powder pattern based on the refinement from single crystal diffraction.

---- Figure 1 and Figure 2 ----

Structure Determination. Data collections and their refinements followed the same procedures as those previous described in this thesis. Several single crystals obtained from sample (2) and (3). Details of the single crystal data collection parameters and crystallographic refinement results for Al/Cr/Zn compounds are listed in the Table 2. The resulting occupancies, atomic parameters, and residuals are listed in the Tables 3 and 4.

---- Tables 2, 3, and 4 ----

Results and Discussion

Structure Description

Ternary $Zn_{39}(Cr_xAl_{1-x})_{81}$ crystallize in the trigonal space group $R\bar{3}m$ (No. 166) at ambient temperature. The asymmetric unit contains nine crystallographically inequivalent sites. Among them, only three sites, 8*h*(1) (*x, y, z*), 18*h*(2) (*x, y, z*), and 3*b* (1/3, 2/3, 1/6), are fully occupied by Zn atoms; The other six sites, 18*h*(3) (*x, y, z*), 18*h*(4) (*x, y, z*), 18*h*(5) (*x, y, z*), 18*h*(6) (*x, y, z*), 6*c* (*0, 0, z*), and 3*a* (*0, 0, 0*), are randomly occupied by Cr and Al atoms.

---- Figure 3 ----

The crystal structures of this ternary compound can be viewed as two alternating layers stacked along the *c*-axis, shown in Figure 3a. The unit cell contains eighteen layers, i.e. a flat layer (F) and a puckered layer (P), in the sequence FPPPF P FPPPF P FPPPF P, is

shown schematically in Figure 3b. Therefore, the structure can be described by three combined thick layers (PFPFP) and a further puckered layer (P) between them.

Similar type of layer structure can be found in other compounds, such as $Al_{10}Mn_3$[2], λ-Al_4Mn[3-4], Al_5Co_2[5], ε-Al_4Cr[6], $Al_{23}V_4$[7], κ-$Al_{177}Cr_{49}Ni$[8], and etc., whose structures are related to icosahedral or decagonal quasicrystals. Their stacking sequences are summarized in Table 2. The layers in each compound are very similar but it can establish a different pattern, because it contains a different distorted clusters and the layers are stacked in different sequences. Now, we focus on the F layer. Comparing the F layer of $Zn_{39}(Cr_xAl_{1-x})_{81}$ with that of the $Al_{10}Mn_3$ phase, geometrically they are completely identical. The F layer forms a triangular arrangement of Zn(3) atoms. Each Zn(3) site has two Zn(3) near neighbors arranged in a Zn triangle. Zn-Zn distances within Zn triangle are about 2.678 Å. These triangles build interpenetrating icosahedra with two P layers located above and below the F layer. The interpenetrating icosahedra, known as "I3 clusters"[3], are three dimensionally infinitely connected in Mn_3Al_{10}, but in $Zn_{39}(Cr_xAl_{1-x})_{81}$ the "I3 clusters" alternate with an other building motif (P layer shown in Figure 3e). The layer structure and the interpenetrated icosahedral chains in this structure can perhaps be seen more clearly in Figure 4. The Zn(1) and Zn(3) atoms occupy the centers of icosahedra, shown in Figure 4d and 4c, respectively. All of these icosahedra are interconnected. Unlike Mn_3Al_{10} structure, this compound contains extra P layer. This P layer has "3c-2e"-like connection between icosahedra, which is shown in Figure 4c. These layered structures are similar to icosahedral Mn-Al quasicrystalline compounds. Therefore, this compound may provide new insights into the formation, composition and structure of quasicrystalline materials.

Conclusion

The crystal structure of $Zn_{39}(Cr_xAl_{1-x})_{81}$ has been determined by X-ray single crystal diffraction. The crystal structure belongs to the trigonal space group $R\bar{3}m$ with lattice parameters $a = 7.59(2)$, and $c = 36.9(1)$ Å. Single crystal diffraction indicated that there are nine crystallographically inequivalent sites: the Cr and Al atoms are randomly ordered at 18*h*(3) (*x, y, z*), 18*h*(4) (*x, y, z*), 18*h*(5) (*x, y, z*), 18*h*(6) (*x, y, z*), 6*c* (*0, 0, z*), and 3*a* (*0, 0, 0*) sites. 8*h*(1) (*x, y, z*), 18*h*(2) (*x, y, z*), and 3*b* (1/3, 2/3, 1/6), are fully occupied by Zn atoms. It has a layered structure consisting of FPPPF P FPPPF P FPPPF P layers, where F is a flat and P a puckered layer. The icosahedral clusters and their arrangements in this structure are similar to Mn_3Al_{10}, but the sequence of layer is different. Therefore, we consider this as a new structure type ternary compound. More systematic investigation is needed for this compound to investigate the role of extra P layer in the structure.

References

1. Villars, P.; Calvert, L. D. *Pearson's Handbook of Crystallographic Data for Intermetallic Phases*, ASM International Materials Park, OH, Desk ed., **1997**

2. Taylor, M. A. *Acta Cryst.* **1959**, 12, 393.

3. Kreiner, G.; Franzen, H. F. *J alloys Comp.* **1995**, 221, 15.

4. Kreiner, G.; Franzen, H. F. *J alloys Comp.* **1997**, 261, 83.

5. Newkirk, J. B.; Black, P. J.; Damjanovic, A. *Acta Cryst.* **1961**, 14, 532.

6. Li, X. Z.; Sugiyama, K.; Hiraga, K.; Sato, A.; Yamamoto, A.; Sui, H. X.; Kuo, K. H. *Z.Kristallogr.* **1997**, 212, 628.

7. Ray, A. E. *Acta Cryst.* **1960**, 13, 876.

8. Sato, A.; Yamamoto, A.; Li, X. Z.; Hiraga, K.; Haibach, T.; Sturer, W. *Acta Cryst.* **1997**. C53, 1531.

Table 1. The reactant composition, reaction condition, and crystalline products identified by powder X-ray diffraction.

Loaded Composition	Reactant Ratio (%) Al	Cr	Zn	Reaction Conditions	Products
(1)$Al_{1.20}Cr_{0.87}Zn$	39.09	28.34	32.57	(a) 700°C, 7 days, 450°C, 7 days.	Al_2Cr* :Cu_5Zn_8-type structure
(2)$Al_{1.23}Cr_{0.85}Zn$	39.94	27.60	32.47		Mixed phase : target phase + Al_2Cr
(3)$Al_{1.25}Cr_{0.82}Zn$	40.72	26.71	32.57		Target phase* + impurity
(4)$Al_{1.28}Cr_{0.79}Zn$	41.69	25.73	32.57		Al_2Cr* :Cu_5Zn_8-type structure
(5)$Al_{1.31}Cr_{0.77}Zn$	42.53	25.00	32.47		Al_2Cr* :Cu_5Zn_8-type structure
(6)$Al_{1.34}Cr_{0.75}Zn$	43.37	24.27	32.36		Al_2Cr* :Cu_5Zn_8-type structure
				(b) 1000°C, 7 days, 450°C, 7 days.	Both cases, the container reacted with reactants. Apparently, the container was brittle.
				(c) 800°C, 7 days, 450°C, 7 days.	

*major phase (solely determined by comparing the highest peak)

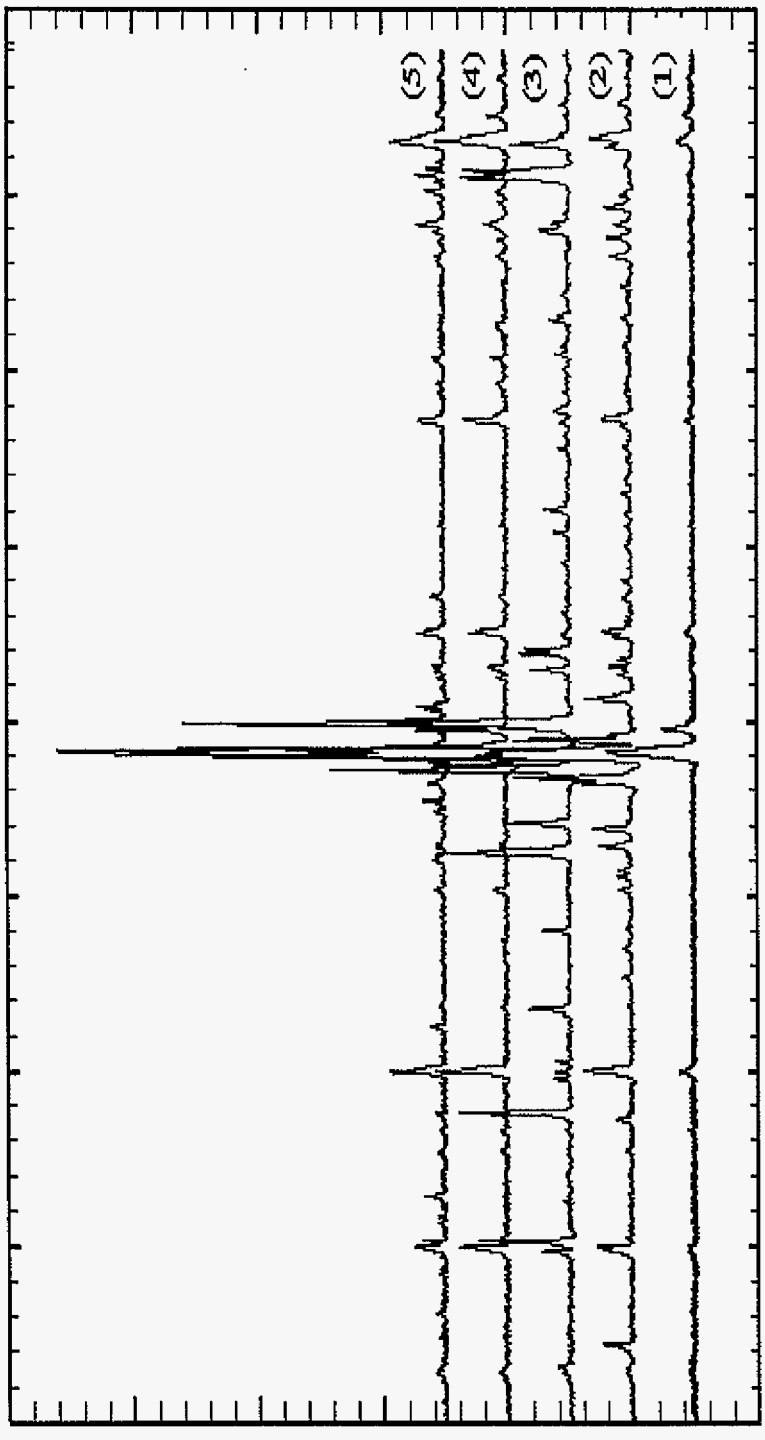

Figure 1. X-ray powder pattern of sample (1)-(6). Only sample (3) shows the target phase x-ray powder pattern as a major phase, and sample (2) shows mixing of two phases; Target phase + Al_2Cr + unidentified peaks.

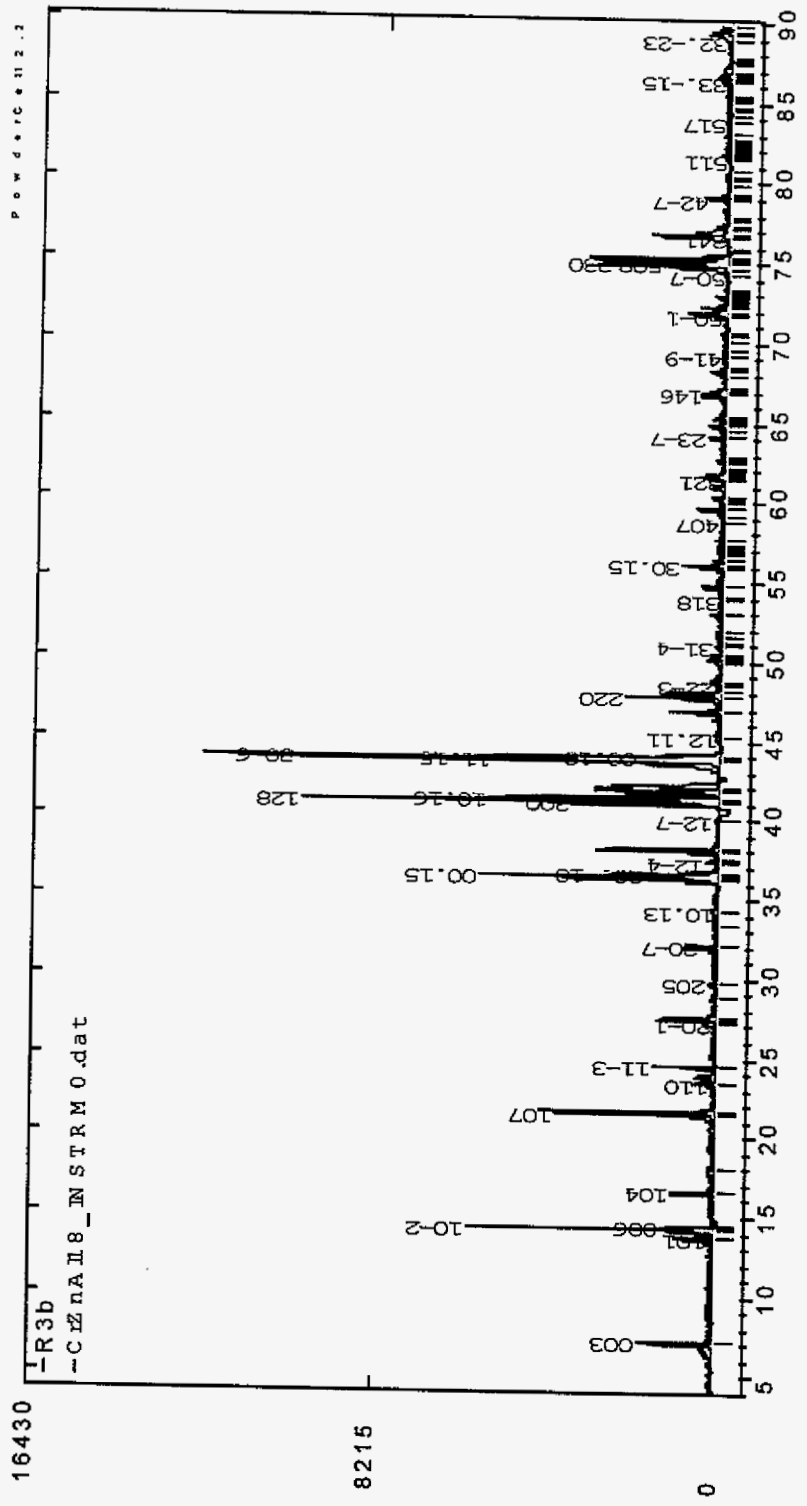

Figure 2. Calculated X-ray pattern (red) and experimentally obtained X-ray powder pattern of sample (3) $Al_{1.25}Cr_{0.82}Zn$.

Table 2. Intermetallic phases with similar types of layer structure. Flat layers (F) and puckered layers (P)

Compounds	Stacking sequence	Space group	Lattice parameter, Å		
			a	*b*	*c*
$Cr_{39}(Zn_xAl_{1-x})_{81}$	PFPFP P	$R\bar{3}m$	7.595		36.958
$Al_{10}Mn_3$	PF	$P6_3/mmc$	7.543		7.898
Al_5Co_2	PF	$P6_3/mmc$	7.656		7.593
$Al_{23}V_4$	PFP P	$P6_3/mmc$	7.692		17.04
λ-Al_4Mn	PFP	$P6_3/m$	28.382		12.38
κ-$Al_{177}Cr_{49}Ni$	PFP	$P6_3/m$	17.674		12.516
ε-Al_4Cr	PFP PFFP	*Cmcm*	12.521	34.705	20.223

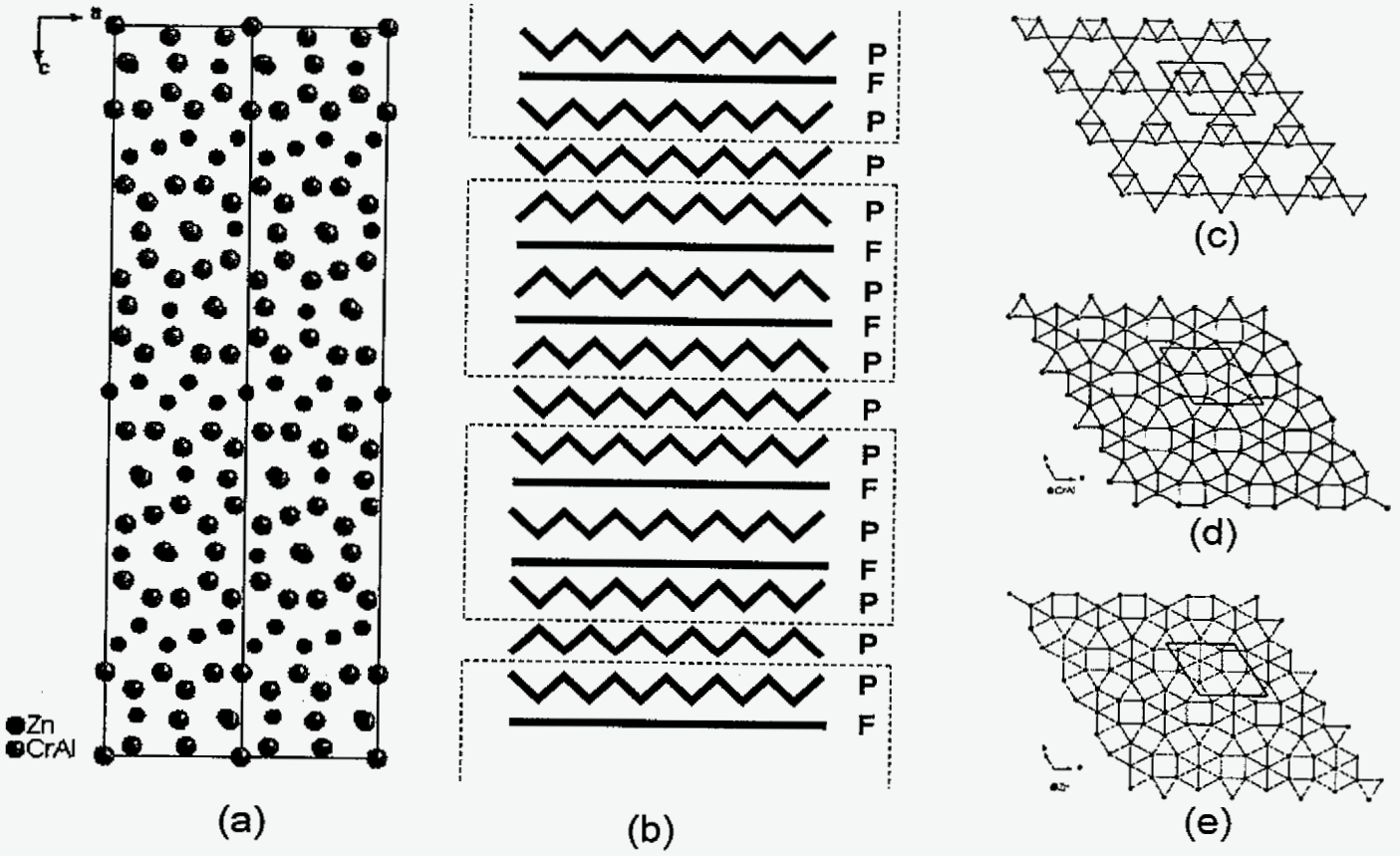

Figure 3. (a) Projection of the structure of $Zn_{39}(Cr_xAl_{1-x})_{81}$ along the *c*-axis, (b) Schematic diagram of stacking sequence of eighteen layers. (c)-(e) The projections of the arrangement of atoms in the F and P layers perpendicular *c*-axis. One puckered layer (d) is consisting of Cr and Al atoms and the other puckered layer (e) is consisting of Zn atoms.

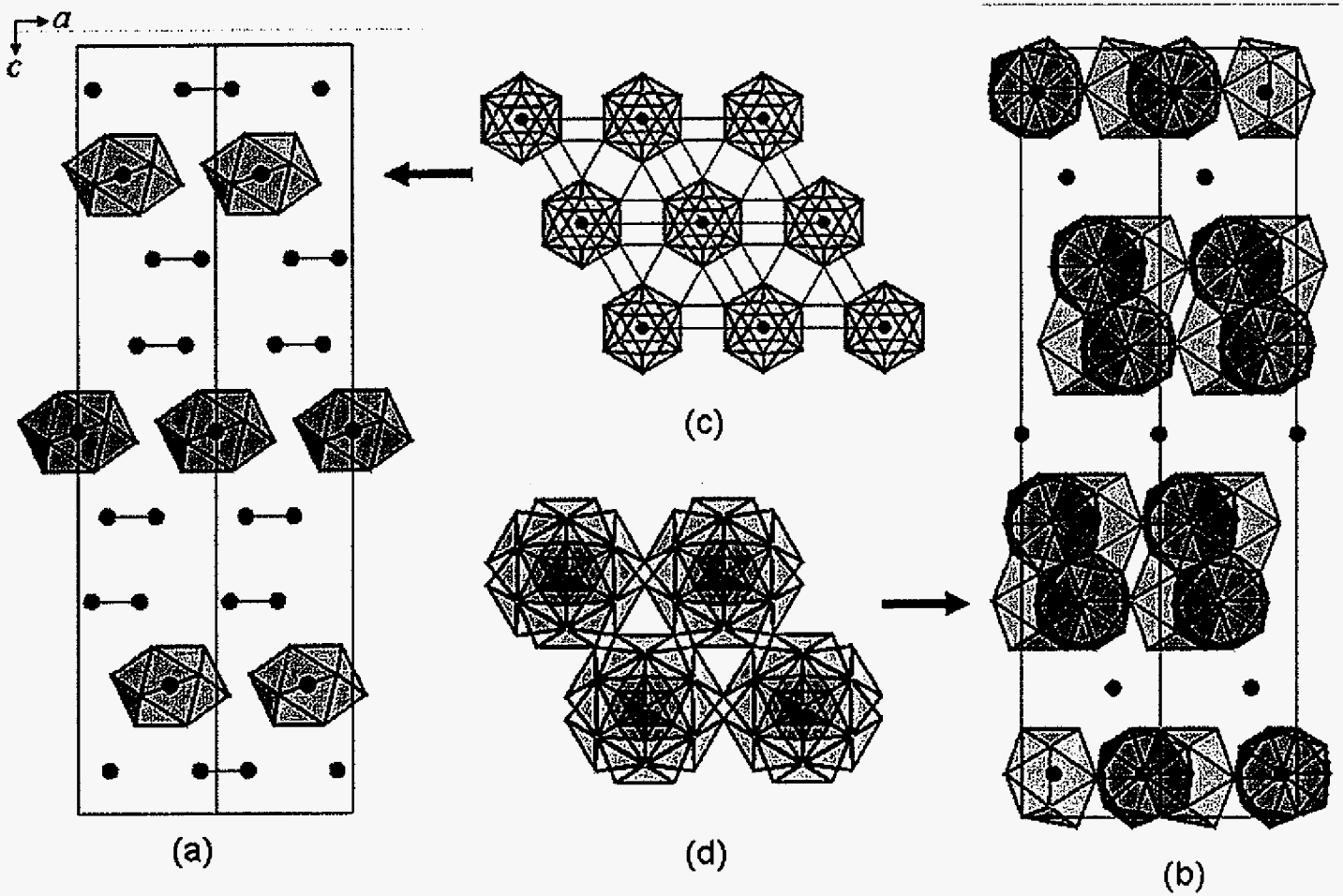

Figure 4. (a) and (B) The crystal structure of $Zn_{39}(Cr_xAl_{1-x})_{81}$ described in terms of icosahedral clusters centered on the atoms, (c) Zn(3) centered icosahedral network, and (d) interpenetrated icosahedron

Table 2. Crystal data and structure refinement for $Zn_{39}(Cr_xAl_{1-x})_{81}$ compounds.

x	0.40	0.39	0.36	0.34
Composition	**$Zn_{39}Cr_{32.04}Al_{48.96}$**	**$Zn_{39}Cr_{31.98}Al_{49.6}$**	**$Zn_{39}Cr_{29.1}Al_{51.9}$**	**$Zn_{39}Cr_{27.6}Al_{53.4}$**
Temperature, K	293(2)	293(2)	293(2)	293(2)
Wavelength, Å	0.71073	0.71073	0.71073	0.71073
Crystal system	trigonal	trigonal	trigonal	trigonal
Space group	R -3 m	R -3 m	R -3 m	R -3 m
Unit cell dimension (Å), a	7.5990(11)	7.5949(11)	7.6020(11)	7.6130(11)
b	7.5990(11)	7.5949(11)	7.6020(11)	7.6130(11)
c	36.976(7)	36.958(7)	36.988(7)	37.068(7)
Volume, $Å^3$	1849.1(5)	1846.2(5)	1851.2(5)	1860.6(5)
Z	1	1	1	1
Absorp. coeff., mm^{-1}	19.879	19.034	18.983	17.005
F(000)	2864	2655	2655	2180
Crystal size, mm^3	0.24 × 0.23 × 0.28	0.23 × 0.25 × 0.26	0.24 × 0.21 × 0.29	0.25 × 0.27 × 0.21
$2\theta_{max}$	56.58	56.58	56.56	56.46
Index ranges, *h,k,l*	-9/10, -10/10, -47/48	-10/9, -9/10, -48/47	-9/10, -10/9, -48/48	-9/8, -9/7, -47/40
Reflections collected	5346	4497	5435	3901
Independent reflections	620 [R(int) = 0.0793]	612 [R(int) = 0.0336]	624 [R(int) = 0.0376]	605 [R(int) = 0.0912]
Data / parameters	620 / 51	612 / 51	624 / 51	605 / 51
Goodness-of-fit on F^2	1.114	1.090	1.109	1.084
R indices [I>2sigma(I)]	R1 = 0.0546, wR2 = 0.1346	R1 = 0.0430, wR2 = 0.1241	R1 = 0.0418, wR2 = 0.1191	R1 = 0.0537, wR2 = 0.1097
R indices (all data)	R1 = 0.0580, wR2 = 0.1377	R1 = 0.0456, wR2 = 0.1278	R1 = 0.0453, wR2 = 0.1232	R1 = 0.0852, wR2 = 0.1221
Extinction coefficient	0.00058(11)	0.00088(12)	0.00038(9)	0.00032(8)
Δ(r) peak and hole, e.Å-3	2.491 / -2.215	1.781 / -1.827	1.517 a/ -1.599	2.091 / -1.553

Table 2. Atomic coordinates and equivalent isotropic displacement parameters ($Å^2 \times 10^3$) for $Zn_{39}(Cr_xAl_{1-x})_{81}$ compounds. U(eq) is defined as one third of the trace of the orthogonalized U_{ij} tensor.

x	Wyck.		occ.	x	y	z	U(eq)
0.40	Zn(1)	18*h*		0.1167(1)	0.8833(1)	0.0557(1)	9(1)
	Zn(2)	18*h*		0.1212(1)	0.1242(2)	0.1801(1)	11(1)
	Zn(3)	3*b*		1/3	2/3	2/3	9(1)
	Cr/Al(4)	6*c*	0.43(3)	0	0	0.1148(1)	6(1)
	Cr/Al(5)	18*h*	0.39(2)	0.4581(2)	0.9161(4)	0.0504(1)	9(1)
	Cr/Al(6)	18*h*	0.36(2)	0.4139(4)	0.1207(2)	0.0912(1)	8(1)
	Cr/Al(7)	18*h*	0.54(2)	0.2010(2)	0.7990(2)	-0.0138(1)	10(1)
	Cr/Al(8)	3*a*	0.34(5)	0	0	0	7(2)
	Cr/Al(9)	18*h*	0.29(2)	0.2086(2)	0.7914(2)	0.1145(1)	6(1)
0.39	Zn(1)	18*h*		0.1165(1)	0.8836(1)	0.0557(1)	10(1)
	Zn(2)	18*h*		0.1211(1)	0.12422(2)	0.1801(1)	10(1)
	Zn(3)	3*b*		1/3	2/3	2/3	10(1)
	Cr/Al(4)	6*c*	0.44(3)	0	0	0.1148(1)	6(1)
	Cr/Al(5)	18*h*	0.39(2)	0.4581(2)	0.9162(3)	0.0503(1)	8(1)
	Cr/Al(6)	18*h*	0.35(2)	0.4141(3)	0.1207(2)	0.0913(1)	8(1)
	Cr/Al(7)	18*h*	0.55(2)	0.2012(2)	0.7988(2)	-0.0138(1)	11(1)
	Cr/Al(8)	3*a*	0.36(4)	0	0	0	7(2)
	Cr/Al(9)	18*h*	0.28(2)	0.2088(2)	0.7912(2)	0.1146(1)	6(1)
0.36	Zn(1)	18*h*		0.1167(1)	0.8833(1)	0.557(1)	10(1)
	Zn(2)	18*h*		0.1210(1)	0.1242(2)	0.1801(1)	10(1)
	Zn(3)	3*b*		1/3	2/3	2/3	9(1)
	Cr/Al(4)	6*c*	0.41(3)	0	0	0.1146(1)	5(1)
	Cr/Al(5)	18*h*	0.39(2)	0.4581(2)	0.9161(3)	0.0503(1)	9(1)
	Cr/Al(6)	18*h*	0.35(2)	-0.2071(2)	0.5857(3)	0.0912(1)	8(1)
	Cr/Al(7)	3*a*	0.37(4)	0	0	0	7(2)
	Cr/Al(8)	18*h*	0.54(2)	0.2009(2)	0.7991(2)	-0.0138(1)	11(1)
	Cr/Al(9)	18*h*	0.28(2)	0.2087(2)	0.7913(2)	0.1146(1)	5(1)
0.34	Zn(1)	18*h*		0.1173(1)	0.8827(1)	0.0557(1)	10(1)
	Zn(2)	18*h*		0.1212(1)	0.1242(2)	0.1801(1)	13(1)
	Zn(3)	3*b*		1/3	2/3	2/3	9(1)
	Cr/Al(4)	6*c*	0.38(3)	0	0	0.1145(1)	8(2)
	Cr/Al(5)	18*h*	0.34(2)	0.4577(2)	0.9155(5)	0.0502(1)	7(1)
	Cr/Al(6)	18*h*	0.31(2)	0.4139(5)	0.1207(2)	0.0910(1)	6(1)
	Cr/Al(7)	18*h*	0.35(2)	0.2001(2)	0.7999(2)	-0.0137(1)	7(1)
	Cr/Al(8)	3*a*	0.40(4)	0	0	0	8(2)
	Cr/Al(9)	18*h*	0.34(2)	0.2088(2)	0.7912(2)	0.1146(1)	9(1)

occ. is occupancies for Cr in mixed sites.

Table 3. (a) Anisotropic displacement parameters ($Å^2 \times 10^3$) for $Zn_{39}(Cr_xAl_{1-x})_{81}$ (x = 0.40, 0.39). The anisotropic displacement factor exponent takes the form: $-2\pi^2[h^2a^2U_{11} + ... + 2\ h\ k\ a\ b\ U_{12}]$

x		U11	U22	U33	U23	U13	U12
0.40	Zn(1)	9(1)	9(1)	9(1)	0(1)	0(1)	5(1)
	Zn(2)	15(1)	7(1)	7(1)	0(1)	0(1)	4(1)
	Zn(3)	9(1)	9(1)	9(1)	0	0	4(1)
	Cr(4)	6(2)	6(2)	6(2)	0	0	3(1)
	Cr(5)	6(1)	10(1)	11(1)	2(1)	1(1)	5(1)
	Cr(6)	7(1)	7(1)	9(1)	-1(1)	-2(1)	4(1)
	Cr(7)	10(1)	10(1)	12(1)	0(1)	0(1)	5(1)
	Cr(8)	8(2)	8(2)	4(3)	0	0	4(1)
	Cr(9)	8(1)	8(1)	4(1)	1(1)	-1(1)	6(1)
0.39	Zn(1)	11(1)	11(1)	10(1)	0(1)	0(1)	6(1)
	Zn(2)	15(1)	7(1)	5(1)	0(1)	0(1)	3(1)
	Zn(3)	11(1)	11(1)	8(1)	0	0	5(1)
	Cr(4)	6(1)	6(1)	5(2)	0	0	3(1)
	Cr(5)	6(1)	10(1)	10(1)	1(1)	1(1)	5(1)
	Cr(6)	8(1)	7(1)	8(1)	-1(1)	-1(1)	4(1)
	Cr(7)	10(1)	10(1)	11(1)	0(1)	0(1)	4(1)
	Cr(8)	7(2)	7(2)	5(2)	0	0	4(1)
	Cr(9)	8(1)	8(1)	4(1)	1(1)	-1(1)	6(1)

Table 3. Continued (b) Anisotropic displacement parameters ($Å^2 \times 10^3$) for $Zn_{39}(Cr_xAl_{1-x})_{81}$ (x = 0.36, 0.34)compounds. The anisotropic displacement factor exponent takes the form: $-2\pi^2[h^2a^2U_{11} + ... + 2\,h\,k\,a\,b\,U_{12}]$

x		U11	U22	U33	U23	U13	U12
0.36	Zn(1)	10(1)	10(1)	9(1)	0(1)	0(1)	6(1)
	Zn(2)	15(1)	7(1)	6(1)	1(1)	0(1)	4(1)
	Zn(3)	10(1)	10(1)	8(1)	0	0	5(1)
	Cr(4)	5(1)	5(1)	5(2)	0	0	2(1)
	Cr(5)	7(1)	10(1)	10(1)	1(1)	0(1)	5(1)
	Cr(6)	7(1)	9(1)	8(1)	2(1)	1(1)	4(1)
	Cr(7)	8(2)	8(2)	4(2)	0	0	4(1)
	Cr(8)	10(1)	10(1)	11(1)	0(1)	0(1)	4(1)
	Cr(9)	8(1)	8(1)	3(1)	1(1)	-1(1)	5(1)
0.34	Zn(1)	10(1)	10(1)	9(1)	0(1)	0(1)	6(1)
	Zn(2)	18(1)	11(1)	8(1)	2(1)	1(1)	5(1)
	Zn(3)	12(1)	12(1)	5(2)	0	0	6(1)
	Cr(4)	10(2)	10(2)	5(3)	0	0	5(1)
	Cr(5)	6(1)	8(2)	7(2)	1(1)	0(1)	4(1)
	Cr(6)	7(2)	6(1)	6(2)	-1(1)	-3(1)	4(1)
	Cr(7)	7(1)	7(1)	5(2)	1(1)	-1(1)	3(1)
	Cr(8)	11(3)	11(3)	3(4)	0	0	6(2)
	Cr(9)	11(2)	11(2)	6(2)	1(1)	-1(1)	8(2)

CHAPTER 9

General Conclusions

Our explorations of rare-earth, transition metal intermetallics have resulted in the synthesis and characterization, and electronic structure investigation, as well as understanding the structure-bonding-property relationships. Our work has presented the following results:

1. *Understanding the relationship between compositions and properties in $LaFe_{13-x}Si_x$ system*: A detailed structural and theoretical investigation provided the understanding of the role of a third element on stabilizing the structure and controlling the transformation of cubic $NaZn_{13}$-type structures to the tetragonal derivative, as well as the relationship between the structures and properties.
2. *Synthesis of new ternary rare-earth iron silicides $RE_{2-x}Fe_4Si_{14-y}$ and proposed superstructure*: This compound offers complex structural challenges such as fractional occupancies and their ordering in superstructure.
3. *Electronic structure calculation of $FeSi_2$*: This shows that the metal-semiconductor phase transition depends on the structure. The mechanism of band gap opening is described in terms of bonding and structural distortion. This result shows that the electronic structure calculations are an essential tool for understanding the relationship between structure and chemical bonding in these compounds.

4. *Synthesis of new ternary rare-earth Zinc aluminides* $Tb_3Zn_{3.6}Al_{7.4}$: Partially ordered structure of $Tb_3Zn_{3.6}Al_{7.4}$ compound provides new insights into the formation, composition and structure of rare-earth transition-metal intermetallics. Electronic structure calculations attribute the observed composition to optimizing metal-metal bonding in the electronegative (Zn, Al) framework, while the specific ordering is strongly influenced by specific orbital interactions.
5. *Synthesis of new structure type of* $Zn_{39}(Cr_xAl_{1-x})_{81}$: These layered structures are similar to icosahedral Mn-Al quasicrystalline compounds. Therefore, this compound may provide new insights into the formation, composition and structure of quasicrystalline materials.

APPENDIX

Summary of Single Crystal Refinements on Various Compounds

APPENDIX A-1

The Crystal Structure of YMgZn

Introduction

In the course of explaining the substitution of divalent Zn for Mg in Y_5Mg_{24}, a new compound YMgZn (1:1:1) with ZrNiAl-type structure was found.

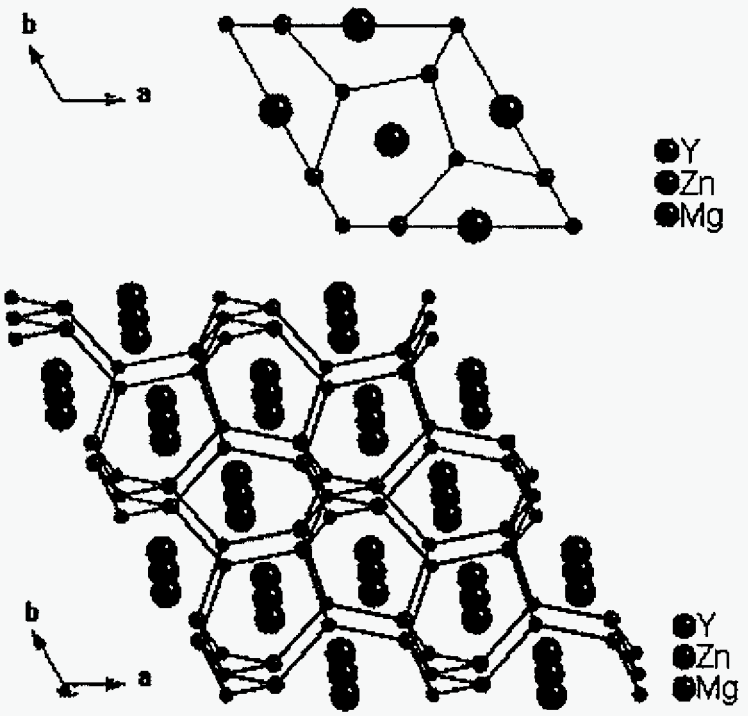

Discussion

Details of the single crystal data collection parameters and crystallographic refinement results for YMgZn are listed in the Table 1. The resulting occupancies, atomic parameters, and residuals are listed in Tables 2 and 3.

Table 1. Crystal data and structure refinement for YMgZn.

Empirical formula	YMgZn
Formula weight	218.47
Temperature	293(2) K
Wavelength	0.71073 Å
Crystal system	hexagonal
Space group	*P* -6 2 *m* (no. 189)
Unit cell dimensions	a = 7.2829(10) Å
	b = 7.2829(10) Å
	c = 4.4297(9) Å
Volume	203.48(6) Å3
Z	3
Absorption coefficient, mm^{-1}	59.427
F(000)	390
Crystal size	0.20 × 0.15 × 0.22 mm^3
Theta range for data collection	3.23 to 28.18°.
Index ranges	$-9 \le h \le 4$, $-8 \le k \le 9$, $-5 \le l \le 5$
Reflections collected	1087
Independent reflections	196 [R(int) = 0.0328]
Refinement method	Full-matrix least-squares on F^2
Data / restraints / parameters	196 / 14
Goodness-of-fit on F2	1.014
Final R indices [I>2sigma(I)]	R1 = 0.0144, wR2 = 0.0346
R indices (all data)	R1 = 0.0147, wR2 = 0.0348
Extinction coefficient	0.117(6)
Largest diff. peak and hole	0.458 and -0.323 e.$Å^{-3}$

Table 2. Atomic coordinates and equivalent isotropic displacement parameters ($Å^2 \times 10^3$) for YMgZn. U(eq) is defined as one third of the trace of the orthogonalized U_{ij} tensor.

	Wyck.	Occ.	x	y	z	U(eq)
Y(1)	3*f*	1	0.5730(1)	0	0	8(1)
Zn(2)	1*a*	1	0	0	0	8(1)
Zn(3)	2*d*	1	2/3	1/3	½	6(1)
Mg(4)	3*g*	1	0	0.2439(3)	½	9(1)

Table 3. Anisotropic displacement parameters ($Å^2 \times 10^3$) for YMgZn. The anisotropic displacement factor exponent takes the form: $-2\pi^2[h^2a^2U_{11} + ... + 2\ h\ k\ a\ b\ U_{12}\ ]$.

	U_{11}	U_{22}	U_{33}	U_{23}	U_{13}	U_{12}
Y(1)	8(1)	7(1)	8(1)	0	0	4(1)
Zn(2)	9(1)	9(1)	6(1)	0	0	4(1)
Zn(3)	5(1)	5(1)	6(1)	0	0	3(1)
Mg(4)	10(1)	7(1)	12(1)	0	0	5(1)

APPENDIX A-2

The Crystal Structure of

$Y_{5-x}Mg_{24+x}$ (x = 1.47, 0.94)

Introduction

During a study on the structure types of ternary Y/Zn/Mg intermetallic phases, in which Zn atoms replace Mg atoms in the Y_5Mg_{24} structure, several single crystals with different refined compositions $Y_{5-x}Mg_{24+x}$ were found. $Y_{5-x}Mg_{24+x}$ compounds preserve the parent α-Mn structure type.

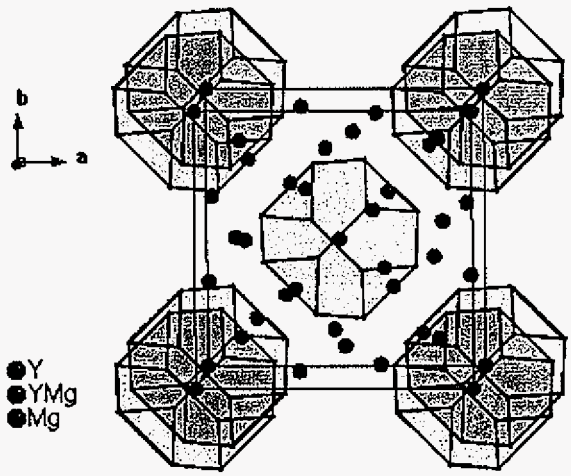

Discussion

Details of the single crystal data collection parameters and crystallographic refinement results for $Y_{5-x}Mg_{24+x}$ are listed in the Table 1. The resulting occupancies, atomic parameters, and residuals are listed in Tables 2 and 3.

Table 1. Crystal data and structure refinements for $Y_{5-x}Mg_{24+x}$.

x	1.47	0.94
Empirical formula	$Y_{4.06(3)}Mg_{24.94(3)}$	$Y_{3.52(2)}Mg_{25.47(4)}$
Temperature	293(2) K	293(2) K
Wavelength	0.71073 Å	0.71073 Å
Crystal system	cubic	cubic
Space group	I -4 3 m (no. 217)	I -4 3 m (no. 217)
Unit cell dimensions, Å	a = 11.2225(13)	a = 11.2578(13)
Volume, $Å^3$	1413.4(3)	1426.8(3)
Z	2	2
Absorption coeff., mm^{-1}	23.014	10.578
F(000)	2052	966
Crystal size, mm^3	0.23 × 0.22 × 0.35	0.16 × 0.23 × 0.31
$2\theta_{max}$ for data collection, °	56.30	56.38
Index ranges, *h,k,l*	-14/14, -10/14, -11/14	-14/14, -14/14, -14/14
Reflections collected	4333	5889
Independent reflections	356 [R(int) = 0.0372]	356 [R(int) = 0.0437]
Data / parameters	356 / 19	356 / 18
Goodness-of-fit on F^2	1.188	1.032
R indices [I>2sigma(I)]	R1 = 0.0194, wR2 = 0.0499	R1 = 0.0142, wR2 = 0.0278
R indices (all data)	R1 = 0.0202, wR2 = 0.0500	R1 = 0.0160, wR2 = 0.0279
Extinction coefficient	0.0031(4)	0.016(9)
($\Delta\rho$) peak and hole, $e.Å^{-3}$	0.289 and -0.288	0.277 and -0.180

Table 2. Atomic coordinates and equivalent isotropic displacement parameters ($Å^2 \times 10^3$) for $Y_{5-x}Mg_{24+x}$. U(eq) is defined as one third of the trace of the orthogonalized U_{ij} tensor.

Atom	Wyck.	Occ.	x	y	z	U(eq)
$Y_{4.06(3)}Mg_{24.94(3)}$						
Y1	2*a*	1	0	0	0	14(1)
Y2	8*c*	0.633(4)	0.1867(1)	0.1867(1)	0.8133(1)	17(1)
Mg2	8*c*	0.367(4)	0.1867(1)	0.1867(1)	0.8133(1)	17(1)
Mg3	24*g*	1	0.0908(1)	0.0908(1)	0.2794(1)	19(1)
Mg4	24*g*	1	0.1429(1)	0.4654(1)	0.1429(1)	26(1)
$Y_{3.52(2)}Mg_{25.47(2)}$						
Y1	2*a*	1	0	0	0	13(1)
Y2	8*c*	0.764(3)	0.1870(1)	0.1870(1)	0.1870(1)	16(1)
Mg2	8*c*	0.236(3)	0.1870(1)	0.1870(1)	0.1870(1)	16(1)
Mg3	24*g*	1	0.0904(1)	0.0904(1)	0.21948	19(1)
MgG4	24*g*	1	0.1431(1)	0.4658(1)	0.1431(1)	23(1)

Table 3. Anisotropic displacement parameters ($Å^2 \times 10^3$) for $Y_{5-x}Mg_{24+x}$. The anisotropic displacement factor exponent takes the form: $-2\pi^2[h^2a^2U_{11} + ... + 2\,h\,k\,a\,b\,U_{12}]$

	U_{11}	U_{22}	U_{33}	U_{23}	U_{13}	U_{12}
$Y_{4.06(3)}Mg_{24.94(3)}$						
Y(1)	14(1)	14(1)	14(1)	0	0	0
Y(2)	17(1)	17(1)	17(1)	0(1)	0(1)	0(1)
Mg(2)	17(1)	17(1)	17(1)	0(1)	0(1)	0(1)
Mg(3)	20(1)	20(1)	18(1)	-2(1)	2(1)	1(1)
Mg(4)	27(1)	24(1)	27(1)	0(1)	-2(1)	0(1)
$Y_{3.52(2)}Mg_{25.47(2)}$						
Y(1)	13(1)	13(1)	13(1)	0	0	0
Y(2)	16(1)	16(1)	16(1)	0(1)	0(1)	0(1)
Mg(2)	16(1)	16(1)	16(1)	0(1)	0(1)	0(1)
Mg(3)	19(1)	19(1)	18(1)	-1(1)	-1(1)	-1(1)
Mg(4)	24(1)	20(1)	24(1)	1(1)	1(1)	1(1)

APPENDIX A-3

The Crystal Structure of

$Al_{12-x}Zn_xMg_{17}$ (x = 0, 1.19, and 1.58)

Introduction

New $Al_{12-x}Zn_xMg_{17}$ compounds were synthesized to investigate the structure of pseudobinary $Al_{12}Mg_{17}$ intermetallics in which Zn atoms replace Al atoms.

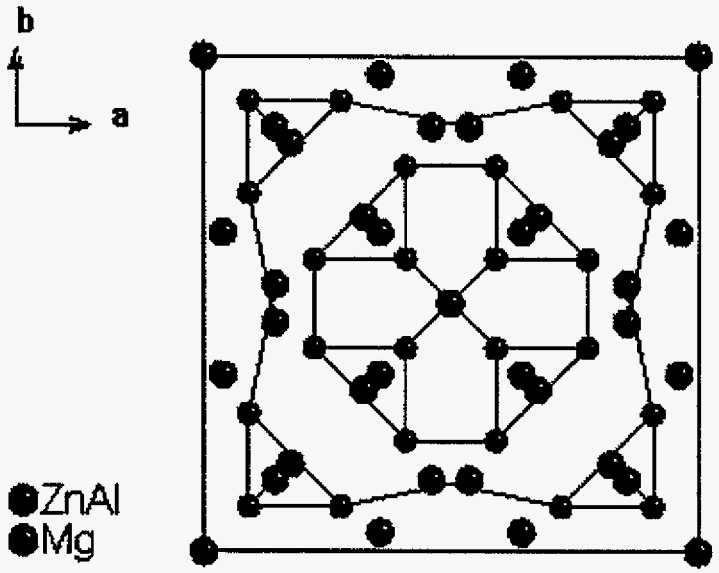

Discussion

First, I refined the structure without mixed sites and, then, I refined again with shared sites. The R indices [$I>2\sigma(I)$] are listed in Table 1.

Table 1. Two different refinement methods for ternary $Al_{12-x}Zn_xMg_{17}$ compounds.

R1	$Al_{12}Mg_{17}$	$Al_{10.43(5)}Zn_{1.58(5)}Mg_{17}$	$Al_{10.81(5)}Zn_{1.19(5)}Mg_{17}$
without mixing sites	1.90	4.37	3.23
with mixing sites	1.90	2.38	1.74

Details of the single crystal data collection parameters and crystallographic refinement results for $Al_{12-x}Zn_xMg_{17}$ are listed in the Table 2. The resulting occupancies, atomic parameters, and residuals are listed in Tables 3 and 4.

Table 2. Crystal data and structure refinement for $Al_{12-x}Zn_xMg_{17}$ compounds.

Identification code	1	2	3
Empirical formula	$Al_{12}Mg_{17}$	$Al_{10.43(5)}Zn_{1.58(5)}Mg_{17}$	$Al_{10.81(5)}Zn_{1.19(5)}Mg_{17}$
Temperature , K	293(2)	293(2)	293(2)
Wavelength , Å	0.71073	0.71073	0.71073
Crystal system	cubic	cubic	cubic
Space group	I -4 3 m (no. 217)	I -4 3 m (no. 217)	I -4 3 m (no. 217)
Unit cell dimensions, Å	a = 10.5089(12)	a = 10.4609(12)	a = 10.4498(12)
Volume, $Å^3$	1160.6(2)	1144.7(2)	1141.1(2)
Z	2	2	2
Absorption coeff., mm^{-1}	1.462	2.787	1.474
F(000)	750	648	394
Crystal size, mm^3	0.16 × 0.23 × 0.11	0.18 × 0.25 × 0.23	0.14 × 0.19 × 0.13
$2\theta_{max}$, °	56.52	56.48	56.54
Index ranges, h k l	-13/13 -13/13 -13/13	-7/13 -13/12 -11/13	-9/13 -13/13 -13/13
Reflections collected	5032	3544	3549
Independent reflections	295 [R(int) = 0.0226]	292 [R(int) = 0.0310]	284 [R(int) = 0.0352]
Data /parameters	295 / 18	292 / 18	284 / 18
Goodness-of-fit on F^2	1.204	1.156	1.089
R indices [I>2sigma(I)]	R1 = 0.0113, wR2 = 0.0248	R1 = 0.0146, wR2 = 0.0336	R1 = 0.0166, wR2 = 0.0352
R indices (all data)	R1 = 0.0115, wR2 = 0.0249	R1 = 0.0159, wR2 = 0.0338	R1 = 0.0180, wR2 = 0.0356
Extinction coefficient	0.0010(3)	0.03(5)	0.0000(3)
$\Delta(\rho)$peak and hole, $e.Å^{-3}$	0.121 and -0.130	0.163 and -0.219	0.242 and -0.161

Table 3. Atomic coordinates and equivalent isotropic displacement parameters ($Å^2 \times 10^3$) for $Al_{12-x}Zn_xMg_{17}$. U(eq) is defined as one third of the trace of the orthogonalized U_{ij} tensor.

	Wyck.	Occ.	*x*	*y*	z	U(eq)
$Al_{12}Mg_{17}$						
Al(1)	24*g*	1	0.0906(1)	0.0906(1)	0.7233(1)	17(1)
Mg(2)	8*c*	1	0.1745(1)	0.1745(1)	0.1745(1)	22(1)
Mg(3)	24*g*	1	0.1433(1)	0.1433(1)	0.4607(1)	18(1)
Mg(4)	2*a*	1	0	0	0	21(1)
$Al_{10.43(5)}Zn_{1.58(5)}Mg_{17}$						
Al(1)	24*g*	0.869(2)	0.0905(1)	0.0905(1)	0.2766(1)	18(1)
Zn(1)	24*g*	0.132(2)	0.0905(1)	0.0904(1)	0.2766(1)	18(1)
Mg(1)	8*c*	1	0.1745(1)	0.1745(1)	0.1745(1)	19(1)
Mg(2)	24*g*	1	0.1438(1)	0.1438(1)	0.4613(1)	24(1)
Mg(3)	2*a*	1	0	0	0	24(1)
$Al_{10.81(5)}Zn_{1.19(5)}Mg_{17}$						
Al(1)	24*g*	0.901(2)	0.0906(1)	0.0906(1)	0.7231(1)	19(1)
Zn(1)	24*g*	0.099(2)	0.0906(1)	0.0906(1)	0.7231(1)	19(1)
Mg(2)	8*c*	1	0.1752(1)	0.1752(1)	0.1752(1)	25(1)
Mg(3)	24*g*	1	0.1437(1)	0.1437(1)	0.4616(1)	20(1)
Mg(4)	2*a*	1	0	0	0	24(1)

Table 4. Anisotropic displacement parameters ($Å^2 \times 10^3$) for $Al_{12-x}Zn_xMg_{17}$. The anisotropic displacement factor exponent takes the form: $-2\pi^2[h^2a^2U_{11} + ... + 2\ h\ k\ a\ b\ U_{12}\ ]$.

	U_{11}	U_{22}	U_{33}	U_{23}	U_{13}	U_{12}
$Al_{12}Mg_{17}$						
Al(1)	18(1)	18(1)	16(1)	0(1)	0(1)	0(1)
Mg(2)	22(1)	22(1)	22(1)	1(1)	1(1)	1(1)
Mg(3)	19(1)	19(1)	17(1)	2(1)	2(1)	3(1)
Mg(4)	21(1)	21(1)	21(1)	0	0	0
$Al_{10.43(5)}Zn_{1.58(5)}Mg_{17}$						
Al(1)	19(1)	19(1)	17(1)	0(1)	0(1)	0(1)
Zn(1)	19(1)	19(1)	17(1)	0(1)	0(1)	0(1)
Mg(1)	20(1)	18(1)	20(1)	3(1)	4(1)	3(1)
Mg(2)	24(1)	24(1)	24(1)	2(1)	2(1)	2(1)
Mg(3)	24(1)	24(1)	24(1)	0	0	0
$Al_{10.81(5)}Zn_{1.19(5)}Mg_{17}$						
Al(1)	17(1)	19(1)	19(1)	-1(1)	0(1)	0(1)
Zn(1)	17(1)	19(1)	19(1)	-1(1)	0(1)	0(1)
Mg(2)	25(1)	25(1)	25(1)	-2(1)	2(1)	-2(1)
Mg(3)	18(1)	21(1)	21(1)	-4(1)	3(1)	-3(1)
Mg(4)	24(1)	24(1)	24(1)	0	0	0

APPENDIX A-4

The Crystal Structure of

$Ta_4Mn_{2.18(3)}Al_{5.82(3)}$ compound

Introduction

During a study on possible ternary Mn/Mg/Al intermetallic phases, when the reaction temperature exceeds 1000°C, the Ta container reacts with reactants and, thus, $Ta_4Mn_{2.18(3)}Al_{5.82(3)}$ with the $MgZn_2$-type structure was found.

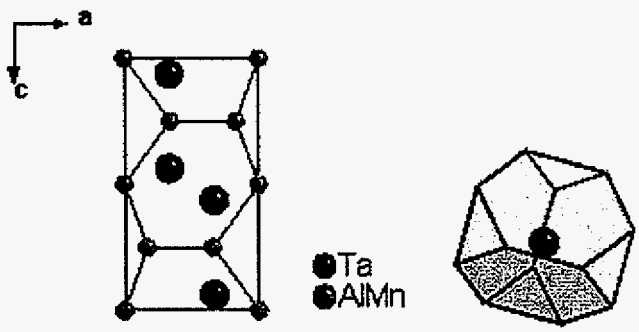

Discussion

Details of the single crystal data collection parameters and crystallographic refinement results for $Ta_4Mn_{2.18(3)}Al_{5.82(3)}$ are listed in the Table 1. The resulting occupancies, atomic parameters, and residuals are listed in Tables 2 and 3.

Table 1. Crystal data and structure refinement for $Ta_4Mn_{2.18(3)}Al_{5.82(3)}$.

Identification code	$Ta_4Mn_{2.18(3)}Al_{5.82(3)}$
Temperature	293(2) K
Wavelength	0.71073 Å
Crystal system	hexagonal
Space group	$P\,6_3/m\,m\,c$ (no. 194)
Unit cell dimensions	a = 5.0429 (7) Å
	c = 8.2161(16) Å
Volume	180.95(5) $Å^3$
Z	1
Absorption coefficient	20.921 mm^{-1}
F(000)	393
Crystal size	0.25 × 0.26 × 0.30 mm^3
Theta range for data collection	4.67 to 27.80°.
Index ranges	$-6 \le h \le 6, -6 \le k \le 6, -10 \le l \le 10$
Reflections collected	907
Independent reflections	107 [R(int) = 0.0521]
Completeness to theta = 27.80°	100.0 %
Refinement method	Full-matrix least-squares on F^2
Data / parameters	107 / 13
Goodness-of-fit on F^2	1.224
Final R indices [I>2sigma(I)]	R1 = 0.0217, wR2 = 0.0466
R indices (all data)	R1 = 0.0241, wR2 = 0.0475
Extinction coefficient	0.0021(10)
Largest diff. peak and hole	1.287 and -1.576 e.$Å^{-3}$

Table 2. Atomic coordinates and equivalent isotropic displacement parameters ($Å^2 \times 10^3$) for $Ta_4Mn_{2.18(3)}Al_{5.82(3)}$. U(eq) is defined as one third of the trace of the orthogonalized U_{ij} tensor.

Atom	Wyck.	Occ.	x	y	z	U(eq)
Ta1	4*f*	1	1/3	2/3	0.0627(1)	4(1)
Al2	2a	0.90(4)	0	0	0	8(2)
Mn2	2a	0.10(4)	0	0	0	8(2)
Al3	6h	0.67(2)	0.1711(4)	0.8289(4)	¼	8(1)
Mn3	6h	0.33(2)	0.1711(4)	0.8289(4)	¼	8(1)

Table 3. Anisotropic displacement parameters ($Å^2 \times 10^3$) for $Ta_4Mn_{2.18(3)}Al_{5.82(3)}$. The anisotropic displacement factor exponent takes the form: $-2\pi^2[h^2a^2U_{11} + ... + 2\ h\ k\ a\ b\ U_{12}\ ]$.

	U_{11}	U_{22}	U_{33}	U_{23}	U_{13}	U_{12}
Ta(1)	4(1)	4(1)	4(1)	0	0	2(1)
Al(2)	9(3)	9(3)	6(4)	0	0	5(1)
Mn(2)	9(3)	9(3)	6(4)	0	0	5(1)
Al(4)	10(2)	10(2)	9(2)	0	0	7(1)
Mn(4)	10(2)	10(2)	9(2)	0	0	7(1)

APPENDIX A-5

The Crystal Structures of

$REFe_2Si_2$ (RE = La, and Ce)

Introduction

In the course of a systematic search for novel magnetocaloric effect materials in the $REFe_{13-x}Si_x$ system, single crystals of $REFe_2Si_2$ (RE = La, Ce) with $BaAl_4$-type structure are obtained whose structures are only reported from X-ray powder refinement.

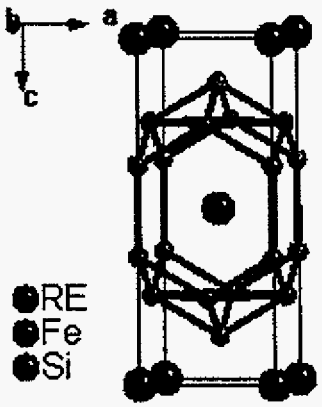

Discussion

Details of the single crystal data collection parameters and crystallographic refinement results for $REFe_2Si_2$ are listed in the Table 1. The resulting occupancies, atomic parameters, and residuals are listed in Table 2 and 3.

Table 1. Crystal data and structure refinements for $REFe_2Si_2$ (RE = La, Ce)

Identification code	$LaFe_2Si_2$	$CeFe_2Si_2$
Temperature, K	293(2)	293(2)
Wavelength, Å	0.71073	0.71073
Crystal system	tetragonal	tetragonal
Space group	*I* 4/*mmm* (no. 139)	*I* 4/*mmm* (no. 139)
Unit cell dimensions, Å	$a = 4.0380(6)$	$a = 3.9967(6)$
	$c = 10.172(2)$	$c = 9.870(2)$
Volume, Å^3	165.85(5)	157.66(5)
Z	2	2
Absorption coefficient, mm^{-1}	21.706	23.722
F(000)	274	276
Crystal size, mm^3	0.18 × 0.23 × 0.25	0.21 × 0.16 × 0.28
$2\theta_{max}$ for data collection, °	46.44	54.66
Index ranges *h, k, l*	-4/4, -4/4, -11/10	-4/5, -4/5, -12/11
Reflections collected	490	407
Independent reflections	52 [R(int) = 0.0170]	76 [R(int) = 0.0352]
Refinement method	Full-matrix least-squares on F^2	Full-matrix least-squares on F^2
Data / parameters	52 / 9	76 / 9
Goodness-of-fit on F^2	1.321	1.210
Final R indices [I>2sigma(I)]	R1 = 0.0264, wR2 = 0.0655	R1 = 0.0199, wR2 = 0.0428
R indices (all data)	R1 = 0.0280, wR2 = 0.0669	R1 = 0.0199, wR2 = 0.0428
Extinction coefficient	0.000(3)	0.013(2)
Largest diff. peak and hole e.Å^{-3}	2.704 and -0.596	1.147 and -0.869

Table 2. Atomic coordinates and equivalent isotropic displacement parameters ($Å^2 \times 10^3$) for $REFe_2Si_2$. U(eq) is defined as one third of the trace of the orthogonalized U_{ij} tensor.

	x	y	z	U(eq)
$LaFe_2Si_2$				
La(1)	0	0	0	7(1)
Fe(2)	0	½	¼	9(1)
Si(3)	0	0	0.3669(5)	8(1)
$CeFe_2Si_2$				
Ce(1)	0	0	0	7(1)
Fe(2)	0	½	¼	7(1)
Si(3)	0	0	0.3716(2)	7(1)

Table 3. Anisotropic displacement parameters ($Å^2 \times 10^3$) for $REFe_2Si_2$. The anisotropic displacement factor exponent takes the form: $-2\pi^2[h^2a^2U_{11} + ... + 2\ h\ k\ a\ b\ U_{12}]$.

	U11	**U22**	**U33**	**U23**	**U13**	**U12**
$LaFe_2Si_2$						
La(1)	4(1)	4(1)	12(1)	0	0	0
Fe(2)	6(1)	6(1)	14(2)	0	0	0
Si(3)	5(2)	5(2)	15(3)	0	0	0
$CeFe_2Si_2$						
Ce(1)	6(1)	6(1)	9(1)	0	0	0
Fe(2)	6(1)	6(1)	8(1)	0	0	0
Si(5)	7(1)	7(1)	8(1)	0	0	0

APPENDIX A-6

The Crystal Structure of A New binary iron silicide:

$Fe_4(Fe_{1-x}Si_x)_3$ (x = 0.503)

Introduction

This compound is obtained as a side product from the synthesis of $LaFe_{13-x}Si_x$. This is a new binary iron silicide with Fe_3Ga_4-type structure. It adopts a base-centered monoclinic structure with space group of *C* 2/m (no. 12) (lattice parameter of a = 10.1588(13), b = 7.8638(13), c = 8.0239(13) Å, and β =105.609 Å). Only two compounds are known for the Fe_3Ga_4-type structure: Fe_3Ga_4 and Cr_3Ga_4.

Magnetic properties of pseudobinary $(Fe_{1-x}T_x)_3Ga_4$ (T = Ti, Cr) ($0 \leq x \leq 0.15$ for Ti, and $0 \leq x \leq 0.20$ for Cr) show competition between ferromagnetic and antiferro-magnetic interactions, which leads to interesting spin glass properties.[1-2] Also these compounds show different site preferences for different Fe sites depending on the transition metals. Several iron silicides are known[3], and listed in Table 1.

Table 1. Crystal parameters for binary metal silicides.

	Crystal system	Space group	Prototype	Lattice constants (Å)		
				a	b	c
Fe_3Si	Cubic	*Im*3*m*	W	2.841		
Fe_2Si	Cubic	*Pm*3*m*		2.81		
Fe_5Si_3	Hexagonal	$P6_3/mcm$	Mn_5Si_3	2.759		4.720
FeSi	Cubic	$P2_13$		4.488		
α-$FeSi_2$	Tetragonal	*P*4/*mmm*		2.694		5.136
β-$FeSi_2$	Orthorhombic	*Cmca*	$FeSi_2$	9.879	7.799	7.839

Discussion

Details of the single crystal data collection parameters and crystallographic refinement results for $Fe_4(Fe_{1-x}Si_x)_3$ (x = 1.51) are listed in the Table 2. The resulting occupancies, atomic parameters, and residuals are listed in Table 3 and 4

Table 2. Crystal data and structure refinement for $Fe_4(Fe_{1-x}Si_x)_3$ (x = 0.503)

Empirical formula	$Fe_{5.49(1)}Si_{1.51(1)}$
Temperature	293(2) K
Wavelength	0.71073 Å
Crystal system	monoclinic
Space group	*C* 1 2/m 1 (no. 12)
Unit cell dimensions	a = 10.159(2) Å
	b = 7.8636(16) Å β= 105.61(3)°
	c = 8.0239(16) Å
Volume	617.3(2) $Å^3$
Z	6
Absorption coefficient	27.894 mm^{-1}
F(000)	1388
Crystal size	0.10 × 0.08 × 0.12 mm^3
$2\theta_{max}$ for data collection	56.38°
Index ranges	$-13 \le h \le 13, -10 \le k \le 10, -10 \le l \le 10$
Reflections collected	2637
Independent reflections	764 [R(int) = 0.0366]
Completeness to theta = 28.19°	94.0 %
Refinement method	Full-matrix least-squares on F^2
Data / parameters	764 / 61
Goodness-of-fit on F^2	1.099
Final R indices [I>2sigma(I)]	R1 = 0.0288, wR2 = 0.0660
R indices (all data)	R1 = 0.0349, wR2 = 0.0682
Extinction coefficient	0.0027(2)
Largest diff. peak and hole	0.878 and -1.246 e.$Å^{-3}$

Table 3. Atomic coordinates and equivalent isotropic displacement parameters ($Å^2 \times 10^3$) for $Fe_4(Fe_{1-x}Si_x)_3$ (x = 0.503). U(eq) is defined as one third of the trace of the orthogonalized U_{ij} tensor.

	Wyck.	occ.*	*x*	*y*	*z*
Fe(1)	8*j*	1	0.1521(1)	0.01923(1)	0.5563(1)
Fe(2)	8*j*	1	0.1044(1)	0.2094(1)	0.1526(1)
Fe(3)	4*i*	1	0.4527(1)	0	0.6466(1)
Fe(4)	4*i*	1	0.2188(1)	0	0.9121(1)
Fe/Si(5)	2*b*	0.601(11)	0	½	0
Fe/Si(6)	4*i*	0.484(8)	0.2700(1)	0	0.3467(2)
Fe/Si(7)	8*j*	0.483(6)	0.1400(1)	0.3073(1)	0.8503(1)
Fe/Si(8)	4*i*	0.484(8)	-0.0018(1)	0	0.6744(2)

* Fe occupancy within the mixed site.

Table 4. Anisotropic displacement parameters ($Å^2 \times 10^3$) for $Fe_4(Fe_{1-x}Si_x)_3$ (x = 0.503). The anisotropic displacement factor exponent takes the form: $-2\pi^2[h^2a^2U_{11} + ... + 2\ h\ k\ a\ b\ U_{12}]$.

	U_{11}	U_{22}	U_{33}	U_{23}	U_{13}	U_{12}
Fe(1)	14(1)	12(1)	8(1)	-5(1)	8(1)	-8(1)
Fe(2)	5(1)	11(1)	7(1)	5(1)	3(1)	2(1)
Fe(3)	9(1)	10(1)	7(1)	0	-2(1)	0
Fe(4)	13(1)	5(1)	11(1)	0	-6(1)	0
Fe/Si(5)	11(1)	9(1)	9(1)	0	4(1)	0
Fe/Si(6)	11(1)	9(1)	7(1)	0	1(1)	0
Fe/Si(7)	10(1)	11(1)	9(1)	-1(1)	4(1)	0(1)
Fe/Si(8)	11(1)	11(1)	9(1)	0	4(1)	0

References

1. Philippe, Par M. J.; Roques, M. *Acta Cryst.* **1975**, B31, 477.

2. Kobeissi, M.A. ; Hutchings, J.A. ; Appleyard, P.G. ; Thomas, M.F. ; Booth, J.G. *J. Phys. ; Condens. Matter.* **1992**, 11, 6251.

3. Maex, Karen; Van Rossum, , Marc *Properties of Metal Silicides* **1995**; INSPEC, the Institution of Electrical Engineers, London, United Kingdom, No.14.

ACKNOWLEDGMENT

My special thanks go to Dr. Gordon J. Miller for his guidance, support, and commitment to me and my graduate research experience through this endeavor. I also want to express my sincerest appreciation to other members of my dissertation committee: Dr. John D.Corbett, Dr. Pat Thiel, Dr. Keith Woo, and Dr. Vitalij Pecharsky.

I would like to thank my colleagues in the Miller group for their support as well: Hyunjin Ko, Tae-Soo You, Smouahn Misra, Yurij Mozharivskyj and Wonyoung Choe. Thanks to many of the chemistry and material science & engineering faculty members for helpful discussions and assistance about my research and my career in chemistry.

Last, but certainly not the least, my deepest gratitude goes to my *precious children*, Hyun-Gi Lee, and Christina Lee, and especially to my *lovely husband*, Chanyoung Lee, for their constant encouragement and total support in my attainment of this goal.

This work was supported by the NSF and the DOE Complex Phenomena Initiative.

ACKNOWLEDGMENT

My special thanks go to Dr. Gordon J. Miller for his guidance, support, and commitment to me and my graduate research experience through this endeavor. I also want to express my sincerest appreciation to other members of my dissertation committee: Dr. John D.Corbett, Dr. Pat Thiel, Dr. Keith Woo, and Dr. Vitalij Pecharsky.

I would like to thank my colleagues in the Miller group for their support as well: Hyunjin Ko, Tae-Soo You, Smouahn Misra, Yurij Mozharivskyj and Wonyoung Choe. Thanks to many of the chemistry and material science & engineering faculty members for helpful discussions and assistance about my research and my career in chemistry.

Last, but certainly not the least, my deepest gratitude goes to my *precious children*, Hyun-Gi Lee, and Christina Lee, and especially to my *lovely husband*, Chanyoung Lee, for their constant encouragement and total support in my attainment of this goal.

This work was performed at Ames Laboratory under Contract No.W-7405-Eng-82 with the U.S. Department of Energy. The United States government has assigned the DOE Report number IS-T 2306 to this thesis.